UNIVERSIDADE FEDERAL DE SANTA CATARINA
CAMPUS REITOR JOÃO DAVID FERREIRA LIMA
CENTRO TECNOLÓGICO
PROGRAMA DE PÓS-GRADUAÇÃO EM ENGENHARIA ELÉTRICA

Luiz Guilherme Luttke Gonçalves da Silva

Energy-based models for the magneto-elastic behavior of ferromagnetic materials

Gif-sur-Yvette/Florianópolis
2024

Luiz Guilherme Luttke Gonçalves da Silva

Energy-based models for the magneto-elastic behavior of ferromagnetic materials

Tese submetida para o Programa de Pós-Graduação em Engenharia Elétrica da Universidade Federal de Santa Catarina e à École doctorale n° 575, Electrical, Optical, Bio : Physics and Engineering (EOBE) da Instituição Université Paris-Saclay em regime de cotutela para a obtenção do grau de Doutor em Engenharia Elétrica.
Orientadores: Prof. Laurent Bernard, Dr. (UFSC) e Prof. Laurent Daniel, Dr. (UPSaclay)

Gif-sur-Yvette/Florianópolis
2024

Luiz Guilherme Luttke Gonçalves da Silva

Energy-based models for the magneto-elastic behavior of ferromagnetic materials

Thesis submitted to the Graduate Program in Electrical Engineering of the Federal University of Santa Catarina and to the École doctorale n° 575, Electrical, Optical, Bio : Physics and Engineering (EOBE) of the Université Paris-Saclay on a co-supervision basis for the degree of Doctor of Electrical Engineering.
Supervisors: Prof. Laurent Bernard, Dr. (UFSC) e Prof. Laurent Daniel, Dr. (UPSaclay)

Gif-sur-Yvette/Florianópolis
2024

Ficha catalográfica gerada por meio de sistema automatizado gerenciado pela BU/UFSC.
Dados inseridos pelo próprio autor.

Silva, Luiz Guilherme Luttke Gonçalves da
Energy-based models for the magneto-elastic behavior of ferromagnetic materials / Luiz Guilherme Luttke Gonçalves da Silva ; orientador, Laurent Bernard, orientador, Laurent Daniel, 2024.
180 p.

Tese (doutorado) - Universidade Federal de Santa Catarina, Centro Tecnológico, Programa de Pós-Graduação em Engenharia Elétrica, Florianópolis, 2024.

Inclui referências.

Trabalho elaborado em regime de co-tutela.

1. Engenharia Elétrica. 2. Engenharia elétrica. 3. Acoplamento magnetoelástico. 4. Histerese magnética. 5. Modelagem multiescala. I. Bernard, Laurent. II. Daniel, Laurent III. Universidade Federal de Santa Catarina. Programa de Pós-Graduação em Engenharia Elétrica. IV. Título.

Luiz Guilherme Luttke Gonçalves da Silva

Energy-based models for the magneto-elastic behavior of ferromagnetic materials

O presente trabalho em nível de doutorado foi avaliado e aprovado por banca examinadora composta pelos seguintes membros:

Prof. Olivier Hubert, Dr.
ENS Paris-Saclay / Université Paris-Saclay (UPSaclay)

Prof. Guillaume Parent, Dr.
Université d'Artois

Prof. Fabien Sixdenier, Dr.
Université Claude Bernard Lyon 1

François Henrotte, Dr.
University of Liège

Prof. Manfred Kaltenbacher, Dr.
Graz University of Technology

Prof. Nelson Sadowski, Dr.
Universidade Federal de Santa Catarina

Prof. Laurent Bernard, Dr.
Orientador
Universidade Federal de Santa Catarina (UFSC)

Prof. Laurent Daniel, Dr.
Orientador
CentraleSupélec / Université Paris-Saclay (UPSaclay)

Certificamos que esta é a **versão original e final** do trabalho de conclusão que foi julgado adequado para obtenção do título de Doutor em Engenharia Elétrica.

Documento assinado digitalmente
Telles Brunelli Lazzarin
Data: 09/07/2024 15:29:57-0300
CPF: ***.400.719-**
Verifique as assinaturas em https://v.ufsc.br

Telles Brunelli Lazzarin, Dr.
Coordenador do Programa de Pós-Graduação em Engenharia Elétrica

Documento assinado digitalmente
Laurent Didier Bernard
Data: 08/07/2024 10:54:11-0300
CPF: ***.804.339-**
Verifique as assinaturas em https://v.ufsc.br

Laurent Bernard, Dr.
Orientador

Gif-sur-Yvette/Florianópolis, 2024

ACKNOWLEDGMENTS

I want to thank my supervisors, Laurent Daniel and Laurent Bernard, for the opportunity to work with them during these past 3 years. With your guidance, patience, and availability for discussions, I could grow as a researcher and person.

I want to thank Guillaume Parent and Fabien Sixdenier for have accepted reported my thesis manuscript, and for their important remarks that helped to improve the quality of this work. I also thank Olivier Hubert for having accepted the position of chair of my thesis jury and for his important comments. I want to thank François Henrotte and Manfred Kaltenbacher for their interest in my work and for the enriching discussions during my thesis defense. Special thanks to Nelson Sadowski for his willingness to take part in my thesis defense, despite the constraints of different time zones. It was a great honor for me to have a jury of such quality.

I would also like to thank Anouar Belahcen and Floran Martin for welcoming me at Aalto University during my stay in Finland, and for the scientific collaborations with them.

Many thanks to my colleagues of Muphy: Abdellahi, Abderraouf, Ali, Chaimae, Frédéric, Laurent S., Marcos, Safae, Taha, Mahmoud, and Mathieu, for the moments of friendship and readiness to help. I also thank Sandrine for helping me with administrative matters.

Thanks to the colleagues of Grucad for all the coffees and general discussions.

I would like to express my gratitude to Laurent Bernard, Laurent Daniel, the members of the EOBE (UPSaclay) and the PPGEEL (UFSC) for making the Cotutelle agreement possible.

Gostaria de agradecer à minha família: Celso, Bernadete, Andrey, Ana, Guilherme, Antonio e Valentina por todo o apoio ao longo desta tese. Vocês foram minha força em muitos momentos difíceis. Finalmente, gostaria de agradecer do fundo do meu coração à minha esposa, Paula, por aceitar embarcar nessa aventura francesa comigo. Obrigado por todo o seu amor, força, paciência e compreensão. Seu apoio foi fundamental para concluirmos essa etapa de nossas vidas.

Many thanks to all of you!

RESUMO

Os materiais ferromagnéticos apresentam magnetização e deformação de magnetostrição que dependem fortemente do campo magnético e da tensão mecânica. Esse comportamento acoplado pode ser utilizado para projetar sensores magnéticos para avaliação não-destrutiva, e máquinas elétricas de alta eficiência. Algumas características do comportamento magnético são a histerese, a anisotropia e a sensibilidade ao estado mecânico. Medições experimentais evidenciam a influência dos carregamentos mecânicos na magnetização e na deformação de magnetostrição, e diferentes comportamentos são observados quando se aplicam cargas magneto-elásticas estáticas ou dinâmicas. Este trabalho tem como objetivo propor um modelo de histerese magneto-elástica no qual as limitações normalmente encontradas em modelos da literatura são tratadas. A modelagem é feita pela associação de um modelo anisterético multiescala com uma abordagem energética da histerese magnética. Os parâmetros do modelo para os comportamentos reversíveis e irreversíveis são identificados a partir da caracterização uniaxial sob tensões mecânicas. Além disso, são apresentados resultados experimentais sob diversos carregamentos magneto-elásticos de forma a testar as capacidades preditivas da modelagem. O modelo é inicialmente desenvolvido para representar o comportamento magneto-elástico sob tensão mecânica constante, levando em conta o caráter multiaxial dos carregamentos, os efeitos da textura cristalográfica, o efeito da tensão mecânica no campo coercitivo, o comportamento não-monotônico da permeabilidade em função da tensão mecânica, e a queda das perdas por histerese sob campo girante próximo à saturação. O modelo é analisado em diversas configurações complexas com resultados satisfatórios. Uma abordagem semelhante é desenvolvida para representar a histerese magneto-elástica sob campo magnético constante e tensão mecânica variável. Esses dois modelos baseados no balanço energético são termodinamicamente consistentes, com parâmetros identificados a partir de medições uniaxiais, e podem representar o comportamento magnético em configurações complexas (3D). Por fim, dois modelos são propostos para considerar variações simultâneas no campo magnético e na tensão mecânica. Suas limitações são discutidas, e possíveis melhorias são apresentadas como perspectivas para este trabalho.

Palavras-chave: Modelo de histerese, Acoplamento magneto-elástico, Modelagem multiescala, Tensão mecânica multiaxial

RESUMO EXPANDIDO

Introdução

Materiais magnéticos são essenciais em diversas aplicações, incluindo sensores para avaliação não-destrutiva Bouterfas et al. [2023], Eslamlou et al. [2023], captura de energia (do inglês *energy harvesting*) Daniel et al. [2023], Liu et al. [2024], Zangho et al. [2024] e máquinas elétricas Krings et al. [2017]. Ainda que diferentes em relação ao respectivo uso - sensores magnéticos, sistemas de recuperação de energia, ou conversão eletromecânica - em comum a todas as aplicações o desenvolvimento de modelos que descrevam o comportamento de materiais magnéticos é essencial no projeto de dispositivos de alta confiabilidade e eficiência.

O comportamento de materiais magnéticos é complexo devido a efeitos como a anisotropia magnética Jiang et al. [2018], Tolentino et al. [2022], a histerese ou comportamento dissipativo, a dependência da frequência do carregamento aplicado de La Barrière et al. [2012], e efeitos acoplados, os quais resultam em modificações no comportamento magnético devido à aplicação de tensões mecânicas Li et al. [2024] ou temperatura Banu et al. [2023].

O efeito de tensões mecânicas em materiais magnéticos resulta em efeitos positivos ou negativos, dependendo da aplicação. Por exemplo, processos de fabricação podem induzir tensões mecânicas nas partes magnéticas de máquinas elétricas, podendo resultar em aumento das perdas magnéticas, e por consequência, afetar a eficiência do dispositivo. Por outro lado, sistemas de captura de energia e sensores magnéticos beneficiam-se desse comportamento acoplado.

O principal objetivo dessa tese é a análise e desenvolvimento de um modelo de histerese magneto-elástico no qual as limitações presentes em modelos da literatura são parcialmente ou totalmente removidas. Três fatores chaves são considerados no desenvolvimento de uma relação constitutiva: (a) a possibilidade de considerar carregamentos magneto-mecânicos multiaxiais, (b) a consistência termodinâmica, de forma que as perdas possam ser calculadas com precisão em qualquer ponto de operação, e (c) o custo computacional de forma que o modelo possa ser implementado em ferramentas de análise numérica.

Capítulo 2: Modelagem do comportamento magneto-elástico

Os conceitos físicos e expressões relacionadas ao comportamento desacoplado mecânico

e magnético são introduzidos nesse capítulo. Os conceitos de deformação e tensão mecânica são definidos a partir de uma abordagem de mecânica dos meios contínuos sob a hipótese de deformações infinitesimais. As noções de magnetização, campo magnético e indução são estabelecidas por meio das equações de Maxwell restritas ao regime quase-estático.

A modelagem do comportamento acoplado magneto-elástico pode ser separada em duas classes: comportamento reversível ou anisterético (efeitos dissipativos não são considerados), e comportamento irreversível ou histerese. O processo de magnetização envolve fenômenos complexos observados em diferentes escalas. Dessa forma, uma abordagem multi-escala Daniel et al. [2008] é apresentada na literatura. Essa abordagem permite a aplicação de carregamentos multiaxiais e o protocolo de identificação dos parâmetros é claro.

Em relação a histerese magnetoelástica, a modelagem geralmente é definida na escala macros-cópica. Embora diversos modelos são apresentados na literatura, como por exemplo Jiles-Atherton, Preisach e Armstrong, nenhum desses atende simultaneamente os três fatores chaves mencionados na Introdução. Uma abordagem que atende os requisitos de consistência termodinâmica e baixo tempo de simulação, mas inicialmente desenvolvida apenas para o caso sem tensão mecânica é a modelo baseado na energia (do inglês, *energy-based*).

Capítulo 3: Caracterização experimental do comportamento magnetoelástico

Evidências experimentais do comportamento magneto-elástico são apresentadas nesse capítulo, de forma que medidas são realizadas em dispositivo uniaxial. O material ensaiado é um aço de baixo carbono (DC04) utilizado na indústria automotiva. O aparato experimental para a caracterização magneto-elástica é apresentado na Fig. 0.0.1. A parte mecânica consiste de uma máquina de tração/compressão. A parte magnética é composta por dois núcleos magnéticos de Fe-Si para assegurar o caminho do fluxo magnético. Um amplificador fornece corrente para uma bobina de excitação. O campo magnético é medido por meio de uma sonda de efeito Hall. A indução é obtida por meio da integração numérica da tensão induzida em uma bobina de medição disposta em torno da amostra (observe a área de medidas na Fig. 0.0.1). A magnetostrição é medida utilizando um sensor de deformação colado na amostra.

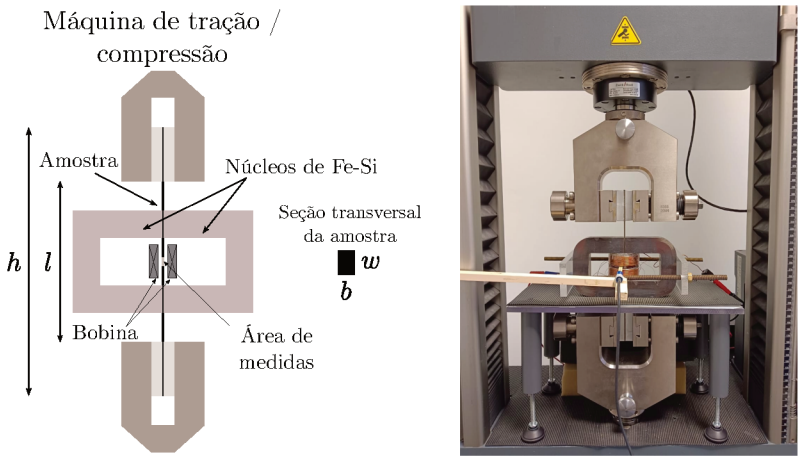

Figura 0.0.1: Bancada experimental para caracterização magneto-elástica sob tensões mecânicas uniaxiais.

Medidas do comportamento anisterético sob tensões mecânicas uniaxiais são realizadas. Além disso, o comportamento da histerese magnética é medido sob diversas configurações de carregamento magnetoelástico: considerando campo magnético variável e tensão mecânica estática, considerando tensão mecânica variável e campo magnético estático, e considerando que ambos campo magnético e tensão mecânica variam ao mesmo tempo.

Capítulo 4: Modelo de histerese magnetoelástico baseado na energia com aplicações sob tensão mecânica estática

Modelagem reversível - Modelo multiescala simplificado

O comportamento anisterético é modelado utilizando uma abordagem multiescala simplificada Daniel et al. [2015]. As escalas consideradas são ilustradas na Fig. 0.0.2. Nesta tese, o interesse é a modelagem do comportamento material na escala RVE. As seguintes premissas são consideradas: (a) o material é inicialmente isotrópico, (b) efeitos demagnetizantes internos são desprezíveis e (c) o campo magnético e a tensão mecânica sao homogêneos na escala do volume elementar representativo.

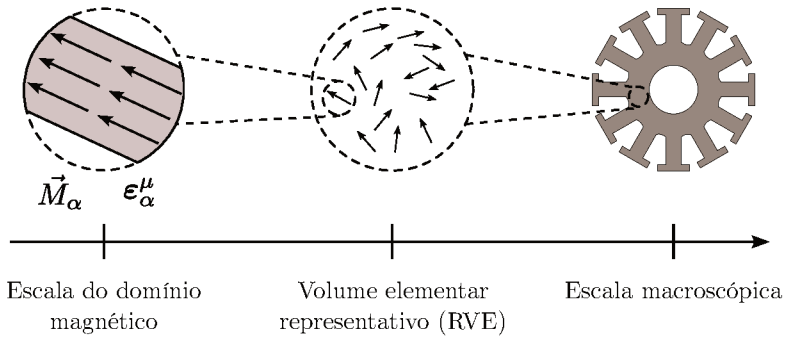

Figura 0.0.2: Escalas envolvidas na abordagem multiescala.

Por meio de um balanço energético na escala do dominio magnético, o qual consiste de termos de densidade de energia magnética e magneto-mecânica, a fração volumétrica correspondente a cada orientação de domínio é calculada utilizando uma distribuição Boltzmann. A magnetização e magnetostrição na escala macroscópica são então calculadas por meio da média ponderada das frações volumétricas.

É observado na literatura que o efeito de carregamentos mecânicos na magnetização é não monótono. O modelo simplificado multiescala não reproduz tal tendência. Esse comportamento pode ser descrito na modelagem adicionando um termo de segunda ordem na definição da energia magnetoelástica Hubert [2019]. Dessa forma, uma nova proposição de energia magnetoelástica é definida nesse trabalho, em termos de um único parâmetro, o qual é identificado a partir de medidas de permeabilidade magnética sob carregamentos mecânicos uniaxiais.

Modelagem irreversível

A histerese magnética é modelada utilizando uma abordagem termodinâmica e o conceito de variáveis internas. Tais variáveis são uma escolha de modelagem no qual complexos processos microscópicos que resultam em dissipação são unificados em uma ou mais grandezas. Na abordagem baseada na energia Henrotte et al. [2006], a magnetização é escolhida como variável interna. A dissipação é modelada por meio da analogia da histerese magnética com um sistema de atrito seco. Nesse caso, um parâmetro de dissipação é introduzido, e é relacionado diretamente com o campo coercitivo do laço de histerese. Além disso, o campo magnético é descrito pela soma de uma parte reversível, relacionada com processos termodinamicamente reversiveis, e uma parte irreversivel, relacionada com a dissipação. Efeitos de tensão mecânica são levados em conta por meio do comportamento anisterético, no qual o modelo multiescala é utilizado. Além disso, é experimentalmente observado que o campo coercitivo é fortemente

influenciado pelo estado mecânico, dessa forma, uma descrição fenomenológica do efeito de tensões mecânicas no campo coercitivo é proposta.

Validação sob tensão mecânica uniaxial e campo magnético alternado

O comportamento magnético anisterético sob tensões mecânicas uniaxiais é apresentado na Fig. 0.0.3, e o modelo descreve corretamente o comportamento medido, especialmente sob compressão. Por meio da Fig. 0.0.4, é possível observar que a inclusão do termo de segunda ordem permite capturar o efeito não monótono dos carregamentos mecânicos na permeabilidade magnética relativa. Diferenças são mais expressivas sobretudo no caso de tração de 100 MPa, no qual o modelo subestima a permeabilidade para baixos campos magnéticos.

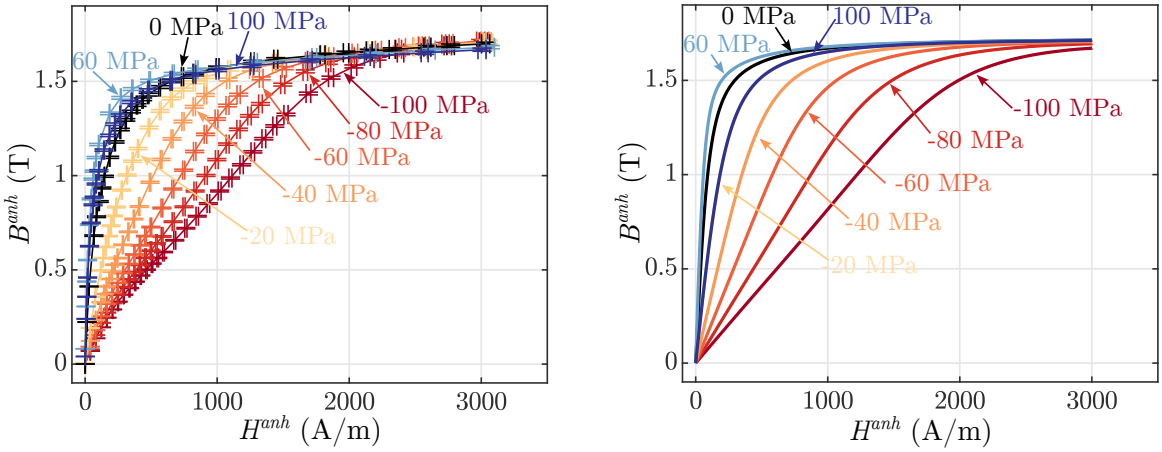

Figura 0.0.3: Efeito de carregamentos uniaxiais no comportamento anisterético: medições (esquerda) e modelo (direita).

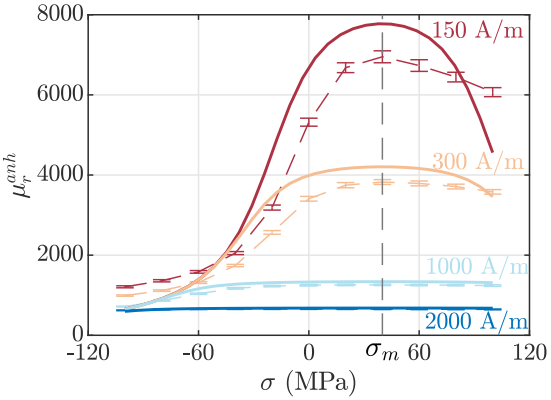

Figura 0.0.4: Comparação entre a permeabilidade magnética relativa medida (barra de erro) e modelada (linha sólida) para diferentes valores de campo magnético. A permeabilidade máxima é observada em σ_m = 40 MPa.

Uma validação independente das medidas utilizadas para identificação dos parâmetros

é apresentada na Fig. 0.0.5, na qual a forma de onda do campo magnético é especificada com conteúdo harmônico. É observado que o modelo representa com boa acurácia o comportamento medido para dois níveis de tensão mecânica.

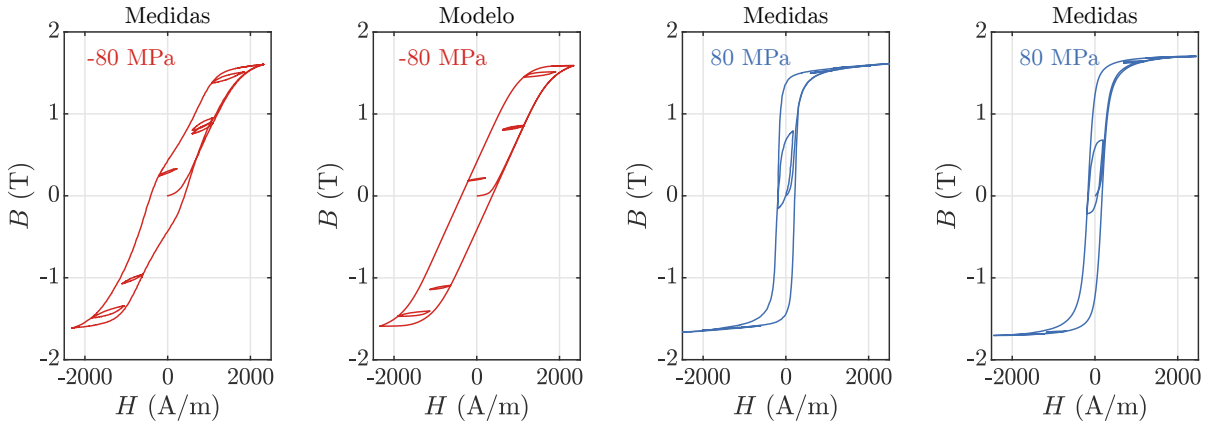

Figura 0.0.5: Laços de histerese sob carregamentos mecânicos uniaxiais e forma de onda do campo magnético com conteúdo harmônico.

Validação sob tensão mecânica multiaxial e campo magnético alternado

Utilizando medidas experimentais apresentadas na literatura Aydin et al. [2019b], Singh et al. [2016], as capacidades do modelo são testadas em configurações mecânicas multiaxiais e campo magnético alternado. Os parâmetros são identificados a partir de medidas uniaxiais ao longo de apenas a direção de laminação (RD). Além disso, efeitos da textura cristalográfica são levadas em conta por meio do comportamento anisterético, utilizando uma abordagem multiescala. Considerando um carregamento mecânico biaxial e campo magnético aplicado na direção RD, o comportamento magnético medido Aydin et al. [2019b] é apresentado na Fig. 0.0.6 (esquerda). Os resultados do modelo na Fig. 0.0.6 (direita) mostram que o modelo representa a degradação no comportamento magnético sob cisalhamento. Contudo, particularmente sob bi-compressão, o modelo superestima a degradação na magnetização. Uma possível razão para essa diferença é devido a consideração de tensão mecânica homogênea no modelo multiescala, o que não é necessariamente o caso no material real.

Validação sob tensão mecânica multiaxial e campo magnético rotativo

Utilizando o mesmo conjunto de parâmetros identificados a partir de medidas uniaxiais, o modelo de histerese magnética é aplicado sob carregamentos de campos magnéticos rotativos e tensões mecânicas multiaxiais. As medidas experimentais são apresentadas em Ay-

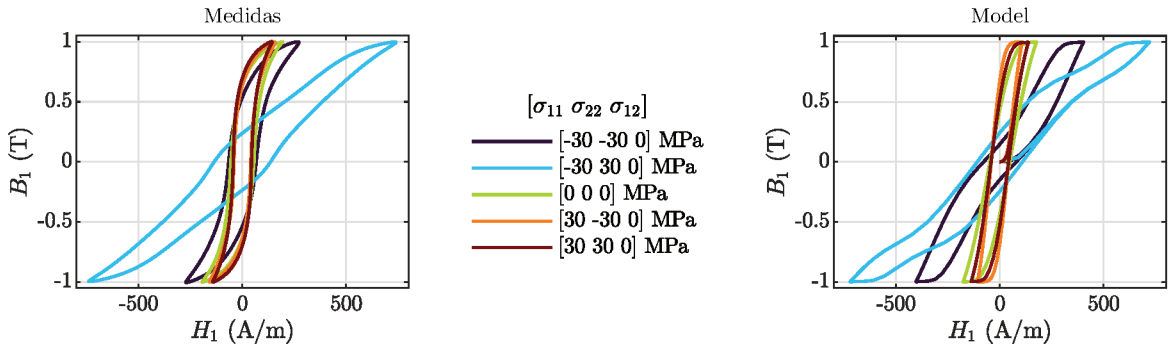

Figura 0.0.6: Comparação entre medidas Aydin et al. [2019b] (esquerda) e modelagem (direita) dos laços de histerese (em 1T) sob tensão mecânica biaxial e campo aplicado na direção RD.

din et al. [2019a]. Contudo, o modelo de histerese baseado em energia não reproduz a queda de perdas por histerese sob campos rotativos próximo da saturação Bergqvist [1997]. Para corrigir essa limitação, uma adaptação do parâmetro de dissipação, proposta em Sauseng et al. [2022], é utilizada.

Em uma configuraçao desafiadora, no qual é aplicado cisalhamento e um campo magnético rotativo, conforme apresentado na Fig. 0.0.7, uma excelente concordância entre medidas e o modelo é observada. O modelo representa a tendência de perdas por histerese sob carregamentos mecânicos multiaxiais, conforme apresentado na Fig. 0.0.8. Utilizando a adaptação no parâmetro de histerese é possível modelar a queda das perdas por histerese na região de rotação dos domínios magnéticos. Uma colaboração está em andamento com a Aalto University para obter as medições sob altos níveis de campo magnético.

Capítulo 5: Modelo de histerese magnetoelástico sob carregamentos mecânicos quase-estáticos

Neste capítulo, duas abordagens para modelar o comportamento da histerese magnética sob tensões mecânicas quase-estáticas são apresentadas. A primeira, inspirada na decomposição do campo magnético apresentada anteriormente, introduz a decomposição da tensão mecânica em partes reversível e irreversível. A definição da tensão mecânica irreversível é baseada na descrição do campo magnético irreversível, e um parâmetro de dissipação mecânica é introduzido. A identificação do parâmetro de dissipação mecânica é realizada utilizando medidas piezomagnéticas. Além disso, efeitos de textura são levados em conta por meio da utilização de uma textura cristalográfica simplificada no modelo anisterético multiescala.

Validação sob tensão mecânica variável

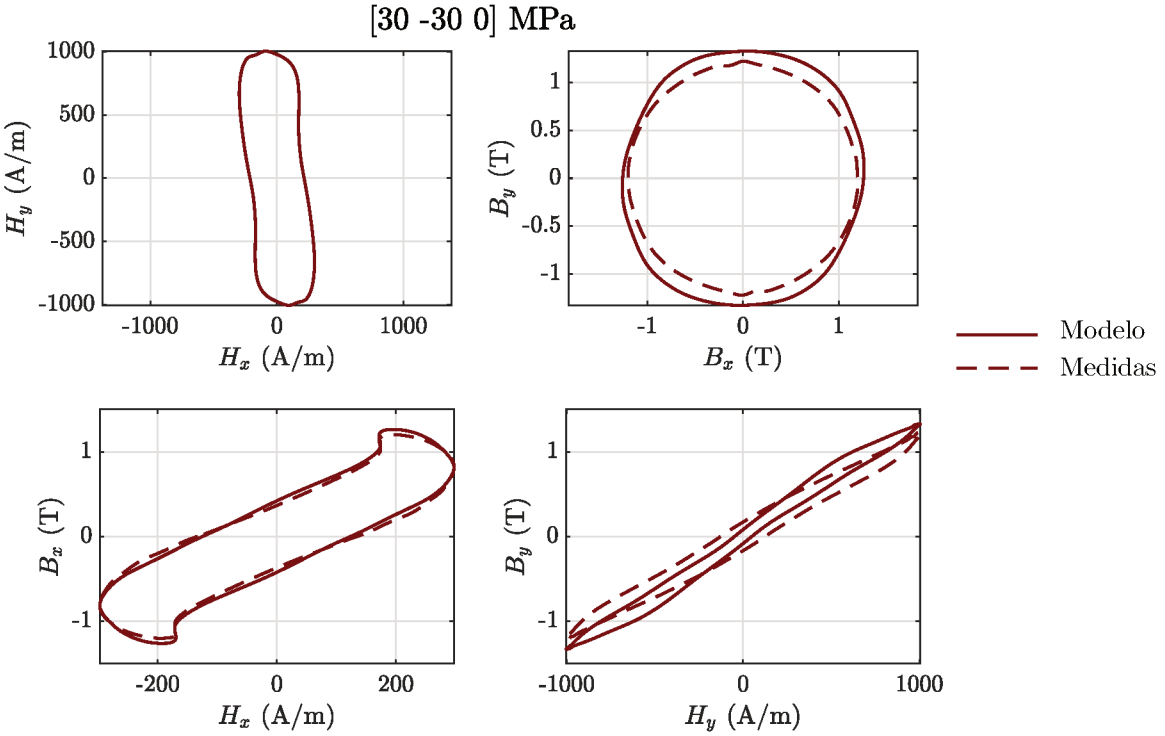

Figura 0.0.7: Comportamento magnético sob campo rotativo e cisalhamento. Comparação entre medidas (linhas tracejadas) Aydin et al. [2019a] e modelo (linhas solidas).

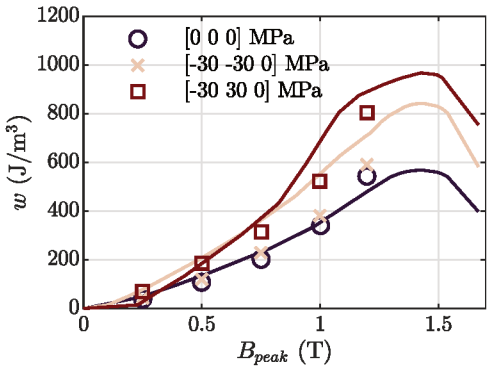

Figura 0.0.8: Comparação entre medidas Aydin et al. [2019a] (marcadores) e modelo (linhas sólidas) das perdas por histerese sob campos rotativos e tensões mecânicas.

Aplicando um carregamento uniaxial do tipo tensão mecânica variável e campo magnético estático, o modelo reproduz o comportamento piezomagnético sob diversos níveis de campo estático, conforme ilustra a Fig. 0.0.9. O efeito conhecido como reversão de Villari, relacionado com a textura cristalográfica, é representado por meio do comportamento aproximadamente constante da indução sob alta tração, é reproduzido pelo modelo.

Um caso de validação complexo é obtido aplicando simultaneamente variações de campo magnético e carregamento mecânico, conforme apresentado na Fig. 0.0.10 (a). A indução magnética resultante é mostrada na Fig. 0.0.10 (b) em função do campo magnético,

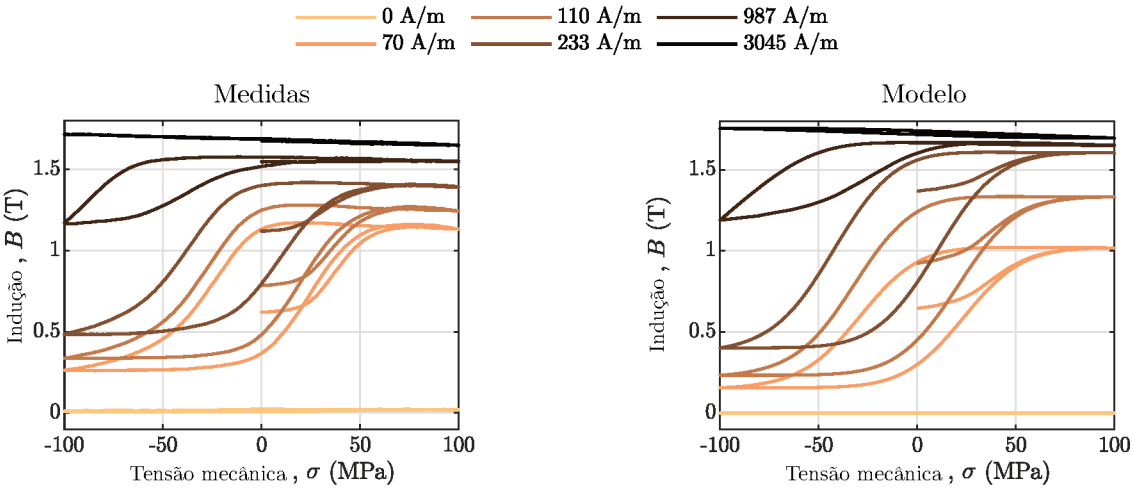

Figura 0.0.9: Comparação entre laços piezomagnéticos medidos (esquerda) e modelados (direita) sob incrementos de campo estático.

e na Fig. 0.0.10 (c) em termos do carregamento mecânico. Uma excelente concordância entre medidas e modelo é observada, destacando as capacidades do modelo em representar a histerese magnética mesmo no caso de carregamentos complexos.

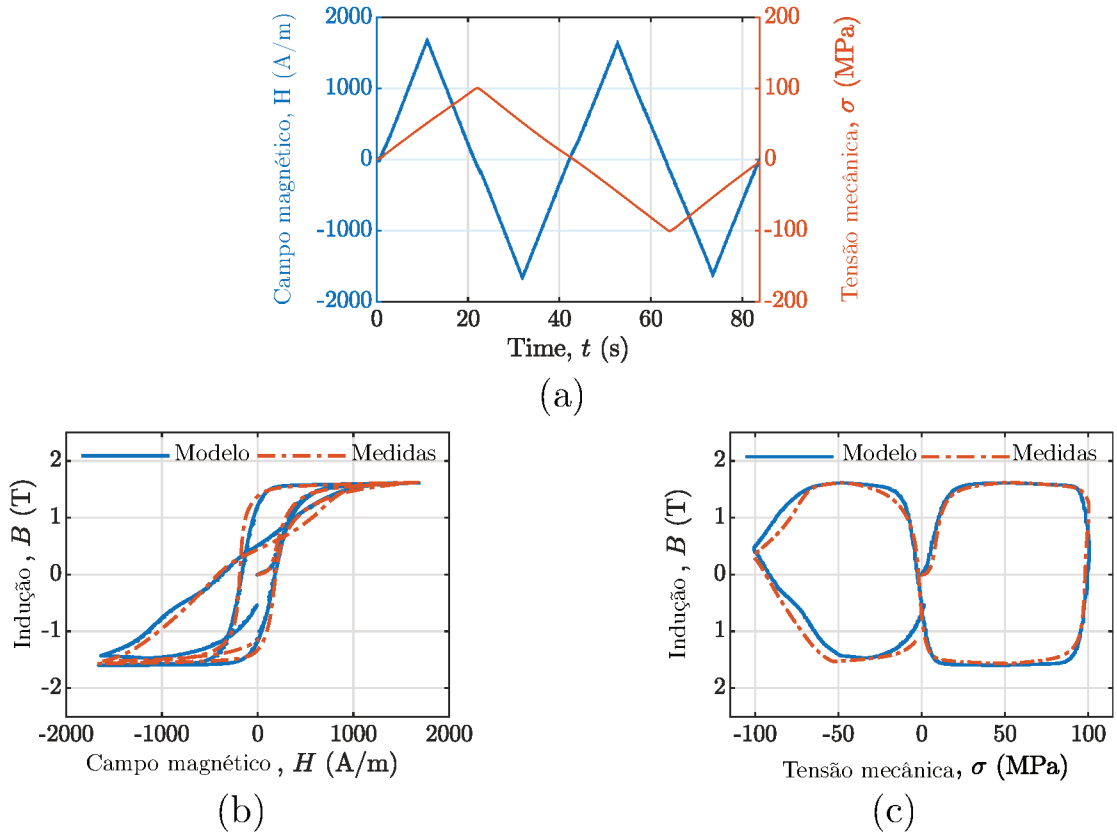

Figura 0.0.10: Resposta magnética sob carregamentos magnetoelásticos quase-estáticos (a). Comparação entre a indução medida e calculada em função do campo magnético (b) e em função da tensão mecânica (c).

A abordagem proposta para modelar a histerese magnetoelástica é termodinamicamente consistente no caso de carregamentos mecânicos estáticos e campo variável, e na situação de campo estático e carregamento mecânico variável. Contudo, uma análise é apresentada indicando que o modelo resulta em comportamento não-físico dependendo do tipo de carregamento magnetoelástico. Dessa maneira, uma segunda abordagem de modelo é apresentada, na qual as frações volumétricas de dominio são definidas como variáveis internas para descrever a dissipação. Essa abordagem é apresentada por meio de uma descrição energética, de forma que a consistência termodinâmica é garantida para qualquer configuração de carregamento magnetoelástico. O modelo utiliza um processo de minimização numérica para calcular as frações volumétricas para cada passo de tempo, resultando em um modelo computacionalmente custoso. O modelo utilizando frações volumétricas é um ponto de partida, no qual possíveis melhorias são sugeridas para trabalhos futuros.

Conclusão

O objetivo deste trabalho foi o desenvolvimento de um modelo de histerese magnética sob tensões mecânicas no qual fatores-chave como consistência termodinâmica, possibilidade de carregamentos multiaxiais e tempo de simulação compatível para ser aplicado em elementos finitos sejam atendidos. Medidas experimentais realizadas mostraram a influência de carregamentos magneto-elásticos — em diversas configurações — no comportamento magnético de um aço de baixo carbono. O conjunto de dados experimentais obtidos durante esta tese representa uma base sólida para o desenvolvimento e a validação de modelos de histerese magneto-elásticos.

Os modelos magneto-elásticos desenvolvidos neste trabalho consistem em uma combinação entre um modelo de histerese — utilizando uma abordagem energética com solução explícita — e um modelo anisterético multiescala. Para carregamentos do tipo tensão mecânica constante e campo magnético variável, e tensão mecânica variável e campo magnético constante, o modelo proposto é termodinamicamente consistente, e, a partir de parâmetros identificados por meio de medidas uniaxiais, foi validado para diversos carregamentos e configurações multiaxiais magneto-elásticas. Limitações na abordagem proposta são analisadas para o complexo caso de simultâneas variações de campo magnético e tensão mecânica. Para determinados carregamentos nessa configuração, o modelo pode resultar em comportamento não-físico.

Sugere-se para trabalhos futuros o acoplamento do modelo proposto em simulação por elementos finitos de uma máquina elétrica, de maneira a se analisar o efeito do acoplamento magneto-mecânico nas propriedades magnéticas e perdas por histerese de um dispositivo, comparado a abordagens utilizadas comumente utilizadas na literatura. Para melhorar a modelagem para qualquer carregamento magneto-elástico, garantindo a consistência termodinâmica, sugere-se o estudo e desenvolvimento de uma solução explícita para um modelo baseado em frações volumétricas, o qual parece ser uma abordagem promissora para a descrição de fenômenos dissipativos em materiais ferromagnéticos. Além disso, uma perspectiva promissora para o trabalho é a inclusão de efeitos plásticos na modelagem da histerese magnética.

ABSTRACT

Ferromagnetic materials exhibit magnetization and magnetostriction strain that are highly dependent on the magnetic field and mechanical stress loadings. This coupled behavior can be used to design magnetic sensors for non-destructive evaluation and high-efficiency electrical machines. Some features of the magnetic behavior are hysteresis, anisotropy, and dependency on the mechanical state. Experimental measurements evidence the influence of mechanical loadings on magnetization and magnetostriction strain, and different behaviors are observed when applying static or variable magneto-elastic loadings. This work aims to propose a magneto-elastic hysteresis model in which limitations usually found in literature models are covered. The modeling is made by associating an anhysteretic multiscale model with an energy-based hysteresis approach. The material parameters for reversible and irreversible behaviors are identified from uniaxial characterization under mechanical stress. In addition, further experimental results are presented for various magneto-elastic loadings to test the modeling prediction capabilities. The model is first developed to represent the magneto-elastic behavior under constant stress, taking into account the multiaxiality of the loading, the crystallographic texture effects, the stress effect on the coercive field, the non-monotonic behavior of permeability as a function of stress, and the vanishing of hysteresis losses under rotating field close to saturation. The model is analyzed in several complex configurations with satisfactory results. A similar approach is developed to represent the magneto-elastic hysteresis at constant field and variable stress. These two energy-based models are thermodynamically consistent, with parameters identified from uniaxial measurements, and can represent the magnetic behavior in complex (3D) configurations. Lastly, two models are proposed to consider simultaneous variations in field and stress. Their limitations are discussed, but left as perspectives for this work.

Keywords: Hysteresis model, Magneto-elastic coupling, Multiscale modeling, Multiaxial stress

RÉSUMÉ

Les matériaux ferromagnétiques présentent une aimantation et une déformation de magnétostriction qui dépendent fortement du champ magnétique et des contraintes mécaniques auxquels ils sont soumis. Leur comportement magnéto-élastique peut être utilisé pour concevoir des capteurs magnétiques pour l'évaluation non destructive et des machines électriques à haute efficacité. Certaines caractéristiques du comportement magnétique sont l'hystérésis, l'anisotropie et la dépendance à l'état mécanique. Les mesures mettent en évidence l'influence des chargements mécaniques sur l'aimantation et la déformation de magnétostriction, et différents comportements sont observés lors de l'application de chargements magnéto-élastiques statiques ou dynamiques. L'objectif de ce travail est de proposer un modèle d'hystérésis magnéto-élastique dans lequel les limitations classiques des modèles de la littérature peuvent être dépassées. La modélisation est réalisée par l'association d'un modèle multi-échelle anhystérétique et d'un modèle d'hystérésis basé sur une approche énergétique. Les paramètres de modélisation pour les comportements réversibles et irréversibles sont identifiés à partir de la caractérisation uniaxiale sous contrainte mécanique. De plus, d'autres résultats expérimentaux sont présentés pour une variété de chargements magnéto-élastiques permettant de tester la prédictivité des modèles. Un modèle est d'abord développé pour représenter le comportement magnéto-élastique sous contrainte constante, prenant en compte la multiaxialité du chargement, les effets de texture, l'effet des contraintes sur le champ coercitif, la non-monotonie de la perméabilité en fonction de la contrainte ainsi que l'annulation des pertes à saturation sous champ tournant. Ce modèle est analysé dans plusieurs configurations complexes et montre des résultats très satisfaisants. Un modèle analogue est développé pour représenter l'hystérésis magnéto-élastique à champ constant, sous contrainte variable. Ces deux modèles basés sur l'approche énergétique présentent la cohérence thermodynamique espérée, leur paramètres peuvent être identifiés à partir de mesures uniaxiales et ils sont capables de représenter le comportement dans des configurations complexes (3D). Enfin, deux modèles permettant de prendre en compte des chargements avec contrainte et champ variable sont proposés. Ceux-ci présentent chacun des points faibles dont le traitement est laissé en perspective à ce travail.

Mots clés: Modèle d'hystérésis, Couplage magnéto-élastique, Modélisation multi-échelle, Contrainte multiaxiale

Notations

Scalar

μ_0	Vacuum permeability
μ_r	Relative magnetic permeability
u	Internal free energy density
f	Helmholtz free energy density
g	Gibbs free energy density
s	Entropy
T	Temperature
D	Dissipation
κ, κ_H	Pinning field
ω	Weight corresponding to each pinning field or pinning stress
κ_σ	Pinning stress
M_s	Saturation magnetization
H_c	Coercive field
σ_c	Coercive stress
p_α	Volume fraction of domains α
λ_s	Saturation magnetostriction strain of an isotropic material
λ_{100}	Magnetostriction strain along $< 100 >$ direction
λ_{111}	Magnetostriction strain along $< 111 >$ direction
K_1, K_2	Magnetocrystalline anisotropy constants
σ_{eq}	Equivalent stress

Vector

$\vec{H}$	Magnetic field
$\vec{B}$	Magnetic induction
$\vec{M}$	Magnetization
$\vec{H}_{rev}$	Reversible magnetic field
$\vec{H}_{irr}$	Irreversible magnetic field

Tensors of order 2 and higher

ε	Second-order strain tensor
ε^{e}	Second-order elastic strain tensor
ε^{μ}	Second-order magnetostriction strain tensor
σ	Second-order stress tensor
σ_{rev}	Second-order reversible stress tensor
σ_{irr}	Second-order irreversible stress tensor
I	Second-order identity tensor
$\mathscr{C}$	Fourth-order stiffness tensor

Operations

grad_s	Symmetric gradient, e.g. $\varepsilon = \text{grad}_\text{s}\,\vec{u} \;\rightarrow\; \varepsilon_{ij} = \frac{1}{2}\left[\frac{\partial u_i}{\partial x_j} + \frac{\partial u_j}{\partial x_i}\right]$
:	Double contraction, e.g. $\sigma = \mathscr{C} : \varepsilon \;\rightarrow\; \sigma_{ij} = \mathscr{C}_{ijkl}\varepsilon_{kl}$
tr	Trace, e.g. $\text{tr}(\varepsilon) = \varepsilon_{ii}$
div	Divergence of a vector field, e.g. $\text{div}\,\vec{B} = \frac{\partial B_i}{\partial x_i}$
curl	Curl of a vector field, e.g. $\text{curl}\,\vec{H} = \varepsilon_{ijk}\frac{\partial H_k}{\partial x_j}\vec{e}_i$
ε	Levi-Civita permutation symbol: $\varepsilon_{ijk} = \begin{cases} 1, & \text{if } (i,j,k) = (1,2,3) \text{ or } (2,3,1) \text{ or } (3,1,2) \\ -1, & \text{if } (i,j,k) = (3,2,1) \text{ or } (1,3,2) \text{ or } (2,1,3) \\ 0, & \text{otherwise} \end{cases}$

Contents

1 Introduction

Magnetic materials are essential in an extensive range of applications, including sensors for non-destructive evaluation Bouterfas et al. [2023], Eslamlou et al. [2023], energy harvesting Daniel et al. [2023], Liu et al. [2024], Zangho et al. [2024], and electrical machines Krings et al. [2017]. The industrial sector corresponds to about one-third of the total energy consumed in the world, in which electrical machines correspond to more than 60 % of industrial sector energy consumption Errigo et al. [2022]. The evolution of manufacturing processes such as additive manufacturing Selema et al. [2023] and the development of materials including soft magnetic composites Guo et al. [2023] open vast possibilities in researching new topologies of electrical machines for more sustainable options Fernandes et al. [2022]. Even different in the respective utilization - magnetic sensors, energy recovery systems, or electromechanical conversion - in common with all these applications and processes, developing models that describe the behavior of magnetic materials is essential in designing devices with high reliability and efficiency.

The behavior of magnetic materials is complex due to anisotropy Jiang et al. [2018], Tolentino et al. [2022], hysteresis or dissipative behavior, dependence on the frequency of the applied loading de La Barrière et al. [2012], and coupled effects, which result in modifications in the magnetic behavior due to the application of mechanical stress Li et al. [2024] or temperature Banu et al. [2023].

Notably, the mechanical stress effect in magnetic materials can have positive or negative effects depending on the application. For instance, manufacturing processes can induce mechanical stress in electrical machines, which can increase iron losses and thus affect efficiency and modify the magnetic permeability in certain magnetic parts of the device Takahashi et al. [2008], Yamazaki and Takeuchi [2017]. Conversely, energy harvesting systems benefit from the stress-dependence of the magnetization in magnetic materials Daniel et al. [2023]. The stress effect in magnetic materials can also be utilized in developing transducers, such as force sensors Dapino [2004]. The coupled magneto-mechanical behavior also has an inverse effect in magnetic materials: a magnetic field induces a strain, denoted by magnetostriction. A negative impact of the magnetostriction is noted in the core of transformers, in which this strain is one of the sources of vibration and noise Moses et al. [2016].

Several scales can be considered in modeling the coupled magneto-mechanical beha-

vior of magnetic materials. Multiscale strategies with proper transition rules have been developed to define constitutive relations Bernard et al. [2019], Daniel et al. [2008]. Such approaches successfully depict the coupled magneto-mechanical behavior and the anisotropy from an energy description. However, these multiscale models do not usually describe the hysteresis dissipation. The multiscale approaches can be combined with hysteresis models to describe the irreversible behavior.

The main goal of this thesis is to analyze and develop a magneto-elastic hysteresis model in which the limitations present in some models of the literature are partially or totally covered. Three key features are defined in developing a constitutive relation: (a) the ability to consider multiaxial magneto-elastic loadings, (b) thermodynamic consistency such that the losses can be accurately evaluated at any operating point, and (c) low computational time such that the model can be implemented into numerical analysis tools.

The manuscript is organized as follows:

The first chapter introduces the physical basis of the magneto-mechanical problem, followed by the description of some hysteresis models under magneto-elastic loadings available in the literature, detailing the main features and limitations. A thermodynamically consistent model, developed for the stress-free case only, is then introduced, covering some of the limitations of the previous approaches.

The second chapter presents experimental measurements performed on a DC04 low-carbon steel, illustrating the coupled magneto-mechanical behavior of a magnetic material under various loading conditions.

In the third chapter, an energy-based magnetic hysteresis approach is combined with multiscale models to describe the dissipative hysteresis behavior under static mechanical loadings and variable fields. The parameters of the proposed association are identified from uniaxial measurements only, and the model is validated considering multiaxial stress states and rotating fields.

In the fourth chapter, two approaches are presented to describe the piezomagnetic behavior - under variations of stress and constant field - and under variations in both field and stress. The modeling results are then compared to the measurements, allowing to discuss the limitations and a route for the following works.

2 Magneto-elastic behavior modeling

This chapter provides an overview of the existing models describing the magneto-elastic behavior of ferromagnetic materials. In Section 2.1, the physics concepts and expressions related to the mechanical and magnetic processes in matter are briefly recalled. The concepts of strain and stress are defined from a continuum mechanics framework under the hypothesis of small strains. The notions of magnetization, magnetic field, and induction are established through the Maxwell equations - here restricted to a quasi-static regime. Ferromagnetic materials, studied in this work, are then introduced.

In Section 2.2, the strong coupling between magnetic and mechanical quantities in a ferromagnetic material is observed from experimental measurements extracted from the literature. The magnetization process is strongly affected by the application of stress. In addition, the magnetostriction, a strain related to the magnetic state of a matter, is another phenomenon that emphasizes this coupled behavior. Such a coupled behavior can be explained by an energy balance at a microscopic scale, further detailed.

The modeling of the coupled magneto-elastic behavior is a challenging task due to the hysteretic and non-linear magnetic response. In the literature, macroscopic modeling can be performed considering the assumption of no losses - resulting in a thermodynamic reversible behavior - or considering the dissipation mechanism. In Section 2.3, two approaches to model the anhysteretic behavior are presented, and in Section 2.4 macroscopic hysteresis models are introduced. The main flaws of each approach are discussed.

2.1 Introduction of the uncoupled physics basis

2.1.1 Continuum mechanics

Continuum mechanics is a branch of Physics that deals with the interaction between force and motion in a continuum media. In continuum mechanics, a body is defined as a collection of elements - the material points. As exemplified in Fig. 2.1.1, at time t_0 - the reference configuration - a body is denoted by $\mathscr{B}_0$. The vector $\vec{X}$ defines the position of a material point $P(t_0)$. After motion and deformation, at time t, the vector $\vec{x}$ characterizes the new material point position. The deformation field $\vec{u}$ is introduced, linking the set of material points location on both configurations Eringen and Maugin [1990]:

$$\vec{u}(\vec{X},t) = \vec{x} - \vec{X}, \tag{2.1.1}$$

where a one-to-one relation for the position of each material point in the two configurations is considered. Using a Taylor expansion of the neighborhood around $\vec{X}$ and $\vec{x}$, results in the second-order deformation tensor F defined as Eringen and Maugin [1990]:

$$F(\vec{X},t) = \frac{\partial \vec{x}}{\partial \vec{X}} \qquad \text{with} \qquad \det F \neq 0, \tag{2.1.2}$$

with det representing the determinant operator.

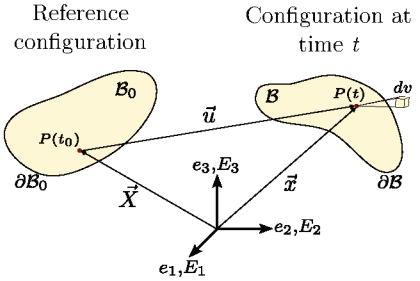

Figura 2.1.1: Motion of a continuum body.

Information on the body strain can be obtained from the second-order tensors E and e, in Lagrangian and Eulerian descriptions, respectively. These tensors are defined by:

$$\begin{aligned} E &= \frac{1}{2}\left(F^T F - I\right) = \frac{1}{2}\left[\left(\frac{\partial \vec{u}}{\partial \vec{X}}\right)^T + \frac{\partial \vec{u}}{\partial \vec{X}} + \left(\frac{\partial \vec{u}}{\partial \vec{X}}\right)^T \frac{\partial \vec{u}}{\partial \vec{X}}\right] \\ e &= \frac{1}{2}\left(I - F^{-T}F^{-1}\right) = \left[\frac{\partial \vec{u}}{\partial \vec{x}} + \left(\frac{\partial \vec{u}}{\partial \vec{x}}\right)^T - \left(\frac{\partial \vec{u}}{\partial \vec{x}}\right)^T \frac{\partial \vec{u}}{\partial \vec{x}}\right]. \end{aligned} \tag{2.1.3}$$

If the norm of the displacement gradient is small, the hypothesis of small strains can be used. In this case, the description in the deformed configuration is approximately the same as in the reference configuration. The tensors E and e, then, result in:

$$\begin{aligned} E \approx e &= \varepsilon \\ \varepsilon &= \frac{1}{2}\left[\frac{\partial \vec{u}}{\partial \vec{x}} + \left(\frac{\partial \vec{u}}{\partial \vec{x}}\right)^T\right] = \text{grad}_\text{s}\, \vec{u}, \end{aligned} \tag{2.1.4}$$

where the compact notation of symmetric gradient grad_s is introduced. From now on, ε designates the second-order strain tensor.

The mass m of a continuum does not depend on motion. This statement is defined mathematically from the conservation of mass principle Kovetz [2000]:

$$\dot{m} = 0, \qquad \text{with} \qquad m = \int_{\mathscr{B}} \rho\left(\vec{x},t\right)\, dv, \tag{2.1.5}$$

with $\rho\left(\vec{x},t\right)$ the volumetric mass density. From the balance of linear momentum postulate, the force $\vec{F}$ exerted on the body is introduced. This quantity comprises a volume $\vec{f}$ and a surface $\vec{t}$ force components. The Cauchy hypothesis states that the surface forces depend on the vector $\vec{n}$, normal to the surface $\partial\mathscr{B}$. From this assumption, the second-order Cauchy stress tensor σ is introduced Kovetz [2000]:

$$\vec{F} = \int_{\mathscr{B}} \rho\vec{f}\, dv + \int_{\partial\mathscr{B}} \vec{t}\, ds \qquad \text{with} \qquad \vec{t} = \sigma\vec{n}. \tag{2.1.6}$$

The balance of angular momentum and the Cauchy hypothesis lead to the symmetry of the stress tensor Kovetz [2000]:

$$\sigma = \sigma^t, \tag{2.1.7}$$

with the superscript t denoting the transpose operator. Volume forces, such as gravity and electromagnetic forces, are not treated in this work in developing constitutive models. The reader is referred to Eringen and Maugin [1990], Kankanala and Triantafyllidis [2004], Kovetz [2000] for an extensive analysis of the electromagnetic forces contribution on a continuum mechanics framework.

2.1.2 Linear elastic behavior

In addition to the mass conservation postulate and the balance laws, constitutive equations, which consider specific material properties, are defined to solve a mechanical problem. If a material, under the hypothesis of small strains, deforms depending on the stress level, such that it presents a thermodynamically reversible behavior, the material exhibits an elastic behavior. Moreover, if the material deforms linearly under mechanical loading, the constitutive relation between strain and stress is defined by the Hooke law:

$$\sigma = \mathscr{C} : \varepsilon, \tag{2.1.8}$$

with $\mathscr{C}$ the fourth-order stiffness tensor. The operator : represents the double-contraction product. If the material is elastically isotropic, and considering the symmetries of the quantities, the Hooke law can be written as:

$$\sigma = 2\,\mu_l\,\varepsilon + \lambda_l\left(\mathrm{tr}(\varepsilon)\right) I \qquad \text{with} \qquad \mu_l = \frac{E}{2(1+\nu)} \qquad \text{and} \qquad \lambda_l = \frac{2\,\mu_l\,\nu}{1-2\nu}, \tag{2.1.9}$$

tr is the trace operator. The Lamé coefficients μ_l and λ_l can be evaluated from the Young's modulus E and the Poisson's ratio ν and vice-versa.

2.1.3 Introduction to magnetism and ferromagnetic materials

The Maxwell equations govern the interactions between magnetic and electrical quantities. The magnetic set of the Maxwell equations under the assumption of quasi-static fields linking the magnetic field $\vec{H}$, the magnetic induction $\vec{B}$, the current density $\vec{J_c}$, and the electric field $\vec{E}$ are Bastos and Sadowski [2003]:

$$\mathrm{curl}\,\vec{H} = \vec{J_c} \qquad \text{(Ampère law)} \tag{2.1.10}$$

$$\mathrm{div}\,\vec{B} = 0 \qquad \text{(Gauss law)} \tag{2.1.11}$$

$$\mathrm{curl}\,\vec{E} = -\frac{\partial \vec{B}}{\partial t} \qquad \text{(Faraday-Lenz law)} \tag{2.1.12}$$

with the operators curl and div representing the curl and the divergence, respectively. The relationship of magnetic fields is:

$$\vec{B} = \mu_0\left(\vec{H} + \vec{M}\right), \tag{2.1.13}$$

where it is introduced the magnetization $\vec{M}$, and μ_0 is the vacuum permeability. As in the previous section, the definition of constitutive relations is necessary to solve a magnetic problem. In the case of materials with linear anhysteretic magnetic behavior, the constitutive equation writes:

$$\vec{B} = \mu_0\,(\chi + I)\,\vec{H} = \mu\vec{H}, \tag{2.1.14}$$

with χ and μ the constant second-order tensors of susceptibility and permeability, respectively. If the material is magnetically isotropic, $\chi = \chi I$, with χ a scalar susceptibility. Materials can be classified based on χ, which can be measured from a magnetization $M(H)$ curve. Fig. 2.1.2 presents the susceptibility for some materials. Due to their excellent magnetic response under an applied field, ferromagnetic materials are employed in constructing electrical machines and magnetic transducers.

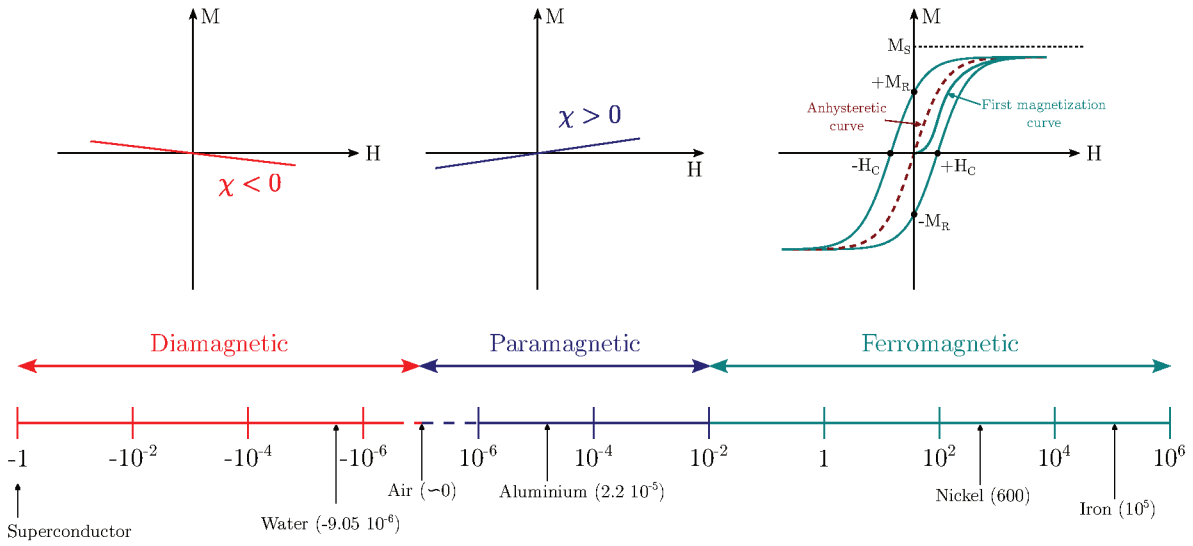

Figura 2.1.2: Classification of materials based on the magnetic susceptibility Frenea-Robin and Marchalot [2022].

The magnetization process of ferromagnetic materials (see Fig. 2.1.2) can be described as follows: considering a unidirectional field and starting from the demagnetized state ($M = 0$ A/m), an increase on the magnetic field will increase the magnetization - following the first magnetization curve - until the saturation is reached ($M = M_s$). If the magnetic field decreases until zero, the magnetization does not reach zero, but a remanent point ($M = M_r$). Now, the demagnetized state can be reached when a field of the amplitude of the coercive field H_c is applied. Therefore, the magnetic behavior of ferromagnetic materials is non-linear and hysteretic.

2.2 Magneto-elastic coupling in ferromagnetic materials

The magneto-elastic coupling lies in the interaction between magnetic and mechanical quantities in a material. The origin of such a coupled behavior in ferromagnetism is explained from a microscopic perspective, further detailed. Two primary examples that show the depen-

dence of magnetic and mechanical quantities are the magnetostriction strain and the effects of stress on magnetization.

2.2.1 Magnetostriction strain

Magnetostriction is the strain of a body due to the change in its magnetic microstructure. The Joule magnetostriction is represented by the second-order tensor ε^{μ} considering a volume-conserving strain ($\mathrm{tr}(\varepsilon^{\mu}) = 0$) De Lacheisserie [1993]. For electrical steels, measurements indicate (see Fig. 2.2.1) that this strain is of the order of 10^{-6}, so the small deformation theory can be applied. Despite its magnitude, the magnetostriction strain is one of the sources of noise and vibration of transformer cores Moses et al. [2016]. As shown in Fig. 2.2.1a, the magnetostriction depends on the magnetization direction: an anisotropy effect is noted. Another characteristic of this behavior is the non-monotonic evolution with the magnetization. In addition to the dependence of magnetostriction to magnetization, Fig. 2.2.1b depicts the influence of constant mechanical stress on the relation between magnetostriction and magnetization.

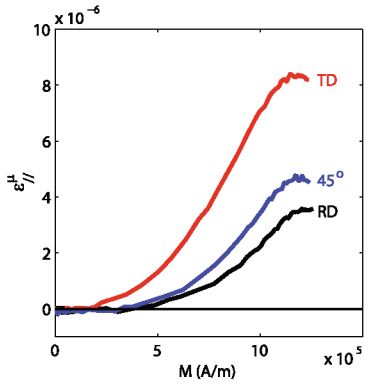

(a) Anisotropy of the stress-free longitudinal magnetostriction strain Daniel et al. [2014].

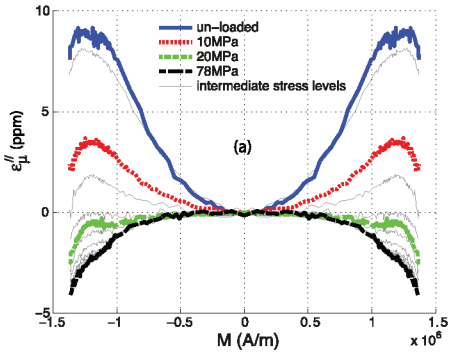

(b) Longitudinal magnetostriction strain under field and uniaxial stress applied along the longitudinal direction Hubert [2019].

Figura 2.2.1: Anhysteretic magnetic measurements on non-oriented electrical steels.

2.2.2 Stress effects on magnetization

Another remarkable example of the magneto-elastic coupling is the influence of the mechanical state on magnetization. As observed in Fig. 2.2.2, static stress significantly modifies the shape of hysteresis loops. Compared to the stress-free case, compression increases the hysteresis losses and the coercive field of electrical steel for the same maximum induction level. Moreover, under a magneto-elastic loading of static field and variable stress, the induction/s-

tress relation also presents a hysteretic behavior, as shown in Fig. 2.2.3, with non-monotonic branches under tension and compression.

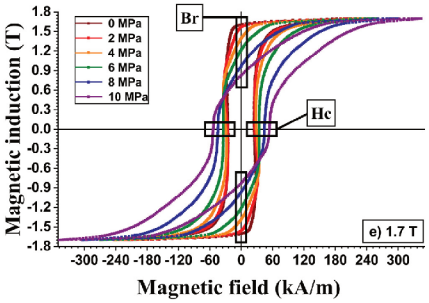

Figura 2.2.2: Compression effect on the hysteresis behavior of a non-oriented electrical steel Dias and Landgraf [2020].

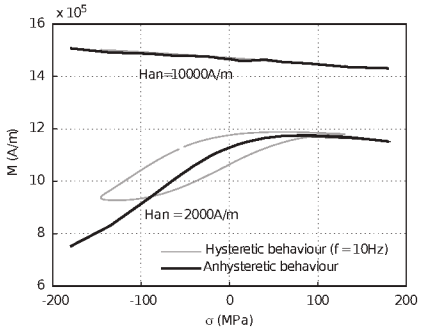

Figura 2.2.3: Magnetic behavior of a low-carbon steel under variable stress and constant field Hubert and Rizzo [2008].

2.2.3 Magnetization process

2.2.4 Atomic origins

The magnetization is the macroscopic response of a material whose atomic origin is related to the motion of electrons that generates a magnetic moment. Two primary sources of the electrons magnetic moment are the orbital momentum and the spin. A simplified example of the orbital motion of an electron, with position described by the vector $\vec{r}$ and speed $\vec{v}$ around the nucleus, is presented in Fig. 2.2.4. In this configuration, the magnetic moment $\vec{\mu}_l$ is given by Purcell and Morin [2013]:

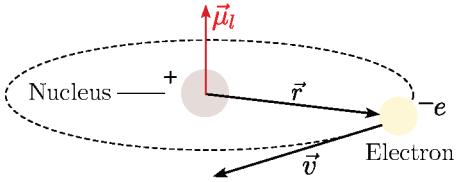

Figura 2.2.4: Orbital motion of an electron in an atom (adapted from Purcell and Morin [2013]).

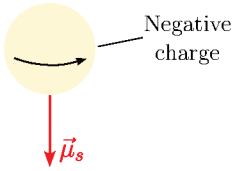

Figura 2.2.5: Spin of an electron (adapted from Purcell and Morin [2013]).

$$\vec{\mu}_l = -\frac{e}{2m_e}\vec{L} \qquad \text{with} \qquad \vec{L} = m_e\,(\vec{v}\times\vec{r}), \tag{2.2.1}$$

e is the electron charge ($e = 1.602\,10^{-19}$ C), m_e is the electron mass ($m_e = 9.109\,10^{-31}$ kg), and $\vec{L}$ is the orbital angular momentum. The second source of magnetic moment is the

rotation of an electron around its own axis or spin. This motion is represented in Fig. 2.2.5. The spin results in a magnetic moment given by Purcell and Morin [2013]:

$$\vec{\mu}_s = -g_l \frac{e}{2m_e}\vec{S}, \tag{2.2.2}$$

with $\vec{S}$ the angular momentum. g_l is the Landé factor, a quantum mechanics factor that depends on the atomic state, and $g_l = 2$ under a pure electron spin. The total magnetic moment $\vec{\mu}$ of an electron is given by the sum of the contributions of orbital motion and spin:

$$\vec{\mu} = -\frac{e}{2m_e}\left(\vec{L} + g_l\,\vec{S}\right). \tag{2.2.3}$$

The total magnetic moment in a free atom - with several electrons - can be evaluated from a vector sum of all magnetic moments of the electrons. The atomic magnetization is given by the volumetric sum of the total magnetic moment. A much more detailed analysis of the quantum state of an electron in an atom and its interaction with a magnetic field can be found in Chikazumi [1997], Jiles [1991]. Here, we emphasize the influence of the magnetic moments - at the atomic scale - on the macroscopic magnetic behavior of a material. For instance, as noted in Fig. 2.1.2, diamagnetic materials have a minimal and negative susceptibility. This behavior can be explained from an atomic perspective, where the electrons are so paired that the total magnetic moment of the atom is zero. Moreover, under an applied field, the magnetization generated by the electrons motion of a diamagnetic material opposes the increasing of the field, resulting in a negative susceptibility Jiles [1991].

On the other hand, paramagnetic materials exhibit a total magnetic moment due to unpaired electrons. Under an applied field, the magnetization proportionally increases with the field (see Fig. 2.1.2). Below the Curie temperature, ferromagnetic materials manifest a much more significant magnetic response under an applied field when compared to paramagnetic ones (see Fig. 2.1.2). The atomic structure of ferromagnetic materials, with the magnetic moment of adjacent atoms aligned in parallel - arranged in the so-called magnetic domains structure - favors the magnetization changes with the applied field Jiles [1991].

2.2.5 Domains and grains

The magnetic domains are a large set of magnetic moments aligned in parallel - characteristic of ferromagnetic materials. At the domain scale (denoted by the index α) the mag-

netization $\vec{M}_\alpha$ of a domain is:

$$\vec{M}_\alpha = M_s \vec{\alpha}, \tag{2.2.4}$$

with M_s the saturation magnetization and $\vec{\alpha}$ the unit vector that defines the domain orientation. A region with uniform crystalline lattice is a grain or crystal. A simplified schematic of a grain corresponding to the domains with $< 100 >$ orientations is reproduced in Fig. 2.2.6 (a). The transition between two adjacent domains is a domain wall. The domain walls can be classified according to the spatial change of the magnetic moments orientation - a rotation of 180° or a rotation of 90° Chikazumi [1997].

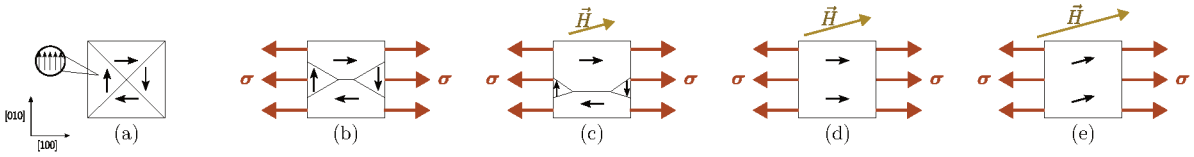

Figura 2.2.6: Simplified schematic of the magnetization process in a grain with four domains under a magneto-elastic loading. Material with positive magnetostriction.

The arrangement of a domain can be explained from a thermodynamics perspective. The energy balance of a volume element is given by:

$$w_\alpha = w_\alpha^{ex} + w_\alpha^{an} + w_\alpha^{mag} + w_\alpha^{mec} \tag{2.2.5}$$

- Exchange energy density w_α^{ex}: The exchange energy characterizes the atomic magnetic moments interaction. This energy term is minimum when the magnetization is uniform. w_α^{ex} is given by Hubert and Schäfer [2008]:

$$w_\alpha^{ex} = A^{ex} \left(\text{grad}\, \vec{\alpha}\right)^2, \tag{2.2.6}$$

  with A^{ex} a material parameter that characterizes the exchange, and grad is the gradient operator. The exchange energy, together with the anisotropy and demagnetizing energies further detailed, is used in micromagnetic modeling to describe the formation of the domain structure. Here, we assume the existence of the magnetic structure.

- Anisotropy energy density w_α^{an}: The anisotropy energy describes the preference of a domain magnetization for specific orientations - the easy axes. This energy term is minimal

when the magnetization is aligned with an easy axis. For materials with cubic crystallographic symmetry, the magnetocrystalline anisotropy energy density is evaluated by Hubert and Schäfer [2008]:

$$w_\alpha^{an} = K_1\left(\alpha_1^2\alpha_2^2 + \alpha_1^2\alpha_3^2 + \alpha_2^2\alpha_3^2\right) + K_2\left(\alpha_1^2\alpha_2^2\alpha_3^2\right), \tag{2.2.7}$$

with K_1 and K_2 the anisotropy constants. As an example of a material with cubic symmetry, consider a grain of iron, whose easy axes are along the $< 100 >$ directions. The anisotropy constants for iron are $K_1 = 42.7$ kJ/m^3 and $K_2 = 15$ kJ/m^3 Jiles [1991]. The anisotropy energy density for a grain of iron - presented in Fig. 2.2.7 - is minimum for the domain orientations aligned along the easy axes.

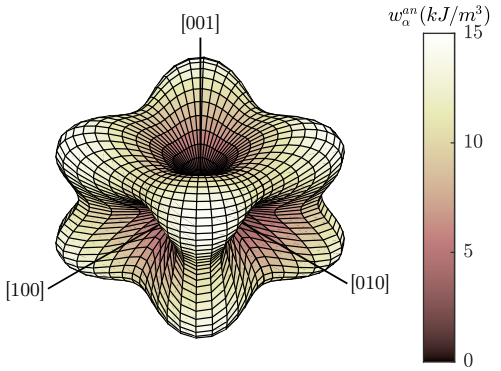

Figura 2.2.7: Anisotropy magnetocrystalline energy density of a grain of iron.

- Magnetostatic energy w_α^{mag}: The magnetostatic energy is characterized by two contributions: the first one, the Zeeman energy w_α^z, describes the interaction between an externally applied field and the magnetization. For a uniform magnetic field, w_α^z writes Hubert and Schäfer [2008]:

$$w_\alpha^z = -\mu_0 \vec{H} \cdot \vec{M}_\alpha. \tag{2.2.8}$$

The Zeeman energy w_α^z is minimum when the magnetization is parallel to the applied field. The second contribution of the magnetostatic energy is due to demagnetizing effects and is denoted by w_α^d. From the Gauss law (2.1.11), spatial variations of magnetization result in a magnetic field, denoted as demagnetizing $\vec{H}_d$:

$$\operatorname{div} \vec{H}_d = -\operatorname{div} \vec{M}_\alpha. \tag{2.2.9}$$

The energy contribution due to demagnetizing effects is Hubert and Schäfer [2008]:

$$w_\alpha^d = -\frac{1}{2}\mu_0 \vec{H}_d \cdot \vec{M}_\alpha. \tag{2.2.10}$$

The magnetostatic energy is then:

$$w_\alpha^{mag} = w_\alpha^z + w_\alpha^d = -\mu_0 \vec{H}_{\text{eff}} \cdot \vec{M}_\alpha \qquad \text{with} \qquad \vec{H}_{\text{eff}} = \vec{H} + \frac{1}{2}\vec{H}_d \tag{2.2.11}$$

- Magneto-elastic energy w_α^{mec}: The arrangement of domains is altered by applying mechanical loadings. Considering uniform stress within the grain and a linear dependence of w_α^{mec} on the mechanical loading, the magneto-elastic energy can be defined as Hubert and Schäfer [2008]:

$$w_\alpha^{mec} = -\sigma : \varepsilon_\alpha^\mu. \tag{2.2.12}$$

For materials with cubic crystallographic symmetry, the magnetostriction strain ε_α^μ is defined by:

$$\varepsilon_\alpha^\mu = \frac{3}{2}\begin{bmatrix} \lambda_{100}\left(\alpha_1^2 - \frac{1}{3}\right) & \lambda_{111}\alpha_1\alpha_2 & \lambda_{111}\alpha_1\alpha_3 \\ \lambda_{111}\alpha_2\alpha_1 & \lambda_{100}\left(\alpha_2^2 - \frac{1}{3}\right) & \lambda_{111}\alpha_2\alpha_3 \\ \lambda_{111}\alpha_3\alpha_1 & \lambda_{111}\alpha_3\alpha_2 & \lambda_{100}\left(\alpha_3^2 - \frac{1}{3}\right) \end{bmatrix} \tag{2.2.13}$$

with the constants λ_{100} and λ_{111} indicating the magnetostriction strain along the $< 100 >$ and $< 111 >$ directions, respectively.

The magnetization process in a grain under a magneto-elastic loading is illustrated in Fig. 2.2.8 for a Fe-Si material. Without field and under static tension, the volume fraction of the domain orientations more favorably aligned to the tension direction will increase. By increasing the field in the direction of the tension, the material almost reaches a magnetic saturation, with most of the domains oriented along the direction of the magneto-elastic loading.

A simplified schematic of the domain arrangement under a magneto-elastic loading is presented in Fig. 2.2.6. In this schematic, two main parts concerning the magnetization process can be highlighted: under moderate loadings (Fig. 2.2.6 (b-d)), a domain wall motion takes

place, resulting in a substantial increase in magnetization. Under a strong loading (Fig. 2.2.6 (e)), before the saturation, a rotation of the magnetization is observed, and so the orientation of domains will tend to align with the loading direction. The rotation mechanism also can be observed in Fig. 2.2.1b, in which the magnetostriction strain decreases under high magnetization levels.

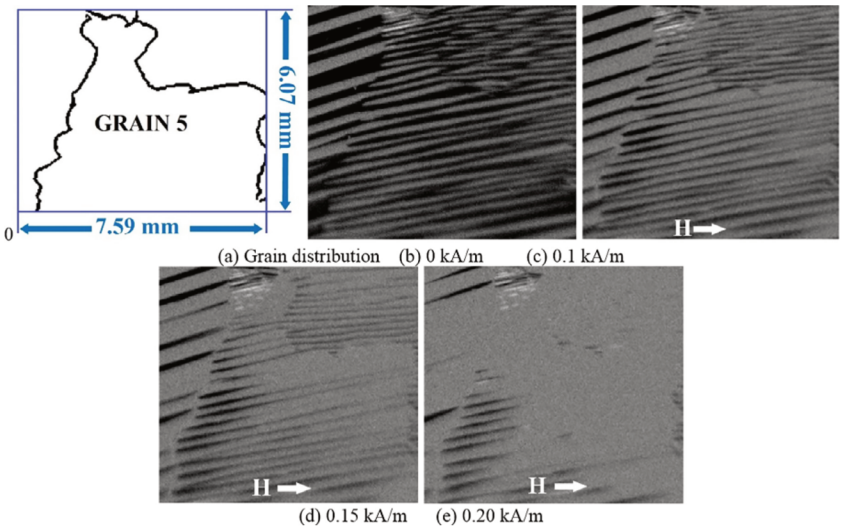

Figura 2.2.8: Domain wall motion of a grain of a silicon steel sheet under a tension of 130 MPa and increasing magnetic field Liu et al. [2019].

The irreversible (hysteretic) domain wall motion is attributed to the presence of defects in ferromagnetic materials, such as impurities, dislocations, and grain boundaries, that have different magnetic properties than the matrix material. For example, considering a non-magnetic spherical defect, as shown in Fig. 2.2.9a, a free-poles distribution on its surface results in a magnetostatic energy due to the demagnetizing effect. This magnetostatic energy is reduced when a domain wall passes through the inclusion, as observed in Fig. 2.2.9b. In an isolated defect, spike domains can be formed around it, as seen in Fig. 2.2.9c, which also reduces the magnetostatic energy of the system. Therefore, the inclusions can be viewed as an energetic local minimum that attracts the domain walls, pinning their motion. In this case, to continue the magnetization process, it is necessary to increase the energy of the system for the domain wall to escape from the defect. This threshold value can be related to the coercive field on a hysteresis curve and notably characterizes the dissipative behavior of ferromagnetic materials Cullity and Graham [2009].

In addition to the stress sensitivity and anisotropy, the magnetic hysteresis also strongly depends on the loading frequency Appino et al. [2020] and on the temperature Sixdenier

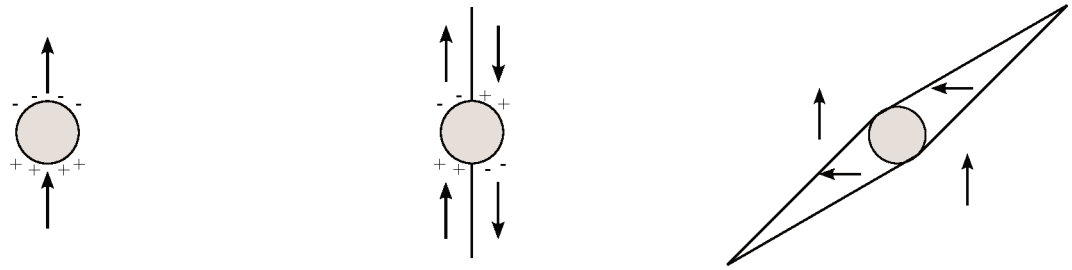

(a) Poles distribution on an inclusion.

(b) Intersection between the inclusion and the domain wall.

(c) Spike domain around an inclusion.

Figura 2.2.9: Influence of a defect on the domain wall motion (adapted from Jiles [1991]).

et al. [2015]. This work considers only quasi-static loadings, and isothermal processes. Moreover, only mechanical stresses below the elastic limit are considered. However, it should be noted that plasticity is another phenomenon that modifies the hysteretic behavior of ferromagnetic materials Domenjoud and Daniel [2023].

The modeling of the coupled magneto-elastic behavior can be split into two classes: reversible or anhysteretic behavior (the dissipation mechanisms are not considered) and the irreversible or hysteresis behavior. In what follows, only the main approaches for the modeling of the macroscopic magneto-elastic behavior are introduced.

2.3 Reversible modeling

2.3.1 Multiscale model

The magnetization process, as introduced in the previous section, involves complex phenomena taking place at different scales. Consequently, a multiscale approach can be used to model the macroscopic magneto-mechanical behavior of a volume element with a proper definition of localization and homogenization schemes. The scales involved in the anhysteretic multiscale modeling are shown in Fig. 2.3.1. The minor scale considered is the magnetic domain one (denoted by the index α), where the magnetic moments are aligned in the same direction - with minimal domain exchange energy - so the magnetization and magnetostriction strain are homogeneous. The following scale is the crystal or grain (denoted by the index g). A grain comprises a group of domains with several orientations, and each domain orientation is characterized by a volume fraction p_α. On the following scale, the polycrystalline representative volume element (RVE) is a continuum element that represents, on average, the material behavior. The last scale is the structure, where the geometry and dimensions of a device are

necessary - with the proper boundary conditions - to simulate its operation. The multiscale approach presented here focuses on modeling the magneto-elastic behavior at the RVE (macroscopic) scale Daniel et al. [2008].

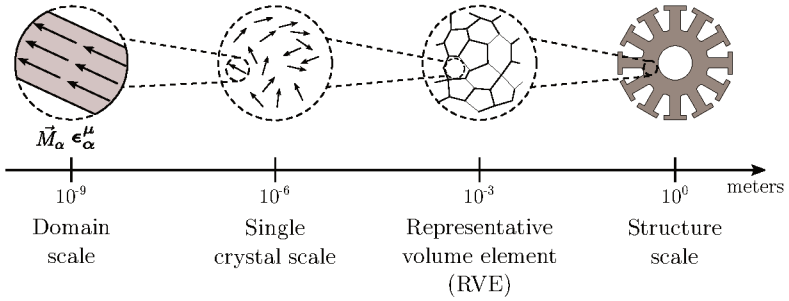

Figura 2.3.1: Scales involved in the multiscale modeling.

The first law of thermodynamics at the domain scale can be expressed as Hubert et al. [2022]:

$$\dot{u}_\alpha = \vec{H}_\alpha \cdot \dot{\vec{B}}_\alpha + \sigma_\alpha : \dot{\varepsilon}_\alpha - \operatorname{div}(\vec{q}_\alpha), \tag{2.3.1}$$

u_α is the domain internal energy density, the dot-product $\vec{H}_\alpha \cdot \dot{\vec{B}}_\alpha$ represents the domain magnetic power density, the double-contraction $\sigma_\alpha : \dot{\varepsilon}_\alpha$ represents the domain mechanical power, and $\vec{q}_\alpha$ is the heat flux. The second-law of thermodynamics can be written as:

$$T_\alpha \dot{s}_\alpha \geq -\operatorname{div}(\vec{q}_\alpha) + \operatorname{grad} T_\alpha \cdot \frac{\vec{q}_\alpha}{T_\alpha}, \tag{2.3.2}$$

with T_α the temperature and s_α the entropy. From the Legendre transformations of u_α, the Helmholtz f_α and the Gibbs g_α free energy densities are introduced and defined as:

$$f_\alpha = u_\alpha - T_\alpha s_\alpha \qquad \text{and} \qquad g_\alpha = f_\alpha - \vec{H}_\alpha \cdot \vec{B}_\alpha - \sigma_\alpha : \varepsilon_\alpha. \tag{2.3.3}$$

Combining (2.3.1), (2.3.2) and (2.3.3), neglecting spatial thermal variations ($\operatorname{grad} T_\alpha = \vec{0}$), temporal thermal variations ($\dot{T}_\alpha = 0$), and the dissipation, the power balance writes:

$$\dot{g}_\alpha = -\mu_0 \vec{M}_\alpha \cdot \dot{\vec{H}}_\alpha - \varepsilon_\alpha : \dot{\sigma}_\alpha. \tag{2.3.4}$$

The energy variation dg_α for a time step dt is:

$$dg_\alpha = -\mu_0 \vec{M}_\alpha \cdot d\vec{H}_\alpha - \varepsilon_\alpha : d\sigma_\alpha. \tag{2.3.5}$$

Considering small perturbations, the strain ε_α can be expressed as:

$$\varepsilon_\alpha = \varepsilon_\alpha^e + \varepsilon_\alpha^\mu = \mathscr{C}_\alpha^{-1} : \sigma_\alpha + \varepsilon_\alpha^\mu, \tag{2.3.6}$$

with ε_α^e the elastic strain at the domain scale, ε_α^μ is the magnetostriction strain tensor of (2.2.13) for cubic crystallographic symmetric, and $\mathscr{C}_\alpha$ the domain stiffness tensor. The integration of (2.3.5) over the stress path gives the magneto-elastic part of the Gibbs free energy Hubert [2019]:

$$g_\alpha^{me} = -\frac{1}{2}\sigma_\alpha : \mathscr{C}_\alpha^{-1} : \sigma_\alpha - \varepsilon_\alpha^\mu : \sigma_\alpha. \tag{2.3.7}$$

From the Helmholtz free energy, defined using a Taylor expansion of magnetization Hubert [2019] and considering a cubic symmetry, the magnetic and the anisotropy parts of the Gibbs free energy are written as:

$$\begin{aligned} g_\alpha^{mag} &= -\mu_0 \vec{M}_\alpha \cdot \vec{H}_\alpha \\ g_\alpha^{an} &= K_1 \left(\alpha_1^2\alpha_2^2 + \alpha_1^2\alpha_3^2 + \alpha_2^2\alpha_3^2\right) + K_2 \left(\alpha_1^2\alpha_2^2\alpha_3^2\right). \end{aligned} \tag{2.3.8}$$

To simplify the modeling, the field and stress are considered homogeneous within the material ($\vec{H} = \vec{H}_\alpha$ and $\sigma = \sigma_\alpha$). The Gibbs free energy is then:

$$g_\alpha = g_\alpha^{mag} + g_\alpha^{me} + g_\alpha^{an} \qquad \text{with} \qquad \begin{cases} g_\alpha^{mag} = -\mu_0 \vec{M}_\alpha \cdot \vec{H} \\ g_\alpha^{me} = -\varepsilon_\alpha^\mu : \sigma \\ g_\alpha^{an} = K_1 \left(\alpha_1^2\alpha_2^2 + \alpha_1^2\alpha_3^2 + \alpha_2^2\alpha_3^2\right) + K_2 \left(\alpha_1^2\alpha_2^2\alpha_3^2\right). \end{cases} \tag{2.3.9}$$

The heterogeneity of field and stress can be considered in a more complete multiscale approach Daniel et al. [2008]. In this case, using localization schemes allows for modeling the non-homogeneous distribution of the magneto-elastic loadings in a polycrystal.

As shown in Fig. 2.3.2 and in earlier works Daniel et al. [2014], Hubert [2019], the effect of stress on magnetization is non-monotonic. The formulation of (2.3.9) does not capture such a tendency. This drawback can be solved by adding a stress-dependent demagnetizing term in the energy balance Daniel et al. [2014], or by adding a higher-order development of the magneto-elastic Hubert [2019]. The magneto-elastic energy, including a second-order term -

quadratic in stress - is proposed in Hubert [2019]. In da Silva et al. [2022], a development of the magneto-elastic energy using an equivalent stress σ_{eq} is presented and defined as:

$$g_\alpha^{me} = g_\alpha^{me(1)} + g_\alpha^{me(2)} = -\varepsilon_\alpha^\mu : \sigma - \frac{3}{2}\lambda_s' \sigma_{eq}^2 \left(\vec{\alpha} \otimes \vec{\alpha} - \frac{1}{3} I \right) : \left(\vec{h} \otimes \vec{h} \right). \tag{2.3.10}$$

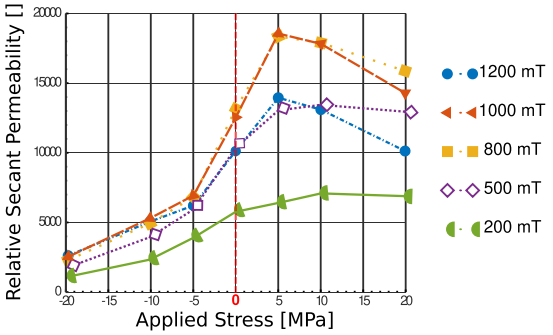

Figura 2.3.2: Uniaxial stress effect on the relative secant permeability of an electrical steel Mailhé et al. [2020].

In (2.3.10) the second-order magnetostriction constant λ_s' is introduced, and an equivalent stress Daniel and Hubert [2009], written in terms of $\vec{h} = \vec{H}/\|\vec{H}\|$ and the deviatoric part of σ, is used. σ_{eq} is:

$$\sigma_{eq} = \frac{3}{2} \vec{h}^t \left(\sigma - \frac{1}{3} \mathrm{tr}(\sigma) I \right) \vec{h}. \tag{2.3.11}$$

The magnetostriction constant λ_s' can be identified as (see Appendix B) da Silva et al. [2022]:

$$\lambda_s' = -\frac{\lambda_s}{2\sigma_m}, \tag{2.3.12}$$

where σ_m is the value of the applied uniaxial stress corresponding to the maximum magnetic permeability (obtained from a uniaxial characterization of permeability under stress). λ_s is the saturation magnetostriction, which can be evaluated considering the Reuss hypothesis of uniform stress within an isotropic material Daniel et al. [2008]:

$$\lambda_s = \frac{2}{5}\lambda_{100} + \frac{3}{5}\lambda_{111}. \tag{2.3.13}$$

The volume fraction p_α of a domain family with direction $\vec{\alpha}$ is established using a

Boltzmann relation Buiron et al. [1999]:

$$p_\alpha = \frac{\exp\left(-A_s\, g_\alpha\right)}{\sum_\alpha \exp\left(-A_s\, g_\alpha\right)}, \tag{2.3.14}$$

with A_s a material parameter that is proportional to the initial susceptibility χ_0 of the stress-free anhysteretic curve Daniel et al. [2008]:

$$A_s = \frac{3\chi_0}{\mu_0 M_s^2}. \tag{2.3.15}$$

The set of possible domain orientations is defined through the nodes of an icosphere - a geometric mesh that approximates a sphere using triangular faces Daniel and Galopin [2008]. With the definition of p_α, the magnetization $\vec{M}_g$ and the magnetostriction strain ε_g^μ at the grain scale are evaluated by:

$$\vec{M}_g = \sum_\alpha p_\alpha \vec{M}_\alpha \qquad \text{and} \qquad \varepsilon_g^\mu = \sum_\alpha p_\alpha \varepsilon_\alpha^\mu. \tag{2.3.16}$$

The macroscopic (see RVE in Fig. 2.3.1) magnetization $\vec{M}$ and magnetostriction strain ε^μ are then evaluated by an operation of volume average:

$$\vec{M} = \sum_g p_g \vec{M}_g \qquad \text{and} \qquad \varepsilon^\mu = \sum_g p_g \varepsilon_g^\mu, \tag{2.3.17}$$

where p_g represents the proportion of each grain orientation, which can be defined from crystallographic texture measurements of the sample.

Simplifications on this multiscale approach can be made, namely considering an equivalent simplified crystallographic texture with a reduced number of grain orientations, leading to a simplified texture multiscale model (STMSM) Bernard et al. [2019]. A further simplification consists in representing the macroscopic behavior using a fictitious single-crystal, leading to the so-called simplified multiscale model (SMSM) Daniel et al. [2015] or even limiting the number of possible domain orientations to six, resulting in analytical formulas for the magneto-elastic behavior Daniel [2018], Daniel [2013].

Similarly to the approach introduced in this section, a multiscale modeling is also presented in Ito et al. [2015]. First, this modeling defines a simplified six-domain structure, with orientations corresponding to the easy axes of the cubic symmetry. A minimization procedure of the total energy results in the magnetic state of this simplified structure domain. Then,

the macroscopic response corresponds to the assembly of several simplified domain structures. Such a minimization approach is also presented in Daniel [2003].

2.3.2 Thermodynamic macroscopic model

In this approach Dorfmann and Ogden [2003], Fonteyn et al. [2010], the induction $\vec{B}$ and the strain ε are independent variables. The magnetization $\vec{M}$ and mechanical stress σ are calculated by:

$$\vec{M} = -\frac{\partial f}{\partial \vec{B}} \qquad \text{and} \qquad \sigma = \frac{\partial f}{\partial \varepsilon}, \tag{2.3.18}$$

$f(\varepsilon, \vec{B})$ represents the Helmholtz free-energy density. Considering an isotropic material, $f(\varepsilon, \vec{B})$ can be expressed through six invariants Fonteyn et al. [2010]:

$$\begin{gathered} f = f(I_1, I_2, I_3, I_4, I_5, I_6) \qquad \text{with} \\ I_1 = \text{tr}(\varepsilon),\ \ I_2 = \frac{1}{2}(\text{tr}(\varepsilon))^2,\ \ I_3 = \det(\varepsilon),\ \ I_4 = \vec{B}\cdot\vec{B},\ \ I_5 = \vec{B}\cdot\varepsilon\cdot\vec{B},\ \ I_6 = \vec{B}\cdot\varepsilon^2\cdot\vec{B}. \end{gathered} \tag{2.3.19}$$

Analytical expressions for $f(\varepsilon, \vec{B})$ are presented in Aydin et al. [2017], Fonteyn et al. [2010], Rasilo et al. [2019b]. This approach with invariants is flexible to changes in the state variables - originally $(\varepsilon, \vec{B})$ - and so $(\vec{H}, \sigma)$ could be chosen depending on the application, and a new set of invariants is defined Rasilo et al. [2019b]. One drawback of this modeling is identifying the parameters that define the energy density, which usually requires several measurements Rasilo et al. [2019b]. A magneto-mechanical anhysteretic model based on the invariant theory is also presented in Taurines et al. [2022].

Despite its simplifications when compared to micromagnetics modeling, the multiscale approach has good prediction capabilities of the macroscopic anhysteretic magnetic behavior of a ferromagnetic material under stress, as observed in Hubert et al. [2022]. Moreover, it accounts for a multiaxial loading condition with a clear parameters identification protocol. One drawback of the multiscale approach is the use of magnetic field and stress as state variables, which implies the inversion of the model for application with classical finite element formulations Bernard et al. [2019]. On the other side, in the thermodynamic model, by using the invariant theory, the model is flexible to changes in the state variables. However, the complexity of identifying the parameters increases by increasing the number of invariants that express the energy density.

2.4 Irreversible modeling

Macroscopic hysteresis models are generally developed from a Physics or purely mathematical description. In this section, models based on these two perspectives will be presented, detailing the main features and drawbacks of each approach.

2.4.1 Jiles-Atherton model

In scalar Jiles-Atherton (JA) approaches Sablik and Jiles [1993], Sablik et al. [1987, 1988], the magnetization M is defined by the sum of M_b, that represents the bending of domain walls, and M_{irr}, which denotes the irreversible domain wall motion:

$$M = M_b + M_{irr} \qquad \text{with} \qquad M_b = c\,(M_{an} - M_{irr})\,, \tag{2.4.1}$$

with c a material parameter and M_{an} the anhysteretic magnetization. Often, the anhysteretic behavior is described by the Langevin function in Jiles-Atherton-Sablik approaches:

$$M_{an} = M_s \left[\coth\left(\frac{H_e}{a}\right) - \frac{a}{H_e} \right], \tag{2.4.2}$$

where M_s represents the saturation magnetization, and a is a material parameter that controls the slope of the anhysteretic curve. An effective field H_e is introduced, and its terms are evaluated from an energy balance as presented in Sablik and Jiles [1993]. H_e is then:

$$H_e = H + \alpha M + H_\sigma \qquad \text{with} \qquad H_\sigma = \frac{3}{2}\frac{\sigma}{\mu_0}\left(\frac{\partial \varepsilon^\mu(\sigma, M)}{\partial M}\right), \tag{2.4.3}$$

where α is a material parameter, σ is a mechanical stress coaxial to H, and ε^μ is a scalar magnetostriction strain - dependent of M and σ. Expressions for $\varepsilon^\mu(\sigma, M)$ are proposed in Sablik and Jiles [1993], Sablik et al. [1987, 1988]. In the JA modeling theory, the energy balance in a dissipative material can be written as Sablik and Jiles [1993]:

$$\mu_0 \int M dH_e = \mu_0 \int M_{an} dH_e - \mu_0 \kappa \int \frac{dM_{irr}}{dH_e} dH_e, \tag{2.4.4}$$

with κ a pinning parameter describing the dissipation. Differentiating (2.4.4) with respect to H_e, the evolution of M is then evaluated by:

$$M = M_{an}(H_e) - \delta \kappa \left(\frac{dM_{irr}}{dH_e}\right), \tag{2.4.5}$$

the direction coefficient δ is introduced to enforce a positive dissipation:

$$\delta = \begin{cases} -1, & \text{if } dH/dt < 0 \\ 1, & \text{if } dH/dt \geq 0. \end{cases} \tag{2.4.6}$$

An energy analysis of Jiles-Atherton approaches is presented in Zirka et al. [2012], and it can be highlighted the inconsistency of the model when considering only a reversible behavior. Particularly, the magnetic anhysteretic characteristic goes to the second quadrant on a $B-H$ curve (see Fig. 2.4.1) which is a non-physical behavior.

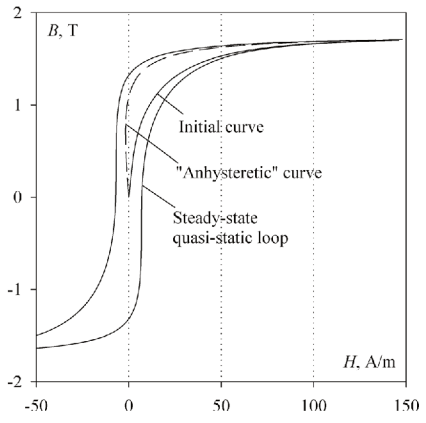

Figura 2.4.1: Magnetic behavior simulated with a JA approach Zirka et al. [2012].

The limitation of mechanical stress coaxial with the magnetic field is addressed in

Sablik et al. [1993]. To consider the influence of biaxial stress on magnetic behavior, in Sablik and Jiles [1999], Sablik et al. [1999], two uniaxial magneto-mechanical energies corresponding to the stresses applied along two perpendicular axes are introduced, and further added to the effective field definition. The inclusion of 3-D fields in Jiles-Atherton approaches is addressed in Bergqvist [1996]. Moreover, the non-physical representation of minor loops with classical Jiles-Atherton approach (see Fig. 2.4.2) can be overcome by adapting the pinning parameter Benabou et al. [2008], Leite et al. [2009].

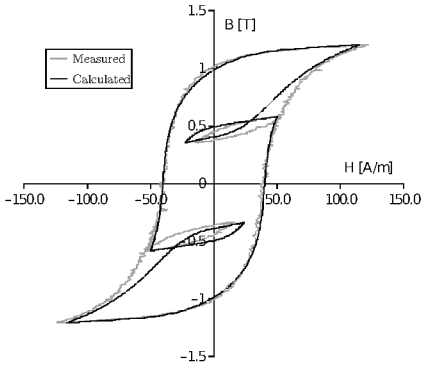

Figura 2.4.2: Comparison between measured and simulated stress-free hysteresis behavior of Fe-Si 3% under harmonic excitation Leite et al. [2009].

Another possibility to extend the Jiles-Atherton modeling to the magneto-elastic behavior consists of a combination approach: the reversible behavior is modeled with a magneto-elastic anhysteretic model in place of the Langevin function, and the pinning parameter is adapted to mechanical loadings. Examples of this strategy under a quasi-static field and constant stress Bernard and Daniel [2015], Bernard et al. [2020], Ram et al. [2020], and under a quasi-static stress and constant field Zhao et al. [2021], are presented in the literature, where a simplified multiscale model (introduced in Section 2.3.1) represents the reversible behavior. Moreover, the thermodynamic approach (introduced in Section 2.3.2) can also be coupled with a Jiles-Atherton model, as shown in Rasilo et al. [2016].

2.4.2 Armstrong model

In the Armstrong approach, the dissipative behavior is described from irreversible changes in the domain volume fraction. Considering a scalar field, an anhysteretic volume fraction p_α^{anh} is evaluated from the Boltzmann distribution (2.3.14). The irreversible part of the volume fraction is then evaluated by Armstrong [2003]:

$$dp_\alpha = \frac{1}{\kappa}\left(p_\alpha^{anh} - p_\alpha\right)|dH|, \tag{2.4.7}$$

with κ a material parameter representing the domain walls pinning. This approach is then applied to predict the magnetic behavior of Terfenol-D. However, it was pointed out in Evans and Dapino [2010] that the Armstrong model exhibits non-physical behavior in the region of asymmetric minor loops. A further development on the definition of the irreversible volume fraction was presented in Evans and Dapino [2010], and the model showed its capabilities to predict the magnetic response of Galfenol under a quasi-static field and under a quasi-static stress.

2.4.3 Hauser model

The polycrystal hysteretic magnetic response of a ferromagnetic material is modeled in Daniel et al. [2014], as a combination of a magneto-mechanical anhysteretic model Daniel et al. [2008] with a magnetic hysteresis approach Hauser [2004]. The dissipative behavior is captured from the definition of an irreversible field whose norm is evaluated at the grain scale as:

$$\|\vec{H}_{irr}\| = \delta\left(\frac{k_r}{\mu_0 M_s} + c_r\|\vec{H}\|\right)\left[1 - \kappa_g \exp\left(-\frac{k_a}{\kappa_g}\|\vec{M} - \vec{M}^{(inv)}\|\right)\right], \tag{2.4.8}$$

with k_r, c_r, k_a and κ_g material parameters. δ is a sign function of the loading. $\vec{M}^{(inv)}$ is the value of $\vec{M}$ at the previous inversion of the loading direction Daniel et al. [2014]. The parameter k_r defines the coercive field and is adapted to a stress dependence. To avoid the long-time simulation of a polycrystal, in Daniel et al. [2015], the RVE is represented by an equivalent single-crystal - with anhysteretic behavior defined through a SMSM. This single-crystal approach can also reproduce the magnetic behavior under a biaxial stress state. The main drawback of this approach is the update of only the norm of the irreversible field at each time step. This limitation may cause problems in the case of simulation with a rotating field.

The combination of multiscale model and the Hauser approach is also used to simulate the piezomagnetic behavior, as presented in Ouaddi et al. [2019]. By analogy with the field decomposition, piezomagnetic effects are considered through the definition of an irreversible

stress σ_{irr}, where a coercive stress captures the dissipative magnetostriction strain under variable mechanical loading. However, the model proposed in Ouaddi et al. [2019] is limited to uniaxial loadings.

2.4.4 Plasticity based models

A strategy to describe the magnetic hysteresis comes from the analogy of this phenomenon with plasticity. Some models of plastic behavior start from thermodynamics principles with the definition of internal variables that describe the dissipation. These internal variables are a modeling choice in a way that they unify in a single (or more) variable (or variables) the complex microscopic process that manifests in the form of dissipation at the macroscopic scale Maugin [2015]. Examples of internal variables are the irreversible magnetization in the Jiles-Atherton approaches, the domain volume fraction in the Armstrong model, and the irreversible field in the Hauser model.

Some thermodynamically consistent plasticity approaches introduce a switching surface, a quantity that controls the material behavior, whether reversible or dissipative. The switching surface is defined to ensure that the constraint of the second law of thermodynamics is respected - namely, dissipation is always positive - and is a function of the internal variables. In Landis [2002], a macroscopic thermodynamic framework for the ferroelectric hysteresis is proposed, also considering stress effects. The remanent polarization and strain are chosen as internal variables. Another example, presented in Kiefer et al. [2012], is applying the internal variables approach to simulate the strain response of magnetic shape memory alloys.

2.4.5 Preisach model

In the classical Preisach model, first, it is introduced the notion of hysterons denoted by γ. These hysteresis operators are represented by a rectangular loop, as presented in Fig. 2.4.3a, whose width is controlled by the fields H_u and H_d. The set of hysterons is defined by a distribution $\phi(H_u, H_d)$. The hysteretic magnetization can be calculated by Mayergoyz [1991]:

$$M(t) = \int\int \phi(H_u,H_d)\gamma(H_u,H_d)H(t)dH_u dH_d \quad \text{with} \quad \gamma H(t) = \begin{cases} -M_s, & \text{if } H_u, H_d \in T^{(+)} \\ M_s, & \text{if } H_u, H_d \in T^{(-)}. \end{cases} \tag{2.4.9}$$

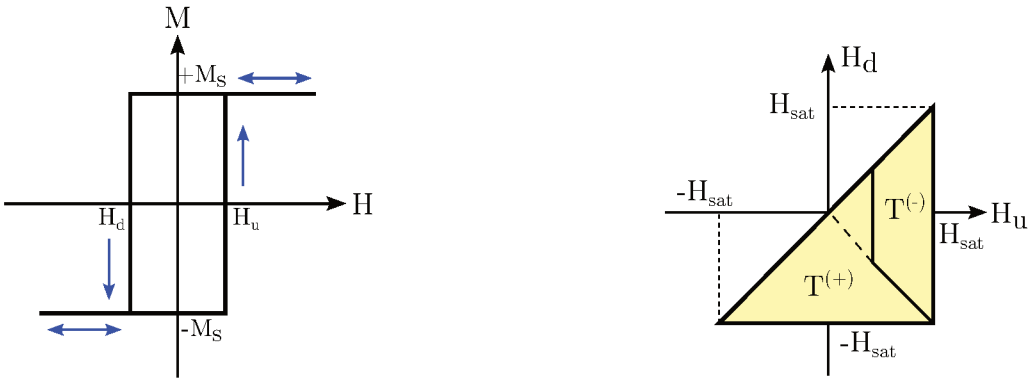

(a) Hysteresis loop of a hysteron.

(b) Hysteron state triangle.

Figura 2.4.3: Elements of Preisach hysteresis modeling.

The state of the hysterons is graphically represented by the Preisach triangle (Fig. 2.4.3b). For example, starting from the demagnetized state, consider the application of a scalar magnetic field $H_a < H_{sat}$, with H_{sat} the magnetic field in which saturation occurs. A set of hysterons changes its states from negative to positive, so the region $T^{(+)}$ increases. This process continues for all time steps of the magnetic field, including minor loops Mayergoyz [1991]. Due to the mathematical nature of the Preisach approach, the identification of the distribution $\phi(H_u, H_d)$ can be complex. Some works in the literature propose using analytical distributions to represent $\phi(H_u, H_d)$ Consolo et al. [2006], Sutor et al. [2010]. The inclusion of vector fields can be achieved by considering vector hysterons Della Torre et al. [2006].

A uniaxial magneto-elastic extension of the Preisach model is proposed in Bergqvist and Engdahl [1991] by including a stress-dependent equivalent field. This modification allows the simulation of hysteresis loops under a constant stress and time-varying field or a constant field and time-varying stress. Other uniaxial propositions Bolshakov and Lapovok [1996], Sipeky and Ivanyi [2008] consider mechanical loadings through the distribution as a stress function.

2.4.6 Play model

The play operator is another popular mathematical hysteresis model. In magnetism, the hysteretic response of induction B with the input of magnetic field H can be described by Bobbio et al. [1997]:

$$B = \sum_{k=1}^{N} f^k \left(P^k[H] \right), \tag{2.4.10}$$

considering a system made of N hysterons. P^k the play operator that defines the state

of the k hysteron, and f^k a shape function. The scalar play operator P^k is defined by Bobbio et al. [1997]:

$$P^k = \begin{cases} P^k_{(p)} & \text{if} \quad \|H - P^k_{(p)}\| \leq \zeta^k \\ H - \zeta^k \dfrac{H - P^k_{(p)}}{\|H - P^k_{(p)}\|} & \text{otherwise,} \end{cases} \tag{2.4.11}$$

with ζ^k the width of the k hysteron. As an example, consider the single hysteron operator shown in Fig. 2.4.4. The induction remains constant for an increasing field before reaching a threshold, as seen in Fig. 2.4.4 (a). After the threshold is reached, the induction increases linearly with the field (Fig. 2.4.4 (b)). These steps continue when the field changes its direction (Figs. 2.4.4 (c)-(d)). For this example, the play operator is illustrated in Fig. 2.4.4 (e). Including a proper shape function allows the model to capture the saturation mechanism of the magnetic hysteresis.

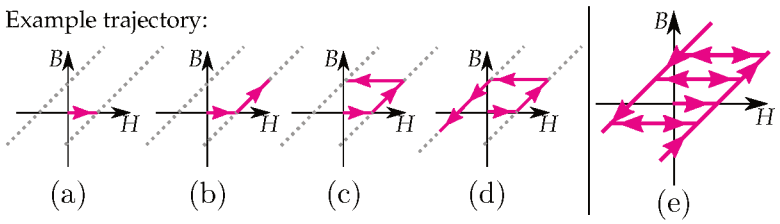

Figura 2.4.4: An example of trajectory and the play operator Mörée and Leijon [2023].

An extension of the scalar play model to mechanical loadings is proposed in Ito et al. [2018], and a decomposition of the field into reversible and irreversible parts is presented. The reversible behavior is evaluated from a multiscale approach Ito et al. [2015], and a probability distribution of pinning fields is introduced to evaluate the irreversible part of the field.

A superposition of scalar play-operators allows considering vector fields in the play approach Matsuo and Shimasaki [2008]. In Matsuo et al. [2020, 2023], a vector play model, including stress effects, is presented. In these approaches, the hysteresis mechanism is evaluated at the grain scale, and the dissipation parameter is weighted by the volume fraction, which results in a parameter identification with stress-free measurements only. However, the hysteresis evaluation at the grain scale may increase the computational cost compared to the hysteresis mechanism applied directly at the macroscopic scale.

The magnetic response of a ferromagnetic material, as observed in the hysteresis curves, is the result of a complex evolution of the domain structure. Usually, the magnetic hysteresis models are defined from either a macroscopic approach, a multiscale approach, or a combination of both. Although many hysteretic magneto-elastic modeling approaches are available in the literature, as described above, none of them simultaneously combines three key features for the numerical analysis of electromagnetic devices. The first is the ability to consider fully multiaxial loadings as encountered in practical applications, the second is thermodynamic consistency to compute losses accurately, and the last is the implementation into numerical analysis tools, which requires low computation time for behavior evaluation. One modeling approach that checks the last two requirements is the energy-based model. However, this approach, further detailed, was developed for the stress-free case only.

2.4.7 Stress-free energy-based hysteresis model

In this stress-free energy-based approach, the magnetization is the internal variable that describes dissipative effects. The Clausius-Duhem inequality at the macroscopic scale of a ferromagnetic material can be written as Bergqvist [1997], Henrotte et al. [2006]:

$$D = \mu_0 \vec{H} \cdot \dot{\vec{M}} - \dot{f} \geq 0, \tag{2.4.12}$$

with D the dissipation and $\dot{f}$ the time-derivative of the Helmholtz free energy density. In a reversible framework, a reversible magnetic field $\vec{H}_{rev}$ is introduced, and it is defined as:

$$\vec{H}_{rev} = \frac{1}{\mu_0} \frac{\partial f}{\partial \vec{M}}. \tag{2.4.13}$$

Combining (2.4.12) and (2.4.13) yields:

$$D = \mu_0 \left(\vec{H} - \vec{H}_{rev} \right) \cdot \dot{\vec{M}} \geq 0. \tag{2.4.14}$$

In a dissipative framework, an irreversible field $\vec{H}_{irr}$ is introduced and defined by $\vec{H}_{irr} = \vec{H} - \vec{H}_{rev}$. The dissipation is modeled by analogy with a mechanical dry-friction system Henrotte et al. [2006]. The defects that pin domain walls at specific positions are represented by a pinning field κ, a positive scalar in the isotropic case. The dissipation writes:

$$D = \mu_0 \kappa \|\dot{\vec{M}}\| = \mu_0 \vec{H}_{irr} \cdot \dot{\vec{M}}. \tag{2.4.15}$$

As in (2.4.13) - where a relation between $\vec{H}_{rev}$ and f was defined - the irreversible field $\vec{H}_{irr}$ can be written as a function of the partial derivative of D. Since D is not differentiable at $\dot{\vec{M}} = \vec{0}$, the subdifferential of a convex function is considered Henrotte et al. [2006]. An illustrative example of a subdifferential is presented in Appendix A. The subdifferential of $D(\dot{\vec{M}})$ is the set Prigozhin et al. [2016]:

$$\partial D(\dot{\vec{M}}) := \left\{ \vec{H}_{irr} \in {R_e}^3 : \ \kappa\|\vec{y}\| \geq \kappa\|\dot{\vec{M}}\| + \vec{H}_{irr} \cdot (\vec{y} - \dot{\vec{M}}), \quad \forall\, \vec{y} \in {R_e}^3 \right\}. \tag{2.4.16}$$

The elements $\vec{H}_{irr} \in \partial D(\dot{\vec{M}})$ are the subgradients of D at $\dot{\vec{M}}$. At $\dot{\vec{M}} = \vec{0}$, the subgradient writes:

$$\kappa\|\vec{y}\| \geq \|\vec{0}\| + \vec{H}_{irr} \cdot \left(\vec{y} - \vec{0}\right), \quad \forall\, \vec{y} \in {R_e}^3. \tag{2.4.17}$$

From the inequality:

$$\vec{H}_{irr} \cdot \vec{y} \leq \|\vec{H}_{irr}\| \ \|\vec{y}\|, \quad \forall\, \vec{y} \in {R_e}^3, \tag{2.4.18}$$

the condition of (2.4.17) will hold when:

$$\|\vec{H}_{irr}\| \leq \kappa. \tag{2.4.19}$$

At $\dot{\vec{M}} \neq \vec{0}$, D is differentiable so:

$$\frac{\partial D}{\partial \dot{\vec{M}}} = \kappa \frac{\dot{\vec{M}}}{\|\dot{\vec{M}}\|} = \vec{H}_{irr}. \tag{2.4.20}$$

The subdifferential of $D(\dot{\vec{M}})$ is then written as:

$$\frac{\partial D}{\partial \dot{\vec{M}}} = \begin{cases} \vec{H}_{irr}, \|\vec{H}_{irr}\| \leq \kappa, & \text{if } \dot{\vec{M}} = \vec{0} \\ \vec{H}_{irr} = \kappa \dfrac{\dot{\vec{M}}}{\|\dot{\vec{M}}\|}, & \text{otherwise.} \end{cases} \tag{2.4.21}$$

This set implies that for $\|\vec{H}_{irr}\| < \kappa$ the magnetization $\vec{M}$ remains constant until a threshold κ is reached. From the previous definitions:

$$\vec{H} - \vec{H}_{rev} - \vec{H}_{irr} = \vec{0}. \tag{2.4.22}$$

The analogy of the magnetic hysteresis with a dry-friction mechanism is illustrated in Fig. 2.4.5, with the magnetic field $\vec{H}$ representing the driving force, and the strain of the system corresponding to variations on magnetization:

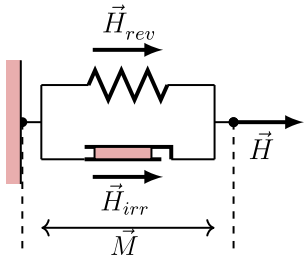

Figura 2.4.5: Analogy of the magnetic hysteresis phenomena with a mechanical system Jacques [2018].

When the threshold is reached ($\dot{\vec{M}} \neq 0$), and from the definitions of (2.4.13) and (2.4.21), the relation of (2.4.22) can be written as:

$$\vec{H} - \frac{1}{\mu_0}\frac{\partial f}{\partial \vec{M}} - \frac{\partial D}{\partial \dot{\vec{M}}} = \vec{0} \qquad \rightarrow \qquad \vec{H} - \frac{1}{\mu_0}\frac{\partial f}{\partial \vec{M}} - \kappa\frac{\dot{\vec{M}}}{\|\dot{\vec{M}}\|} = \vec{0}. \tag{2.4.23}$$

Considering a scalar case, Fig. 2.4.6 illustrates this energy-based approach. Neglecting the dissipation mechanism results in a magnetic anhysteretic behavior. The hysteresis modeling essentially involves translating the anhysteretic curve along the pinning parameter κ. Therefore, κ is the coercive field and can be identified from a standard magnetic characterization. This modeling has limitations in representing the first magnetization curve and minor loops, as observed in Fig. 2.4.6.

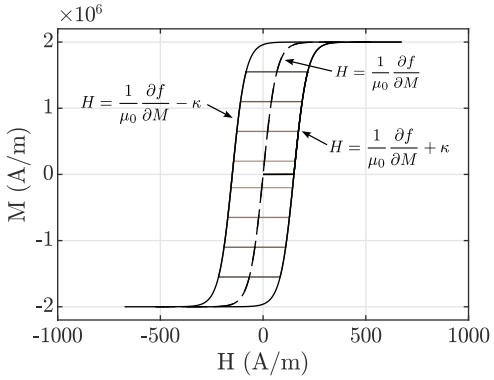

Figura 2.4.6: Application of the energy-based model to a scalar loading.

To solve the limitation of representing minor loops and the first magnetization curve, the pinning field κ can be represented by a discrete distribution of pinning fields Henrotte et al. [2006]. In this case, the single dry-friction system of Fig. 2.4.5 is replaced by a series connection of dry-friction systems or cells. In Fig. 2.4.7, a structure with N cells is presented.

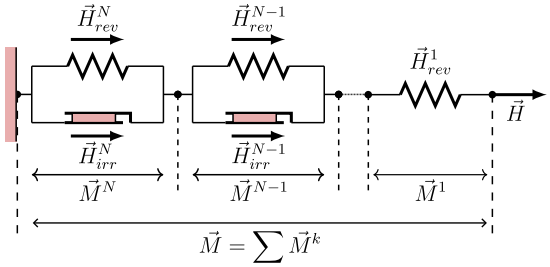

Figura 2.4.7: Analogy of the magnetic hysteresis phenomena with a mechanical system made of N dry-friction cells Jacques [2018].

In this multicells context, the fields at each k-cell are defined as Jacques [2018]:

$$\vec{H} - \vec{H}^k_{rev} - \vec{H}^k_{irr} = \vec{0} \quad \rightarrow \quad \vec{H} - \frac{1}{\mu_0}\frac{\partial f^k}{\partial \vec{M}^k} - \partial D^k(\dot{\vec{M}}^k) \in \begin{cases} \vec{H}^k_{irr}, \|\vec{H}^k_{irr}\| \leq \kappa^k, & \text{if } \dot{\vec{M}}^k = \vec{0} \\ \vec{H}^k_{irr} = \kappa^k \dfrac{\dot{\vec{M}}^k}{\|\dot{\vec{M}}^k\|}, & \text{otherwise.} \end{cases} \tag{2.4.24}$$

The constant κ^k represents the pinning field at the k-cell. By using a weighted sum, the total magnetization $\vec{M}$ is then:

$$\vec{M} = \sum_{k=1}^{N} \omega^k \vec{M}^k, \tag{2.4.25}$$

where the weight ω^k of each cell is introduced. It verifies:

$$\sum_{k=1}^{N} \omega^k = 1. \tag{2.4.26}$$

Concerning the numerical implementation of the model, three approaches are usually performed and detailed hereafter. The first one is an explicit solution of (2.4.24) or vector-play approach. In this modeling, the unit vector that defines the direction of $\vec{H}_{irr}$ is approximated by Henrotte et al. [2006], Jacques [2018]:

$$\vec{e}_{\vec{H}^k_{irr}} = \frac{\vec{H}^k_{irr}}{\|\vec{H}^k_{irr}\|} = \frac{\vec{H} - \vec{H}^k_{rev}}{\|\vec{H} - \vec{H}^k_{rev}\|} \approx \frac{\vec{H} - \vec{H}^k_{rev(p)}}{\|\vec{H} - \vec{H}^k_{rev(p)}\|}. \tag{2.4.27}$$

Using this approximation, the explicit update procedure of $\vec{H}^k_{rev}$ at each cell is:

$$\vec{H}^k_{rev} = \begin{cases} \vec{H}^k_{rev(p)}, & \text{if } \|\vec{H} - \vec{H}^k_{rev(p)}\| \leq \kappa^k \\ \vec{H} - \kappa^k \dfrac{\vec{H} - \vec{H}^k_{rev(p)}}{\|\vec{H} - \vec{H}^k_{rev(p)}\|}, & \text{otherwise.} \end{cases} \tag{2.4.28}$$

The induction $\vec{B}$ then is evaluated by:

$$\vec{B} = \mu_0 \vec{H} + \sum_{k=1}^{N} M_{an}(\vec{H}^k_{rev}), \tag{2.4.29}$$

with $M_{an}(\vec{H}^k_{rev})$ a function that defines the reversible behavior.

A second approach to evaluating the energy-based model consists of directly solving (2.4.24) using a minimization procedure François-Lavet et al. [2013]. In this case, the functional $g(\vec{H}, \vec{M}^k)$ is introduced:

$$g(\vec{H}, \vec{M}^k) = f^k(\vec{M}^k) - \mu_0 \vec{H} \cdot \vec{M}^k, \tag{2.4.30}$$

with the partial derivative:

$$\frac{1}{\mu_0} \frac{\partial g}{\partial \vec{M}^k} = \frac{1}{\mu_0} \frac{\partial f}{\partial \vec{M}^k} - \vec{H}. \tag{2.4.31}$$

For sufficiently small time steps, the time-derivative of the dissipation is approximated by:

$$D \approx \mu_0 \kappa^k \frac{\|\vec{M}^k - \vec{M}^k_{(p)}\|}{\Delta t}, \tag{2.4.32}$$

with $\vec{M}^k_{(p)}$ the magnetization at the previous time step. The subgradient of (2.4.32) is given by the set:

$$\partial D^k(\vec{M}^k) \in \begin{cases} \vec{H}^k_{irr}, \|\vec{H}^k_{irr}\| \leq \kappa^k, & \text{if } \vec{M}^k = \vec{M}^k_{(p)} \\ \vec{H}^k_{irr} = \kappa^k \dfrac{\vec{M}^k - \vec{M}^k_{(p)}}{\|\vec{M}^k - \vec{M}^k_{(p)}\|}, & \text{otherwise.} \end{cases} \tag{2.4.33}$$

Finally, (2.4.24) can be written as the unconstrained minimization problem:

$$\begin{aligned} &\frac{\partial}{\partial \vec{M}^k}\left[g(\vec{H},\vec{M}^k) + \Delta t\, D(\vec{M}^k)\right] = 0 \quad \rightarrow \\ &\vec{M}^k = \min_{\vec{M}^k} \quad \left[f^k(\vec{M}^k) - \mu_0 \vec{H}\cdot\vec{M}^k + \mu_0 \kappa^k \|\vec{M}^k - \vec{M}^k_{(p)}\|\right]. \end{aligned} \tag{2.4.34}$$

In another minimization procedure Prigozhin et al. [2016], the reversible field $\vec{H}^k_{rev}$ is updated at each time step. As pointed out in Kaltenbacher et al. [2022], the implementations presented in Prigozhin et al. [2016] and in François-Lavet et al. [2013] are mathematically equivalent. A feature of the energy-based model presented in Prigozhin et al. [2016] is the definition of κ as a symmetric positive-definite matrix, which can employ different thresholds when the field is applied along rolling or transverse directions, and results in a scalar parameter in the isotropic case. Such an approach requires measurements along rolling and transverse directions to identify the components of the matrix κ, as shown in Upadhaya et al. [2020].

In Jacques [2018], a comparison between the vector-play approach Henrotte et al. [2006] and the minimization procedure François-Lavet et al. [2013] is presented, considering an isotropic magnetic behavior. Both approaches lead to the same values under uniaxial magnetic loading and under a purely circular rotating field. The two approaches show slight differences when applying a 2D spiral field. Another difference between the two approaches is related to the simulation time. The vector-play approximation results in an explicit model whose simulation time is reduced compared to a minimization procedure.

A common drawback of this energy-based approach is the limitation to reproducing the hysteresis losses in the range of saturation, which can be attributed to the absence of the rotation mechanism description in the model development. Correcting this drawback requires adapting the pinning parameter to vanish the hysteresis losses under high induction Bergqvist [1997], Sauseng et al. [2022].

The energy-based approach is a rate-independent magnetic hysteresis model defined directly in a vector form. Its energetic description ensures a thermodynamic consistency. Notably, the vector-play approximation results in a computational light version of the complete minimization approach, which is mandatory for reasonable finite element simulations. Moreover, symmetric and asymmetric minor loops can be modeled using a pinning field distribution. Due to these improvements compared to classical approaches, the energy-based model in a vector-play form is chosen in this study and extended to the magneto-elastic case, further detailed in Chapter 4.

3 Experimental characterization of the magneto-elastic behavior

This chapter deals with the uniaxial magneto-elastic measurements performed on a magnetic material. First, the experimental apparatus is detailed, specifying the main parts to supply and measure the magnetic and mechanical quantities. The measurement methodology is briefly introduced, considering different quasi-static loadings: static stress and varying field, static field and varying stress, and varying both field and stress. The material used in the experimental tests is a high-formability low-carbon steel (DC04) used in the automotive industry. The experimental measurements are then presented, highlighting the magneto-mechanical coupling in the material, and are related to results already presented in the literature.

3.1 Experimental setup

The apparatus used to carry out the magneto-mechanical characterization of a sample under uniaxial stress is detailed in Domenjoud et al. [2019] and shown in Fig. 3.1.1. The mechanical setup is composed of a tension/compression machine Zwick/Roell Z030 with the possiblity to control in force or displacement. The resolution and accuracy are 0.2 N $\pm$ 0.06% in force control, and 1 μm $\pm$ 0.1% in displacement control. Force measurements are performed using a 10 kN load cell (strain gauge sensor TC-LC010kN).

The magnetic setup is composed of two U-shaped Fe-Si yokes to ensure the closure of the magnetic flux. A Kepco 72-14MG amplifier, that can deliver 14 A and 72 V with 0.2% accuracy, supplies current to an excitation coil (28 turns) positioned around the sample. The current is measured with a LA 125-P transducer with 0.6% accuracy. A Teslameter FM302 and a transverse Hall proble 20 mT AS-VTP, which can operate from DC to 1 kHz, measure the magnetic field with accuracy of 0.5% and measured noise of 19 A/m in the range of 0 - 15.9 kA/m.

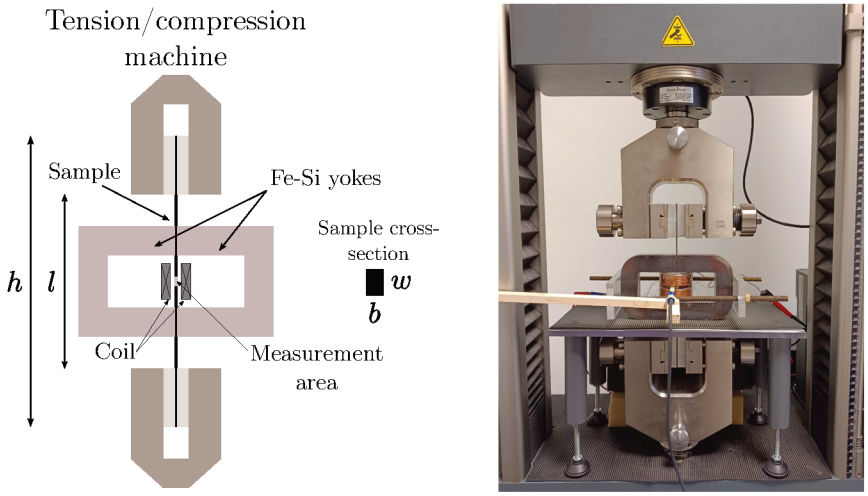

Figura 3.1.1: Experimental setup for magnetic characterization under uniaxial stress.

From the Faraday-Lenz law, the measured induction is evaluated from the numerical integration of the induced voltage $v(t)$ of a B-coil wound around the sample:

$$\Delta B = -\frac{1}{NS}\int_t v(t)\,dt, \tag{3.1.1}$$

with N the number of turns (85) of the B-coil and S the cross-section of the sample. The measured noise on induction is about 0.1 mT with accuracy of 0.2%. The magnetostriction strain is measured with a strain gauge rosette glued on the measurement area surface (Fig. 3.1.1) of the sample. The signal is amplified with a 4-channel strain gauge conditioner Vishay 2120 B with about 0.5% of accuracy and measured noise of about 10^{-6}. A DS 1006 dSPACE processor board performs the acquisition and control of signals with a sampling frequency of 50 kHz. More information on the control and acquisition system can be found in Domenjoud et al. [2019]. A measurement reproducibility error is found to be about 0.5% in the magnetic field and 0.3% in the induction.

3.2 Characteristics of the sample

The material studied in this work is a low-carbon steel DC04. Crystallographic texture measurements for this material are presented in Fig. 3.2.1. Such measurements are obtained from the electron back-scattering diffraction (EBSD) technique[1]. More details about this technique and the representation of pole figures are shown in Appendix C.

[1]The author gratefully acknowledges Anne-Laure Helbert (ICMMO) for the EBSD measurements.

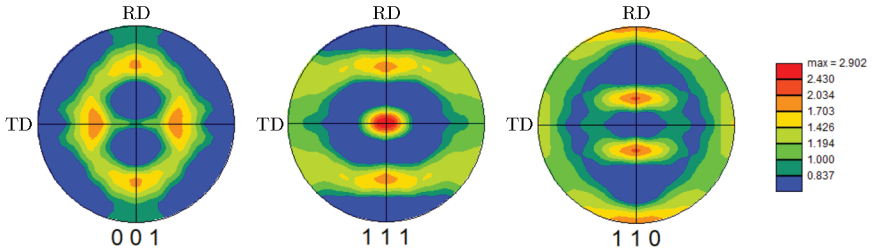

Figura 3.2.1: Pole figures for a DC04 steel obtained by stereographic projection.

The chemical composition of this sample, according to the datasheet of the manufacturer, is shown in Table 3.2.1. The Young modulus E and the Yield stress R_e are estimated as 200 GPa and 120 MPa, respectively Domenjoud and Daniel [2023].

Tabela 3.2.1: Chemical composition of the DC04 low-carbon steel (wt%) ArcelorMittal [1996].

Fe	C	Mn	Si
99.32	0.08	0.5	0.1

Under compression, a buckling analysis is necessary to determine the critical loading that ensures the integrity of the sample. Using the classical Euler analysis, the critical stress level σ_{cr} can be evaluated as Ziegler [1953]:

$$\sigma_{cr} = \frac{k_b}{S}\frac{\pi^2 EI}{l^2} = \frac{k_b}{S}\frac{\pi^2 E}{l^2}\frac{b^3 w}{12}, \tag{3.2.1}$$

with l the free length, I the moment of inertia for the cross-section, and k_b a factor that depends on the fixing conditions of the sample. The sample is fixed at both sides on the grips of the machine (see the schematic of Fig. 3.1.1 - left), so $k_b = 4$ Ziegler [1953]. The dimensions of the sample and the critical buckling loading are presented in Table 3.2.2. However, it must be noted that fixing yokes on both sides of the sample will reduce the free length, so it is expected an increase in the critical loading. In what follows, the maximum applied compression is about 100 MPa.

Tabela 3.2.2: Critical buckling condition of the sample.

Material	h (mm)	b (mm)	w (mm)	l (mm)	σ_{cr} (MPa)
DC04	250	2	20	150	117

3.3 Measurement methodology

In the experimental tests presented in this chapter, the uniaxial magneto-elastic loadings are applied along the rolling direction of the sample. Following, the anhysteretic and hysteresis measurement methodologies will be detailed.

3.3.1 Anhysteretic tests

The procedure to measure the anhysteretic magnetic behavior is presented in Domenjoud and Daniel [2023]. First, a sinusoidal current of amplitude I_{max} is applied, describing a major hysteresis loop. Then, the controlled current I is set as an exponentially decaying sine wave superimposed to a bias level:

$$I = I_{max} \sin(2\pi f t) \exp(-k_d\, t) + I_{bias} \left(1 - \exp(-k_d\, t)\right) \tag{3.3.1}$$

with k_d a damping factor, I_{bias} the bias current, and f is the frequency. The damping factor is set to 0.34 s^{-1} for a frequency $f = 1$ Hz. After stabilization, the resulting magnetic field and magnetization correspond to a point of the anhysteretic curve. Fig. 3.3.1 depicts the anhysteretic measurement process. This approach is repeated at several bias levels and under static uniaxial stresses, as summarized in Table 3.3.1.

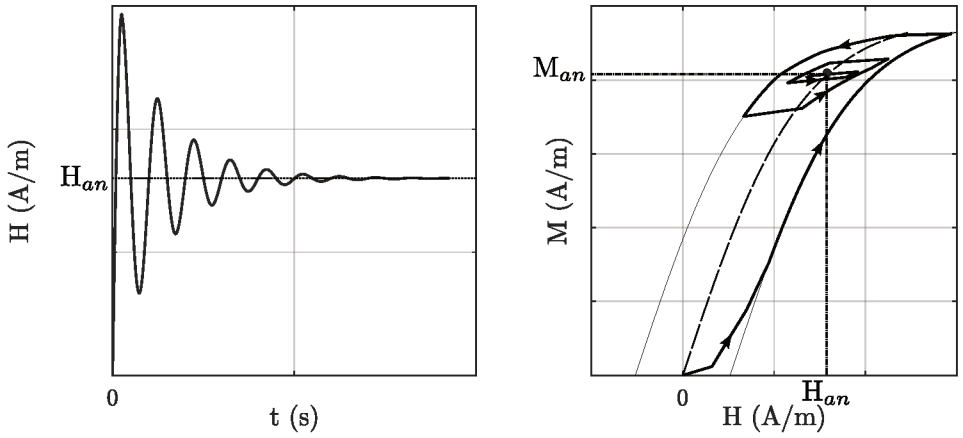

Figura 3.3.1: Representation for measuring a point of the anhysteretic curve.

3.3.2 Hysteresis tests

For the magnetic hysteresis measurements, first, the material is demagnetized. Thus, the controlled current is set as an exponentially decaying sine wave (3.3.1) with zero bias current

Tabela 3.3.1: Summary of the anhysteretic tests.

Static stress and quasi-static field		
	Loading	**Measurements**
Anhysteretic	Uniaxial stress $\sigma = [-100 : 20 : 100]$ MPa Bias H-field: 20 values between 0 A/m and 3000 A/m	Induction $B_{an}(H_{an}, \sigma)$

($I_{bias} = 0$ A). After demagnetization, the controlled magnetic current is set as a sine wave to reach the same maximum magnetic field values $\pm H_{max}$. The maximum magnetic induction B_{max} (see Fig. 3.3.2) is evaluated as:

$$B_{max} = \frac{1}{2}\left(B_{H_{max}} + |B_{-H_{max}}|\right). \tag{3.3.2}$$

The demagnetization process is imperfect, so a residual induction B_{res} can be found in the measurements. For each test, B_{res} is evaluated by:

$$B_{res} = \frac{1}{2}\left(B_{H_{max}} - |B_{-H_{max}}|\right). \tag{3.3.3}$$

Following Domenjoud et al. [2019], the demagnetization process is successful if the following condition is verified:

$$B_{res} < 0.02\, B_{max}. \tag{3.3.4}$$

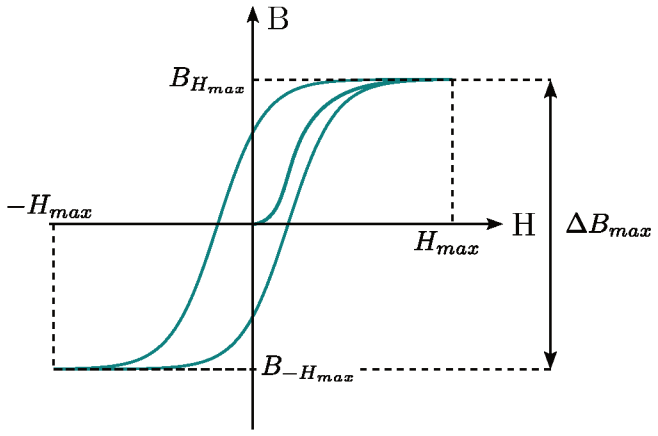

Figura 3.3.2: Major loop obtained after the demagnetization process.

The hysteresis measurement procedure is repeated under several static uniaxial stress

levels. Table 3.3.2 summarizes the hysteresis measurements and loadings.

Tabela 3.3.2: Summary of the hysteresis tests.

Static stress and quasi-static field		
	Loading	**Measurements**
Hysteresis	Uniaxial stress $\sigma = [-100 : 20 : 100]$ MPa	Induction $B(H,\sigma)$
	Peak field H_{peak}: 15 values between 140 A/m and 6800 A/m	Longi. and transv. magnetostriction $\varepsilon^{\mu}_{//}(H,\sigma)$ $\varepsilon^{\mu}_{\perp}(H,\sigma)$

3.3.3 Tests under variable stress

As seen in Chapter 2, the variation of magnetization due to stress variations, also known as piezomagnetism, is another characteristic that highlights the magneto-elastic coupling. The piezomagnetic behavior is measured as follows: the field is set as an exponentially decaying sine wave superimposed to a bias level, as in the anhysteretic test. A quasi-static cyclic force is applied after stabilizing the field at the bias level. Fig. 3.3.3 (left) summarizes the magneto-elastic loading conditions in a piezomagnetic test. After the mechanical cycle, the resulting piezomagnetic loop is illustrated in Figure 3.3.3 (right). This test is repeated at several bias field levels. Table 3.3.3 summarizes the loadings in the piezomagnetic tests.

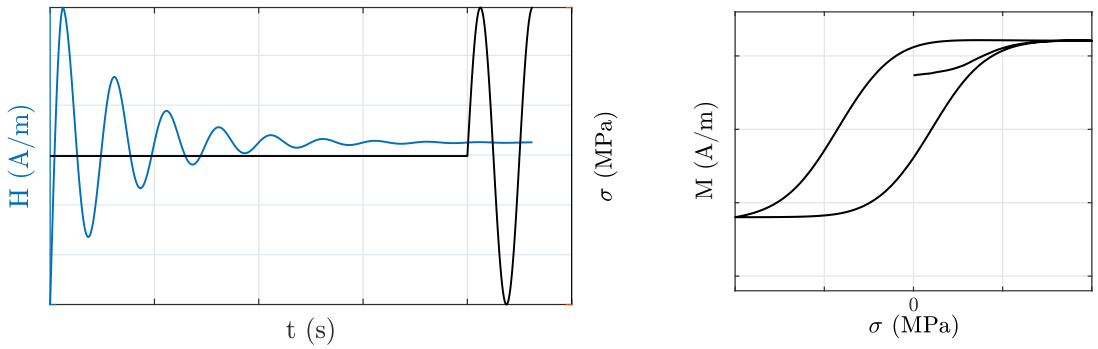

Figura 3.3.3: Magneto-elastic loading conditions in a piezomagnetic test (left) and the corresponding piezomagnetic loop (right).

A complex magneto-elastic test consists of setting both field and stress as quasi-static, as illustrated in Fig. 3.3.4. Such an experiment is not usually performed in the literature, but the magneto-mechanical setup allows the evaluation of the magnetic material response under this loading condition, which can be further used for modeling validation. As in the hysteresis measurements, first, the sample is demagnetized. Then, a quasi-static field and stress are applied.

Tabela 3.3.3: Summary of the piezomagnetic tests.

	Static field and quasi-static stress	
Piezomagnetic	Peak uniaxial stress $\sigma_{peak} = 100$ MPa Bias H-field: 5 values between 0 A/m and 3000 A/m	Induction $B(H, \sigma)$

Table 3.3.4 summarizes this test.

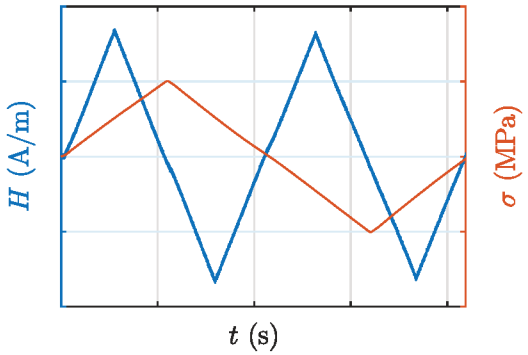

Figura 3.3.4: Quasi-static field and quasi-static stress loadings.

Tabela 3.3.4: Summary of the varying field and stress tests.

	Quasi-static field and quasi-static stress	
Hysteresis	Peak uniaxial stress $\sigma_{peak} = 100$ MPa Peak field $H_{peak} = 1500$ A/m	Induction $B(H, \sigma)$

According to the magneto-elastic loading, the experimental measurements are classified into three main categories: (a) Under static stress and quasi-static field, (b) Under static field and quasi-static stress - leading to the piezomagnetic behavior - and (c) with both field and stress quasi-static. The experimental results are presented in the following sections, with the error bars representing the error in the previously described measurement process.

3.4 Measurements under static stress and quasi-static field

3.4.1 Magnetic anhysteretic behavior

The effect of uniaxial stress on the anhysteretic magnetic behavior is presented in Fig. 3.4.1a. Notably, it is observed an important degradation of magnetization under compression.

Similar results for low-carbon steels are found in Dobranski et al. [1985], Hubert and Rizzo [2008]. The anhysteretic relative secant permeability μ_r^{anh} can be evaluated by:

$$\mu_r^{anh} = \frac{1}{\mu_0}\frac{B_{an}}{H_{an}}. \tag{3.4.1}$$

The anhysteretic relative secant permeability as a function of the applied stress for different field values is shown in Fig. 3.4.1b. In particular, it highlights the non-monotonic effect of stress on the magnetization. The maximum anhysteretic permeability is reached under $\sigma_m = 40$ MPa. Then, the permeability decreases under increments of tension.

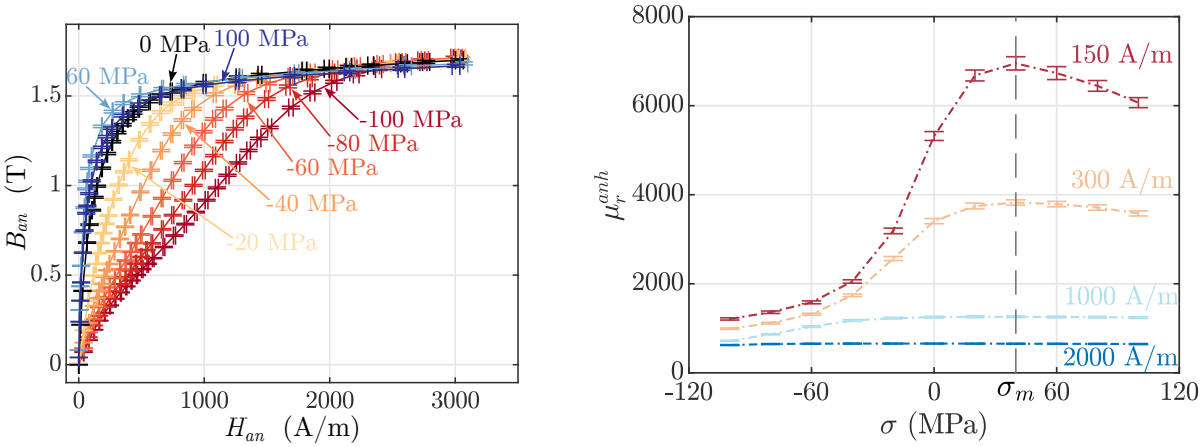

(a) Effect of uniaxial stress on the anhysteretic behavior.

(b) Magnetic permeability for different values of applied magnetic field.

Figura 3.4.1: Anhysteretic measurements.

3.4.2 Magnetic hysteresis

The magnetic hysteresis is the behavior under a quasi-static regime. Such a regime is defined as being independent of the loading frequency. An experimental analysis is presented to define the conditions for which the magnetic material response is approximately independent of the loading frequency. However, a drift may appear during the integration of the low frequency voltage of the B-coil. A drift correction method is then addressed. Subsequently, experimental measurements of the hysteresis behavior under static stress are presented. An explanation of the coupled magnetic behavior from a microscopic perspective is detailed.

3.5 Definition of the quasi-static regime

A characterization without stress indicates that a frequency of 1 Hz does not allow a quasi-static assumption for this material sample, as seen in Fig. 3.5.1a, where a significant change is observed in the coercive field H_c when comparing measurements at 1 Hz and 25 mHz. The remanent induction (Fig. 3.5.1b) is less sensitive to changes in frequency for this stress-free case. The hysteresis measurements under uniaxial stress are performed considering that the frequency of 25 mHz allows reaching the quasi-static regime. Such a value cannot be considered general since it is dependent on the prescribed waveform for the current, but it was empirically determined as relevant for the measurements shown here.

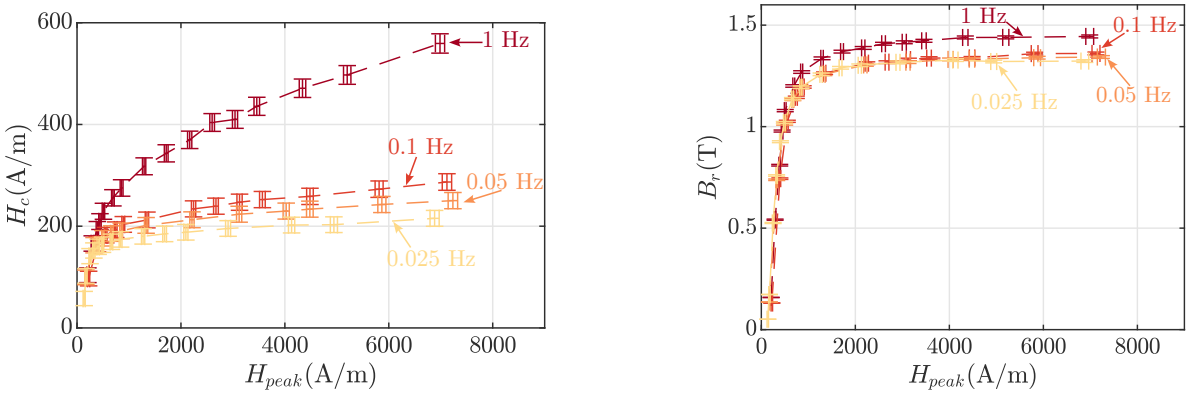

(a) Coercive field.

(b) Remanent induction.

Figura 3.5.1: Stress-free measurements at several frequency levels.

3.6 Correction of drift in magnetic induction

The integration DC drift - or a cumulative offset - in voltage measurements can be related with thermal variation of electronic components Garcia and Rivas [2005]. This becomes more problematic with the choice of the frequency of 25 mHz for the input waveform. The drift in the measured induction B_{mes} is linearly corrected with:

$$B_{cor} = B_{mes} + \frac{t}{\Delta t}\left(B_{max}^{(1)} - B_{max}^{(2)}\right), \tag{3.6.1}$$

considering the difference between two peaks: in Fig. 3.6.1 they are taken as $B_{max}^{(1)}$ at $t = 0$ s and $B_{max}^{(2)}$ at $t = 40$ s, with time difference denoted by Δt.

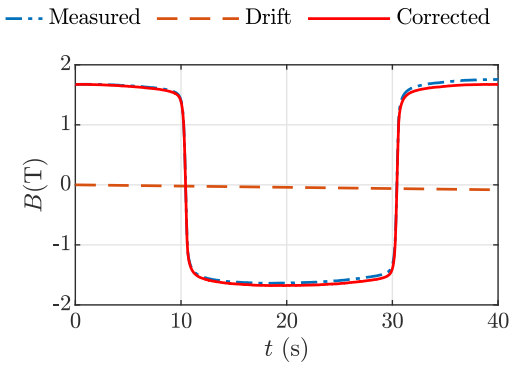

Figura 3.6.1: Drift correction in induction after the first magnetization.

3.7 Hysteresis measurements

The magnetic hysteresis measurements under uniaxial stress are presented in Fig. 3.7.1. The stress effect on the macroscopic hysteresis loops are noted specially under high compression. For example, at -100 MPa, the bowing of the hysteresis curves in the low field region, also seen in Fe-Si LoBue et al. [2000], Singh et al. [2016], is observed.

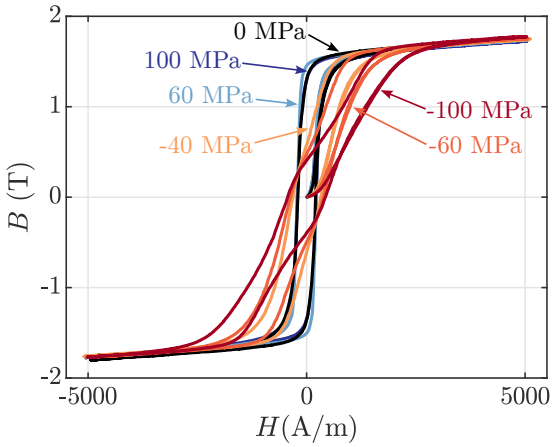

Figura 3.7.1: Hysteresis curves measurements under uniaxial stress.

The hysteresis losses are obtained by numerical integration of the surface of each hysteresis loop. Fig. 3.7.2 shows the hysteresis losses under uniaxial stress as a function of the maximum induction. Comparing the hysteresis losses for the same induction level is a common presentation of these results. The hysteresis losses under uniaxial stress for the same induction level are presented in Fig. 3.7.3. It can be noted that compression applied along the magnetization direction strongly increases the quasi-static losses. Such a loss trend is also observed in Fe-Si LoBue et al. [2000], Singh et al. [2016].

The effect of uniaxial stress on the magnetic hysteresis can also be analyzed at specific

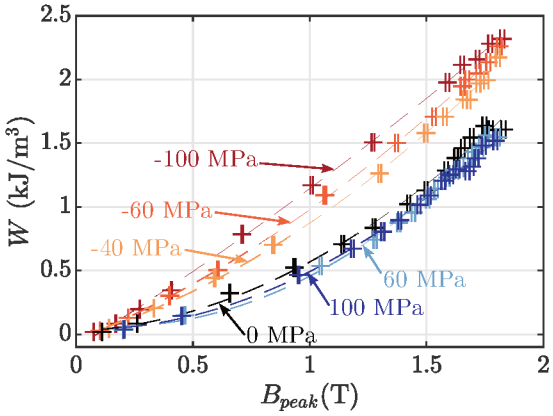

Figura 3.7.2: Measured hysteresis losses as a function of peak induction for different uniaxial stress levels.

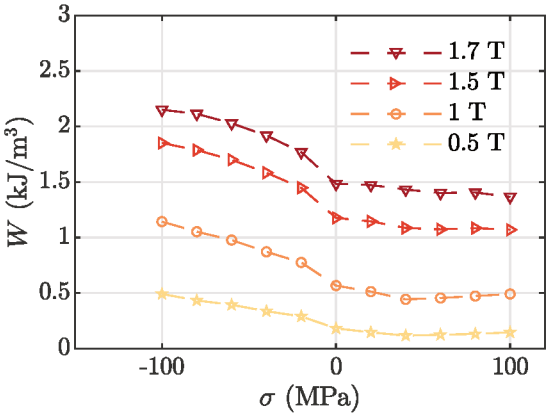

Figura 3.7.3: Hysteresis losses as a function of uniaxial stress.

regions of the hysteresis loop. Figs. 3.7.4 and 3.7.5 present the coercive field H_c under several levels of peak magnetic field and peak induction, respectively. As observed in Fig. 3.7.5, the coercive field follows the trend of the hysteresis losses under uniaxial stress.

The uniaxial stress effect in the remanent induction B_r for several levels of peak magnetic field is presented in Fig. 3.7.6, and in Fig. 3.7.7 under several levels of peak induction. Compression strongly affects the remanent induction.

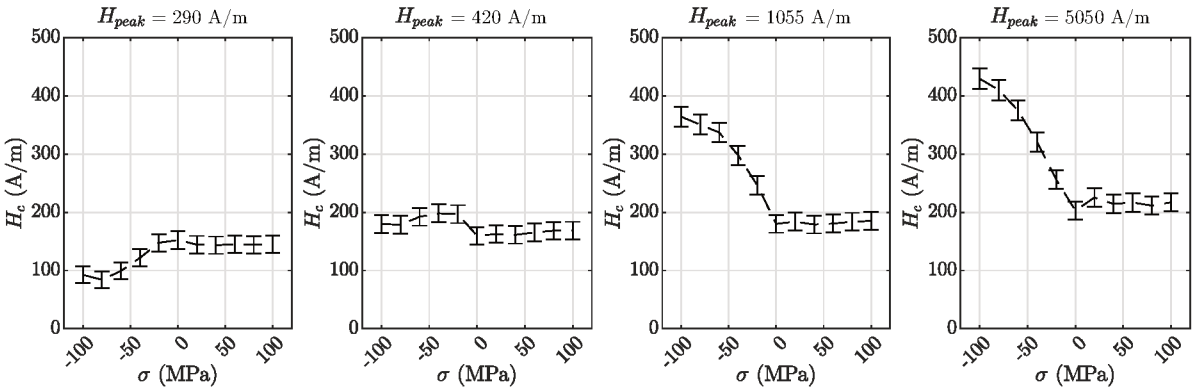

Figura 3.7.4: Measured coercive field as a function of uniaxial stress and under various peak magnetic fields.

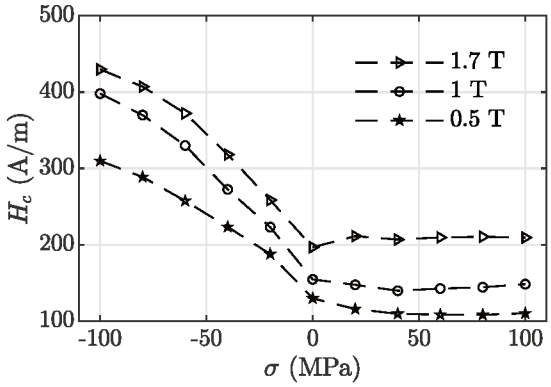

Figura 3.7.5: Measured coercive field as a function of uniaxial stress and under various peak induction levels.

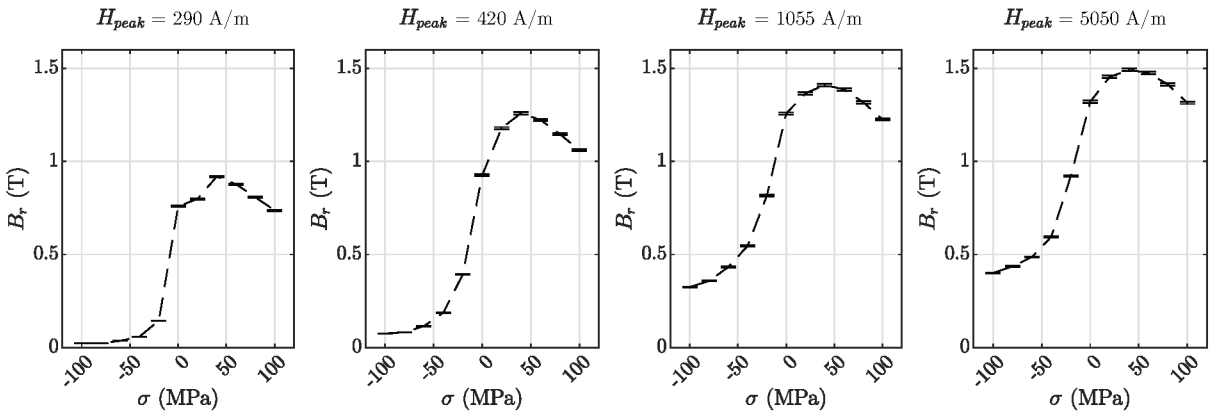

Figura 3.7.6: Measured remanent induction as a function of uniaxial stress and under various peak magnetic fields.

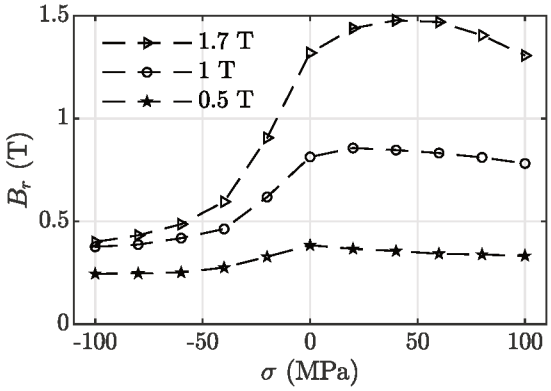

Figura 3.7.7: Measured remanent induction as a function of uniaxial stress and under various peak induction levels.

The longitudinal and transverse magnetostriction strain under uniaxial stress are presented in Figs. 3.7.8 and 3.7.9, respectively. Despite the noisy measurements, the influence of the stress state on the shape of the magnetostriction butterfly loops is notable. Moreover, by

plotting the relation $\varepsilon^{\mu}(M)$, the hysteresis effects on the magnetostriction strain are significantly reduced. These curves indicate that most of the hysteresis observed on $\varepsilon^{\mu}(H)$ comes from the one observed on the $B(H)$ characteristic. Besides, the $\varepsilon^{\mu}(M)$ measurements highlight the rotation mechanism: for example, taking the stress-free case, the longitudinal magnetostriction strain increases until $M \approx 1.3$ MA/m, then starts to decrease. Such a behavior is characteristic of the rotation mechanism present under high fields.

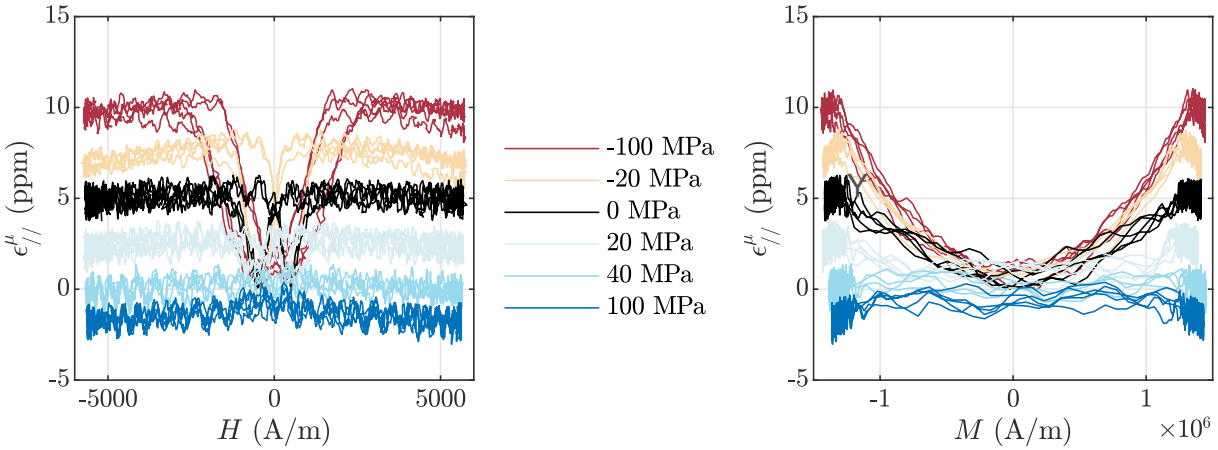

Figura 3.7.8: Longitudinal magnetostriction strain under uniaxial stress.

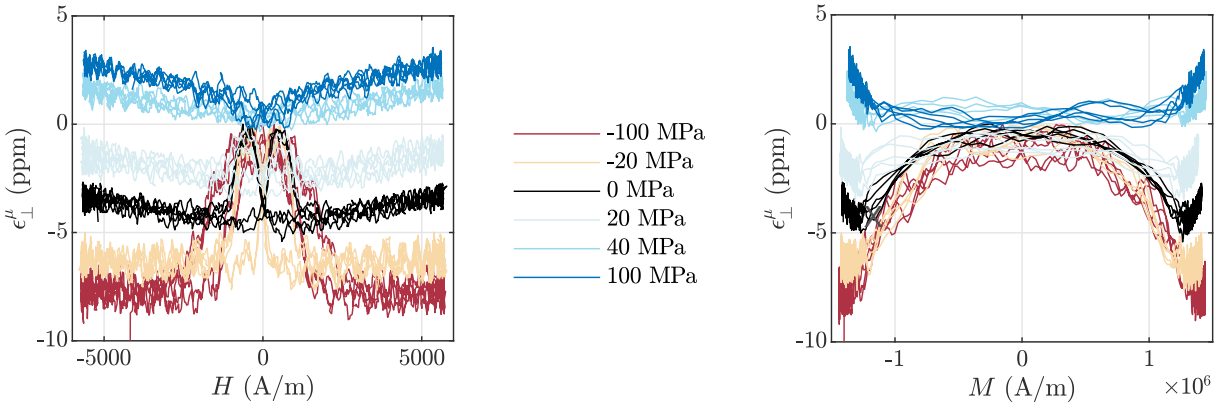

Figura 3.7.9: Transverse magnetostriction strain under uniaxial stress.

Magnetic field with higher harmonics forming asymmetric minor loops increase the hysteresis losses. By applying the magnetic field waveform of Fig. 3.7.10, the magnetic material response under this magnetic field and uniaxial stress is presented in Fig. 3.7.11. The asymmetric minor loops are notable, with the shape varying depending on the level of stress.

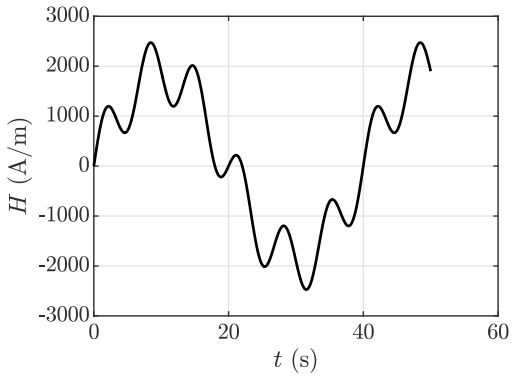

Figura 3.7.10: Applied field to measure asymmetric minor loops.

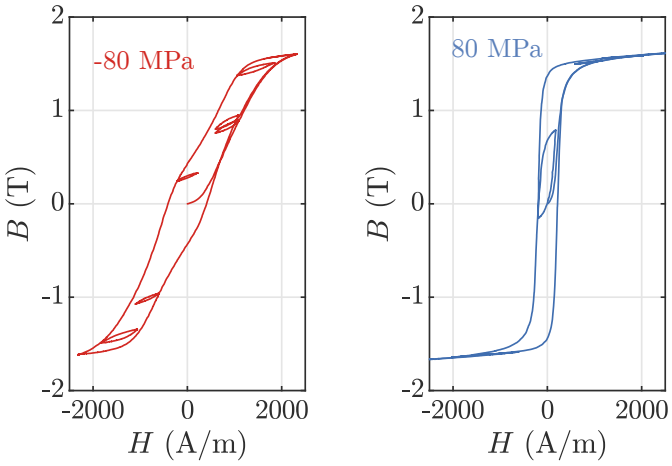

Figura 3.7.11: Magnetic hysteresis under uniaxial stress and field with harmonic content.

3.8 Measurements under static field and quasi-static stress

As previously introduced, to measure the piezomagnetic behavior, the force is applied after stabilizing the current at the bias level. In the results hereafter presented, the cyclic force is applied with a speed of 0.5 mm/s. As in the magnetic hysteresis measurements, a drift correction on induction is performed for each test.

The measured piezomagnetic behavior is shown in Fig. 3.8.1 considering several levels of static field. It can be observed that under a high static field, the relation $B(\sigma)$ is almost linear, which is an interesting behavior for designing force sensors. Another feature is related to the shape of the piezomagnetic loops, for which the anhysteretic results under static stress give some insights. In the region of domain rotation (for fields above 2000 A/m in Fig. 3.4.1a), there is a crossing of the curves implying that the dependence of the magnetization on stress is reversed: a compression leads to a relatively small increase in magnetization. This behavior is also emphasized in the piezomagnetic results of Fig. 3.8.1. Such a mechanism is experimental

evidence of the so-called Villari reversal Cullity and Graham [2009]. Similar observations are made on Hubert [2019], Hubert and Rizzo [2008].

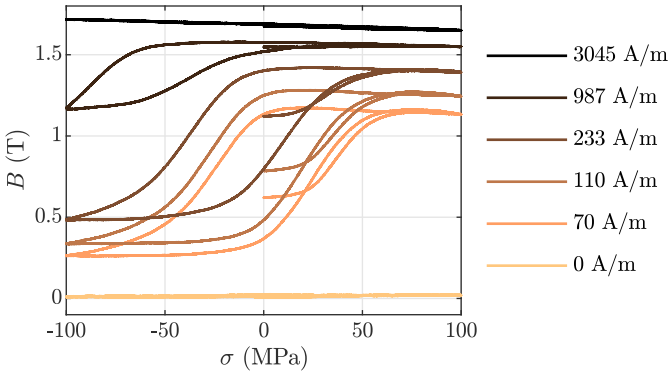

Figura 3.8.1: Piezomagnetic behavior under several levels of static field.

3.9 Measurement under both varying field and stress

The configuration with both variations of magnetic field and stress is not usual in characterizing ferromagnetic materials. However, the magneto-elastic setup allows for this kind of test, which gives a challenging configuration for model validation. The applied magneto-elastic loading is shown in Fig. 3.9.1 (top left), and the magnetic field waveform is set with two times the frequency of the stress waveform. The resulting magnetic hysteresis loops as a function of field and stress are depicted in Fig. 3.9.1 (top right) and Fig. 3.9.1 (bottom), respectively. A magnetic field period in the first half-cycle of stress leads to a $B(H)$ loop similar to the loops observed at constant stress but unsymmetric. In the half-cycle of compression, an interesting phenomenon can be analyzed: the combination of decreasing the magnetic field and increasing the compression (dashed lines region in 3.9.1 (top left)) results in a drop in magnetization observed on both $B(H)$ and $B(\sigma)$ loops.

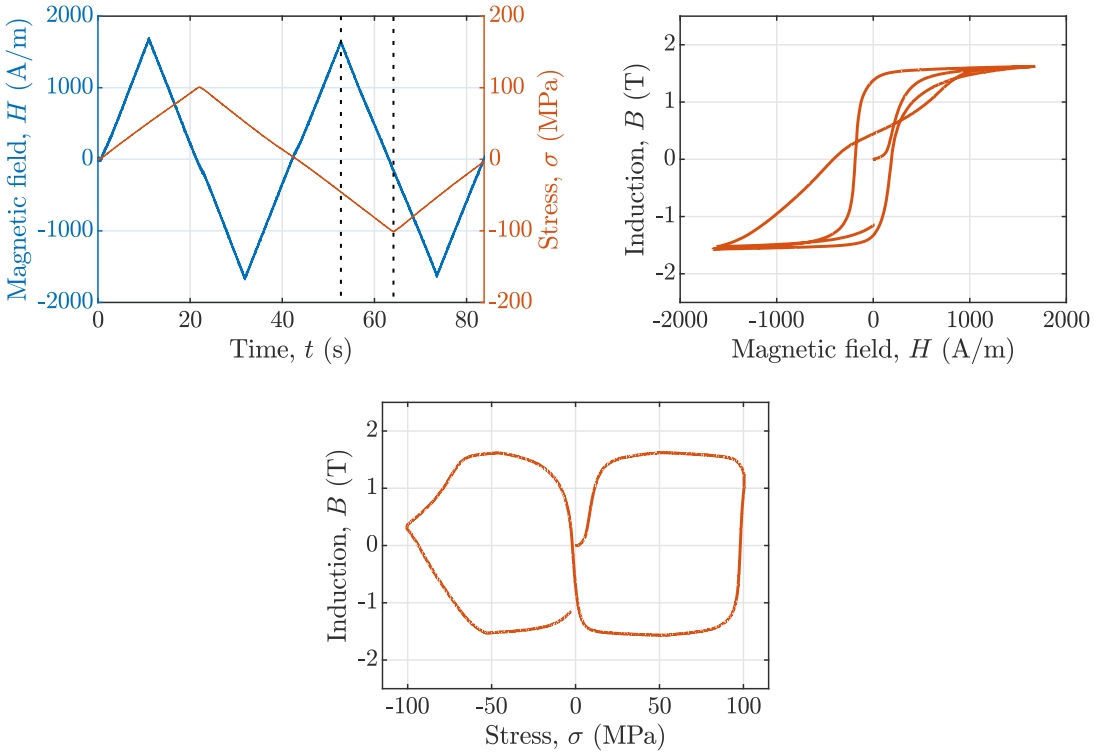

Figura 3.9.1: Magnetic hysteresis under quasi-static field and quasi-static stress.

The experimental measurements presented here highlight the strong coupling between magnetic and mechanical quantities in a ferromagnetic material and some of its particular features, such as the Villari effect and the non-monotonic effect of stress on magnetization. A good predictive modeling strategy should be able to reproduce such a complex behavior, with a limited set of parameters that could be identified from standard material characterizations.

4 Energy-based magneto-elastic hysteresis model under constant stress

This chapter presents a magneto-elastic hysteresis model under static mechanical stresses, mainly based on the papers da Silva et al. [2022, 2023]. As discussed in Chapter 2, an hysteretic magneto-elastic model is sought considering fully multiaxial loadings, thermodynamic consistency, and the implementation into numerical analysis tools. For the stress-free case, the hysteresis energy-based model Henrotte et al. [2006], Jacques [2018] fulfills these requirements. Therefore, this chapter presents an extension to the magneto-elastic case by combining the energy-based hysteresis approach with a multiscale anhysteretic model. Such an association results in an hysteresis model allowing multiaxial magneto-elastic loadings. Three situations under static stress are presented to validate the proposed approach: first, the model is applied to represent the magnetic behavior of a low-carbon DC04 steel - previously introduced in Chapter 3 - under uniaxial stress and alternating field. Then, using experimental data from the literature, the model is applied to a Fe-Si electrical steel under multiaxial stress configurations and alternating and rotating fields.

4.1 Thermodynamic formulation

In the framework of continuum thermodynamics, the energy balance - or first law of thermodynamics - in a ferromagnetic material at the macroscopic scale is composed of mechanical, magnetic, and thermal components. As detailed in Appendix D, the first law of thermodynamics can be written as Kovetz [2000]:

$$\dot{u} = \vec{H} \cdot \dot{\vec{B}} + \sigma : \dot{\varepsilon} - \operatorname{div} \vec{q}, \tag{4.1.1}$$

$\dot{u}$ is the time-derivative of the internal energy density, the dot product $\vec{H} \cdot \dot{\vec{B}}$ represents the magnetic power density, the double-contraction product $\sigma : \dot{\varepsilon}$ represents the mechanical power density, and $\vec{q}$ the heat flux. The second law of thermodynamics can be expressed as Houlsby and Puzrin [2000]:

$$T\dot{s} \geq -\operatorname{div} \vec{q} + \operatorname{grad} T \cdot \left(\frac{\vec{q}}{T} \right), \tag{4.1.2}$$

with s the entropy and T the temperature. Defining the Helmholtz free energy as:

$$f(\varepsilon,\vec{B},T) = u(\varepsilon,\vec{B},s) - Ts, \tag{4.1.3}$$

combining (4.1.1), (4.1.2) and (4.1.3), and neglecting spatial and temporal thermal variations, the Clausius-Duhem inequality (CDI) for the magneto-mechanical case writes:

$$D = \vec{H}\cdot\dot{\vec{B}} + \sigma : \dot{\varepsilon} - \dot{f} \geq 0, \tag{4.1.4}$$

with D the dissipation, which can also be written in terms of the Gibbs free energy g defined by:

$$g(\sigma,\vec{H}) = f(\varepsilon,\vec{B}) - \vec{H}\cdot\vec{B} - \sigma : \varepsilon. \tag{4.1.5}$$

The dissipation is then:

$$D = -\dot{\vec{H}}\cdot\vec{B} - \dot{\sigma} : \varepsilon - \dot{g} \geq 0. \tag{4.1.6}$$

The irreversible behavior is described through the evolution of internal variables. The magnetization $\vec{M}$ is introduced as an internal variable, such that the time-derivative of the Gibbs free energy $\dot{g}$ is given by:

$$\dot{g}(\sigma,\vec{H},\vec{M}) = \frac{\partial g}{\partial \sigma} : \dot{\sigma} + \frac{\partial g}{\partial \vec{H}}\cdot\dot{\vec{H}} + \frac{\partial g}{\partial \vec{M}}\cdot\dot{\vec{M}}. \tag{4.1.7}$$

Replacing (4.1.7) into (4.1.6):

$$D = -\left[\vec{B} + \frac{\partial g}{\partial \vec{H}}\right]\cdot\dot{\vec{H}} - \left[\varepsilon + \frac{\partial g}{\partial \sigma}\right] : \dot{\sigma} - \frac{\partial g}{\partial \vec{M}}\cdot\dot{\vec{M}} \geq 0. \tag{4.1.8}$$

The following relationships are defined and are considered as sufficient conditions to

respect the constraint of the second law of thermodynamics:

$$\vec{B} = -\frac{\partial g}{\partial \vec{H}}, \tag{4.1.9a}$$

$$\varepsilon = -\frac{\partial g}{\partial \sigma}, \tag{4.1.9b}$$

$$D = -\frac{\partial g}{\partial \vec{M}} \cdot \dot{\vec{M}} \geq 0. \tag{4.1.9c}$$

To characterize the irreversible behavior in terms of the internal variables, first, a dissipation function $\phi_d(\dot{\vec{M}})$ is introduced such that $\phi_d : {R_e}^n \to R_e$. The dissipation function can be non-smooth - or non-differentiable at some points - and per definition is characterized by Miehe et al. [2011]:

$$-\frac{\partial g}{\partial \vec{M}} = \frac{\partial \phi_d}{\partial \dot{\vec{M}}}. \tag{4.1.10}$$

From (4.1.9c), the dissipation inequality can be written as:

$$D = \frac{\partial \phi_d}{\partial \dot{\vec{M}}} \cdot \dot{\vec{M}} \geq 0, \tag{4.1.11}$$

and the following constraints in defining ϕ_d are necessary conditions to respect the restrictions of the second-law of thermodynamics:

$$\phi_d(\vec{0}) = 0 \qquad \text{and} \qquad \phi_d(\dot{\vec{M}}) \geq 0. \tag{4.1.12}$$

In the case of rate-independent dissipation functions, which is the interest here, ϕ_d is assumed to be positively homogeneous of degree one and therefore Miehe et al. [2011]:

$$\phi_d(\tau \dot{\vec{M}}) = \tau \phi_d(\dot{\vec{M}}) \qquad \text{with} \qquad \tau \in R_{e+}. \tag{4.1.13}$$

Using the chain rule and the positively homogeneous of degree one property, the following identity is obtained:

$$\frac{\partial \phi_d}{\partial \dot{\vec{M}}} \cdot \dot{\vec{M}} = \phi_d(\dot{\vec{M}}). \tag{4.1.14}$$

Therefore, the dissipation function $\phi_d(\dot{\vec{M}})$ defines the evolution of dissipation D by:

$$D = \phi_d(\dot{\vec{M}}) \geq 0. \tag{4.1.15}$$

From (4.1.10) it can be noted that a minimization procedure can be defined if the energy density g and the dissipation function ϕ_d are identified. Particularly, the definition of $\phi_d(\dot{\vec{M}})$ needs to take into account the constraints of (4.1.12). As discussed in Chapter 2, in this energy-based approach the magnetic hysteresis is modeled by analogy with a mechanical dry-friction system Bergqvist [1997], Henrotte et al. [2006]. The dissipation function ϕ_d is given by:

$$\phi_d(\dot{\vec{M}}) = \mu_0 \kappa \|\dot{\vec{M}}\|, \tag{4.1.16}$$

with κ a pinning parameter, a positive scalar. κ can be defined as a symmetric positive-definite matrix to consider the anisotropy Prigozhin et al. [2016]. As presented in François-Lavet et al. [2013], to formulate a minimization from (4.1.10), first, for small enough time-steps, the dissipation ϕ_d is approximated by:

$$\phi_d(\vec{M}) \approx \mu_0 \kappa \frac{\|\vec{M} - \vec{M}_{(p)}\|}{\Delta t}, \tag{4.1.17}$$

with $\vec{M}_{(p)}$ the magnetization at the previous time-step. Taking into account the approximation for ϕ_d into (4.1.10):

$$\frac{\partial \phi_d}{\partial \dot{\vec{M}}} \approx \frac{\partial \phi_d}{\partial \left(\dfrac{\vec{M} - \vec{M}_{(p)}}{\Delta t} \right)} = \Delta t \, \frac{\partial \phi_d}{\partial \vec{M}}. \tag{4.1.18}$$

The magnetization $\vec{M}$ can be calculated from a minimization given by:

$$\frac{\partial}{\partial \vec{M}} \left[g(\sigma, \vec{H}, \vec{M}) + \Delta t \; \phi_d(\vec{M}) \right] = 0 \quad \rightarrow \quad \vec{M} = \text{argmin} \left[g(\sigma, \vec{H}, \vec{M}) + \mu_0 \kappa \|\vec{M} - \vec{M}_{(p)}\| \right]. \tag{4.1.19}$$

The energy density $g(\sigma, \vec{H}, \vec{M})$ can be chosen as:

$$g(\sigma, \vec{H}, \vec{M}) = \widetilde{f}(\sigma, \vec{M}) - \mu_0 \frac{H^2}{2} - \mu_0 \vec{H} \cdot \vec{M} - \frac{1}{2} \left(\mathscr{C}^{-1} \, \sigma \right) : \sigma, \tag{4.1.20}$$

with $\widetilde{f}(\sigma, \vec{M})$ a free energy density that can be obtained from the partial numerical

inversion of a magnetic anhysteretic model. The time-derivative $\dot{\widetilde{f}}$ is:

$$\dot{\widetilde{f}}(\sigma,\vec{M}) = -\varepsilon^{\mu} : \dot{\sigma} + \mu_0 \vec{H}_{rev} \cdot \dot{\vec{M}} \qquad \text{with} \qquad \frac{\partial \widetilde{f}}{\partial \sigma} = -\varepsilon^{\mu} \qquad \text{and} \qquad \frac{1}{\mu_0}\frac{\partial \widetilde{f}}{\partial \vec{M}} = \vec{H}_{rev}. \tag{4.1.21}$$

and the reversible field $\vec{H}_{rev}$ is introduced. With the choice of $g(\sigma,\vec{H},\vec{M})$, (4.1.9a) and (4.1.9b) are:

$$\begin{aligned} -\frac{\partial g}{\partial \vec{H}} &= \mu_0\left(\vec{H}+\vec{M}\right) = \vec{B} \\ -\frac{\partial g}{\partial \sigma} &= -\frac{\partial \widetilde{f}}{\partial \sigma} + \mathscr{C}^{-1}\sigma = \varepsilon^{\mu} + \varepsilon^{e} = \varepsilon, \end{aligned} \tag{4.1.22}$$

supposing small strains, with $\mathscr{C}$ the stiffness tensor and ε^e the elastic strain. From (4.1.9c):

$$-\frac{\partial g}{\partial \vec{M}} = -\frac{\partial \widetilde{f}}{\partial \vec{M}} + \mu_0 \vec{H} = \mu_0\left(-\vec{H}_{rev}+\vec{H}\right) = \mu_0 \vec{H}_{irr}, \tag{4.1.23}$$

and is introduced the irreversible field $\vec{H}_{irr}$ such that the field decomposition is highlighted $\vec{H} = \vec{H}_{rev} + \vec{H}_{irr}$.

Combining (4.1.19) and (4.1.20), the minimization can be established by:

$$\begin{aligned} \vec{M} = \arg\min \quad & \left[\widetilde{f}(\sigma,\vec{M}) - \mu_0 \vec{H}\cdot\vec{M} + \mu_0 \kappa \|\vec{M} - \vec{M}_{(p)}\|\right] \\ \text{subject to} \quad & \|\vec{M}\| \leq M_s \end{aligned} \tag{4.1.24}$$

by considering that $\mathscr{C}$ does not depends on $\vec{M}$, so the term $\left(\mathscr{C}^{-1}\,\sigma\right) : \sigma$ is constant, and it can be neglected in evaluating $\vec{M}$. The term $\mu_0 \vec{H}\cdot\vec{H}$ also is constant, and can be neglected in the minimization. For the stress-free case, (4.1.24) returns the same formulation as presented in François-Lavet et al. [2013].

A summary of the thermodynamics laws and approximations considered is presented in Table 4.1.1.

4.2 Reversible behavior and simplified multiscale model

The reversible behavior is modeled using a simplified multiscale approach (SMSM) Daniel et al. [2015], a simplified version of the model presented in 2.3.1. The scales considered

Tabela 4.1.1: Summary of the thermodynamic laws for the magneto-elastic case.

1st law	$\dot{u} = \vec{H} \cdot \dot{\vec{B}} + \sigma : \dot{\varepsilon} - \operatorname{div} \vec{q}$
2nd law	$T\dot{s} \geq -\operatorname{div} \vec{q} + \operatorname{grad} T \cdot \left(\frac{\vec{q}}{T}\right)$
CDI	$D = \vec{H} \cdot \dot{\vec{B}} + \sigma : \dot{\varepsilon} - \dot{f} \geq 0$ Considering $\dot{T} = 0$, $\operatorname{grad} T = \vec{0}$

are represented in Figure 4.2.1. In this work, we are interested in modeling the behavior of the RVE. The following assumptions are made: (a) the material behavior is initially isotropic, (b) internal demagnetizing effects are negligible, and (c) both applied magnetic field and mechanical stress are homogeneous at the representative volume element (RVE) scale (denoted by α).

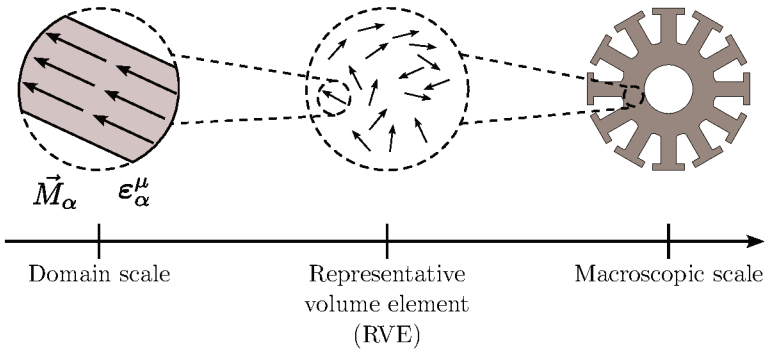

Figura 4.2.1: Scales involved in the reversible modeling.

In a domain family with direction $\vec{\alpha}$, the magnetization $\vec{M}_\alpha$ is:

$$\vec{M}_\alpha = M_s \vec{\alpha} = M_s \left[\alpha_1 \ \alpha_2 \ \alpha_3\right]^t, \tag{4.2.1}$$

with M_s the saturation magnetization. The magnetostriction strain ε^μ_α for isotropic behavior is:

$$\varepsilon^\mu_\alpha = \frac{3}{2}\lambda_s \left(\vec{\alpha} \otimes \vec{\alpha} - \frac{1}{3} I\right), \tag{4.2.2}$$

where λ_s denotes the maximum magnetostriction strain. The energy variation dg_α for

a time step dt at the domain scale is written Hubert [2019]:

$$dg_\alpha = -\mu_0 \vec{M}_\alpha \cdot d\vec{H} - \varepsilon_\alpha : d\sigma, \tag{4.2.3}$$

with ε_α the total strain at the domain scale. The magnetic part of the Gibbs free energy is defined by the integration over the magnetic field path (at constant stress):

$$g_\alpha^{mag} = -\mu_0 \vec{M}_\alpha \cdot \vec{H}. \tag{4.2.4}$$

Considering small perturbations: $\varepsilon_\alpha = \varepsilon_\alpha^e + \varepsilon_\alpha^\mu$, with ε_α^e the elastic strain. Supposing uniform strain in the single-crystal, the magneto-elastic part of the Gibbs free energy is written by integration over the stress path (at constant field):

$$g_\alpha^{me(1)} = -\varepsilon_\alpha^\mu : \sigma. \tag{4.2.5}$$

As shown in Chapter 3, the effect of stress on magnetization is non-monotonic. This simplified approach does not capture such a tendency. This drawback, as discussed in Chapter 2, can be described by adding a second-order term - quadratic in stress - in the magneto-elastic energy definition Hubert [2019]. The magneto-elastic energy is therefore defined as da Silva et al. [2022]:

$$g_\alpha^{me} = g_\alpha^{me(1)} + g_\alpha^{me(2)} = -\sigma : \varepsilon_\alpha^\mu - \frac{3}{2}\lambda_s' \sigma_{eq}^2 \left(\vec{\alpha} \otimes \vec{\alpha} - \frac{1}{3} I \right) : \left(\vec{h} \otimes \vec{h} \right), \tag{4.2.6}$$

with $g_\alpha = g_\alpha^{mag} + g_\alpha^{me}$. In this definition, the second-order magnetostriction constant λ_s' is introduced and the equivalent stress σ_{eq} is chosen as Daniel and Hubert [2009]:

$$\sigma_{eq} = \frac{3}{2} \vec{h}^t \left(\sigma - \frac{1}{3} \mathrm{tr}(\sigma) I \right) \vec{h}. \tag{4.2.7}$$

The magnetostriction strain is composed of the sum of (4.2.2) with a second-order magnetostriction strain $\varepsilon_\alpha^{\mu(2)}$:

$$\varepsilon_\alpha^{\mu(2)} = -\frac{\partial g_\alpha^{me(2)}}{\partial \sigma} = \frac{9}{2} \lambda_s' \sigma_{eq} \left[\left(\vec{\alpha} \otimes \vec{\alpha} - \frac{1}{3} I \right) : \left(\vec{h} \otimes \vec{h} \right) \right] \left(\vec{h} \otimes \vec{h} - \frac{1}{3} I \right), \tag{4.2.8}$$

such that the property $\mathrm{tr}(\varepsilon_{\alpha}^{\mu(2)}) = 0$ is observed.

Considering a particular case with the magnetic field direction $\vec{h} = [1\ 0\ 0]^t$ and $\sigma = \sigma_{11}(\vec{h} \otimes \vec{h})$ yields:

$$\begin{aligned} \varepsilon_{\alpha_{11}}^{\mu(2)} &= 3\lambda_s' \sigma_{11} \left(\alpha_1^2 - \frac{1}{3} \right) \\ \varepsilon_{\alpha_{22}}^{\mu(2)} &= \varepsilon_{\alpha_{33}}^{\mu(2)} = -\frac{3}{2} \lambda_s' \sigma_{11} \left(\alpha_1^2 - \frac{1}{3} \right) \\ \varepsilon_{\alpha_{12}}^{\mu(2)} &= \varepsilon_{\alpha_{13}}^{\mu(2)} = \varepsilon_{\alpha_{23}}^{\mu(2)} = 0. \end{aligned} \tag{4.2.9}$$

Therefore, introducing a second-order term in the magneto-elastic energy results in a magnetostriction strain that is stress-dependent. λ_s' can be defined as (see Appendix B):

$$\lambda_s' = -\frac{\lambda_s}{2\sigma_m}, \tag{4.2.10}$$

where σ_m is the value of applied uniaxial stress corresponding to the maximum magnetic permeability. Combining (4.2.6) and (4.2.10), the magneto-elastic part of the Gibbs free energy is:

$$g_{\alpha}^{me} = -\sigma : \varepsilon_{\alpha}^{\mu} + \frac{\sigma_{eq}^2}{2\sigma_m} \varepsilon_{\alpha}^{\mu} : \left(\vec{h} \otimes \vec{h} \right). \tag{4.2.11}$$

The energy balance at the domain scale in this approach is composed of a magnetic and a magneto-elastic parts. These energy terms are summarized in Table 4.2.1:

Tabela 4.2.1: Summary of the energy description at the domain scale

Energy	Expression
Magnetic	$g_{\alpha}^{mag} = -\mu_0 \vec{M}_{\alpha} \cdot \vec{H}$
Magneto-elastic	$g_{\alpha}^{me} = -\sigma : \varepsilon_{\alpha}^{\mu} + \frac{\sigma_{eq}^2}{2\sigma_m} \varepsilon_{\alpha}^{\mu} : \left(\vec{h} \otimes \vec{h} \right)$
Total	$g_{\alpha} = g_{\alpha}^{mag} + g_{\alpha}^{me}$

The volume fraction p_{α} of a domain family with direction $\vec{\alpha}$ is evaluated using a Boltzmann relation Buiron et al. [1999]:

$$p_{\alpha} = \frac{\exp\left(-A_s\, g_{\alpha}\right)}{\sum_{\alpha} \exp\left(-A_s\, g_{\alpha}\right)}, \tag{4.2.12}$$

where the parameter A_s is proportional to the initial susceptibility χ_0 of the stress-free anhysteretic curve Daniel et al. [2008]:

$$A_s = \frac{3\chi_0}{\mu_0 M_s^2}. \tag{4.2.13}$$

In this simplified approach, the set of possible domain family orientations is defined through the nodes of an icosphere Daniel and Galopin [2008]. Here, an icosphere with 2562 nodes is used to represent the set of possible domain orientations, as illustrated in Fig. 4.2.2.

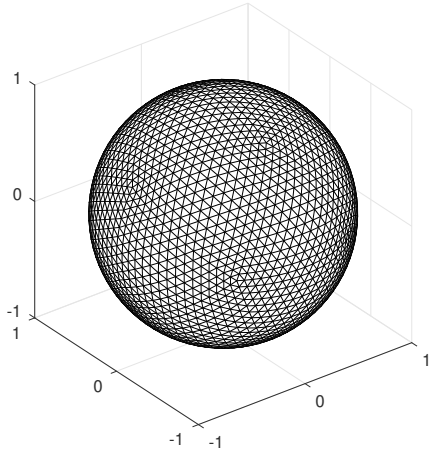

Figura 4.2.2: Icosphere with nodes representing the possible domain orientations.

The macroscopic (see RVE in Fig. 4.2.1) magnetization $\vec{M}$ and magnetostriction strain ε^{μ} are finally defined as:

$$\vec{M} = \sum_{\alpha} p_{\alpha} \vec{M}_{\alpha} \qquad \text{and} \qquad \varepsilon^{\mu} = \sum_{\alpha} p_{\alpha} \varepsilon^{\mu}_{\alpha}. \tag{4.2.14}$$

4.3 Vector-play approximation

The minimization of (4.1.24) can be computationally expensive. An explicit approach presented in Henrotte et al. [2006] is here considered to simplify the implementation. The magnetic field decomposition is here recalled:

$$\vec{H} = \vec{H}_{rev} + \vec{H}_{irr}. \tag{4.3.1}$$

As seen in Chapter 2, because the dissipation $\phi_d(\vec{M})$ in non-differentiable at $\vec{M} = \vec{M}_{(p)}$, the subsequent set defines the derivatives of ϕ_d:

$$\frac{\partial \phi_d(\vec{M})}{\partial \vec{M}} \in \begin{cases} \vec{H}_{irr}, \|\vec{H}_{irr}\| \leq \kappa, & \text{if } \vec{M} = \vec{M}_{(p)} \\ \vec{H}_{irr} = \kappa \dfrac{\vec{M} - \vec{M}_{(p)}}{\|\vec{M} - \vec{M}_{(p)}\|}, & \text{otherwise.} \end{cases} \tag{4.3.2}$$

The following simplification can be made: the direction of $\vec{H}_{irr}$ is written in terms of the reversible field at the previous time step $\vec{H}_{rev(p)}$. This results in a vector-play model Henrotte et al. [2006]. Using this approximation, the explicit update procedure of $\vec{H}_{rev}$ at each cell is:

$$\vec{H}_{rev} = \begin{cases} \vec{H}_{rev(p)} & \text{if} \quad \|\vec{H} - \vec{H}_{rev(p)}\| \leq \kappa \\ \vec{H} - \kappa \dfrac{\vec{H} - \vec{H}_{rev(p)}}{\|\vec{H} - \vec{H}_{rev(p)}\|} & \text{otherwise.} \end{cases} \tag{4.3.3}$$

To model the first magnetization curve, symmetric and asymmetric minor loops, the pinning parameter can be represented by a statistical distribution of pinning fields κ^k with N dry-friction systems (or cells), with normalized weights ω^k that verify François-Lavet et al. [2013]:

$$\sum_{k=1}^{N} \omega^k = 1. \tag{4.3.4}$$

In this case with several cells, the explicit update of the reversible field $\vec{H}^k_{rev}$ at the k cell is given by:

$$\vec{H}^k_{rev} = \begin{cases} \vec{H}^k_{rev(p)}, & \text{if } \|\vec{H} - \vec{H}^k_{rev(p)}\| \leq \kappa^k \\ \vec{H} - \kappa^k \dfrac{\vec{H} - \vec{H}^k_{rev(p)}}{\|\vec{H} - \vec{H}^k_{rev(p)}\|}, & \text{otherwise.} \end{cases} \tag{4.3.5}$$

The weighted sum of all k-cells contributions in magnetization $\vec{M}^k(\sigma, \vec{H}^k_{rev})$ and magnetostriction strain $\varepsilon^{\mu,k}(\sigma, \vec{H}^k_{rev})$ gives the total magnetization $\vec{M}$ and the total magnetostriction strain ε^{μ}:

$$\vec{M} = \sum_{k=1}^{N} \omega^k \vec{M}^k(\sigma, \vec{H}^k_{rev}) \qquad \text{and} \qquad \varepsilon^{\mu} = \sum_{k=1}^{N} \omega^k \varepsilon^{\mu,k}(\sigma, \vec{H}^k_{rev}). \tag{4.3.6}$$

The model can be summarized as follows: the inputs are the magnetic field $\vec{H}_{rev}$ and the mechanical stress σ. The reversible field $\vec{H}^k_{rev}$ is calculated using the analogy with a dry-friction system (4.3.5). $\vec{H}^k_{rev}$ and σ are the inputs of the SMSM. The variables $\vec{M}^k(\sigma, \vec{H}^k_{rev})$ and

$\varepsilon^{\mu,k}(\sigma, \vec{H}^k_{rev})$ are then evaluated. This procedure is repeated for each cell. $\vec{M}$ and ε^{μ} are then defined by (4.3.6). A simplified schematic of the algorithm is presented in Fig. 4.3.1.

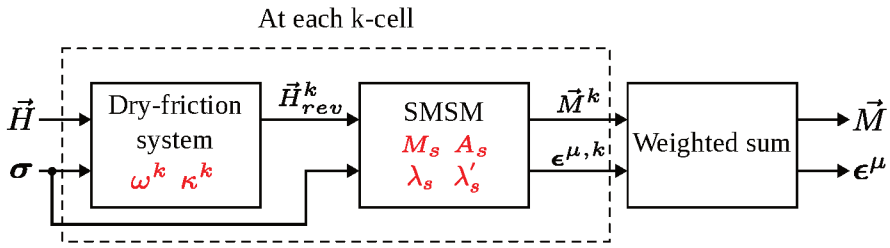

Figura 4.3.1: Principle of the hysteresis model under static stress. The material parameters are indicated in red.

4.4 Application under uniaxial stress and alternating field

The magneto-elastic model is entirely defined by the parameters of the anhysteretic behavior, here based on the SMSM, and the probability distribution of pinning field κ^k and ω^k. The parameters are evaluated from anhysteretic and hysteretic characterizations under uniaxial stress performed on DC04 steel, presented in Chapter 3.

4.4.1 Identification of material parameters

4.4.2 Reversible parameters

The reversible parameters M_s, λ_s, and χ_0 are identified from anhysteretic characterization without applied stress. M_s is the maximum magnetization measured on the stress-free $M(H)$ curve. λ_s is the maximum longitudinal magnetostriction strain obtained on the stress-free magnetostriction curve. χ_0 is the slope, at $H = 0$, of the anhysteretic stress-free $M(H)$ curve. A_s is calculated from χ_0 by using (4.2.13). λ'_s can be identified from (4.2.10) from a set of measured anhysteretic permeability under uniaxial stress, such that the maximum magnetic permeability corresponds to the stress level σ_m.

The identified reversible parameters are given in Table 4.4.1. The modeled anhysteretic behavior is shown in Fig. 4.4.1 (right) and exhibits a good agreement with the measurements in Fig. 4.4.1 (left). Fig. 4.4.2 shows that the SMSM with a second-order term can capture the reversible behavior and the non-monotonic effect. Differences become apparent, especially for tensile stress of 100 MPa, where the model underestimates the relative permeability at low field. Such a tendency is inevitable with the proposed description (second-order elastic energy

term), which imposes the permeability curve to be symmetric with respect to σ_m, as shown in Appendix B, and results in a bell shaped curve. A possibility to improve this drawback would be using a stress-dependent demagnetizing term in the free energy, as proposed in Daniel et al. [2014], instead of or as a complement to the second-order approach. Another option would be introducing higher order terms in the elastic energy, to the price of additional material parameters.

Tabela 4.4.1: Parameters of the SMSM.

M_s (A/m)	λ_s (ppm)	λ_s' (ppm/MPa)	A_s (m^3/J)
$1.39\,10^6$	5.5	$-6.9\,10^{-2}$	$1.4\,10^{-2}$

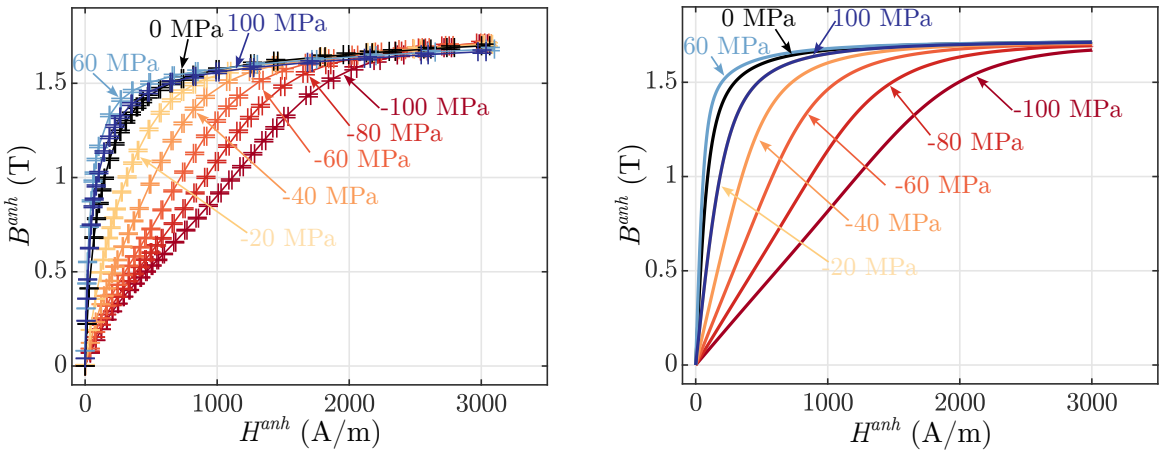

Figura 4.4.1: Effect of uniaxial stress on the anhysteretic behavior: Measurements (left) and model (right).

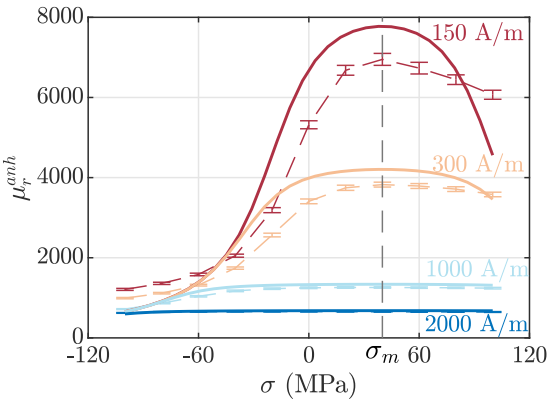

Figura 4.4.2: Comparison of measured (error bars) and modeled (solid lines) anhysteretic relative magnetic permeability for different values of applied magnetic field. The maximum anhysteretic permeability is observed at $\sigma_m = 40$ MPa.

4.4.3 Dissipative parameters

The identification of the distribution $\omega(\kappa)$ usually requires the measured stress-free coercive field under several peak magnetic fields Henrotte et al. [2006], Scorretti and Sixdenier [2022]. Considering a magnetic case with applied field along $\vec{h} = [1\ 0\ 0]^t$, an identification method of ω^k and κ^k is presented in Henrotte et al. [2014], Jacques et al. [2018]. This procedure is based on the homogenization of reversible field, where an auxiliary function $F(H)$ is defined (see Appendix E). The second derivative of $F(H)$ is the probability distribution $\omega(\kappa)$. The identification of $F(H)$ (as explained in Appendix E) can be performed from a set of measured H_c under increasing peak magnetic fields H_{peak}. These experimental measurements are presented in Figs. 4.4.3a and 4.4.3b for the stress-free case. This curve is extrapolated outside the measured range using (4.4.1) Jacques et al. [2018]:

$$H_c(H) = {H_c}^{min}\left(\frac{H}{H^{min}}\right)^2 \quad \text{if} \quad H < H^{min}, \tag{4.4.1}$$

where ${H_c}^{min}$ is the lower measured coercive field on the corresponding peak magnetic field H^{min}. The identified $F(H)$ and its derivatives $\partial_H F(H)$ and $\partial_H^2 F(H)$, are presented in Fig. 4.4.4. The derivatives are evaluated with a finite difference method. The non-zero component for $\kappa(0)$ represents the reversible bending of Bloch walls Henrotte et al. [2006]. The continuous probability distribution is then discretized into 25 cells (see (E.0.10) in Appendix E).

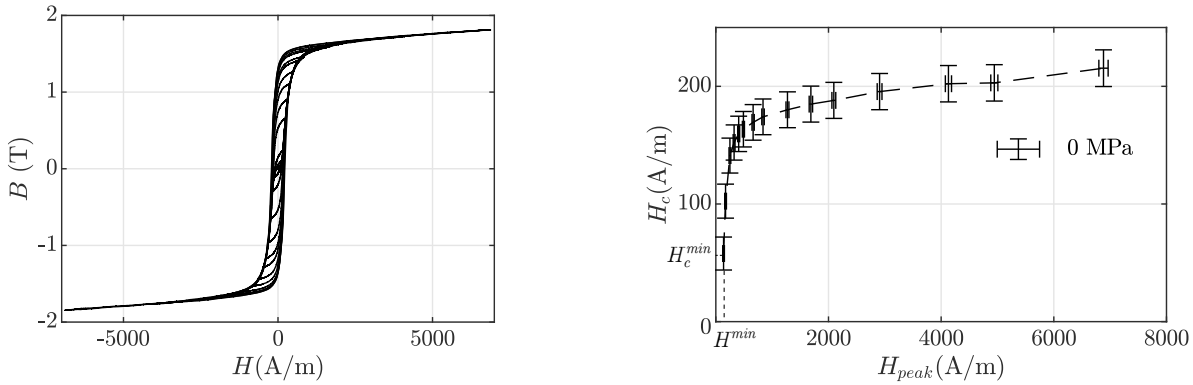

(a) Hysteresis loops.

(b) Coercive field.

Figura 4.4.3: Stress-free measurements under increasing magnetic field.

An applied compression increases the coercive field, as observed in the measured hysteresis curves of Fig. 3.7.1. The pinning parameter κ is directly related to the coercive field. We propose to model the stress dependence of dissipation parameters as follows: starting from the identified discrete pinning field distribution for 0 MPa, the weight ω is kept constant under

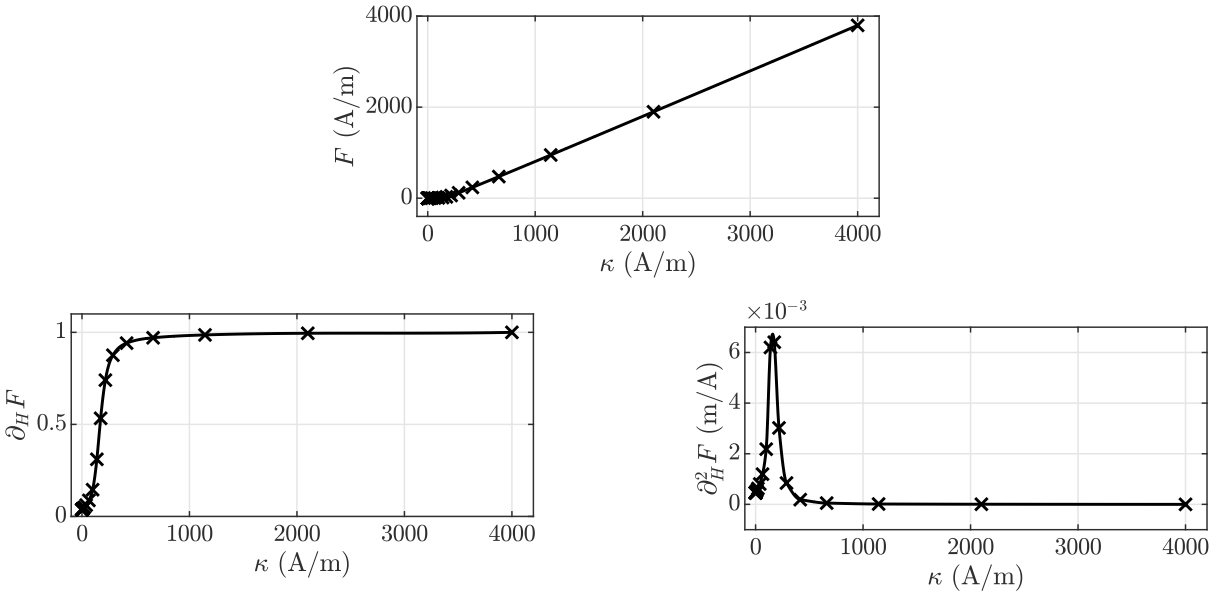

Figura 4.4.4: Identified auxiliary function for the stress-free case, first and second derivatives that represent the pinning field cumulative distribution and probability distribution, respectively.

stress. The pinning field $\kappa(\sigma)$ evolves as:

$$\kappa(\sigma) = a(\sigma_{eq})\kappa(0) \qquad \text{with} \qquad a(\sigma_{eq}) = \frac{H_c(\sigma)}{H_c(0)}, \tag{4.4.2}$$

with $\kappa(0)$ the identified pinning field for 0 MPa, and $a(\sigma_{eq})$ a function that is fitted in order to match with the measured $H_c(\sigma)/H_c(0)$. This coercive field characteristic under stress is presented in Figure 4.4.5 in the case of a uniaxial stress applied parallel to the magnetic field direction. It can be noted an exponential behavior of H_c under compression and a close to constant behavior under tension. For other materials, such as Fe-Si Singh et al. [2016], the exponential tendency of the coercive field under compression is also observed.

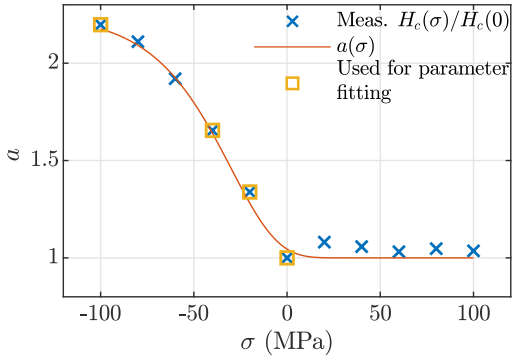

Figura 4.4.5: Function $a(\sigma_{eq})$ at several stress levels.

A phenomenological description of $a(\sigma_{eq})$ is then adopted:

$$a(\sigma_{eq}) = a_1 \exp\left(-\exp(a_2 + a_3\sigma_{eq})\right) + 1, \tag{4.4.3}$$

with σ_{eq} the equivalent stress (4.2.7). The parameters a_1, a_2 and a_3 are fitted (using the Curve Fitting Toolbox of Matlab) from four measured coercive fields under 0 MPa, -20 MPa, -40 MPa and -100 MPa, respectively, for the same peak magnetic field. The identified parameters are presented in Table 4.4.2. Fig. 4.4.5 shows that (4.4.3) is appropriate to represent the measured coercive field characteristic under uniaxial mechanical loading.

Tabela 4.4.2: Fitted parameters for $a(\sigma)$.

a_1	a_2	a_3 (MPa^{-1})
1.25	1.2	0.04

The identification procedure of the dissipation parameters can be summarized as follows: from the stress-free curve of coercive field with increasing magnetic field, the method presented in Henrotte et al. [2014], Jacques et al. [2018] allows identifying $\omega(\kappa(0))$. By using standard measurements of coercive field under stress, the function $a(\sigma_{eq})$ is fitted, and the dependence $\kappa(\sigma)$ is defined based on (4.4.2).

4.4.4 Validation

The proposed magneto-elastic model results in the hysteresis curves presented in Fig. 4.4.6 (right). The tendency of slant under compression - as observed in measurements of Fig. 4.4.6 (left) - is captured by the simulation. However, the model does not reproduce the inflections in the hysteresis curve - more evident under -100 MPa. This measured behavior is attributed to the crystallographic texture, whereas in the proposed model, only an equivalent single crystal representing the macroscopic behavior is considered. A simplified texture multiscale model (STMSM) Bernard et al. [2019] may overcome this limitation, but it is not treated in the validation results presented below.

Fig. 4.4.7 presents a comparison of the modeled coercive field with the measured symmetric minor loops under uniaxial stress. It must be noted that the validation is performed by comparison to experiments that have not been used for identification purposes. For the sake of clarity, the measured values used for identification are explicitly labeled in Fig. 4.4.7. Differences are observed in the major loop under tensile stress (25% for 20 MPa and 5050 A/m)

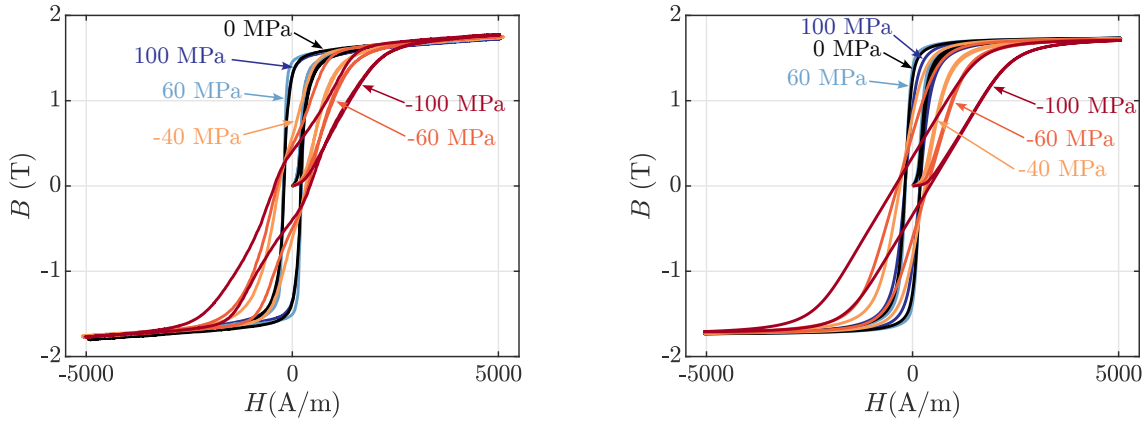

Figura 4.4.6: Hysteresis curves under uniaxial stress: Measurements (left) and model (right).

but the general behavior under stress is captured by the simulation. The second-order term in the magneto-elastic energy definition allows the representation of the non-monotonic effect of tensile stress on the remanent induction B_r as seen in Fig. 4.4.8.

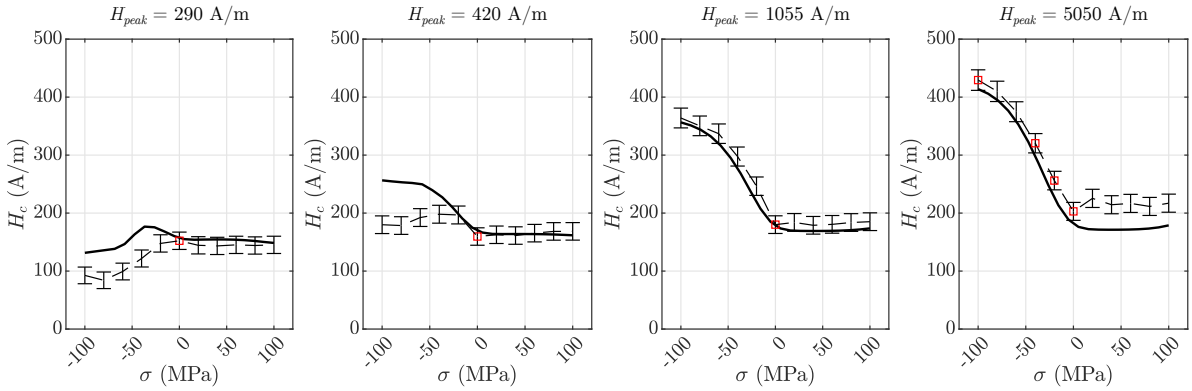

Figura 4.4.7: Comparison of measured (error bars) and modeled results (solid lines) of coercive field as a function of uniaxial stress and under various peak magnetic fields. The red boxes indicate the measurements used in the identification of the parameters of the model.

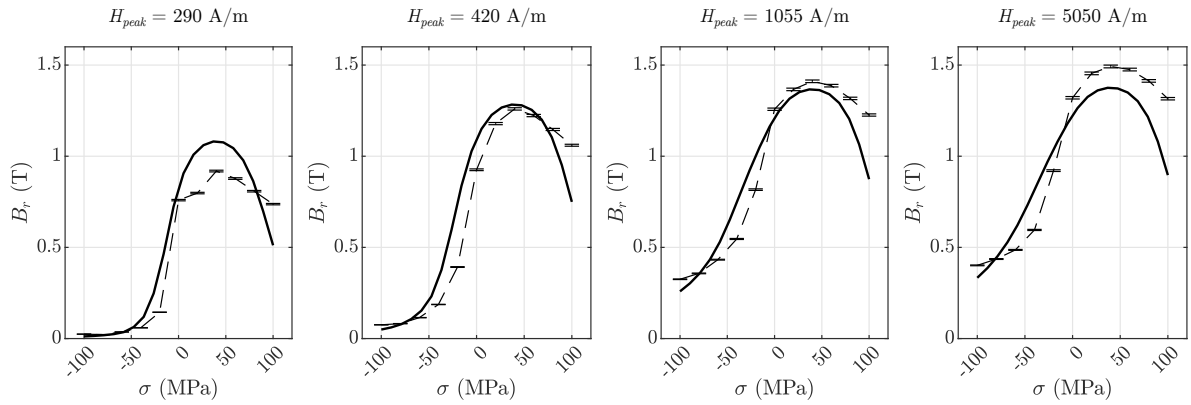

Figura 4.4.8: Comparison of measured (error bars) and modeled results (solid lines) remanent induction as a function of uniaxial stress and under various peak magnetic fields.

The prediction of hysteresis losses under stress is plotted in Fig. 4.4.9 by numerical integration of the surface of each hysteresis loop and is presented as a function of the maximum induction level. This calculation is a blind validation of the modeling approach since no loss measurement was used for material parameter identification. The modeling results show that the tendency to increase losses under compression is reproduced. Significant differences are seen mainly in the major loop under high compression. As already discussed, the SMSM does not consider the inflections in hysteresis curves under compression, which explains the difference of about 30% for the worst case (-100 MPa and 1.7 T).

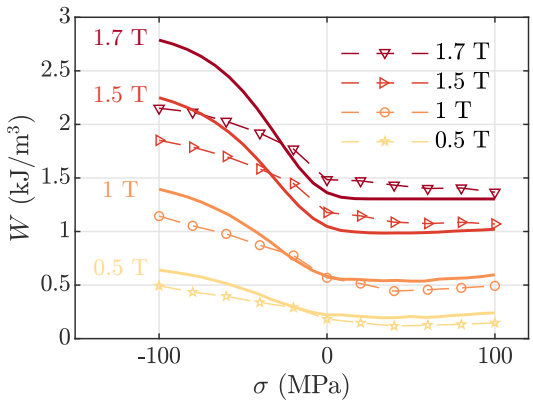

Figura 4.4.9: Prediction of hysteresis losses as a function of uniaxial stress (solid lines). The experimental results (markers) are evaluated using measured data from Fig. 3.7.2 and polynomial interpolation.

The modeled longitudinal and transverse magnetostriction strain components are presented in Figs. 4.4.10 and 4.4.11. The trend under uniaxial stress is captured in modeling. However, as discussed in Hubert [2019], the inclusion of a second-order term in the magnetoelastic energy results in an overestimation of the magnetostriction strain under high stress (see the case of -100 MPa in Figs. 4.4.10 and 4.4.11). Additional considerations on the magnetoelastic energy to correct this drawback - including a vanishing second-order term - are addressed in Taurines et al. [2023].

Considering the magnetic field waveform of Fig. 3.7.10, the comparison of measurements and model is presented in Fig. 4.4.12 for two levels of uniaxial stress. Under a tensile stress of 80 MPa, because the hysteresis curve is less slanted, only one asymmetric minor loop is clearly visible, with the others remaining in a region above 1000 A/m. Again, this comparison is independent of the identification process, so it can serve as a validation for the model. A good agreement between the model and experiment is observed, despite the harmonic content of the H waveform.

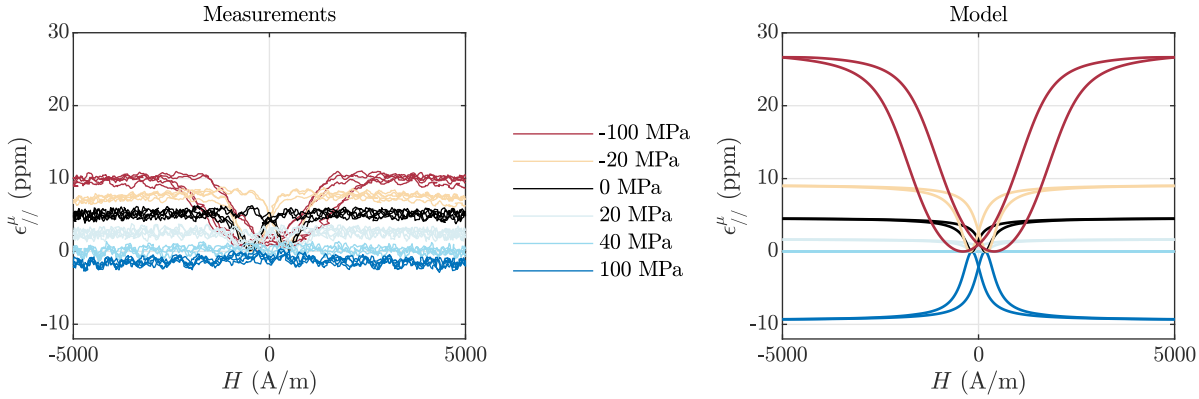

Figura 4.4.10: Longitudinal magnetostriction under uniaxial stress: Measurements (left) and model (right).

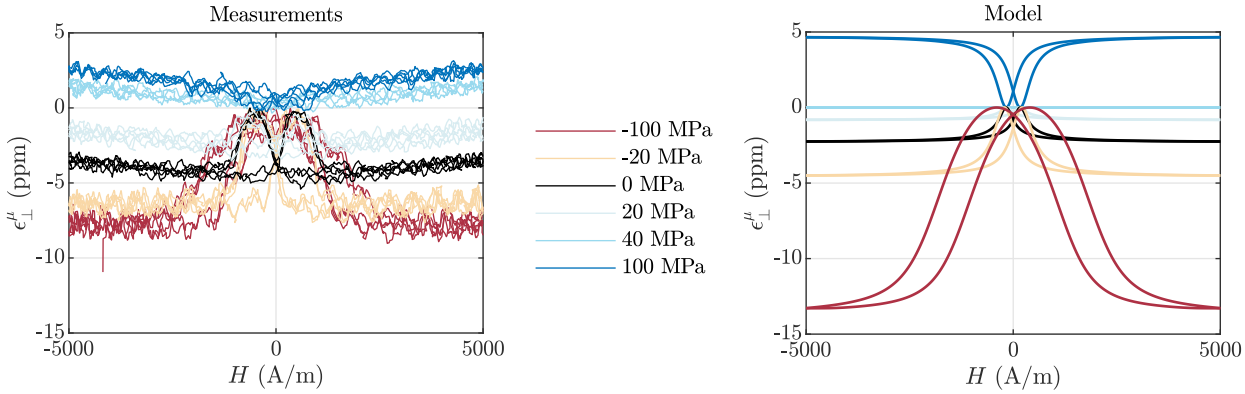

Figura 4.4.11: Transverse magnetostriction under uniaxial stress: Measurements (left) and model (right).

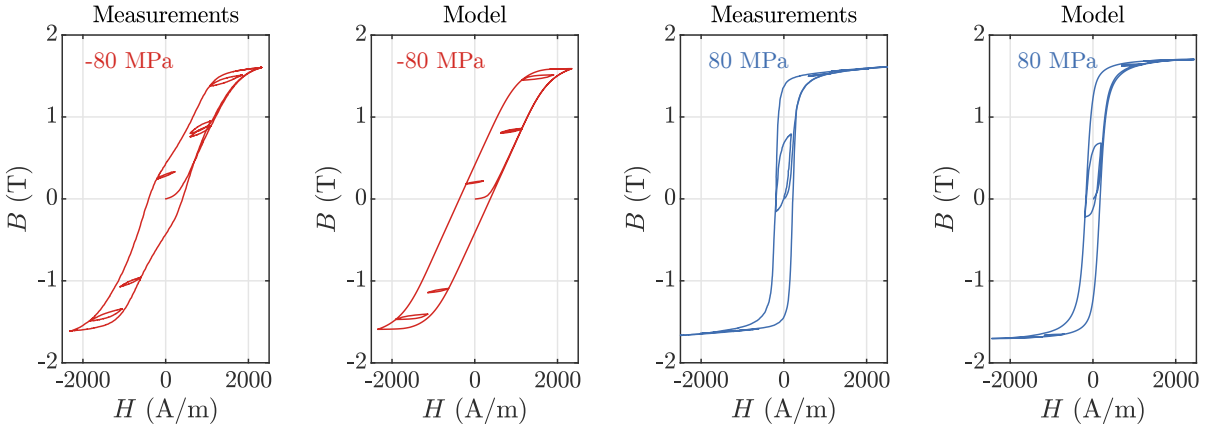

Figura 4.4.12: Hysteresis curves under uniaxial stress and considering the magnetic field waveform of Fig. 3.7.10.

An extension of the energy-based vector-play magnetic hysteresis model has been proposed in order to incorporate the effect of stress on magnetization. This extension essentially consists of the association of the vector-play model with an anhysteretic simplified multiscale approach. This combination results in a magneto-elastic vector model applicable to multi-axial stress configurations. Stress-dependent dissipation parameters can be identified from a few measurements, mostly under compression.

An accurate prediction of coercive field and remanent induction under stress was observed compared to experimental measurements performed on low-carbon steel. Including a second-order development in the magneto-elastic energy enables the description of the non-monotonic evolution of the magnetic permeability under stress, but limitations, especially under high stress, are also observed. The magneto-elastic model can predict the general behavior of hysteresis losses under mechanical loadings from a small set of parameters and reasonably reproduce asymmetric minor loops.

4.5 Application under multiaxial stress and alternating field

In this section, the magnetic response of a non-oriented (NO) Fe-Si steel under a multiaxial mechanical state is simulated using the vector-play model previously presented. In contrast with Section 4.4, where a simplified multiscale model was shown to appropriately represent the reversible behavior of a DC04 steel, the crystallographic texture has a more significant role when analyzing the magnetic response of Fe-Si. Therefore, in what follows, the anhysteretic behavior is modeled from a multiscale approach where the crystallographic texture is considered, as already presented in Section 2.3.1. The model summary is presented in Fig. 4.5.1. Moreover, only the first-order development of the magneto-elastic energy is considered due to the drawbacks of the second-order approach, as previously discussed.

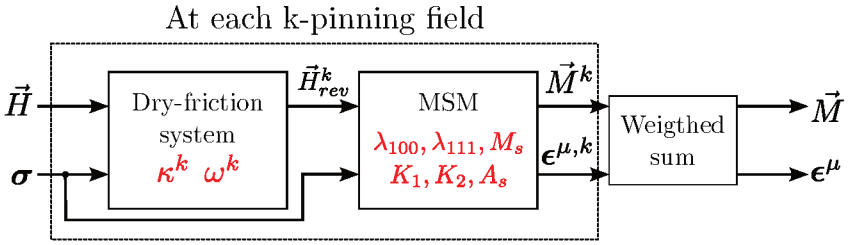

Figura 4.5.1: Principle of the stress-dependent hysteresis model. The material parameters are indicated in red.

The material parameters are identified from the uniaxial measurements presented in Aydin et al. [2019b], Singh et al. [2016], and the losses prediction under biaxial stress is compared with the measurements of Aydin et al. [2019b]. In this multiaxial case, an orthonormal vector basis $(\vec{e}_1, \vec{e}_2, \vec{e}_3)$ is defined, in which $\vec{e}_1$ is the rolling direction (RD), $\vec{e}_2$ the transverse direction (TD), and $\vec{e}_3$ the normal direction.

4.5.1 Identification of material parameters

The measurements performed on a non-oriented (NO) Fe-Si electrical steel Aydin et al. [2019b], Singh et al. [2016] are used for the parameters identification. The discrete pole figures for the NO Fe-Si material are shown in Fig. 4.5.2. This set corresponds to 24 distinct crystallographic orientations with their corresponding volume fraction. The pole figures were obtained using the MTEX toolbox Bachmann et al. [2010] from X-ray measurements reported in Martin et al. [2020].

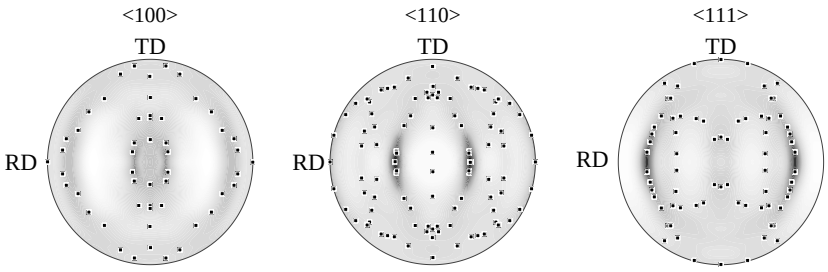

Figura 4.5.2: Pole figures (24 orientations) for a NO Fe-Si alloy.

Due to the flat geometry of the tested electrical steel sheets, the measurements Aydin et al. [2019b], Singh et al. [2016] were performed considering in-plane stress assumption. Therefore, the stress tensor can be written in Voigt notation as:

$$\sigma = [\sigma_{11}\ \sigma_{22}\ \sigma_{12}] \tag{4.5.1}$$

4.5.2 Reversible parameters

The parameters λ_{111}, K_1, and K_2 can be found in Jiles [1991] for a Fe-Si material. Due to the simplifying assumptions to model the reversible behavior, the parameters M_s and λ_{100} are adapted for the modeling results to match with measurements of anhysteretic magnetization and magnetostriction strain for the stress-free case. The parameter A_s is identified from a stress-free anhysteretic curve using (4.2.13). The identified material parameters are listed in Table 4.5.1.

Tabela 4.5.1: Parameters of the reversible modeling.

M_s (A/m)	λ_{100} (ppm)	λ_{111} (ppm)	K_1 (kJ/m^3)	K_2 (kJ/m^3)	A_s (m^3/J)
$1.4\,10^6$	11.5	-4.5	38	0	$1.1\,10^{-2}$

The anhysteretic behavior for the stress-free case is presented in Fig. 4.5.3. The

magnetization is oriented along RD and TD. The model satisfactorily reproduces the measured reversible behavior for the stress-free case with magnetization along RD. The modeling prediction of the anhysteretic behavior along TD highlights the anisotropy of the material due to the crystallographic texture.

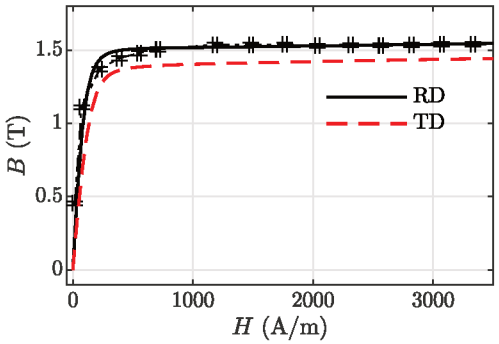

Figura 4.5.3: Comparison between measured (error bars) and modeled (solid line) stress-free anhysteretic behavior along RD. The dashed line represents the prediction of the stress-free anhysteretic behavior along TD.

Fig. 4.5.4 (left) presents the measured longitudinal (along RD) component of the magnetostriction strain with magnetic field and uniaxial stress applied in this same direction Singh et al. [2016]. The model (Fig. 4.5.4 (right)) captures both the trend under uniaxial stress and the rotation mechanism under high field.

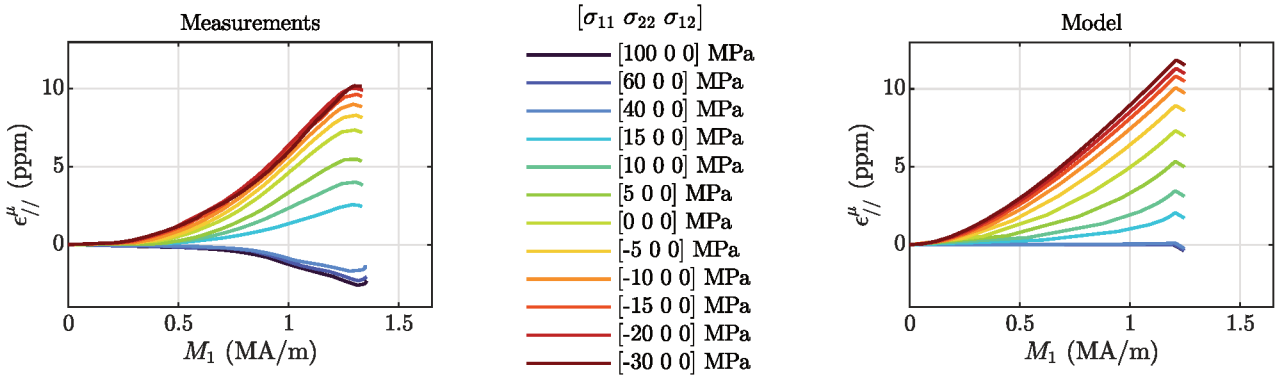

Figura 4.5.4: Comparison between measured (left) Singh et al. [2016] and modeled (right) magnetostriction strain along RD under uniaxial stress. Both magnetic field and stress are applied along RD. In-plane stress tensor in Voigt notation.

4.5.3 Irreversible parameters

The distribution $\omega(\kappa)$ is identified based on the protocol presented in Henrotte et al. [2014], Jacques et al. [2018] for the stress-free case, using a set of measured coercive fields

under several amplitudes of alternating magnetic field. The pinning field κ can be described by a symmetric positive-definite matrix to consider the anisotropy Prigozhin et al. [2016]. However, such an approach would require measurements along RD and TD to characterize the anisotropy and identify the dissipation parameters. Here, the anisotropic effects are considered only from the anhysteretic behavior. The hysteresis loops used for the identification of $\omega(\kappa)$ are shown in Fig. 4.5.5 for applied field and measurements along RD. The identified pinning field distribution is presented in Fig. 4.5.6. For numerical purposes, the continuous distribution presented in Fig. 4.5.6 is discretized into 25 cells.

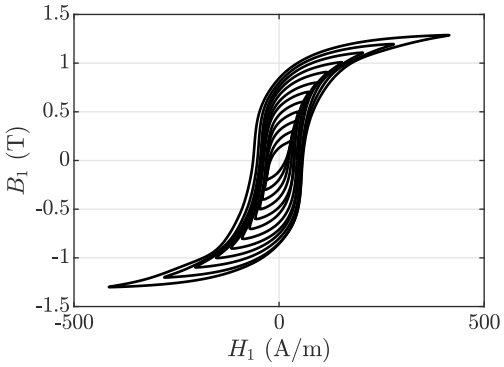

Figura 4.5.5: Measured stress-free hysteresis loops under increasing magnetic field applied along RD.

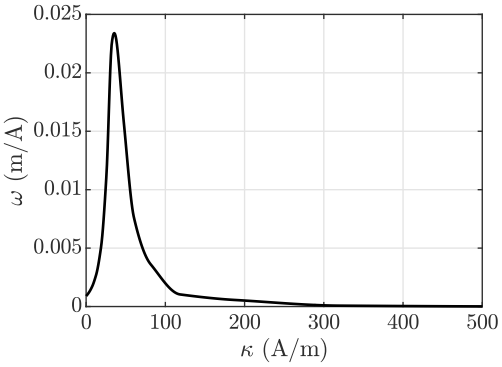

Figura 4.5.6: Identified probability distribution for the stress-free case.

The evolution of the pinning parameter under stress can be defined as:

$$\kappa(\sigma) = a(\sigma_{eq})\kappa(0) \qquad \text{with} \qquad a(\sigma_{eq}) = \frac{H_c(\sigma)}{H_c(0)} \tag{4.5.2}$$

with $a(\sigma_{eq})$ identified from uniaxial stress measurements of the coercive field H_c, and σ_{eq} is an equivalent stress. The effects of shear with respect to the magnetic field are neglected in the equivalent stress of Daniel and Hubert [2009], previously considered in Section 4.4 to evaluate the coercive field evolution under uniaxial stress. In the present section, the equivalent stress proposed in Rasilo et al. [2019a] is used, which allows modeling the influence of different shear loadings on the coercive field. It is defined as:

$$\sigma_{eq} = \begin{cases} \sigma_m - \sqrt{\vec{e}^{\,t}\left(\sigma_m I - \frac{3}{2}d\right)^2 \vec{e}}, & \text{if} \quad \vec{e}^{\,t} d\, \vec{e} \leq \frac{2r}{3} \\ \sigma_m + \sqrt{\vec{e}^{\,t}\left(\sigma_m I - \frac{3}{2}d\right)^2 \vec{e}}, & \text{otherwise} \end{cases} \tag{4.5.3}$$

with $\vec{e}$ the unit vector that defines the direction of $\vec{H}$, $\vec{e}^{\,t}$ the transposed vector, and I the second-order identity tensor. Another material parameter to identify, σ_m is the value of stress corresponding to the maximum permeability in a uniaxial configuration. d is the deviatoric part of the stress tensor defined as:

$$d = \sigma - \frac{1}{3}\mathrm{tr}(\sigma)I \tag{4.5.4}$$

with $\mathrm{tr}(\sigma)$ the trace operator of the stress tensor. The material parameter σ_m can be estimated from the permeability in the region around the coercive field. From the measurements of Singh et al. [2016], σ_m is identified as 10 MPa.

The measured coercive field evolution under uniaxial stress for both experimental setups Aydin et al. [2019b], Singh et al. [2016] is presented in Fig. 4.5.7. It can be noted that despite the common trend under stress, the results differ on the level of the coercive field. This can be attributed to differences in the preparation of samples for uniaxial and multiaxial tests. For example, in the multiaxial setup, the placement of the B-coil involves drilling holes in the sample. In this work, the measurements of the coercive field presented in Singh et al. [2016] will be used for the identification of $a(\sigma_{eq})$ but shifted by ΔH_c - the coercive field difference for the stress-free case, to match with the experimental conditions of Aydin et al. [2019b]. This choice is made because the measurements of Singh et al. [2016] cover a wider range of stress levels.

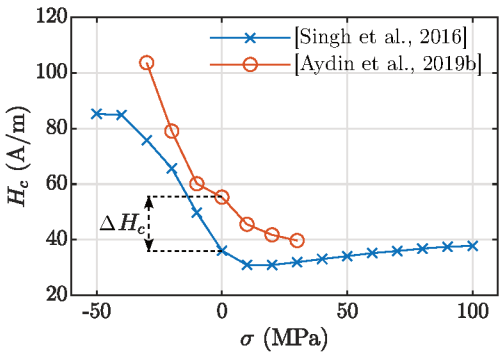

Figura 4.5.7: Measured coercive field characteristic under uniaxial stress applied along RD for the setups presented in Aydin et al. [2019b] and Singh et al. [2016].

The identification of $a(\sigma_{eq})$ is made by using the measurements along RD presented in Singh et al. [2016] but shifted by ΔH_c. In the interpolation interval ($[-40,\ 100]$ MPa), $a(\sigma_{eq})$ is assumed as a piecewise linear function whose shape is presented in Fig. 4.5.8. Beyond the measurement range, we consider this function as a constant with coercive field value defined by

the maximum compression and the maximum tension cases.

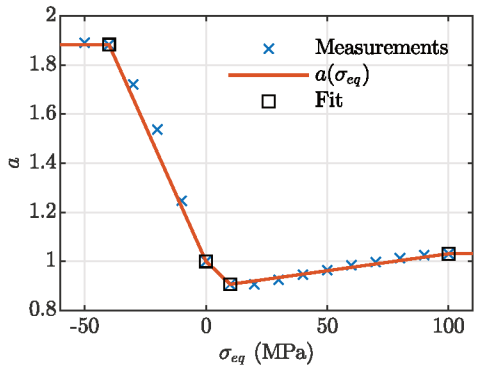

Figura 4.5.8: Identified $a(\sigma_{eq})$ function from measurements along RD presented in Singh et al. [2016] shifted according to Aydin et al. [2019b]. The boxes indicate the experimental data used for the interpolation of $a(\sigma_{eq})$.

4.5.4 Validation

4.5.5 Uniaxial mechanical stress

Considering the magnetic field and uniaxial stress applied along RD, in Fig. 4.5.9, the measurements presented in Aydin et al. [2019b] are compared with the modeling results. The model captures the general trend under uniaxial stress. Differences are more evident when looking at the shape of the hysteresis loops, where it is noted that immediately after field reversals the modeled induction remains constant contrarily to the measured loops.

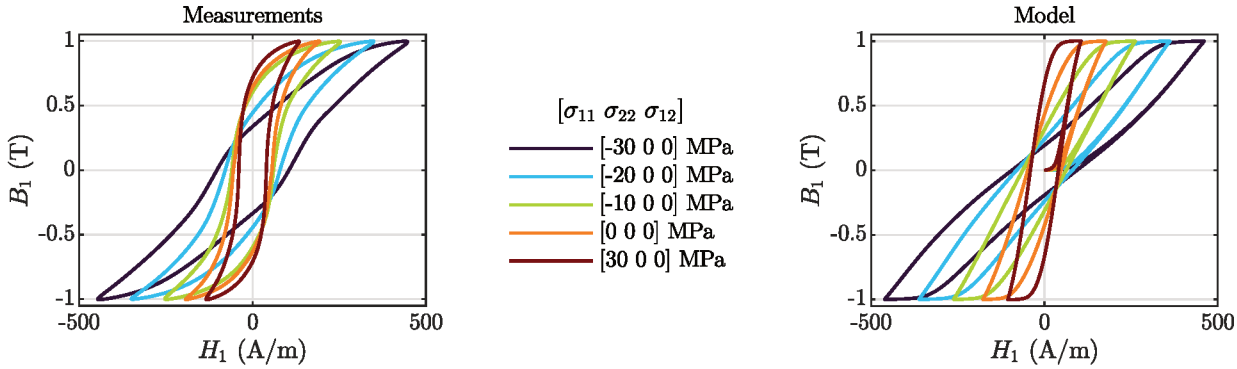

Figura 4.5.9: Comparison between measured Aydin et al. [2019b] (left) and modeled (right) hysteresis curves (at 1T) under uniaxial stress and field applied along RD. In-plane stress tensor in Voigt notation.

The model adequately reproduces the hysteresis losses when the uniaxial stress is applied either along RD or TD, as shown in Fig. 4.5.10.

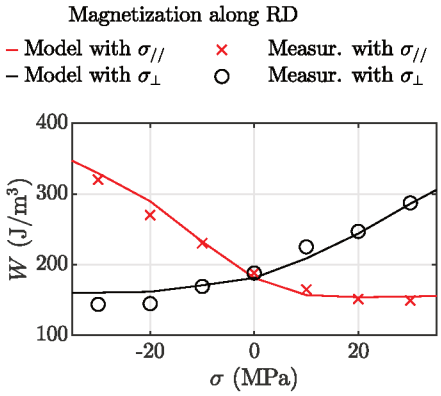

Figura 4.5.10: Hysteresis losses (at 1T) with field applied along RD and under uniaxial stress. Measurements (markers) with stress along RD (denoted by the symbol $\sigma_{//}$) and TD (denoted by the symbol $\sigma_{\perp}$) Aydin et al. [2019b] and modeling results (solid lines).

When the field and uniaxial stress are applied along TD, Fig. 4.5.11 shows the comparison between measurements Aydin et al. [2019b] (left) and model (right). The definition of the pinning field as a function of an equivalent stress allows capturing the evolution of the coercive field for this situation with field and stress applied along TD.

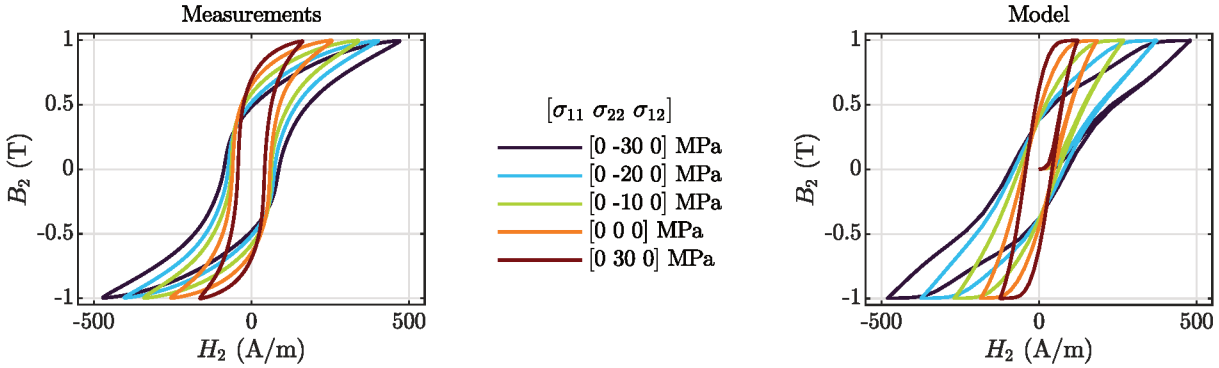

Figura 4.5.11: Comparison between measured Aydin et al. [2019b] (left) and modeled (right) hysteresis curves (at 1T) under uniaxial stress and field applied along TD. In-plane stress tensor in Voigt notation.

The hysteresis losses for the magnetic field applied along TD are presented in Fig. 4.5.12. Despite some differences (about 17% for 0 MPa), the model reasonably predicts the loss evolution when the uniaxial stress is applied either along RD or TD. It is important to note that the hysteresis parameters were identified by using measurements along RD. Therefore, this is a blind prediction test for which the model shows its capability to capture the tendency of losses under uniaxial loading.

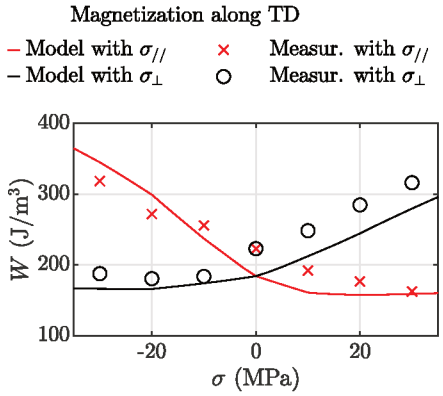

Figura 4.5.12: Hysteresis losses (at 1T) with field applied along TD and under uniaxial stress. Measurements (markers) with stress along TD (denoted by the symbol $\sigma_{//}$) and RD (denoted by the symbol $\sigma_{\perp}$) Aydin et al. [2019b] and modeling results (solid lines).

4.5.6 Multiaxial mechanical stress

Considering a biaxial stress loading and the magnetic field applied along RD, the measured Aydin et al. [2019b] hysteresis loops are presented in Fig. 4.5.13 (left). The modeling results in Fig. 4.5.13 (right) show that the model captures the degradation under shear. However, the modeled hysteresis loop under bi-compression presents curvatures that are not observed in the measurements. One possible reason for this difference is that in the simplified approach presented here, the mechanical stress is taken as homogeneous in the polycrystal, which is not the case in a real material.

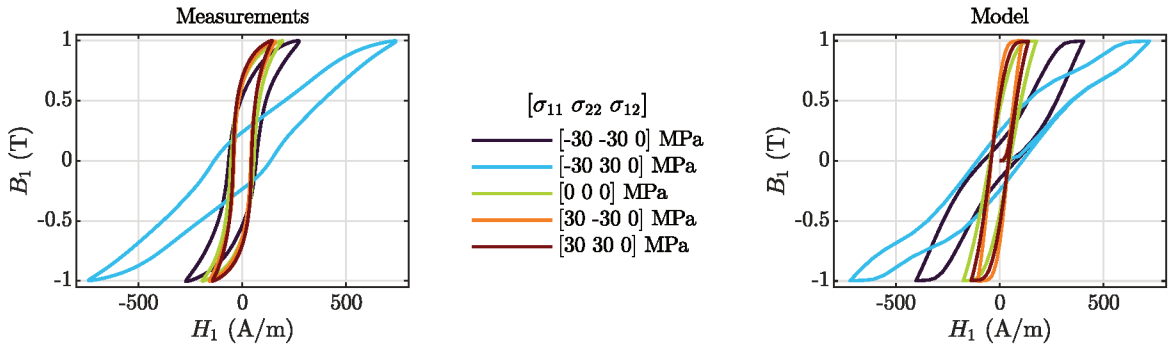

Figura 4.5.13: Comparison between measured Aydin et al. [2019b] (left) and modeled (right) hysteresis loops (at 1T) under biaxial stress with field applied along RD. In-plane stress tensor in Voigt notation.

The variation of the hysteresis losses $\Delta w\ (\%)$ due to the application of stress is evaluated by:

$$\Delta w\left([\sigma_{11}\ \sigma_{22}\ \sigma_{12}]\right) = \left[\frac{w\left([\sigma_{11}\ \sigma_{22}\ \sigma_{12}]\right) - w\left([0\,0\,0]\right)}{w\left([0\,0\,0]\right)}\right] 100 \tag{4.5.5}$$

where $w\left([0\,0\,0]\right)$ and $w\left([\sigma_{11}\ \sigma_{22}\ \sigma_{12}]\right)$ are the hysteresis losses for the stress-free case and under biaxial stress, respectively, in Voigt notation. Fig. 4.5.14 shows this percentage variation for both measurements Aydin et al. [2019b] and model. Notably, the model captures the strong increase in hysteresis losses under shear when compression is applied along RD. Also, the model shows the tendency of a decrease in hysteresis losses under shear when traction is applied along RD.

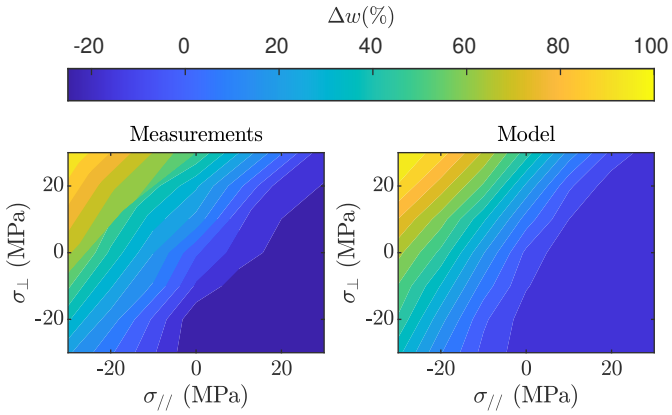

Figura 4.5.14: Percentage variation of the hysteresis losses compared to the stress-free case at 1T. Magnetization along RD, and under biaxial stress. Measurements Aydin et al. [2019b] (left) and model (right).

The error e_{hyst} between measured w_{mes} and modeled w_{mod} hysteresis losses is evaluated as:

$$e_{hyst} = \frac{w_{mod} - w_{mes}}{w_{mes}} \tag{4.5.6}$$

This comparison indicator is presented in Fig. 4.5.15. Overall, the model is capable of modeling the hysteresis losses under biaxial stress, with main differences (around 15%) in the case of bi-compression. The difference in this biaxial configuration is explained because the model overestimates the degradation in the magnetization, as observed in Fig. 4.5.13 (bottom).

For a magnetic field applied along TD, the predicted hysteresis loops are presented in Fig. 4.5.16. Although the tendency of degradation under biaxial stress is captured, some differences are observed in the shape of the hysteresis loops. This is particularly problematic in the case of bi-tension.

Fig. 4.5.17 shows that the trend of hysteresis losses, compared to the stress-free case, is reasonably modeled. It is observed that shear (with compression applied along TD) increases the hysteresis losses of the material.

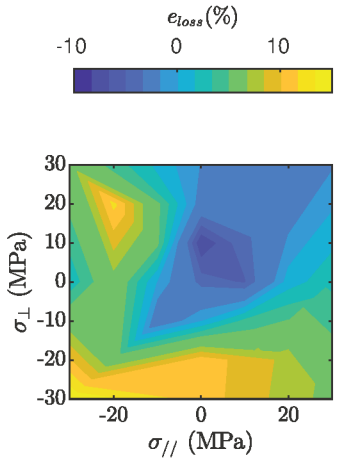

Figura 4.5.15: Percentage error between measured and modeled hysteresis losses (at 1T) under magnetization along RD and biaxial stress.

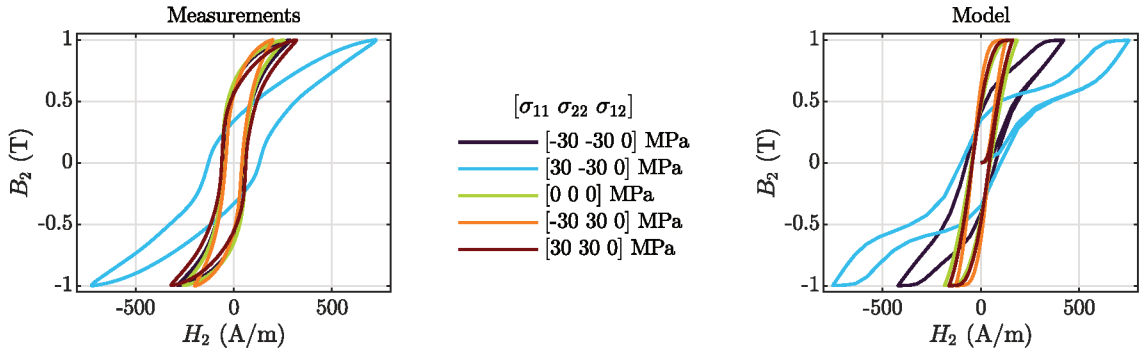

Figura 4.5.16: Comparison between measured Aydin et al. [2019b] (left) and modeled (right) hysteresis loops (at 1T) under biaxial stress with field applied along TD. In-plane stress tensor in Voigt notation.

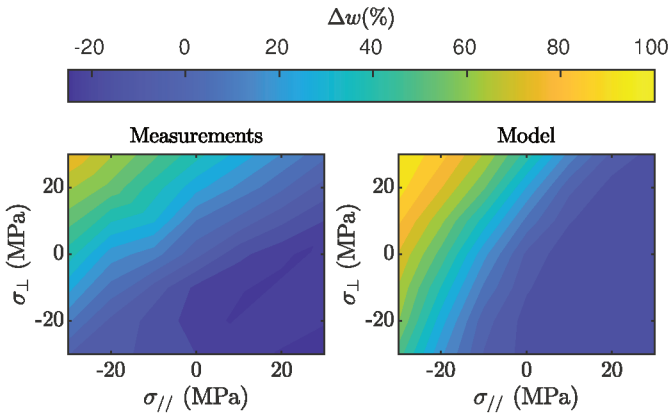

Figura 4.5.17: Percentage variation of the hysteresis losses compared to the stress-free case at 1T. Magnetization along TD and under biaxial stress. Measurements Aydin et al. [2019b] (left) and model (right).

The error in the hysteresis losses between measurements and model is presented in Fig. 4.5.18. Important differences are seen, especially under bi-tension. For this loading, a

significant difference in the modeled coercive field (about 25%) causes a large error in the simulated hysteresis losses.

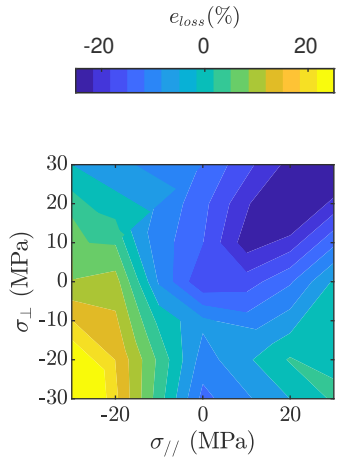

Figura 4.5.18: Percentage error between measured and modeled hysteresis losses (at 1T) under magnetization along TD and biaxial stress.

The percentage variation of hysteresis losses with magnetization along RD and TD is shown in Fig. 4.5.19. This comparison indicator highlights the anisotropy effect. The modeling results exhibit less anisotropy than the measurements, especially in the case of bi-tension. Some factors may contribute to this significant difference, such as the value chosen for λ_{100}, the choice of the pinning parameter identified from measurements along RD only, or imperfections in the simplification of the texture. Moreover, as shown in Fig. 3.4.1a, for maximum induction of 1T, the anisotropic effects are weak compared to higher induction levels.

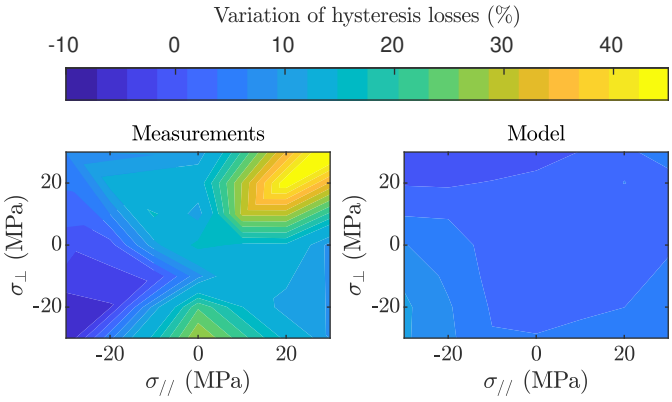

Figura 4.5.19: Percentage variation of hysteresis losses with magnetization along TD compared to magnetization along RD.

The modeled magnetic response under shear loading $\boldsymbol{\sigma} = [0\ 0\ \sigma_{12}]$ and magnetization along RD is shown in Fig. 4.5.20 (right). It is noted that the model underestimates the degradation of magnetization, which is more evident in the measurements Aydin et al. [2019b],

especially under $\sigma_{12} = -30$ MPa. The limitation of the model to represent the degradation under this shear loading results in important differences particularly in the region of the remanent induction. However, using the proposed stress-dependent pining parameter with the equivalent stress Rasilo et al. [2019a] allows capturing the evolution of the coercive field for this mechanical configuration, as observed in Fig. 4.5.21, for magnetization along RD or TD.

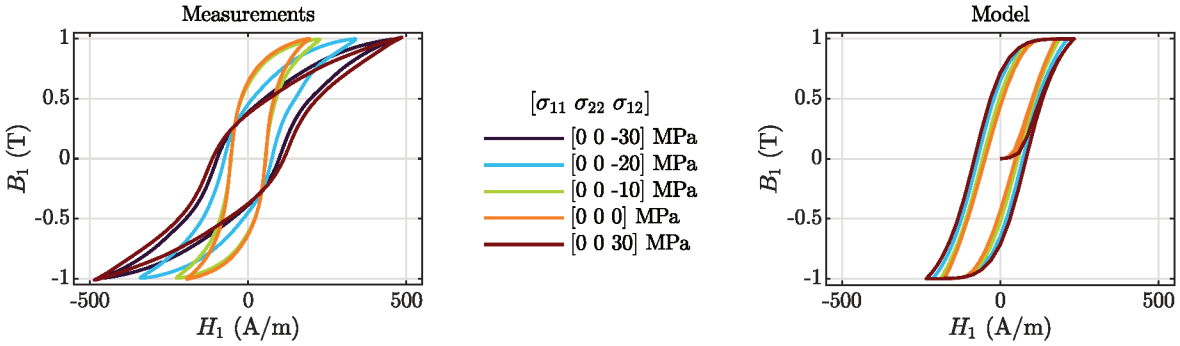

Figura 4.5.20: Comparison between measured Aydin et al. [2019b] (left) and modeled (right) hysteresis loops (at 1T) under shear with field applied along RD. In-plane stress tensor in Voigt notation.

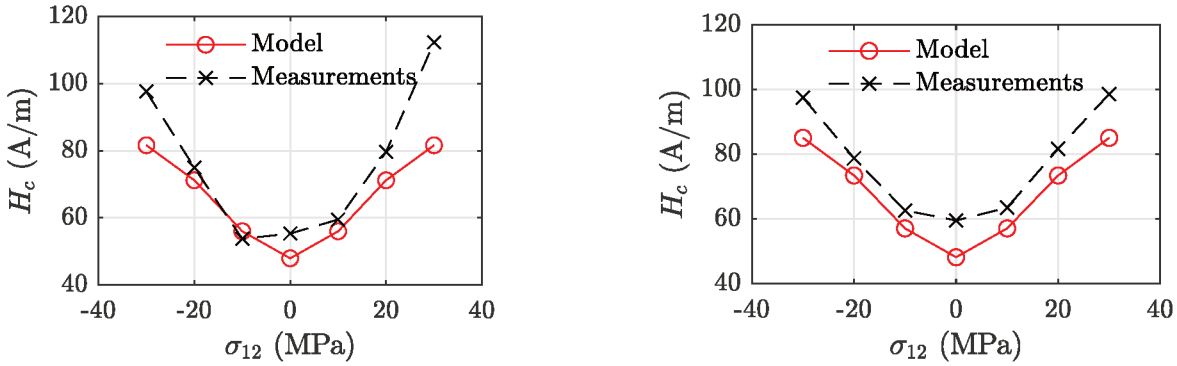

(a) Magnetization along RD.

(b) Magnetization along TD.

Figura 4.5.21: Coercive field evolution at 1T under different levels of shear.

Fig. 4.5.22 presents the percentage variation of the losses compared to the stress-free case when the magnetization is along RD (Fig. 4.5.22a) and when the magnetization is along TD (Fig. 4.5.22b), both under shear. The model reproduces the trend of hysteresis losses increasing depending on the applied stress. However, the model overestimates the level of losses under this shear mode.

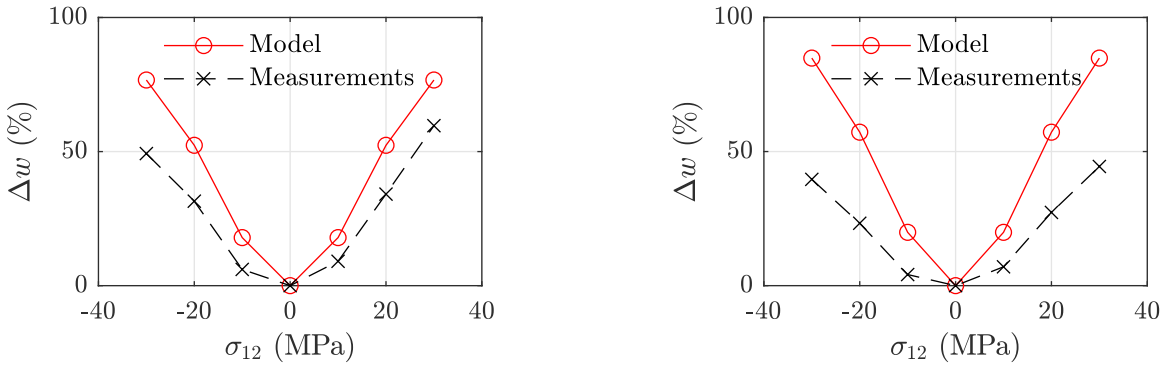

(a) Magnetization along RD.

(b) Magnetization along TD.

Figura 4.5.22: Percentage variation of the hysteresis losses compared to the stress-free case at 1T under different levels of shear.

In this section, an extension of a vector-play model under magneto-elastic loadings has been tested under biaxial stress conditions. A multiscale approach models the reversible behavior, in which homogeneous stress and magnetic field are considered at the RVE scale. Using parameters identified from uniaxial measurements along one direction only, the model captures the trend of the hysteresis losses under biaxial stress when the magnetization is along rolling direction (with errors lower than 15%) or transverse direction (with error lower than 25%). Considering the crystallographic texture, the anisotropic effects, even weak in modeling, slightly change the magnetic response. The use of localization schemes in defining the magnetic field and stress at the grain scale might improve the modeling results, to the price of a significant increase in the simulation time.

4.6 Application under multiaxial stress and rotating field

Using the same set of material parameters identified in Section 4.5 from uniaxial tests, the magneto-elastic hysteresis model is now applied to describe the behavior of a NO Fe-Si under rotating fields and biaxial stress loadings. The measurements were performed controlling the induction and are presented in Aydin et al. [2019a].

The basic energy-based hysteresis approach, however, cannot reproduce the vanishing of hysteresis losses under rotating fields near the saturation, as depicted in Fig. 4.6.1 for the stress-free case. Such a limitation of the hysteresis model was already pointed out in Bergqvist [1997], Domenig et al. [2023]. To correct this drawback Sauseng et al. [2022] proposed to multiply the pinning parameter κ^k by a function f_1:

$$\kappa^k(\vec{M},\sigma) = f_1(\vec{M})\,\kappa^k(\vec{M},\sigma) \qquad \text{with} \qquad f_1(\vec{M}) = 1 - \left(\frac{\|\vec{M}\|}{M_s}\right)^n, \tag{4.6.1}$$

such that κ^k vanishes when the magnetization is close to the saturation. The parameter $n = 10$ is taken from Sauseng et al. [2022]. The effect of using a vanishing pinning field under high magnetization is shown in Fig. 4.6.1, and the decrease of hysteresis losses in the region of domain rotation can be captured by using this adaption. Due to the limitations of the experimental setup, the maximum measured induction amplitude is 1.2 T, so the rotation effect is not reached in the measurements. If tests under higher induction levels are available, the n-parameter can be adapted for the modeling results to match the measurements.

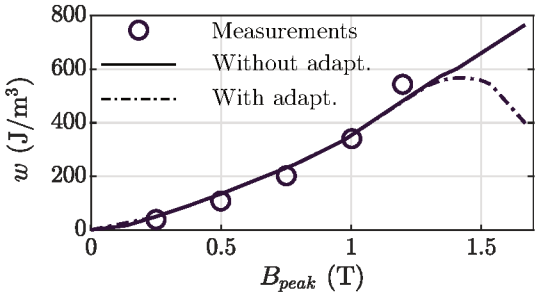

Figura 4.6.1: Stress-free hysteresis losses. Comparison between the measurements (markers) Aydin et al. [2019a] and the model without pinning field adaption (solid line) and with the adaption (dashed line).

4.6.1 Validation

To validate the model under multiaxial magneto-elastic configurations, the measured waveform of the field is used as input for the model. The stress-free hysteresis loops are presented in 4.6.2. Despite differences in the amplitude of the induction loci, the modeled hysteresis loops show a good agreement with the measured B_x and B_y components of $\vec{B}$. Considering compression applied along RD (Fig. 4.6.3) and along TD (Fig. 4.6.4), a satisfying agreement between measurements and model is observed. In challenging multiaxial magneto-elastic configurations with bi-compression (Fig. 4.6.5) and shear (Fig. 4.6.6) applied together with a rotating field, again, a good agreement between measurements and model is noted, despite the complex hysteresis loops shape.

The model captures the trend of hysteresis losses under biaxial stress and rotating field, as observed in 4.6.7. Notably, the increase on losses, specially under shear, is represented

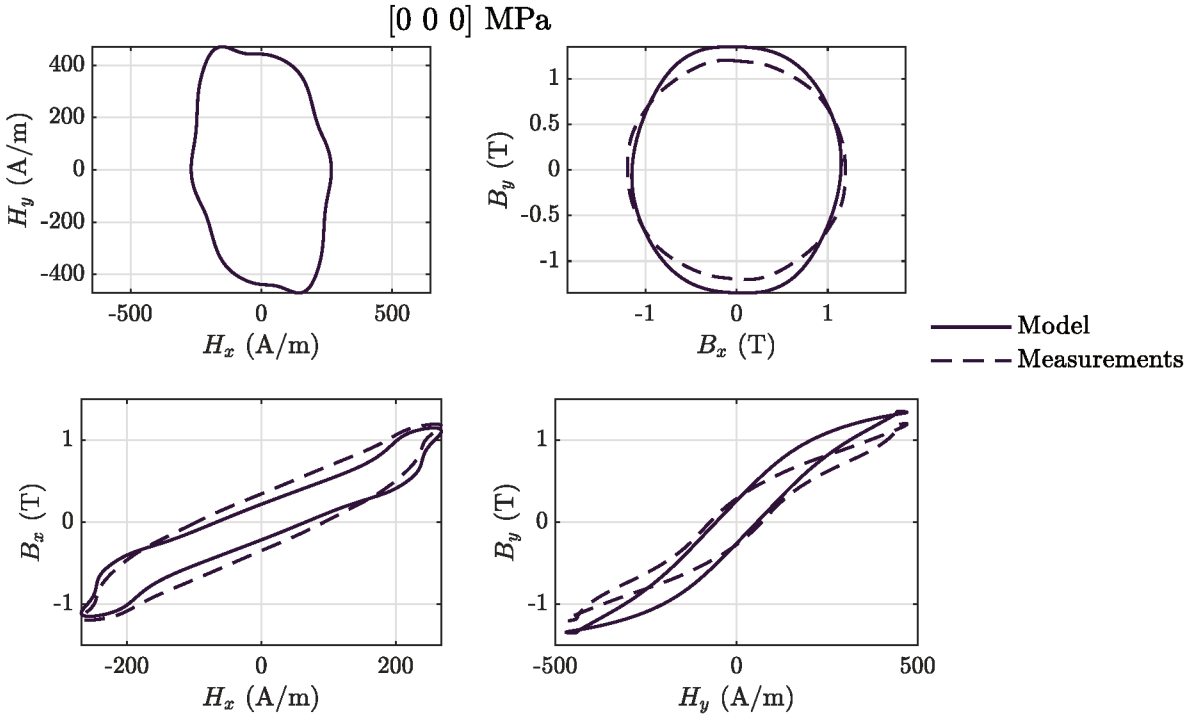

Figura 4.6.2: Stress-free magnetic behavior under rotating field. Comparison between the measurements (dashed lines) Aydin et al. [2019a] and the model (solid lines).

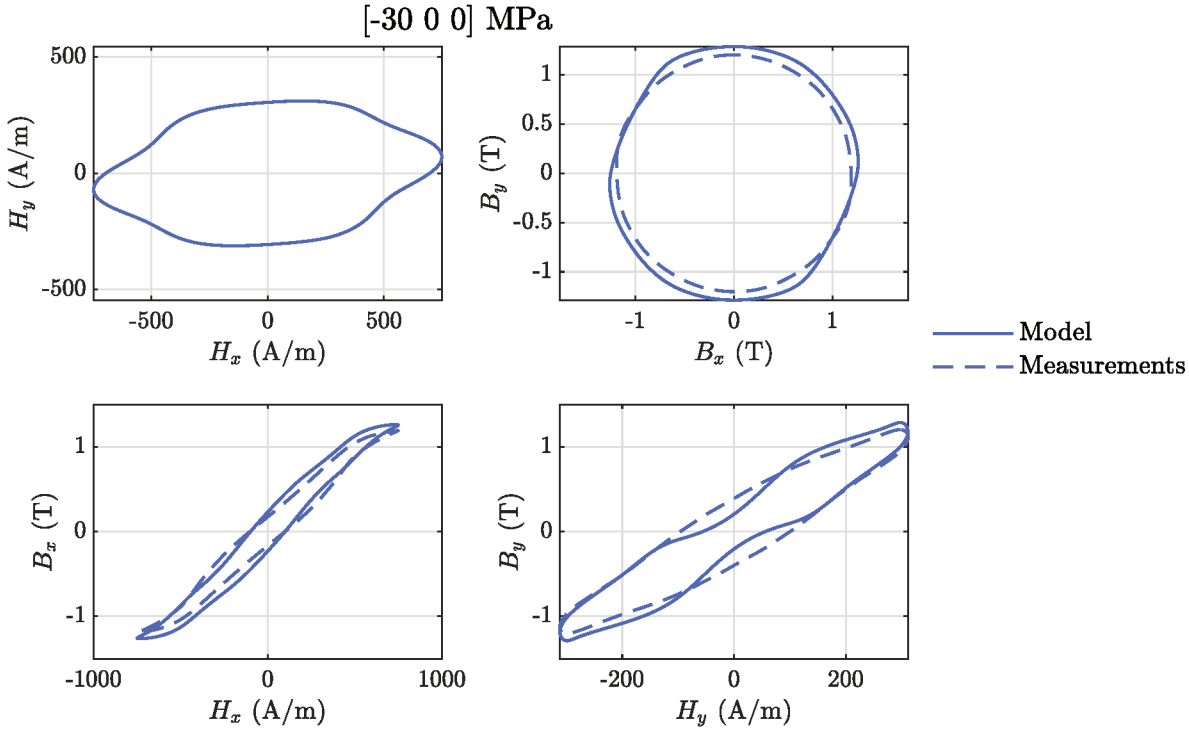

Figura 4.6.3: Magnetic behavior under rotating field and compression applied along RD. Comparison between the measurements (dashed lines) Aydin et al. [2019a] and the model (solid lines).

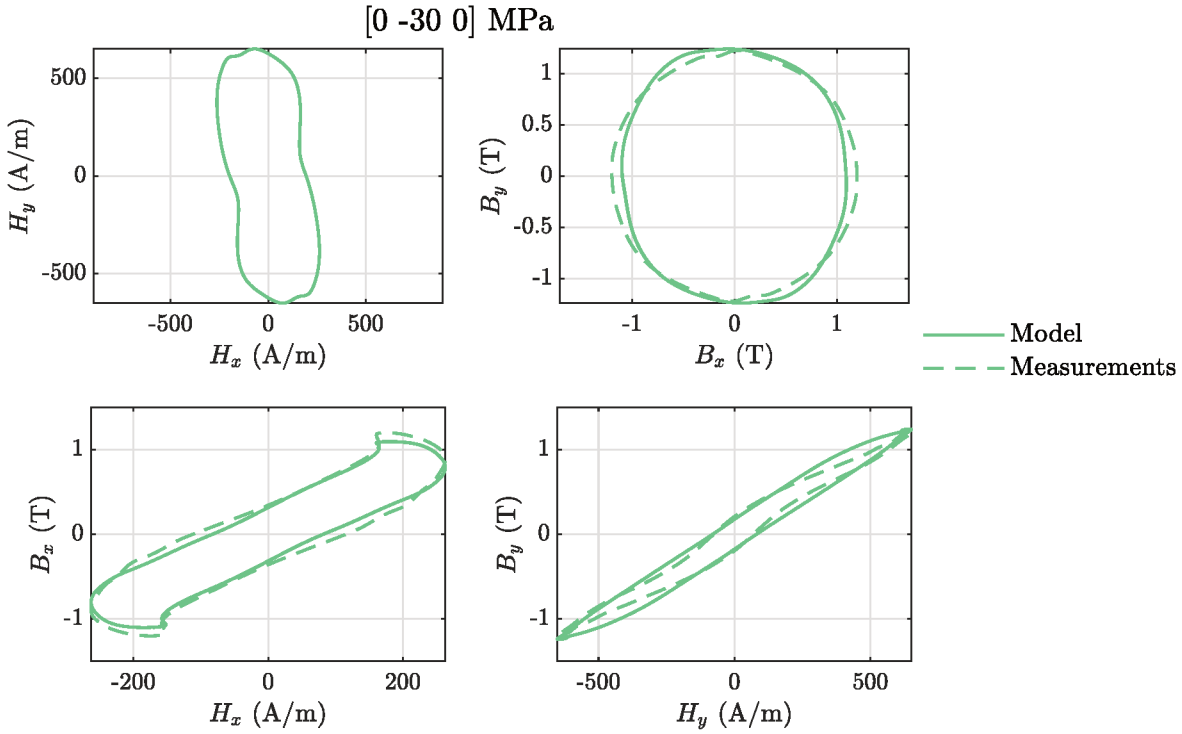

Figura 4.6.4: Magnetic behavior under rotating field and compression applied along TD. Comparison between the measurements (dashed lines) Aydin et al. [2019a] and the model (solid lines).

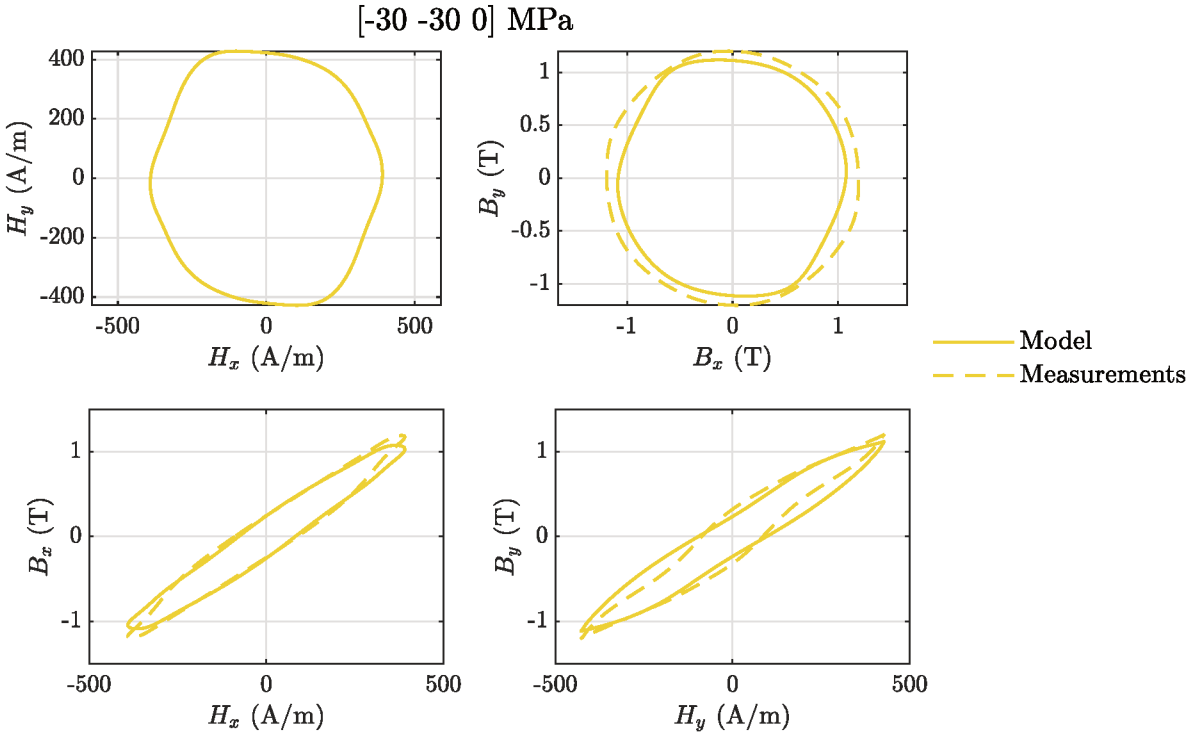

Figura 4.6.5: Magnetic behavior under rotating field and bi-compression. Comparison between the measurements (dashed lines) Aydin et al. [2019a] and the model (solid lines).

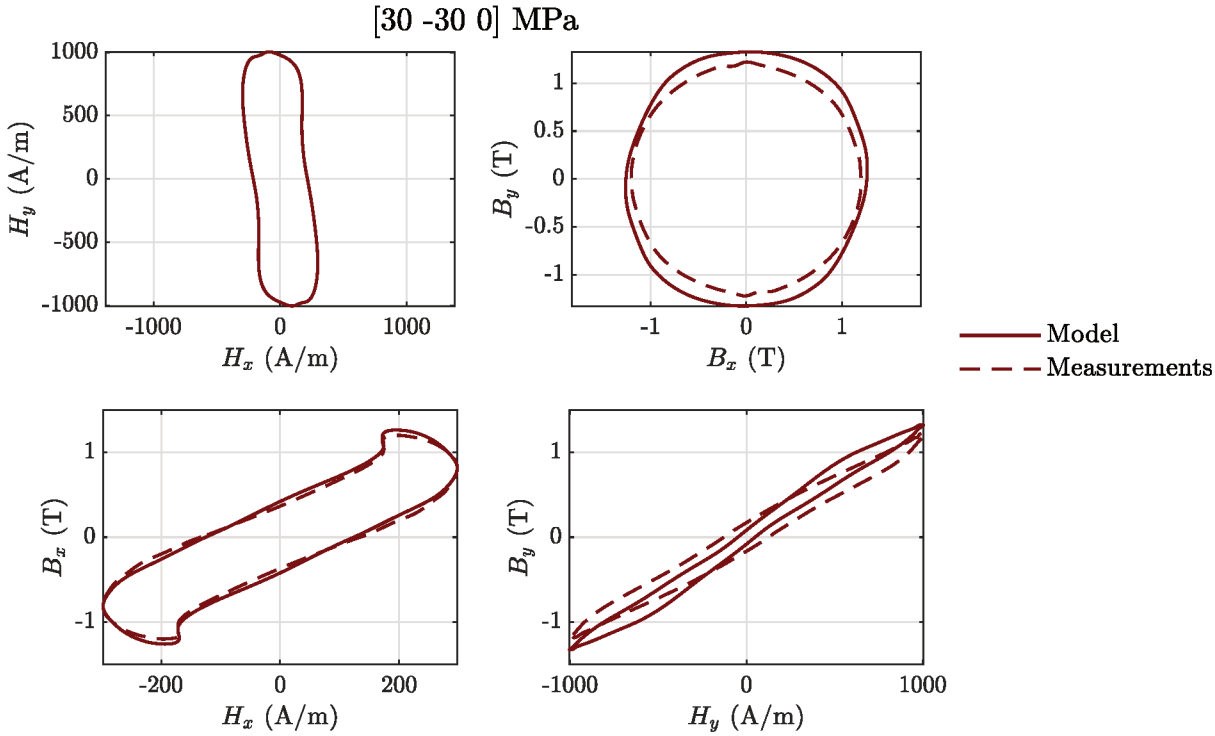

Figura 4.6.6: Magnetic behavior under rotating field and shear. Comparison between the measurements (dashed lines) Aydin et al. [2019a] and the model (solid lines).

in the approach. By adapting the pinning field, the model represents the vanishing of hysteresis losses in the region of domains rotation.

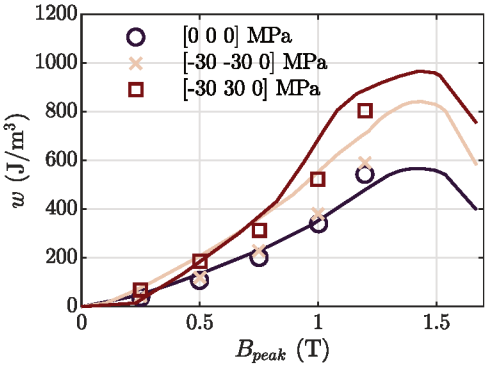

Figura 4.6.7: Comparison between measured Aydin et al. [2019a] (markers) and modeled (solid lines) hysteresis losses under rotating field and stress.

Using material parameters identified from uniaxial tests along one direction only, the combination of a vector-play model and a multiscale approach predicts the magnetic hysteresis loops and the losses trend of a ferromagnetic material under rotating fields and biaxial mechanical loadings. The model validation has been performed by considering complex magneto-elastic loadings different from those used for parameters identification, which were presented in Section 4.5.

5 Magneto-elastic hysteresis modeling under variable stress

This chapter considers the effects of variable stress on the dissipative magnetic behavior and presents two modeling approaches. The first is inspired on the decomposition of the magnetic field - as presented in the vector-play model - and an irreversible stress is introduced, which captures the dissipation due to mechanical loadings. The definition of irreversible stress is based on the description of the irreversible field, and the pinning stress is further introduced. However, because this modeling approach is not based on an energetic description, the thermodynamic consistency is not ensured for any magneto-elastic loading. This opens space for the second approach, in which the dissipation is modeled from the domain volume fractions evolution, and a thermodynamic approach based on internal variables is proposed.

5.1 Irreversible stress approach

As presented in Chapter 4, in the energy-based model approach the magnetic field $\vec{H}$ is decomposed into reversible $\vec{H}_{rev}$ and irreversible parts, with $\vec{H} = \vec{H}_{rev} + \vec{H}_{irr}$. To capture the dissipation due to variation of mechanical stress σ, the following mechanical decomposition is proposed:

$$\sigma = \sigma_{rev} + \sigma_{irr}, \tag{5.1.1}$$

with σ_{rev} and σ_{irr} the reversible and irreversible stresses, respectively. As discussed in Chapter 4, by using the vector-play approach, an explicit approach is defined to evaluate $\vec{H}_{rev}$ at each time-step. This notion is here used to define an explicit update of the reversible stress by[2]:

$$\sigma_{rev} = \begin{cases} \sigma_{rev(p)} & \text{if} \quad \|\sigma - \sigma_{rev(p)}\| \leq \kappa_\sigma |\operatorname{sign}(\|\dot{\sigma}\|)| \\ \sigma - \kappa_\sigma \dfrac{\sigma - \sigma_{rev(p)}}{\|\sigma - \sigma_{rev(p)}\|} |\operatorname{sign}(\|\dot{\sigma}\|)| & \text{otherwise.} \end{cases} \tag{5.1.2}$$

with κ_σ the pinning stress, $\sigma_{rev(p)}$ the previous value of the reversible stress, and $\dot{\sigma}$ the time-derivative of the stress. The sign function is introduced such that it ensures a null

[2]The norm operator of a second-order tensor X is evaluated by $\|X\| = \sqrt{X : X}$.

irreversible stress - so no dissipation - to the case of static mechanical loading. Likewise, the explicit update of $\vec{H}_{rev}$ is given by:

$$\vec{H}_{rev} = \begin{cases} \vec{H}_{rev(p)} & \text{if} \quad \|\vec{H} - \vec{H}_{rev(p)}\| \leq \kappa_H |\operatorname{sign}(\|\dot{\vec{H}}\|)| \\ \vec{H} - \kappa_H \dfrac{\vec{H} - \vec{H}_{rev(p)}}{\|\vec{H} - \vec{H}_{rev(p)}\|} |\operatorname{sign}(\|\dot{\vec{H}}\|)| & \text{otherwise.} \end{cases} \tag{5.1.3}$$

with κ_H the pinning field and $\vec{H}_{rev(p)}$ the previous value of reversible stress. The sign function is defined to enforce zero dissipation in the case of static field.

To model the first magnetization curve, symmetric and asymmetric minor loops, a discrete distribution of κ_H and κ_σ can be used. In this case, several pinning fields and pinning stresses can be considered, defined by the weight ω^k that verifies:

$$\sum_{k=1}^{N} \omega^k = 1. \tag{5.1.4}$$

The explicit update of reversible field $\vec{H}^k_{rev}$ and σ^k_{rev} are given by:

$$\sigma^k_{rev} = \begin{cases} \sigma^k_{rev(p)} & \text{if} \quad \|\sigma - \sigma^k_{rev(p)}\| \leq \kappa^k_\sigma |\operatorname{sign}(\|\dot{\sigma}\|)| \\ \sigma - \kappa^k_\sigma \dfrac{\sigma - \sigma^k_{rev(p)}}{\|\sigma - \sigma^k_{rev(p)}\|} |\operatorname{sign}(\|\dot{\sigma}\|)| & \text{otherwise,} \end{cases} \tag{5.1.5}$$

$$\vec{H}^k_{rev} = \begin{cases} \vec{H}^k_{rev(p)} & \text{if} \quad \|\vec{H} - \vec{H}^k_{rev(p)}\| \leq \kappa^k_H |\operatorname{sign}(\|\dot{\vec{H}}\|)| \\ \vec{H} - \kappa^k_H \dfrac{\vec{H} - \vec{H}^k_{rev(p)}}{\|\vec{H} - \vec{H}^k_{rev(p)}\|} |\operatorname{sign}(\|\dot{\vec{H}}\|)| & \text{otherwise.} \end{cases} \tag{5.1.6}$$

The magnetization $\vec{M}$ and the magnetostriction strain ε^μ are evaluated by the weighted sum:

$$\vec{M} = \sum_{k=1}^{N} \omega^k \vec{M}^k(\sigma^k_{rev}, \vec{H}^k_{rev}) \qquad \text{and} \qquad \varepsilon^\mu = \sum_{k=1}^{N} \omega^k \varepsilon^{\mu,k}(\sigma^k_{rev}, \vec{H}^k_{rev}). \tag{5.1.7}$$

5.1.1 Reversible behavior

The anhysteretic behavior is modeled using a multiscale approach. As pointed out in Hubert and Rizzo [2008], texture effects, such as the Villari reversal, have an important impact on piezomagnetic loops. Therefore, a crystallographic texture is considered here, and a simplified texture multiscale approach (STMSM) - introduced in Chapter 4 - is recalled here. Three scales are defined: the domain scale (denoted by the index α), the grain scale (denoted by the index g), and the polycrystal (or macroscopic) scale. The free-energy density g_α at the domain scale of a domain family α with orientation $\vec{\alpha}$ is given by Bernard et al. [2019]:

$$g_\alpha = g_\alpha^{mag} + g_\alpha^{me} + g_\alpha^{an} \qquad \text{with} \qquad \begin{cases} g_\alpha^{mag} = -\mu_0 \vec{M}_\alpha \cdot \vec{H} \\ g_\alpha^{me} = -\varepsilon_\alpha^\mu : \sigma \\ g_\alpha^{an} = K_1 \left(\alpha_1^2\alpha_2^2 + \alpha_1^2\alpha_3^2 + \alpha_2^2\alpha_3^2 \right) + K_2 \left(\alpha_1^2\alpha_2^2\alpha_3^2 \right), \end{cases} \tag{5.1.8}$$

with $\vec{M}_\alpha$ and ε_α^μ the magnetization and the magnetostriction strain at the domain scale, K_1 and K_2 the magnetocrystalline anisotropy constants. With the definition of g_α, the volume fraction of a domain family α is evaluated using a Boltzmann relation Bernard et al. [2019]:

$$p_\alpha = \frac{\exp\left(-A_s\, g_\alpha\right)}{\sum\limits_\alpha \exp\left(-A_s\, g_\alpha\right)} \tag{5.1.9}$$

where A_s is a material parameter. At the grain scale, the magnetization $\vec{M}_g$ and magnetostriction strain ε_g^μ are evaluated by the weighted sum over all the possible domain orientations:

$$\vec{M}_g = \sum_\alpha p_\alpha \vec{M}_\alpha \quad \text{and} \quad \varepsilon_g^\mu = \sum_\alpha p_\alpha \varepsilon_\alpha^\mu \tag{5.1.10}$$

The macroscopic magnetization $\vec{M}$ and magnetostriction strain ε_g^μ are then calculated by an operation of volume average over all grains:

$$\vec{M} = \sum_g p_g \vec{M}_g \quad \text{and} \quad \varepsilon^\mu = \sum_g p_g \varepsilon_g^\mu \tag{5.1.11}$$

with p_g the proportion of each grain.

The schematic of the algorithm of the hysteresis model is presented in Fig. 5.1.1.

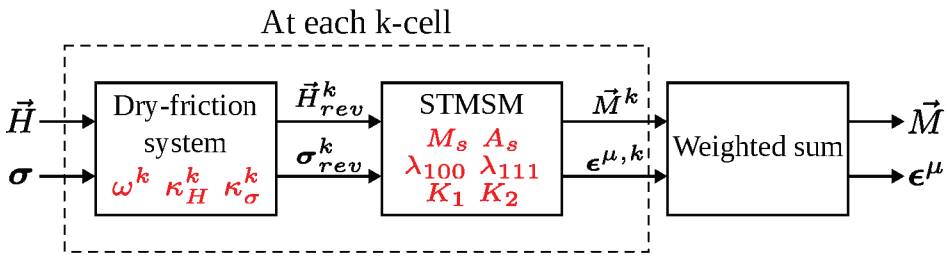

Figura 5.1.1: Principle of the magneto-elastic hysteresis model. The material parameters are indicated in red.

5.1.2 Identification of material parameters

The material parameters are identified from experimental measurements performed on a DC04 low carbon steel and presented in Chapter 3. The crystallographic texture of the DC04 (Fig. 3.2.1) can be reasonably approximated to the texture of a perfect $< 111 >$ fiber, as shown in Fig. 5.1.2, where a simplified texture made of eight grains with equal proportions is presented.

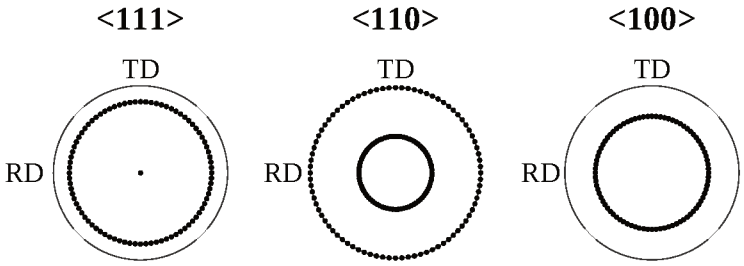

Figura 5.1.2: Pole figures for a perfect $< 111 >$ fiber with eight orientations.

5.1.3 Reversible parameters

The anhysteretic material parameters for the single crystal are taken from pure iron and are listed in Table 5.1.1. The material parameter A_s can be identified from stress-free anhysteretic measurements Daniel et al. [2008] and is identified as 7.5 10^{-3} J/m^3.

Tabela 5.1.1: Single crystal parameters for pure iron Jiles [1991].

M_s (A/m)	λ_{100} (ppm)	λ_{111} (ppm)	K_1 (kJ/m^3)	K_2 (kJ/m^3)
1.71 10^6	21	-21	42.7	15

5.1.4 Irreversible parameters

The dissipation parameters ω^k and κ_H^k can be identified from measured coercive fields under increasing peak magnetic field for the stress-free case and are detailed in Chapter 4. Moreover, the stress-dependent pinning field is also considered here, with parameters identified in Chapter 4.

The identification of κ_σ^k follows the same procedure as that of κ_H^k. However, experimental setup limitations do not allow measuring a field-free magnetostriction strain under variable stress. Indeed, the maximum measured magnetostriction for DC04 is about 5.5 10^{-6} da Silva et al. [2022], and considering a Young modulus of about 192 GPa, a tension of 1 MPa produces the same elastic strain amplitude as the maximum magnetostriction. Therefore, the elastic strain hides the magnetostriction during the stress cycle.

It is proposed here to identify κ_σ^k from piezomagnetic measurements. In this case, the coercive stress σ_c is introduced and defined as the mechanical stress when $B = B_{dc}$ - with B_{dc} the bias level of induction (see Fig. 5.1.3 (left)). Because σ_c is not symmetric with respect to the $\sigma = 0$ axis, σ_c is given by:

$$\sigma_c = \frac{1}{2}\left(\|\sigma_c^+\| + \|\sigma_c^-\|\right) \tag{5.1.12}$$

with σ_c^+ and σ_c^- the negative and positive coercive stresses, respectively (see Fig. 5.1.3 (left)). The identification of κ_σ^k is based on a set of coercive stress σ_c under increasing peak stress σ_{peak}. Because the measured induction is close to zero under $H_{dc} = 0$ A/m in a piezomagnetic test (see Fig. 5.1.9), the κ_σ^k parameter is identified from a level of static field that is close to zero, but for which the induction has a measurable value. The identification of κ_σ^k is performed from measurements under $H_{dc} = 51$ A/m. The piezomagnetic loops under increasing peak stress are depicted in Fig. 5.1.3 (left).

The coercive stress depending on the level of static field H_{dc} is presented in Fig. 5.1.4. It can be noted that σ_c does not vary significantly by increasing H_{dc}. Therefore, the pinning stress κ_σ^k is considered constant under increments of static field in what follows.

The identified continuous distributions of pinning fields and pinning stresses are discretized into 25 cells, and are depicted in Fig. 5.1.5.

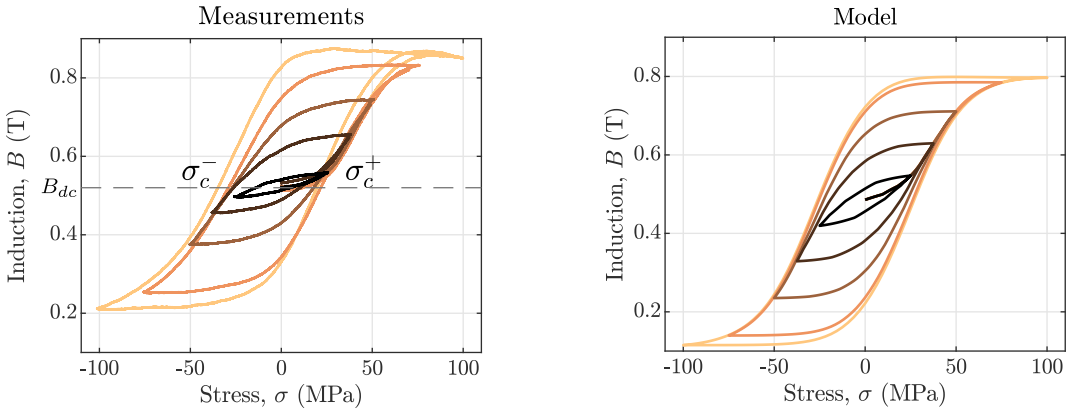

Figura 5.1.3: Comparison between measured (left) and modeled (right) piezomagnetic loops under increasing peak stress and static field. The initial induction B_{dc} is about 0.51 T.

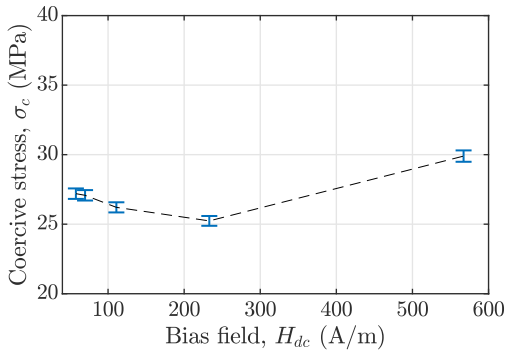

Figura 5.1.4: Coercive stress characteristic under static field.

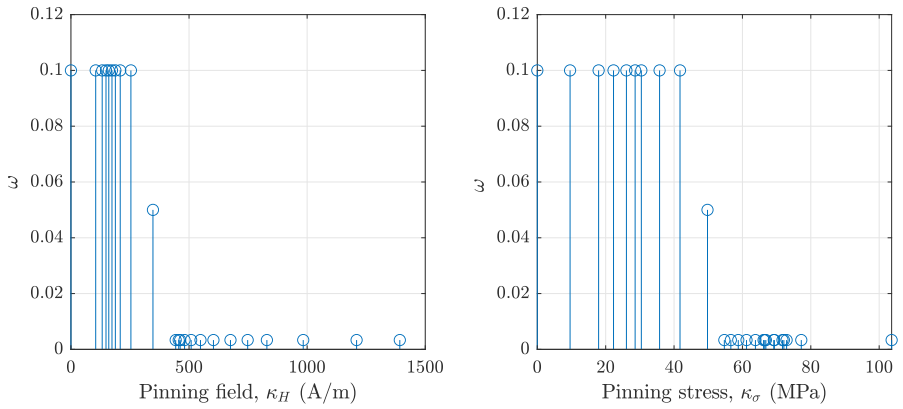

Figura 5.1.5: Discretized pinning field (left) and pinning stress (right) distributions.

5.1.5 Comparison of the model with anhysteretic measurements

The modeled anhysteretic magnetic response under uniaxial stress is presented in Fig. 5.1.6 (right). By considering a simplified crystallographic texture, the Villari reversal - in the region of about 2200 A/m - is captured in modeling. Moreover, inflections (or bowing) under high compression are also captured, though the model overestimates such a texture effect, as observed in the case under -100 MPa.

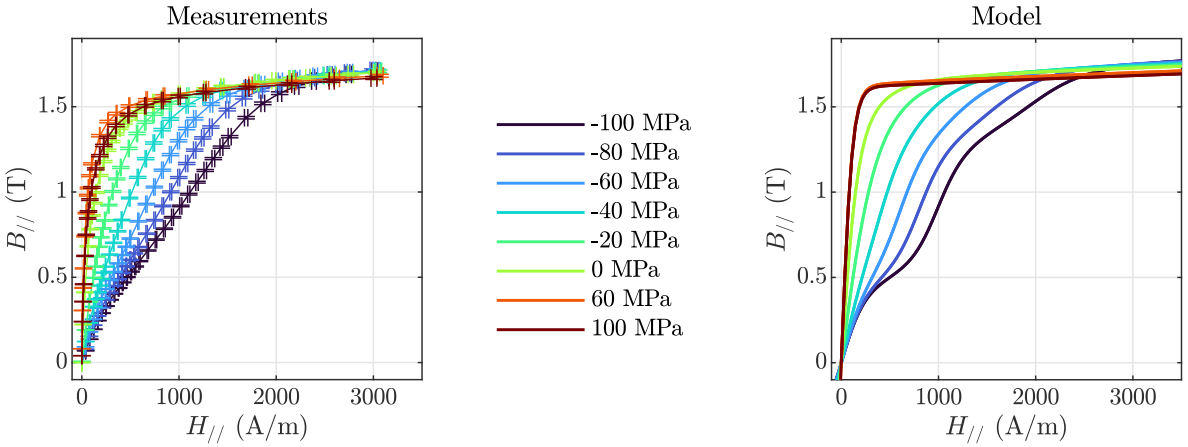

Figura 5.1.6: Comparison between measured (left) and modeled (right) anhysteretic magnetic behavior under several levels of static uniaxial stress.

The anhysteretic longitudinal magnetostriction strain under static uniaxial stress is shown in Fig. 5.1.7. The rotation mechanism - depicted by the drop of magnetostriction at about 1.38 MA/m - is captured by the model. The model captures the trend of the longitudinal magnetostriction under uniaxial stress.

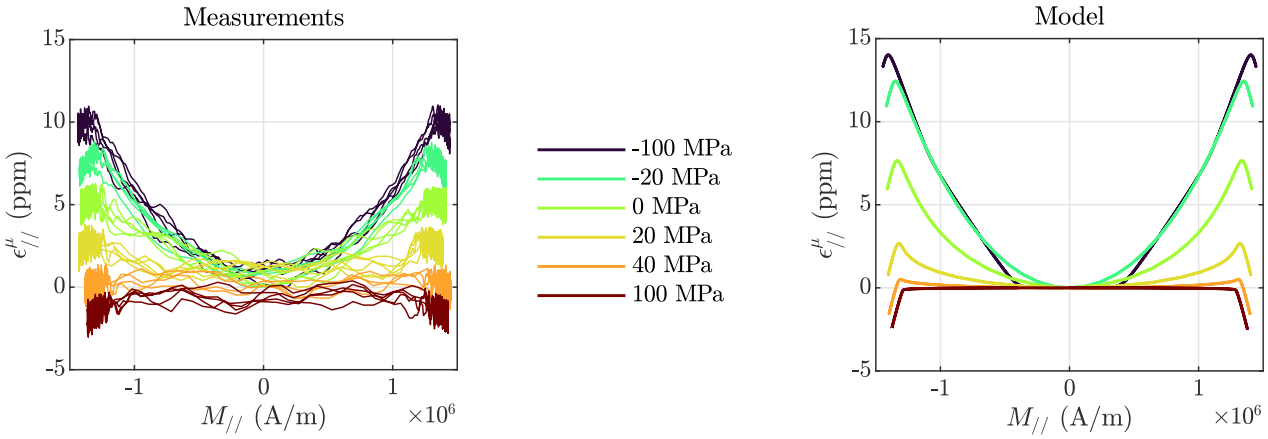

Figura 5.1.7: Comparison between measured (left) and modeled anhysteretic longitudinal magnetostriction under several levels of static uniaxial stress

5.1.6 Comparison of the model with hysteresis measurements

The magnetic hysteresis behavior under static stress is shown in Fig. 5.1.8. As presented in the anhysteretic modeling results, the texture effects, such as the Villari reversal and inflections under high compression, are also captured in the modeled magnetic hysteresis. Comparing these modeling results those in Chapter 4, where an equivalent single-crystal was considered, the improvement in the modeled results is notable by considering the simplified crystallographic texture.

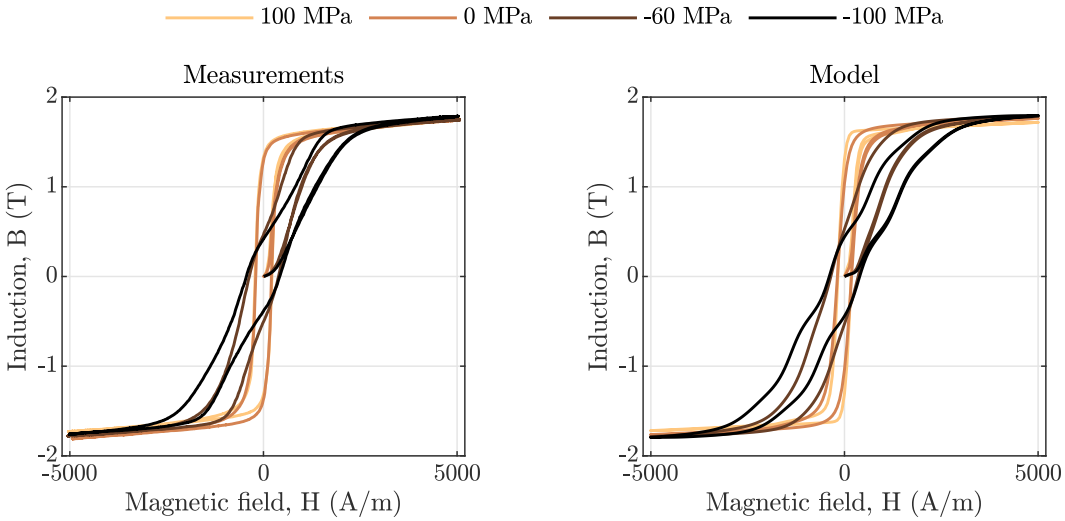

Figura 5.1.8: Comparison between measured (left) and modeled (right) magnetic hysteresis under several levels of static uniaxial stress.

Applying a magneto-elastic loading of static field and quasi-static uniaxial stress, the model reproduces the measured symmetric minor loops, as shown in Fig. 5.1.3 (right). Considering several levels of static field, the modeled piezomagnetic loops are depicted in Fig. 5.1.9. The Villari reversal is evident in the piezomagnetic loops by the slightly decreasing behavior of the induction under high tension. Such a texture-related behavior is captured by the model. The main differences are noted in the area of the loops (20% difference between modeled and measured results under $H_{dc} = 233$ A/m as the worst case). Despite this difference, the measured piezomagnetic trends under increasing bias field are captured by the model.

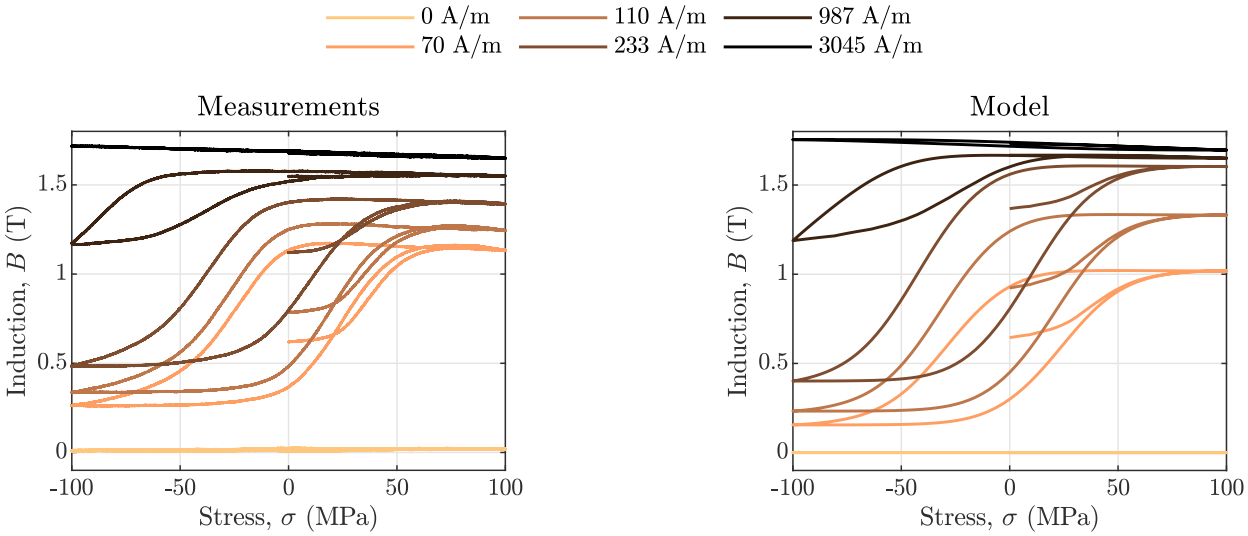

Figura 5.1.9: Comparison between measured (left) and modeled (right) piezomagnetic curves under increasing static field.

To illustrate the effect of mechanical dissipation, Figure 5.1.10 presents the predicted

longitudinal magnetostriction under varying stress and $H_{dc} = 0$ A/m. The mechanical dissipation is estimated as about 0.9 kJ/m^3. As previously pointed out, limitations in the experimental setup do not allow the comparison of this prediction with measurements. Specifically, the elastic strain hides the magnetostriction strain during varying stress.

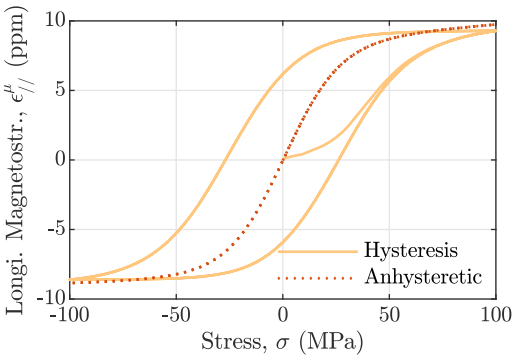

Figura 5.1.10: Modeling prediction of the longitudinal magnetostriction strain behavior under varying stress and zero static field.

A more complex validation configuration is when both the magnetic field and stress vary. Considering the case of the magneto-elastic loading of Fig. 5.1.11 (a), the magnetic response is shown in Fig. 5.1.11 as a function of the magnetic field (b) and of the stress (c). A very good agreement is observed between modeling (blue solid lines) and experiments (red dashed lines). This validation highlights the capabilities of the model to capture the magnetic hysteresis when both field and stress are quasi-static.

5.1.7 Discussions on the model

To study the energetic consistency of the model, the case of static stress and varying magnetic field is analyzed. The approach returns to the same thermodynamically consistent hysteresis model presented in Chapter 4. In the case of varying stress and static magnetic field, first the Clausius-Duhem inequality for the magneto-mechanical behavior is recalled:

$$D = -\dot{\vec{H}} \cdot \vec{B} - \dot{\boldsymbol{\sigma}} : \boldsymbol{\varepsilon} - \dot{g} \geq 0. \tag{5.1.13}$$

The magnetostriction strain $\boldsymbol{\varepsilon}^{\mu}$ is introduced as internal variable to model the irreversible behavior due to stress variations. In this case, the time-derivatives of the Gibbs free energy density $\dot{g}$ are given by:

$$\dot{g}(\boldsymbol{\sigma}, \vec{H}, \boldsymbol{\varepsilon}^{\mu}) = \frac{\partial g}{\partial \boldsymbol{\sigma}} : \dot{\boldsymbol{\sigma}} + \frac{\partial g}{\partial \vec{H}} : \dot{\vec{H}} + \frac{\partial g}{\partial \boldsymbol{\varepsilon}^{\mu}} : \dot{\boldsymbol{\varepsilon}}^{\mu}. \tag{5.1.14}$$

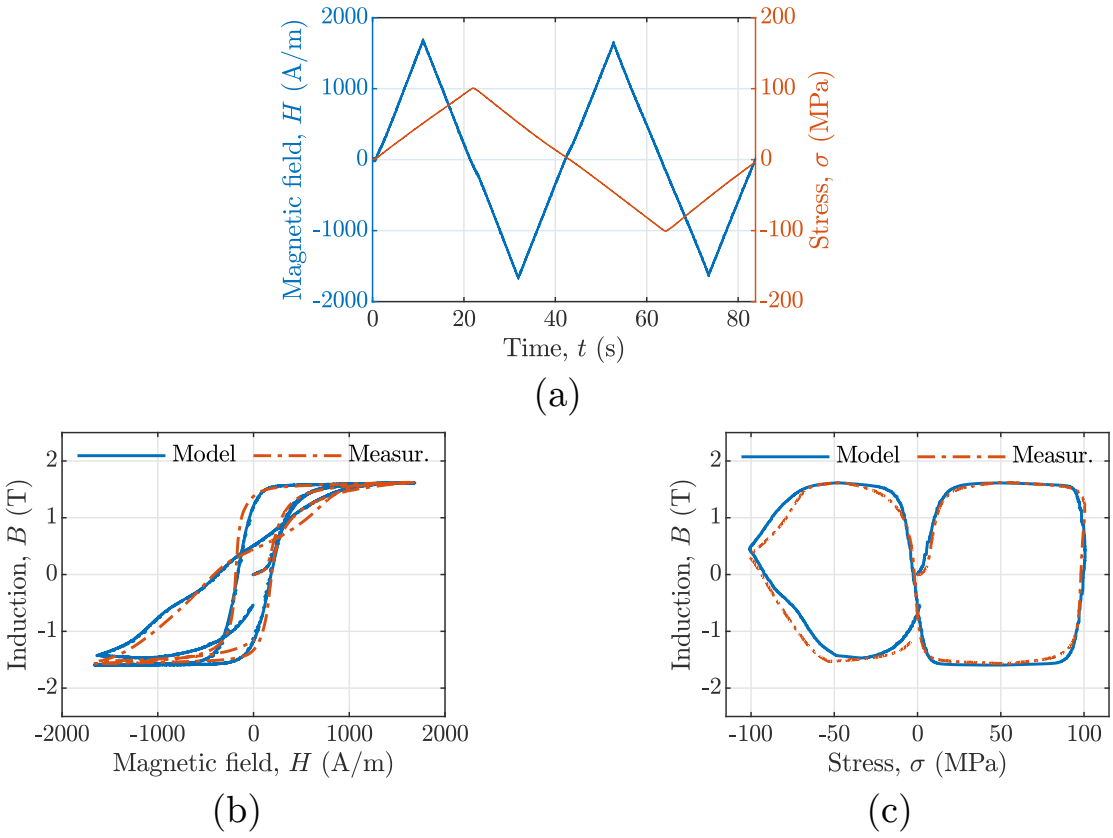

Figura 5.1.11: Magnetic response under quasi-static magneto-elastic loading (a). Comparison between measurements and modeled induction as a function of magnetic field (b) and stress (c).

Replacing (5.1.14) into (5.1.13), it gives:

$$D = -\left[\varepsilon + \frac{\partial g}{\partial \sigma}\right] : \dot{\sigma} - \left[\vec{B} + \frac{\partial g}{\partial \vec{H}}\right] \cdot \dot{\vec{H}} - \frac{\partial g}{\partial \varepsilon^{\mu}} : \dot{\varepsilon^{\mu}} \geq 0. \tag{5.1.15}$$

From (5.1.15), the following relationships are defined, such that the restrictions of the second-law of thermodynamics are fulfilled:

$$\varepsilon = -\frac{\partial g}{\partial \sigma}, \tag{5.1.16a}$$

$$\vec{B} = -\frac{\partial g}{\partial \vec{H}}, \tag{5.1.16b}$$

$$D = -\frac{\partial g}{\partial \varepsilon^{\mu}} : \dot{\varepsilon^{\mu}} \geq 0. \tag{5.1.16c}$$

The irreversible behavior is characterized by a dissipation function in terms of the internal variable $\phi_d(\dot{\varepsilon^{\mu}})$, which is defined by Miehe et al. [2011]:

$$-\frac{\partial g}{\partial \varepsilon^{\mu}} = \frac{\partial \phi_d}{\partial \dot{\varepsilon^{\mu}}}. \tag{5.1.17}$$

The dissipation inequality can be written as:

$$D = \frac{\partial \phi_d}{\partial \dot{\varepsilon^{\mu}}} : \dot{\varepsilon^{\mu}} \geq 0 \qquad \text{with} \qquad \phi_d(0) = 0 \qquad \text{and} \qquad \phi_d(\dot{\varepsilon^{\mu}}) \geq 0. \tag{5.1.18}$$

For rate-independent processes, ϕ_d is defined as positively homogeneous of degree one, so that Miehe et al. [2011]:

$$\phi_d(\tau \dot{\varepsilon^{\mu}}) = \tau \phi_d(\dot{\varepsilon^{\mu}}) \qquad \text{with} \qquad \tau \in R_{e+}. \tag{5.1.19}$$

Using the chain rule and assuming a positively homogeneous function of degree one, the following relationship can be defined:

$$\frac{\partial \phi_d}{\partial \dot{\varepsilon^{\mu}}} : \dot{\varepsilon^{\mu}} = \phi_d(\dot{\varepsilon^{\mu}}). \tag{5.1.20}$$

Therefore, the dissipation function $\phi_d(\dot{\varepsilon^{\mu}})$ defines the evolution of dissipation D by:

$$D = \phi_d(\dot{\varepsilon^{\mu}}) \geq 0. \tag{5.1.21}$$

From (5.1.17), a minimization procedure can be established to evaluate the hysteresis behavior under variable mechanical loadings and static fields. In this case, the energy density g and the dissipation function ϕ_d need to be defined. Following the analogy of the magnetic hysteresis with a dry-friction mechanism Bergqvist [1997], Henrotte et al. [2006], the dissipation function ϕ_d is defined as:

$$\phi_d(\dot{\varepsilon^{\mu}}) = \kappa_{\sigma} \|\dot{\varepsilon^{\mu}}\|, \tag{5.1.22}$$

with κ_{σ} a pinning stress. For sufficient small time-steps, the dissipation ϕ_d is approximated by:

$$\phi_d(\varepsilon^{\mu}) \approx \kappa_{\sigma} \frac{\|\varepsilon^{\mu} - \varepsilon^{\mu}_{(p)}\|}{\Delta t}, \tag{5.1.23}$$

with $\varepsilon^{\mu}_{(p)}$ the magnetostriction strain at the previous time-step. From this approximation, the partial derivative of the dissipation function ϕ_d is given by:

$$\frac{\partial \phi_d}{\partial \dot{\varepsilon^{\mu}}} \approx \frac{\partial \phi_d}{\partial \left(\dfrac{\varepsilon^{\mu} - \varepsilon^{\mu}_{(p)}}{\Delta t} \right)} = \Delta t \, \frac{\partial \phi_d}{\partial \varepsilon^{\mu}}. \tag{5.1.24}$$

In Chapter 4, the magnetization $\vec{M}$ was introduced as internal variable and a minimization evaluates the behavior of $\vec{M}$ under static stress and varying field. Here, from the definition of (5.1.17) and taking into account the approximation (5.1.24), the magnetostriction strain ε^{μ} is calculated from a minimization by:

$$\frac{\partial}{\partial \varepsilon^{\mu}} \left[g(\sigma, \vec{H}, \varepsilon^{\mu}) + \Delta t \; \phi_d(\varepsilon^{\mu}) \right] = 0 \quad \rightarrow$$

$$\begin{aligned} \varepsilon^{\mu} = \arg\min \quad & \left[g(\sigma, \vec{H}, \varepsilon^{\mu}) + \kappa_{\sigma} \| \varepsilon^{\mu} - \varepsilon^{\mu}_{(p)} \| \right] \\ \text{subject to} \quad & \operatorname{tr}(\varepsilon^{\mu}) = 0 \end{aligned} \tag{5.1.25}$$

The energy density $g(\sigma, \vec{H}, \varepsilon^{\mu})$ can be identified as:

$$g(\sigma, \vec{H}, \varepsilon^{\mu}) = \widetilde{f}(\vec{H}, \varepsilon^{\mu}) - \mu_0 \frac{H^2}{2} - \frac{1}{2} \left(\mathscr{C}^{-1} \, \sigma \right) : \sigma - \varepsilon^{\mu} : \sigma, \tag{5.1.26}$$

with $\widetilde{f}(\vec{H}, \varepsilon^{\mu})$ a free energy density that can be obtained from the partial numerical inversion of a magnetic anhysteretic model - here the multiscale approach. The time-derivative $\dot{\widetilde{f}}$ is:

$$\dot{\widetilde{f}}(\vec{H}, \varepsilon^{\mu}) = \sigma_{rev} : \dot{\varepsilon^{\mu}} - \mu_0 \vec{M} \cdot \dot{\vec{H}} \qquad \text{with} \qquad \frac{\partial \widetilde{f}}{\partial \varepsilon^{\mu}} = \sigma_{rev} \qquad \text{and} \qquad \frac{\partial \widetilde{f}}{\partial \vec{H}} = -\mu_0 \vec{M}. \tag{5.1.27}$$

and the reversible stress σ_{rev} is introduced. With the choice of $g(\sigma, \vec{H}, \vec{M})$, (5.1.16a) and (5.1.16b) are:

$$\begin{aligned} -\frac{\partial g}{\partial \vec{H}} &= \mu_0 \left(\vec{H} + \vec{M} \right) = \vec{B} \\ -\frac{\partial g}{\partial \sigma} &= \mathscr{C}^{-1} \sigma + \varepsilon^{\mu} = \varepsilon^{\mu} + \varepsilon^{e} = \varepsilon, \end{aligned} \tag{5.1.28}$$

under the hypothesis of small strains, with $\mathscr{C}$ the stiffness tensor and ε^{e} the elastic

strain. From (5.1.16c):

$$-\frac{\partial g}{\partial \varepsilon^{\mu}} = -\frac{\partial \widetilde{f}}{\partial \varepsilon^{\mu}} + \sigma = -\sigma_{rev} + \sigma = \sigma_{irr}, \tag{5.1.29}$$

and the irreversible stress σ_{irr} is introduced, defining the mechanical loading decomposition into reversible and irreversible parts $\sigma = \sigma_{rev} + \sigma_{irr}$.

Combining (5.1.25) and (5.1.26), the magnetostriction strain is given by the minimization:

$$\begin{aligned} \varepsilon^{\mu} = \arg\min \quad & \left[\widetilde{f}(\vec{H}, \varepsilon^{\mu}) - \varepsilon^{\mu} : \sigma + \kappa_{\sigma} \|\varepsilon^{\mu} - \varepsilon^{\mu}_{(p)}\|\right] \\ \text{subject to} \quad & \operatorname{tr}(\varepsilon^{\mu}) = 0 \end{aligned} \tag{5.1.30}$$

considering that $\mathscr{C}$ does not depends on ε^{μ}, $\left(\mathscr{C}^{-1}\,\sigma\right) : \sigma$ is constant, and it can be neglected in evaluating ε^{μ}. Moreover, the term $\mu_0 \vec{H} \cdot \vec{H}$ is also constant, and can be neglected in the minimization.

As the dissipation $\phi_d(\varepsilon^{\mu})$ in non-differentiable at $\varepsilon^{\mu} = \varepsilon^{\mu}_{(p)}$, the subsequent set defines the derivatives of ϕ_d:

$$\frac{\partial \phi_d(\varepsilon^{\mu})}{\partial \varepsilon^{\mu}} \in \begin{cases} \sigma_{irr}, \|\sigma_{irr}\| \leq \kappa_{\sigma}, & \text{if } \varepsilon^{\mu} = \varepsilon^{\mu}_{(p)} \\ \sigma_{irr} = \kappa_{\sigma} \dfrac{\varepsilon^{\mu} - \varepsilon^{\mu}_{(p)}}{\|\varepsilon^{\mu} - \varepsilon^{\mu}_{(p)}\|}, & \text{otherwise.} \end{cases} \tag{5.1.31}$$

By applying the vector-play approximation, an explicit solution of the model is obtained, and the reversible stress updates are given by:

$$\sigma_{rev} = \begin{cases} \sigma_{rev(p)} & \text{if} \quad \|\sigma - \sigma_{rev(p)}\| \leq \kappa_{\sigma} \\ \sigma - \kappa_{\sigma} \dfrac{\sigma - \sigma_{rev(p)}}{\|\sigma - \sigma_{rev(p)}\|} & \text{otherwise.} \end{cases} \tag{5.1.32}$$

The modeling is thermodynamically consistent in the case of static magnetic fields and varying mechanical loadings. However, as pointed out in Prigozhin et al. [2016], where the vector-play approximation is shown to exhibit limitations in the case of 2D spiral magnetic fields, it is expected that the vector-play approximation for the stress also may show limitations when complex stress loadings are applied.

Consider now a uniaxial configuration and the application of the loading presented in Fig. 5.1.12a, in which both field and stress vary sequentially. Field variations are imposed when

stress is constant, and stress variations are imposed when the field is constant. For simplicity, only one cell is considered with $\kappa_H = 200$ A/m and $\kappa_\sigma = 20$ MPa. Under stress variations (see the A-B segment in Fig. 5.1.12a), the reversible stress will be modified when the threshold κ_σ is reached as shown in Fig. 5.1.12b, with the value given by $\sigma_{rev} = \sigma - \kappa_\sigma$. The reversible field remains constant for this loading case. The magnetic response is shown in Fig. 5.1.13. The induction is close to zero in the A-B segment (see Fig. 5.1.13a), and the magnetostriction strain evolves with increments in the reversible stress (see Fig. 5.1.13b).

As shown in Fig. 5.1.12a, the stress loading is set constant, and the magnetic field varies in the B-C segment. The reversible field will be modified only when the threshold κ_H is reached, with the value given by $H_{rev} = H - \kappa_H$. Due to the formulation of the proposed approach, constant stress yields to $\sigma_{rev} = \sigma$, resulting in a discontinuity of the reversible stress, as observed in the segment B-C in Fig. 5.1.12b. This discontinuity results in a jump in magnetostriction strain, as seen in Fig. 5.1.13b. If now the magnetic field is constant and stress varies, the same discontinuity problem is observed in the reversible field, resulting in jumps in both induction and magnetostriction strain (see Fig. 5.1.13). Therefore, the model can present non-physical behavior for some magneto-elastic loadings.

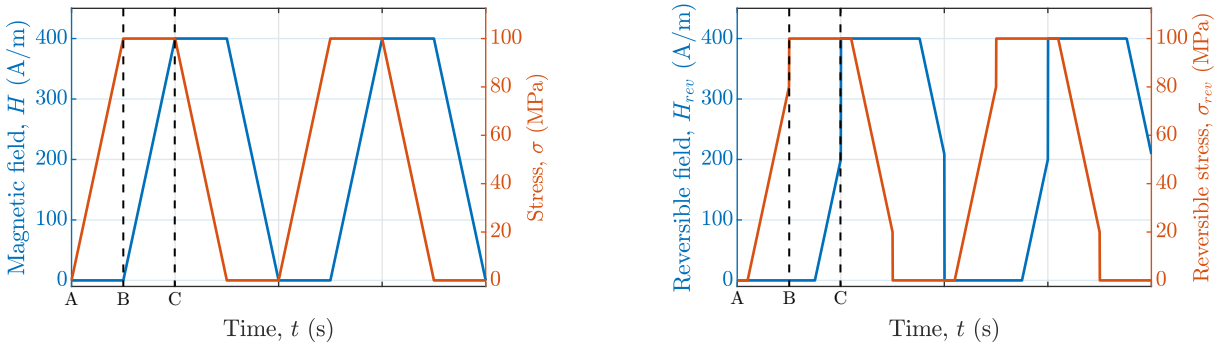

(a) Magneto-elastic loading

(b) Reversible quantities

Figura 5.1.12: Modeling application under variations of both field and stress.

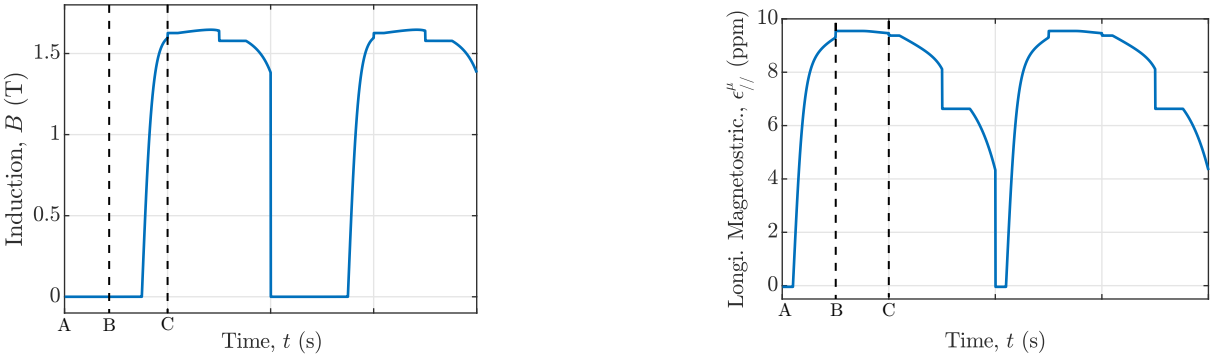

(a) Induction

(b) Longitudinal magnetostriction strain

Figura 5.1.13: Modeled magnetic response.

The dissipation due to variations of mechanical loading is modeled from an analogy of the decomposition of the magnetic field - into reversible and irreversible parts - applied to the mechanical stress. In this case, an irreversible stress describes the dissipative behavior due to mechanical loading variations. A pinning stress parameter is introduced and is identified from piezomagnetic measurements. The model captures the piezomagnetic behavior, and validation under simultaneously varying stress and magnetic fields is performed with satisfying agreement. The model can be summarized as two thermodynamically consistent models in the situation of static stress and varying fields, and in the situation of static field and varying stress. However, non-physical results are observed for some magneto-elastic loadings. The model allows for multiaxial magneto-elastic loadings, such that the model could be applied in a complex application under rotating stress and static field, for example, with thermodynamic consistency.

5.2 Domain volume fraction approach

The dissipation modeling using internal variables is flexible in defining the appropriate quantity to describe the irreversible behavior. The physics of the problem determines such a choice. The domain volume fractions are a set of common variables for both magnetization and magnetostriction evaluation. This section uses the domain volume fraction to describe the dissipation in a thermodynamics framework. The modeling of the magneto-elastic hysteresis is based on a multiscale model, and three scales are defined: the domain scale (denoted by the index α), the grain scale (denoted by the index g), and the polycrystalline representative volume element scale (RVE).

The magneto-elastic hysteresis modeling starts from the thermodynamics principles, as the energy-based approach presented in Chapter 4. The Clausius-Duhem inequality given in terms of the Gibbs free energy $g(\sigma,\vec{H})$ is:

$$D = -\dot{\vec{H}} \cdot \vec{B} - \dot{\sigma} : \varepsilon - \dot{g} \geq 0. \tag{5.2.1}$$

In Chapter 4, the magnetization $\vec{M}$ was chosen as internal variable to describe the irreversible behavior. Here, the domain volume fractions p_α are introduced as internal variables. The domain volume fractions p_α are represented under the following constraints:

$$\sum_\alpha p_\alpha = 1 \qquad \text{and} \qquad 0 \leq p_\alpha \leq 1. \tag{5.2.2}$$

Inserting the internal variables into the Gibbs free energy, the time-derivative $\dot{g}(\sigma,\vec{H},p_\alpha)$ is given by:

$$\dot{g}\left(\sigma,\vec{H},p_\alpha\right) = \frac{\partial g}{\partial \sigma} : \dot{\sigma} + \frac{\partial g}{\partial \vec{H}} \cdot \dot{\vec{H}} + \sum_\alpha \frac{\partial g}{\partial p_\alpha} \dot{p_\alpha}. \tag{5.2.3}$$

Replacing (5.2.3) into (5.2.1) gives:

$$D = -\left(\frac{\partial g}{\partial \sigma} + \varepsilon\right) : \dot{\sigma} - \left(\frac{\partial g}{\partial \vec{H}} + \mu_0 \vec{M}\right) \cdot \dot{\vec{H}} - \sum_\alpha \frac{\partial g}{\partial p_\alpha} \dot{p_\alpha} \geq 0. \tag{5.2.4}$$

The following relationships are defined:

$$\begin{aligned} \varepsilon &= -\frac{\partial g}{\partial \sigma}, \\ \vec{B} &= -\frac{\partial g}{\partial \vec{H}}, \\ D &= -\sum_\alpha \frac{\partial g}{\partial p_\alpha} \dot{p_\alpha} \geq 0, \end{aligned} \tag{5.2.5}$$

such that (5.2.5) can be considered sufficient conditions to fulfill the second law of thermodynamics requirements. As in Chapter 4, a dissipation function $\phi_d(\dot{p_\alpha})$ is introduced, and the variations of domain volume fractions characterize the dissipation. Moreover, $\phi_d(\dot{p_\alpha})$ needs to be defined under the following conditions:

$$\phi_d(0) = 0 \qquad \text{and} \qquad \phi_d(\dot{p_\alpha}) \geq 0, \tag{5.2.6}$$

ensuring that $D = \phi_d(\dot{p_\alpha}) \geq 0$. Following the same notion presented in Chapter 4,

from the definition of $\phi_d(\dot{p_\alpha})$, the following relationship is defined Miehe et al. [2011]:

$$\frac{\partial \phi_d}{\partial \dot{p_\alpha}} + \frac{\partial g}{\partial p_\alpha} = 0, \tag{5.2.7}$$

which is the basis to solve the model by establishing a minimization procedure. To fully characterize the evaluation of the domain volume fractions, it remains to define the Gibbs free energy $g(\sigma, \vec{H}, p_\alpha)$ and the dissipation function $\phi_d(\dot{p_\alpha})$.

5.2.1 Formulation of the Gibbs free energy

The Gibbs free energy density is developed based on a multiscale approach, considering stress and field homogeneous within the grain, and under the hypothesis of small strains. At the domain scale, the Gibbs free energy g_α is given by Daniel et al. [2008]:

$$\begin{aligned}
&g_\alpha = g_\alpha^{mag} + g_\alpha^{an} + g_\alpha^{me} \qquad \text{with} \\
&g_\alpha^{an} = K_1 \left(\alpha_1^2 \alpha_2^2 + \alpha_1^2 \alpha_3^2 + \alpha_2^2 \alpha_3^2 \right) + K_2 \left(\alpha_1^2 \alpha_2^2 \alpha_3^2 \right) \\
&g_\alpha^{mag} = -\frac{1}{2} \mu_0 \vec{H} \cdot \vec{H} - \mu_0 \vec{M}_\alpha \cdot \vec{H} \\
&g_\alpha^{me} = -\frac{1}{2} \varepsilon^e : \sigma - \varepsilon_\alpha^\mu : \sigma = -\frac{1}{2} \sigma : \mathscr{C}^{-1} : \sigma - \varepsilon_\alpha^\mu : \sigma.
\end{aligned} \tag{5.2.8}$$

with $\mathscr{C}$ the stiffness tensor, considered uniform within the single crystal. To define the Gibbs free energy at the grain scale, following Tan and Kochmann [2017], the entropy s related to the volume fractions configuration is first introduced:

$$s = -k \sum_\alpha p_\alpha \log p_\alpha, \tag{5.2.9}$$

with k a positive material parameter. The Gibbs free energy at the grain scale is composed of a weighted sum of the energy of the domains and a contribution of the thermal energy Tan and Kochmann [2017]:

$$g\left(\sigma, \vec{H}, p_\alpha\right) = \sum_\alpha p_\alpha \left[g_\alpha + kT \log p_\alpha \right], \tag{5.2.10}$$

with T the absolute temperature. The partial derivatives of (5.2.10) in terms of stress and field are:

$$
\begin{aligned}
-\frac{\partial g}{\partial \boldsymbol{\sigma}} &= \mathscr{C}^{-1} : \boldsymbol{\sigma} + \sum_{\alpha} p_\alpha \boldsymbol{\varepsilon}_\alpha^{\mu} = \boldsymbol{\varepsilon}^{e} + \boldsymbol{\varepsilon}^{\mu} = \boldsymbol{\varepsilon} \\
-\frac{\partial g}{\partial \vec{H}} &= \mu_0 \left(\vec{H} + \sum_{\alpha} p_\alpha \vec{M}_\alpha \right) = \mu_0 \left(\vec{H} + \vec{M} \right) = \vec{B},
\end{aligned}
\tag{5.2.11}
$$

such that the macroscopic magnetostriction strain $\boldsymbol{\varepsilon}^{\mu}$ and the macroscopic magnetization $\vec{M}$ are given by:

$$
\boldsymbol{\varepsilon}^{\mu} = \sum_{\alpha} p_\alpha \boldsymbol{\varepsilon}_\alpha^{\mu} \qquad \text{and} \qquad \vec{M} = \sum_{\alpha} p_\alpha \vec{M}_\alpha. \tag{5.2.12}
$$

For a polycrystal, the energy density at the macroscopic scale is evaluated from each grain contribution Tan and Kochmann [2017]:

$$
g\left(\boldsymbol{\sigma}, \vec{H}, p_\alpha\right) = \sum_{g} p_g \left[\sum_{\alpha} p_\alpha \left[g_\alpha + kT \log p_\alpha \right] \right], \tag{5.2.13}
$$

with p_g the proportion of each grain orientation. The macroscopic magnetization and magnetostriction strain for a polycrystal are evaluated by:

$$
\boldsymbol{\varepsilon}^{\mu} = \sum_{g} p_g \left[\sum_{\alpha} p_\alpha \boldsymbol{\varepsilon}_\alpha^{\mu} \right] \qquad \text{and} \qquad \vec{M} = \sum_{g} p_g \left[\sum_{\alpha} p_\alpha \vec{M}_\alpha \right]. \tag{5.2.14}
$$

5.2.2 Anhysteretic magnetic behavior

Neglecting dissipation ($\phi_d = 0$), the reversible (or anhysteretic) magnetic response can be evaluated by defining a minimization procedure based on (5.2.7), under the constraints of (5.2.2):

$$
\begin{aligned}
p_\alpha = \arg\min \quad & \sum_{\alpha=1}^{n} p_\alpha \left[g_\alpha + kT \log p_\alpha \right] \\
\text{subject to} \quad & \left(\sum_{\alpha=1}^{n} p_\alpha \right) - 1 = 0, \\
& 0 \leq p_\alpha \leq 1
\end{aligned}
\tag{5.2.15}
$$

From the definition of the energy density g_α, it is noted that the terms

$$
-\frac{1}{2}\boldsymbol{\sigma} : \mathscr{C}^{-1} : \boldsymbol{\sigma} \qquad \text{and} \qquad -\frac{1}{2}\mu_0 \vec{H} \cdot \vec{H}, \tag{5.2.16}
$$

are constants, and will not influence in the minimization. Therefore, these terms can

be neglected in evaluating the domain volume fractions. The Hessian matrix H_g of the Gibbs free energy g is:

$$H_g = \begin{bmatrix} \dfrac{\partial^2 g}{\partial p_1^2} & \dfrac{\partial^2 g}{\partial p_1 \partial p_2} & \cdots & \dfrac{\partial^2 g}{\partial p_1 \partial p_n} \\ \dfrac{\partial^2 g}{\partial p_2 \partial p_1} & \dfrac{\partial^2 g}{\partial p_2^2} & \cdots & \dfrac{\partial^2 g}{\partial p_2 \partial p_n} \\ \vdots & \vdots & \ddots & \vdots \\ \dfrac{\partial^2 g}{\partial p_n \partial p_1} & \dfrac{\partial^2 g}{\partial p_n \partial p_2} & \cdots & \dfrac{\partial^2 g}{\partial p_n^2} \end{bmatrix}, \tag{5.2.17}$$

with $(p_1, p_2, ..., p_n)$ the domain volume fractions. The partial derivatives in the expression of H_g are given by:

$$\begin{aligned} &\frac{\partial g}{\partial p_\alpha} = g_\alpha + kT\left(\log(p_\alpha) + 1\right), \\ &\frac{\partial^2 g}{\partial {p_\alpha}^2} = \frac{kT}{p_\alpha}, \\ &\frac{\partial^2 g}{\partial p_\alpha p_\beta} = 0 \qquad \text{with} \qquad \alpha \neq \beta. \end{aligned} \tag{5.2.18}$$

The Hessian matrix H_g is then:

$$H_g = \begin{bmatrix} \dfrac{kT}{p_1} & 0 & \cdots & 0 \\ 0 & \dfrac{kT}{p_2} & \cdots & 0 \\ \vdots & \vdots & \ddots & \vdots \\ 0 & 0 & \cdots & \dfrac{kT}{p_n} \end{bmatrix}, \tag{5.2.19}$$

with positive eigenvalues, such that H_g is positive definite, and as a consequence, the Gibbs free energy g is a convex function. To evaluate the domain volume fractions that correspond to a minimum of (5.2.15), the Karush-Kuhn-Tucker (KKT) conditions need to be satisfied:

Karush-Kuhn-Tucker conditions

Consider the minimization problem given by Herskovits [1998]:

$$\begin{aligned} \min \quad & f(x) \\ \text{s.t.} \quad & g(x) \leq 0, \\ & h(x) = 0 \end{aligned}$$

with $f : {R_e}^n \to R_e$ a real valued function. The function $g(x)$ defines an inequality constraint and $h(x)$ an equality restriction. x^* is a local minimum if it satisfies the Karush-Kuhn-Tucker conditions Ali et al. [1997]

$$\begin{aligned} & \frac{\partial \mathscr{L}(x^*)}{\partial x} = 0 \qquad \text{with} \qquad \mathscr{L}(x,\mu,\lambda) = f(x) + \mu\, g(x) + \lambda\, h(x) \\ & h(x^*) = 0 \\ & \mu\, g(x^*) = 0 \qquad \text{with} \qquad \mu \geq 0 \\ & g(x^*) \leq 0 \end{aligned}$$

$\mathscr{L}$ is the Lagrangean, and μ and λ the Lagrange multipliers.

The KKT conditions applied to (5.2.15) are:

$$\frac{\partial \mathscr{L}}{\partial p_\alpha} = 0 \qquad \text{with} \qquad \mathscr{L} = g + \lambda \left[\left(\sum_{\alpha=1}^{n} p_\alpha \right) - 1 \right] + \sum_{\alpha=1}^{n} \left[\mu_1^\alpha \left(p_\alpha - 1 \right) - \mu_2^\alpha \left(p_\alpha \right) \right] \tag{5.2.20a}$$

$$\left(\sum_{\alpha=1}^{n} p_\alpha \right) - 1 = 0 \tag{5.2.20b}$$

$$\mu_1^\alpha \left(p_\alpha - 1 \right) = 0 \qquad \text{with} \qquad \mu_1^\alpha \geq 0 \tag{5.2.20c}$$

$$\mu_2^\alpha \, p_\alpha = 0 \qquad \text{with} \qquad \mu_2^\alpha \geq 0 \tag{5.2.20d}$$

$$0 \leq p_\alpha \leq 1, \tag{5.2.20e}$$

with $\mathscr{L}$ the Lagrangean, and μ_1^α, μ_2^α and λ Lagrange multipliers. The KKT conditions (5.2.20c) and (5.2.20d) will be satisfied when $\mu_1^\alpha = \mu_2^\alpha = 0$.

The first condition (5.2.20a) gives:

$$\begin{aligned} \frac{\partial \mathscr{L}}{\partial p_\alpha} &= g_\alpha + kT\log(p_\alpha) + kT + \lambda = 0 \\ p_\alpha &= \exp\left[\frac{1}{kT}(-g_\alpha - \lambda) - 1\right]. \end{aligned} \tag{5.2.21}$$

Combining (5.2.21) and (5.2.20b) gives:

$$\begin{aligned} &\left(\sum_{\alpha=1}^{n} \exp\left[\frac{1}{kT}(-g_\alpha - \lambda) - 1\right]\right) - 1 = 0 \\ &\exp\left(\frac{-\lambda}{kT} - 1\right)\left(\sum_{\alpha=1}^{n} \exp\left(-\frac{g_\alpha}{kT}\right)\right) = 1 \\ &\lambda = -kT\log\left(\frac{1}{\sum_{\alpha=1}^{n} \exp\left(-\frac{g_\alpha}{kT}\right)}\right) - kT. \end{aligned} \tag{5.2.22}$$

Inserting (5.2.22) into (5.2.21), the domain volume fractions can be evaluated by:

$$p_\alpha = \frac{\exp\left(\frac{-g_\alpha}{kT}\right)}{\sum_{\alpha=1}^{n} \exp\left(-\frac{g_\alpha}{kT}\right)}. \tag{5.2.23}$$

Therefore, the minimization of the Gibbs free energy yields to a Boltzmann distribution. A different analysis that yields the same result is presented in Tan and Kochmann [2017]. The parameters k and T are approximated to the multiscale modeling parameter A_s by:

$$A_s \approx \frac{1}{kT}. \tag{5.2.24}$$

The material parameter A_s can be identified from stress-free anhysteretic measurements, and is evaluated by Daniel et al. [2008]:

$$A_s = \frac{3\chi_0}{\mu_0 M_s^2}, \tag{5.2.25}$$

with χ_0 the initial susceptibility and M_s the saturation magnetization.

5.2.3 Irreversible behavior

To characterize the irreversible behavior, it is necessary to define the dissipation function $\phi_d(\dot{p_\alpha})$ in terms of the rate of the internal variables, here the domain volume fractions. The dissipation $\phi_d(\dot{p_\alpha})$ is proposed as:

$$\phi_d = \sum_\alpha |\kappa_\alpha \, \dot{p_\alpha}|, \tag{5.2.26}$$

with κ_α a pinning parameter and $|\,.\,|$ is the absolute value function. For numerical implementation purposes, the time-derivative of the domain volume fraction $\dot{p_\alpha}$ is approximated by:

$$\dot{p_\alpha} = \frac{p_\alpha^{n+1} - p_\alpha^n}{\Delta t}, \tag{5.2.27}$$

with p_α^{n+1} and p_α^n the current and the previous values of the domain volume fraction. The derivative of the dissipation function can be approximated as follows:

$$\frac{\partial \phi_d}{\partial \dot{p_\alpha}} \approx \frac{\partial \phi_d}{\partial \left(\dfrac{p_\alpha^{n+1} - p_\alpha^n}{\Delta t} \right)} = \Delta t \, \frac{\partial \phi_d}{\partial p_\alpha^{n+1}}. \tag{5.2.28}$$

Taking into account the previous approximation into (5.2.7), the following relationship can be defined:

$$\begin{aligned} &\frac{\partial \phi_d}{\partial \dot{p_\alpha}} + \frac{\partial g}{\partial p_\alpha^{n+1}} \approx \frac{\partial}{\partial p_\alpha^{n+1}} \left(g(\sigma, \vec{H}, p_\alpha^{n+1}) + \Delta t \; \phi_d(p_\alpha^{n+1}) \right) = 0 \\ &\frac{\partial \Omega}{\partial p_\alpha^{n+1}} = 0 \qquad \text{with} \qquad \Omega = g(\sigma, \vec{H}, p_\alpha^{n+1}) + \Delta t \; \phi_d(p_\alpha^{n+1}), \end{aligned} \tag{5.2.29}$$

Ω is the objective function to be minimized. The magneto-elastic hysteresis model is evaluated by the constrained minimization:

$$\begin{aligned} \min_{p_\alpha} \quad & \Omega = \sum_{\alpha=1}^{n} p_\alpha^{n+1} \left[g_\alpha + \frac{1}{A_s} \log p_\alpha^{n+1} \right] + \sum_{\alpha=1}^{n} |\kappa_\alpha \left(p_\alpha^{n+1} - p_\alpha^n \right)| \\ \text{s.t.} \quad & \left(\sum_{\alpha=1}^{n} p_\alpha^{n+1} \right) - 1 = 0, \\ & 0 \le p_\alpha^{n+1} \le 1 \end{aligned} \tag{5.2.30}$$

The numerical implementation of the hysteresis model is detailed in Appendix F using the interior points method.

Considering a stress-free case and applied uniaxial magnetic field along the $[1\ 0\ 0]^t$ direction, the pinning parameter κ_α can be identified from the domain magnetic energy at the coercive field. The pinning energy is given by:

$$\kappa_\alpha = -\mu_0 H_c\, \vec{h} \cdot \vec{M}_\alpha \qquad \text{with} \qquad \vec{h} = [1\ 0\ 0]^t, \tag{5.2.31}$$

with H_c the coercive field and $\vec{h}$ the unit vector that defines the direction of $\vec{H}$. Therefore, each domain orientation will have a different pinning energy. To illustrate the modeling approach, consider a single crystal consisting of six domain orientations along the $< 100 >$ directions, with parameters given in Table 5.2.1. The stress-free magnetic response under a variable magnetic field is presented in Fig. 5.2.1.

Tabela 5.2.1: Parameters of the example.

M_s (A/m)	λ_s (ppm)	A_s (m^3/J)	H_c (A/m)
$1.39\,10^6$	5.5	$1.4\,10^{-2}$	200

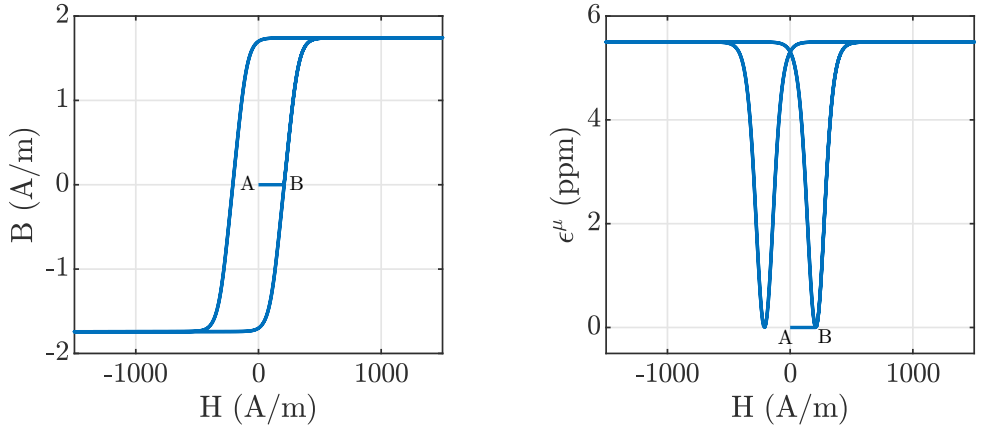

Figura 5.2.1: Stress-free hysteresis loop (left) and magnetostriction strain (right) considering six domain orientations. $M_s = 1$

The hysteretic induction and magnetostriction strain can be explained from the domain volume fractions evolution, as seen in Fig. 5.2.2. The volume fractions remain unchanged until the applied field reaches the coercive field H_c (see the A-B segment in Fig. 5.2.2). As H_c is reached, the domain family oriented in the direction of the increasing field grows, and the

other domain families vanish, following the modeling constraints (5.2.2). As seen in Fig. 5.2.1, $\vec{B}$ varies, but little, and ε^{μ} remain constant along the segment path A-B and then vary with $\vec{H}$ variations.

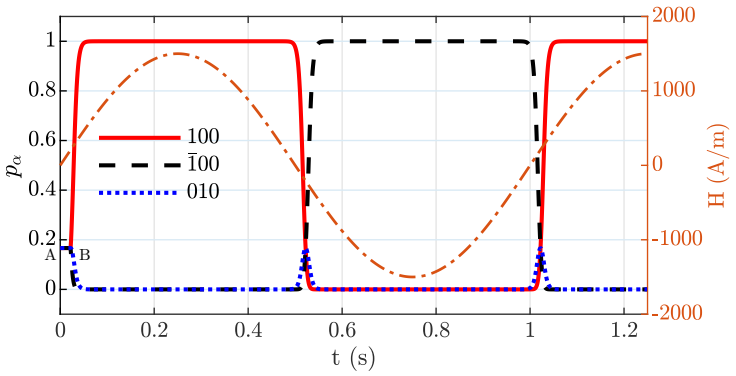

Figura 5.2.2: Domain volume fractions evolution under a magnetic loading.

As observed in Fig. 5.2.1, considering a single pinning energy for each domain orientation does not allow modeling the first magnetization curve and minor loops. Using the same strategy as in the vector-play model, several coercive fields can be considered to characterize pinning energies for each domain orientation. These pinning parameters κ^k are distinguished by the weights ω^k that verify:

$$\sum_{k=1}^{N} \omega^k = 1, \tag{5.2.32}$$

with N the total number of coercive fields. For this situation with several pinning parameters, the magnetostriction strain ε^{μ} and magnetization $\vec{M}$ are given by:

$$\varepsilon^{\mu} = \sum_{k=1}^{N} \omega^k \sum_{g} p_g \left[\sum_{\alpha} p_{\alpha}^k \varepsilon_{\alpha}^{\mu} \right] \qquad \text{and} \qquad \vec{M} = \sum_{k=1}^{N} \omega^k \sum_{g} p_g \left[\sum_{\alpha} p_{\alpha}^k \vec{M}_{\alpha} \right]. \tag{5.2.33}$$

5.2.4 Anhysteretic test

The magnetic anhysteretic curve can be experimentally obtained by setting the magnetic field waveform as an exponentially decaying sine superimposed to a bias field, as presented in Chapter 3. The model can reproduce the magnetic anhysteretic response using the strategy of several pinning energies. Fig. 5.2.3 (markers) illustrates the reversible behavior under static stresses obtained by the model. The solid lines consist of the results of the anhysteretic multiscale model. As expected, both models present the same magnetic anhysteretic response.

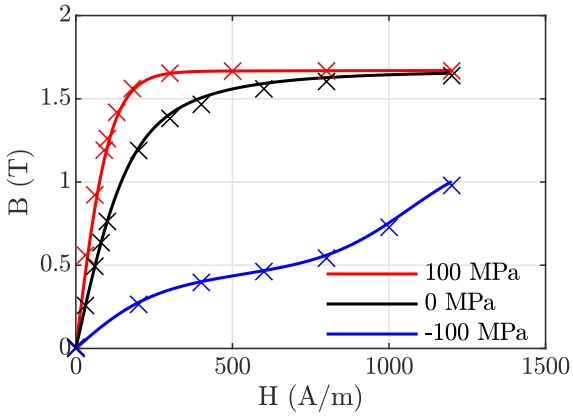

Figura 5.2.3: Anhysteretic test under variable field and static stress.

The anhysteretic test can also be performed under variations of mechanical loading and a static field. As an example, a uniaxial stress waveform is defined as an exponentially decaying sine superimposed to a bias stress and the magnetic field is static. The resulting anhysteretic piezomagnetic curves are shown in Fig. 5.2.4, and again, the anhysteretic test (illustrated by the markers) gives the same results as using the multiscale model (the solid lines).

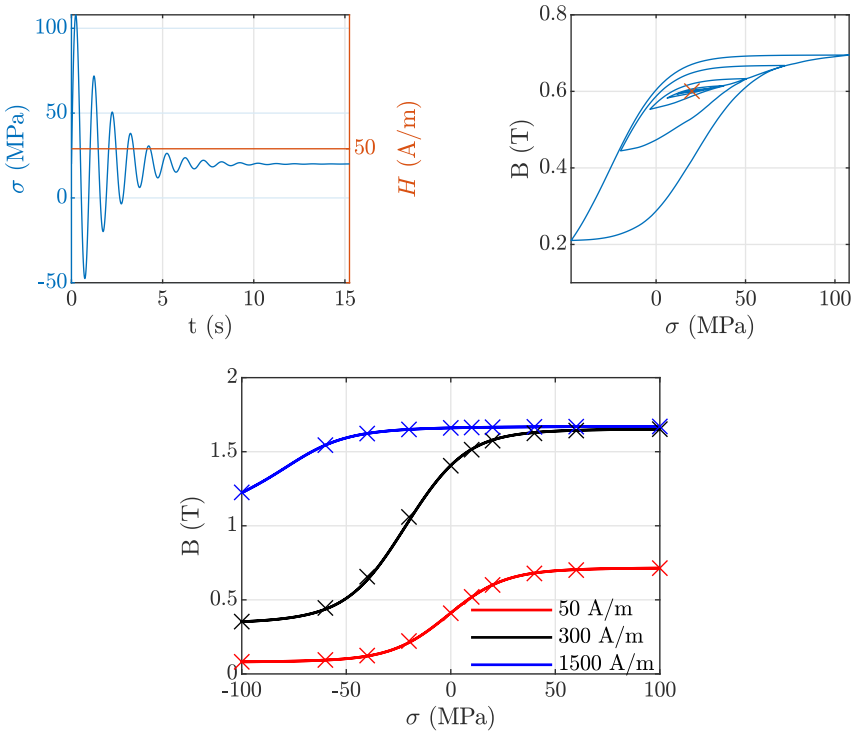

Figura 5.2.4: Anhysteretic test under variable stress and static field.

5.2.5 Identification of parameters

The number of domain orientations is limited to six for numerical implementation purposes, corresponding to the $< 100 >$ directions. Moreover, the crystallographic orientations are described by the texture of a $< 111 >$ fiber, as depicted in Fig. 5.1.2. The single crystal parameters are taken from pure iron. The parameters M_s and λ_{100} are adapted to the modeling results to match the stress-free hysteresis measurements. The reversible parameters are listed in Table 5.2.2.

Tabela 5.2.2: Single crystal parameters.

M_s (A/m)	λ_{100} (ppm)	λ_{111} (ppm)
$1.39\,10^6$	14	-14

Considering a uniaxial stress-free case, the pinning energies κ^k are evaluated from (5.2.31), based on a set of coercive fields. The respective weights ω^k can be fitted from measured stress-free hysteresis loops under increasing magnetic field, as depicted in Fig. 5.2.5 (left). Table 5.2.3 gives the fitted weights from a set of stress-free coercive fields.

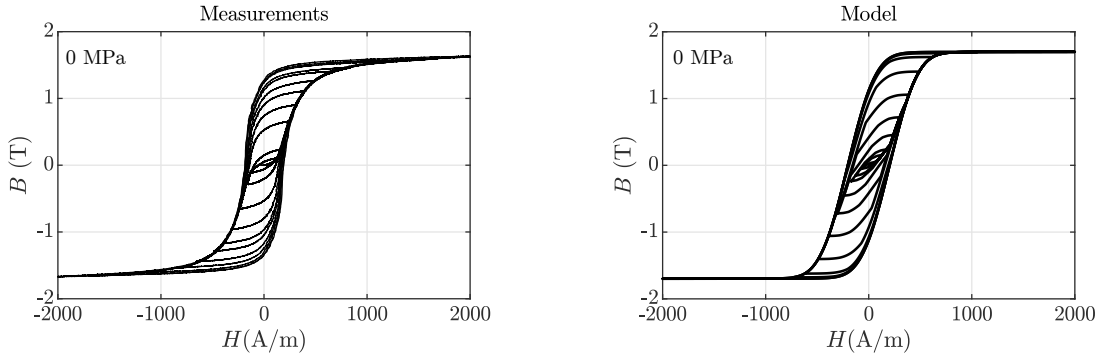

Figura 5.2.5: Stress-free hysteresis loops under increasing magnetic field. Comparison between measurements (left) and model (right).

Tabela 5.2.3: Identified weights from a set of coercive fields.

H_c (A/m)	0	25	50	100	200	350
ω	0.05	0.05	0.1	0.1	0.45	0.25

From this set of coercive fields, the pinning parameters κ_α are identified from the magnetic energy at the domain scale. The same proposition previously used in the vector-play

model is utilized here to model the mechanical loading influence in the pinning parameter κ_α. From the identified pinning parameter from stress-free measurements $\kappa_\alpha(0)$, the weight ω is kept constant under stress. The stress-dependent pinning parameter $\kappa(\sigma)$ is given by:

$$\kappa_\alpha(\sigma) = a(\sigma_{eq})\kappa_\alpha(0) \qquad \text{with} \qquad a(\sigma_{eq}) = \frac{H_c(\sigma)}{H_c(0)}, \tag{5.2.34}$$

with $a(\sigma_{eq})$ a function that is fitted in order to match with the measured $H_c(\sigma)/H_c(0)$. As presented in Chapter 4, the coercive field characteristic $a(\sigma_{eq})$ is described by:

$$a(\sigma_{eq}) = a_1 \exp\left(-\exp(a_2 + a_3\sigma_{eq})\right) + 1. \tag{5.2.35}$$

5.2.6 Modeling results compared to the measurements

By using the strategy of several pinning parameters, the model reproduces the stress-free symmetric minor loops under increasing magnetic field, as shown in Fig. 5.2.5 (right). The modeling results under static uniaxial stress and quasi-static magnetic field are presented in Fig. 5.2.6. Despite the model captures the increasing of losses under compression, the shape of the hysteresis loop in this mechanical configuration results in a difference of about 24% in evaluating the losses.

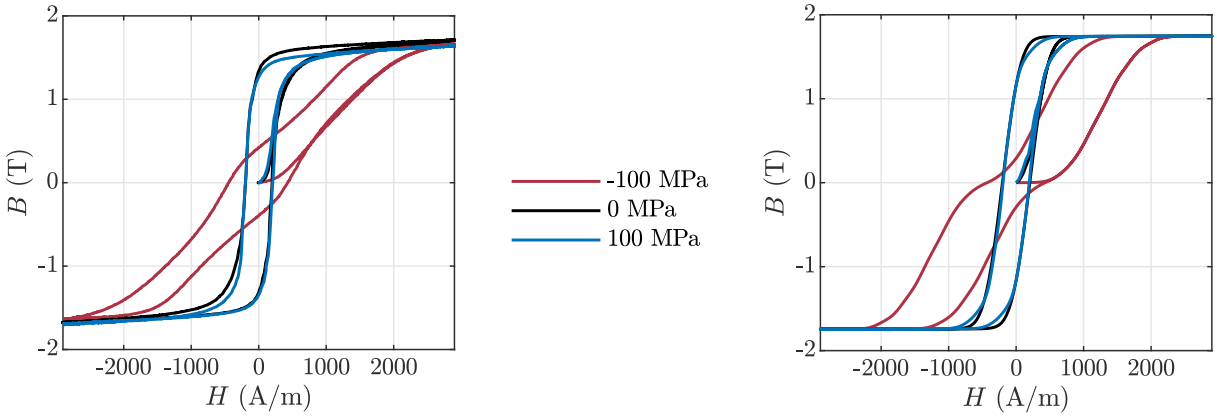

Figura 5.2.6: Comparison between measured (left) and modeled (right) hysteresis loops under uniaxial stress.

The longitudinal magnetostriction strain is presented in Fig. 5.2.7, and it is noted that the model captures the measured trend under static uniaxial stress. Notably, the model also simulates the inversion on the sign of the longitudinal magnetostriction under high tension.

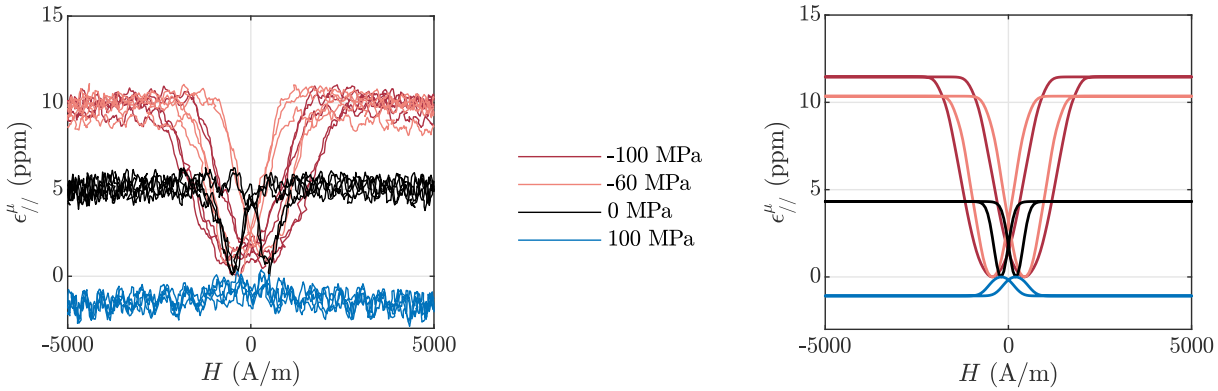

Figura 5.2.7: Comparison between measured (left) and modeled (right) magnetostriction strain under uniaxial stress.

Considering a variable mechanical loading and a static magnetic field, the modeled piezomagnetic loops are depicted in Fig. 5.2.8. A characteristic of the domain volume fraction approach can be highlighted: the model reproduces the piezomagnetic loops from the same set of parameters identified in the case of static stress and variable magnetic field.

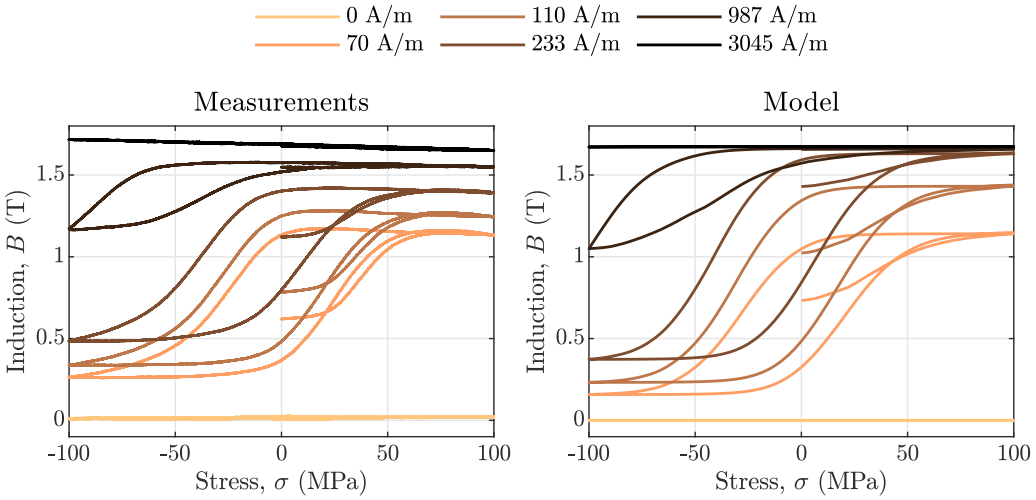

Figura 5.2.8: Comparison between measured (left) and modeled (right) piezomagnetic loops.

Considering that both the magnetic field and stress are variable, the model also reproduces the characteristic of the induction as a function of magnetic field and stress 5.2.9. However, significant differences are observed, especially under high compression, where the modeled induction tends to zero. In this situation where both field and stress vary, the total dissipation can be either evaluated from the sum of the numerical integration of the $\varepsilon^{\mu}(\sigma)$ and $B(H)$ loops, or from the dissipation function (5.2.26).

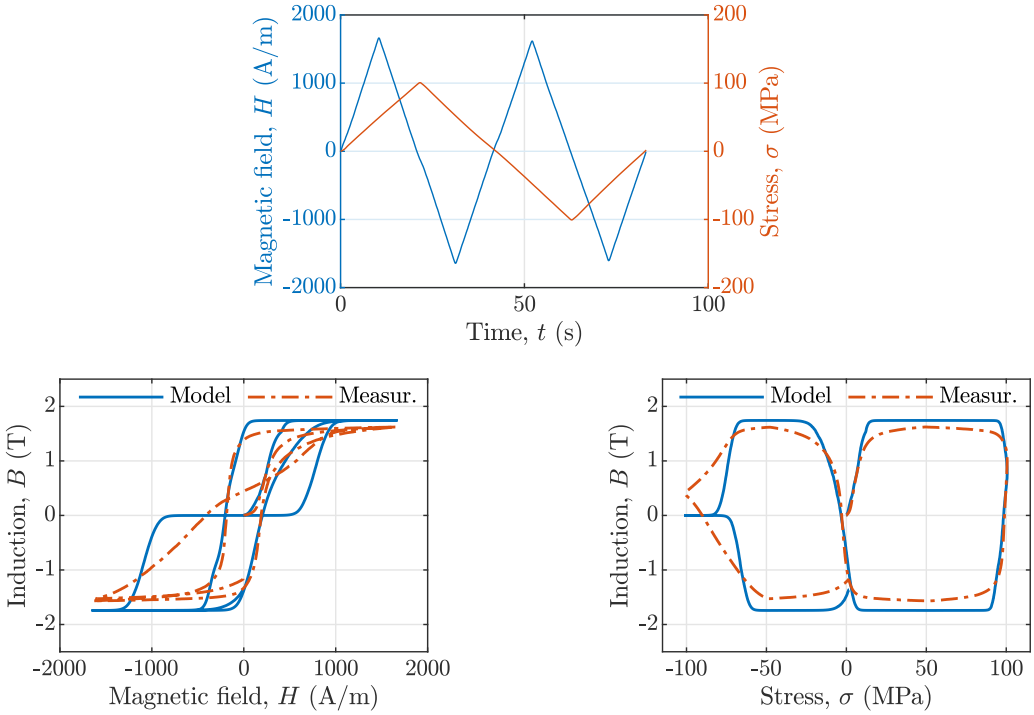

Figura 5.2.9: Magneto-mechanical loading (top) and comparison between measured and modeled induction as a function of magnetic field (bottom left) and mechanical stress (bottom right).

5.2.7 Discussions on the model

In Section 5.1, limitations of the model with irreversible stress were presented when applying a sequential magneto-elastic loading. For simplicity, consider the domain volume fraction approach with a single pinning energy for each domain orientation (with $H_c = 200$ A/m) under the application of a sequential uniaxial magneto-elastic loading shown in Fig. 5.2.10. Fig. 5.2.11 presents the modeled magnetic response. It can be noted that the modeled induction and magnetostriction strain do not present discontinuities when the loadings stop varying. Therefore, the domain volume fraction approach improves the physical modeling description compared to the modeling presented in Section 5.1.

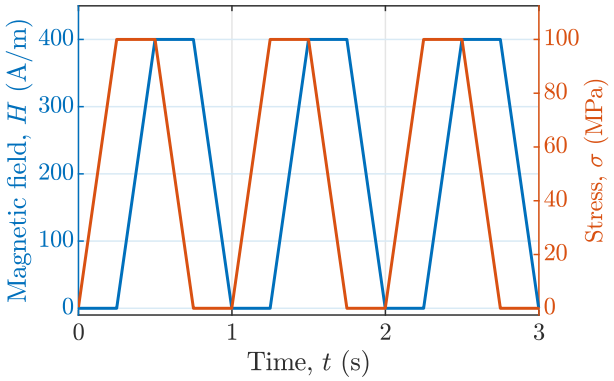

Figura 5.2.10: Uniaxial magneto-elastic loading.

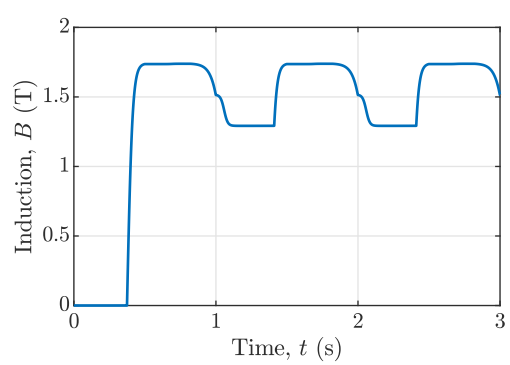

(a) Induction

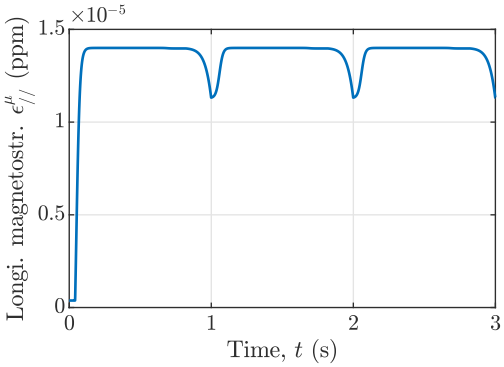

(b) Longitudinal magnetostriction strain

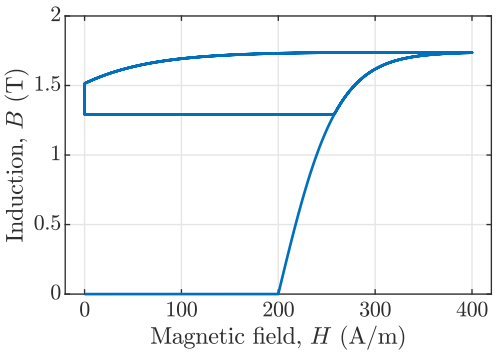

(c) Induction hysteresis loop under field variations

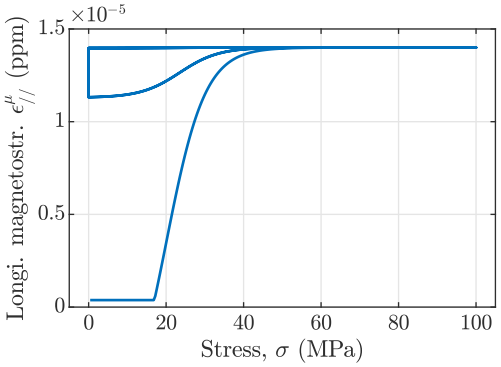

(d) Magnetostriction hysteresis under stress variations

Figura 5.2.11: Modeled magnetic response.

One might ask if the pinning energy can be identified from magnetostriction strain measurements under variable stress. In this case, a coercive stress σ_c defines the pinning energy at the domain scale. Considering a uniaxial example with $\sigma_c = 20$ MPa, the pinning energy is evaluated by:

$$\kappa_\alpha = -\sigma_c \, \boldsymbol{\sigma}_{uni} : \boldsymbol{\varepsilon}^{\mu}_{\alpha} \qquad \text{with} \qquad \boldsymbol{\sigma}_{uni} = [1\,0\,0\,0\,0\,0], \tag{5.2.36}$$

with σ_{uni} the second-order tensor that defines the stress direction in Voigt notation. Under variations of magnetic field and static stress, the resulting hysteresis behavior is depicted in Fig. 5.2.12b. For this case, the domain volume fractions evolution is represented in Fig. 5.2.12a. Constraints (5.2.2) are fulfilled, but it is observed that the volume fractions parallel to the applied field change first. Subsequently, the volume fractions perpendicular to the applied field are changed. This difference in the thresholds results in a modeled hysteresis behavior with stair shape, especially in the region of low magnetic fields, as seen in Fig. 5.2.12b.

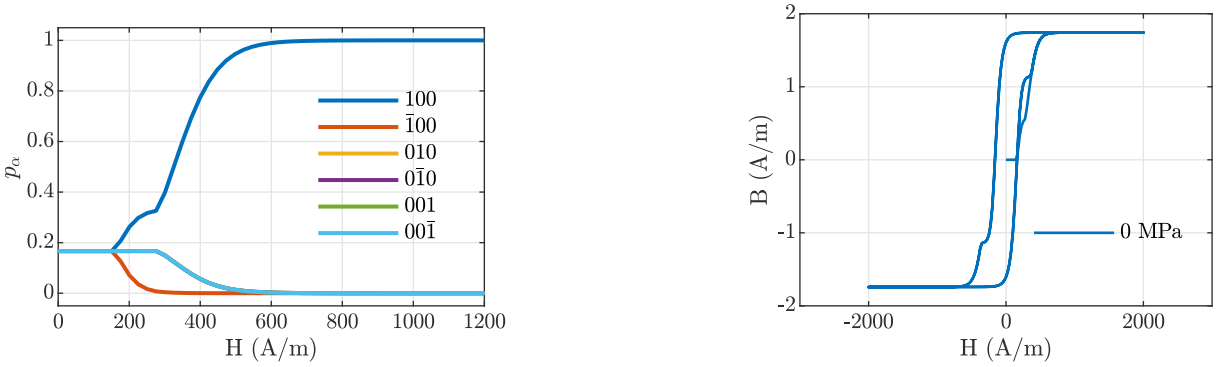

(a) Domain volume fractions evolution (b) Hysteresis behavior

Figura 5.2.12: Modeled magnetic response under static stress and variable field.

If variable stress and a static field are applied now, the previous threshold problem is no longer observed. The domain volume fractions evolve when the stress reaches $\kappa_\sigma = 20$ MPa, as seen in Fig. 5.2.13a, resulting in the piezomagnetic loop depicted in Fig. 5.2.13b. A proper definition of the pinning energy in terms of both coercive field and coercive stress could replace the empirical description given by (5.2.34), such that the model would require only stress-free measurements (under varying field) and field-free tests (under varying stress) for parameter identification.

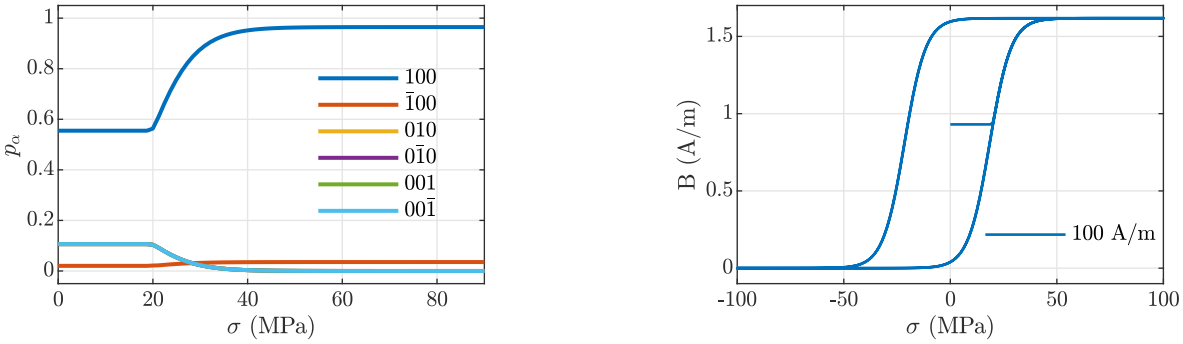

(a) Domain volume fractions evolution (b) Piezomagnetic behavior

Figura 5.2.13: Modeled magnetic response under static field and variable stress.

Another problem of the domain volume fraction approach implemented in this section is the limitation to only six domain orientations - related to the easy axis for a cubic symmetry. Due to the minimization numerical routine of the model, increasing the number of domain orientations can yield prohibitive simulation time. For instance, Fig. 5.2.14 illustrates the stress-free magnetic hysteresis behavior considering 652 possible domain orientations. The simulation time increases about 800 times compared to the approach with only six possible domain orientations. However, by limiting the model to only the easy axis orientations, significant effects, such as anisotropy, are not captured in the simulation. Attempts were made to produce an explicit model for this domain volume fraction approach - based mainly on the vector-play approximation presented in Chapter 4. However, the need to impose the volume fraction constraints makes it difficult to solve the model explicitly.

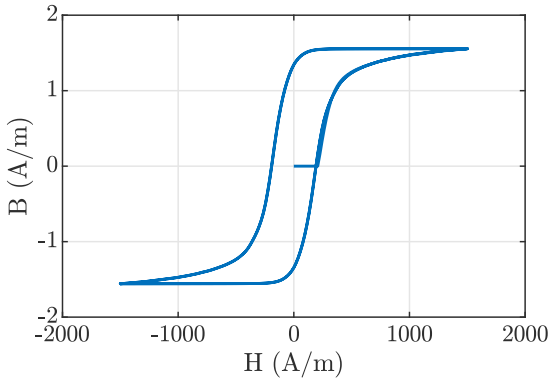

Figura 5.2.14: Stress-free hysteresis loop.

By considering the domain volume fractions as internal variables to describe the magnetic hysteresis behavior, any magneto-elastic loading can be simulated, and the thermodynamic consistency is ensured due to the formulation of the model based on an energetic description. Here, the main goal is to give a route to future works, as the domain volume fraction seems to be an appropriate variable to describe the dissipation under variations of magnetic field and stress. Complementary works are required to improve the approach. One important task will be to increase the number of domain orientations so that anisotropy effects can be described. It may be a challenging task using a minimization approach; therefore, defining an explicit solution to the model, ensuring that the constraints of the domain volume fraction formulation are respected, is an important aspect. Moreover, the pinning energies are identified from a stress-free uniaxial configuration. The impact of this choice in validating the model under rotating fields or stresses needs to be further analyzed.

6 Conclusion

The present thesis deals with the modeling of the hysteretic magneto-elastic behavior of ferromagnetic materials. Experimental characterization of the magneto-elastic behavior is performed in Chapter 3. A uniaxial magneto-mechanical bench is utilized, and tests are carried out on low-Carbon DC04 steel with mechanical loadings below the elastic limit. First, the magnetic response under static stress and varying magnetic loadings is measured. The experimental results show the expected behavior for a material with positive magnetostriction: compression deteriorates the initial permeability, the remanent induction, and the coercive field and increases the hysteresis losses. The application of tension presents a non-monotonic behavior: the initial permeability is increased until a certain stress value and then decreases under further tension.

Experimental tests under varying stress and static fields highlighted another feature of the magneto-mechanical behavior. For low static fields, magnetization increases with stress (increasing from compression to tension). On the contrary, for high static field, magnetization decreases with stress. This change in the magnetization behavior is due to the Villari reversal. In addition, anhysteretic behavior, hysteresis with asymmetric minor loops, and piezomagnetic loops were obtained. The set of experimental data built during this thesis represents a reliable basis for the development and validation of magneto-elastic hysteresis models.

The multiscale nature of the magneto-mechanical behavior is used in an anhysteretic modeling approach, such that the magnetic response of a polycrystal can be simulated, allowing for multiaxial loading conditions. Classical modeling for the hysteresis behavior, such as the Jiles-Atherton and Preisach models, lack thermodynamic consistency and are usually restricted to uniaxial loadings. A promising approach but limited so far in the literature to purely magnetic hysteresis modeling is based on an energy description allowing 3D magnetic field loadings. It uses the analogy of a dry-friction mechanism and can be approximated by a vector-play model under some restrictions.

An extension of the energy-based hysteresis approach to the case when static stress is applied is proposed. An equivalent single-crystal simulates a representative volume element of the material. To describe the magneto-elastic hysteresis behavior, a stress dependence of the pinning field - the quantity that defines the coercive field and, thus, the dissipation - is proposed. The pinning field is defined in terms of an equivalent stress, allowing to capture the influence of a multiaxial stress state on the coercive field. Another feature of the proposed

approach is the use of a second-order development in the definition of the magneto-elastic energy. Such an inclusion allows to capture the non-monotonic stress effect on the magnetic behavior. A new formulation of this second-order magneto-elastic energy is proposed, in terms of an equivalent scalar stress, so that its definition is reduced to only one parameter σ_m. The modeling parameters of the magneto-elastic hysteresis approach can be separated into those related to the anhysteretic behavior and the ones related to the dissipation, and they are all identified from uniaxial measurements along one direction only.

The validation of the modeling is verified by using a different set of measurements than those used for parameter identification. Notably, no additional parameter is required to model asymmetric minor loops in the hysteresis behavior under uniaxial stress when considering a magnetic field waveform with harmonic content. Besides, the model captures the trend of hysteresis losses of DC04 under uniaxial stress. Though the second-order term in the magneto-elastic energy allows the capture of the non-monotonic stress effect on the magnetic behavior. The approach forces the magnetic behavior to be symmetric with respect to σ_m, such that the model underestimates the permeability at low fields under high tension.

The proposed hysteresis model allows multiaxial loadings. The approach is tested under multiaxial stress and alternating field conditions to test the modeling capabilities in complex magneto-elastic cases. In this case, two sets of experimental measurements previously performed at Aalto University on a non-oriented Fe-Si were used: tests under uniaxial loadings along rolling direction only are used to identify the modeling parameters, and measurements under biaxial mechanical loadings are employed for validation. Cases under biaxial stress showed that the model captures the trend of hysteresis losses when the magnetization is along rolling or transverse directions. However, the error in the simulated results increases when magnetization is considered along transverse direction. Main drawbacks are observed under shear stress configurations. It was shown that the modeled anhysteretic behavior is not sensitive to this mechanical loading condition, which seems not compatible with the measurements. The use of stress localization schemes is expected to be a possible solution to this problem. On the other hand, the coercive field trend under shear is captured by modeling. The model is further validated under magneto-elastic loadings for rotating field and multiaxial stress state. A known limitation of the energy-based hysteresis approach is that it does not capture the vanishing of rotating hysteresis losses under high induction. A mathematical modification of the pinning field is applied to correct this drawback, enforcing that the pinning field vanishes when

the magnetization approaches saturation. Applying the measured magnetic field waveform as the input of the model, the model reproduces the hysteresis behavior under several multiaxial stress loadings with satisfying agreement. Therefore, the proposed magneto-elastic hysteresis is predictive in the sense that from parameters identified from uniaxial measurements, it can be applied to several multiaxial loading conditions with reasonable accuracy.

Inspired from the energy-based approach, the hysteresis behavior under static magnetic field and variable stress is modeled through the definition of an irreversible stress. A pinning stress is introduced to control the dissipation under mechanical loadings. This irreversible stress parameter is identified from uniaxial piezomagnetic loop measurements. The model can satisfactorily represent the piezomagnetic behavior under increasing static field. Moreover, the mechanical losses - namely, the magnetostriction strain variation under stress - can be estimated. The proposed energy-based vector-play approach presented in this thesis can represent the hysteresis behavior under static field and variable stress, as well as under static stress and variable field, in multiaxial loading configurations, ensuring thermodynamic consistency.

The model is further applied under a more complex loading configuration with both field and stress variations. A very satisfying agreement was demonstrated between measurements and modeling. However, limitations are noted in this approach: sequential stress and field loadings yield non-physical behavior in the modeled induction and magnetostriction strain. The non-physical behavior is inherent to the proposed approach, in which both induction and magnetostriction are given simultaneously in terms of reversible field and reversible stress.

To fix these limitations, a route for future works is presented in which the dissipative effects are captured through the rate of domain volume fractions. Such an approach is inspired by ferroelectric hysteresis models. The domain volume fraction is a common variable in evaluating both magnetization and magnetostriction and seems to be an adequate internal variable to capture the irreversible behavior for any magneto-elastic loading. A dissipation function based on the rate of volume fractions is proposed. Pinning energies that act as threshold for the evolution of the volume fractions are introduced. The pinning energies are directly related to the coercive field and are identified from stress-free hysteresis measurements. Moreover, no further parameter is necessary to model the piezomagnetic loops and the hysteresis behavior under variations of both field and stress. The approach is thermodynamically consistent for any magneto-mechanical loading. However, limitations in capturing the measured results are observed and attributed to the small number of domain orientations considered in the model. Ideas

to improve the domain volume fraction approach are suggested:

- **Propose an explicit solution for the domain volume fractions approach**

  The domain orientations are usually determined by minimizing the potential energy at the domain scale Daniel et al. [2008]. In Daniel and Galopin [2008], a dense meshed unit sphere is introduced with nodes corresponding to the possible domain orientations to avoid numerical minimization. This proposition significantly reduces the anhysteretic simulation time.

  In the presented hysteresis approach given in terms of the rate of domain volume fractions, only six domain orientations corresponding to the easy axis of cubic symmetry were considered. This choice reduces the predictive capabilities of the model. The minimization evaluation of the hysteresis model makes the simulation of a polycrystal impractical with a great number of domain orientations as given by the nodes of a dense meshed unit sphere. An explicit scheme in the implementation of the model would be very beneficial to avoid minimization ensuring that the volume fractions constraints are respected.

- **Investigate the influence of coercive stress in the pinning energy**

  The pinning energy was identified from stress-free measurements using the coercive field. If the field-free magnetostriction loop under variable stress was available, the pinning energy could be identified from the coercive stress. However, simulations showed that the model presents limitations in representing the hysteresis behavior when the pinning energy is identified from the coercive stress. The relationship between coercive stress and coercive field in defining the pinning energy must be clarified. It could be a route to avoid the phenomenological description of the stress-dependent pinning energy, as shown in Chapter 5.

Next steps regarding the magneto-elastic vector-play model are also suggested:

- **Magnetic measurements of a giant magnetostrictive material**

  The low magnetostriction strain of the tested material (DC04) did not allow the validation of the modeled magnetostriction under variations of mechanical loadings. Due to this limitation, the pinning stress was identified from piezomagnetic loops. To validate the modeled magnetostriction strain and to analyze the pinning stress parameter identification, measuring the hysteresis magnetostriction of giant magnetostrictive materials,

such as Galfenol, under several static field levels is suggested. Moreover, when both field and stress vary, the magnetostriction strain response could also be used for modeling validation.

- **Simulation of an electrical machine**

  The proposed models could be used to simulate the magnetic behavior of an electrical machine to analyze the impact of the magneto-mechanical coupling in losses, compared to classical approaches usually performed in the machinery literature. This requires the magneto-elastic vector-play approach to be numerically inverted to properly plug the model into a vector potential finite element formulation. The numerical inversion of the stress-free energy-based hysteresis model is presented in Jacques [2018], while the inversion of the anhysteretic multiscale approach is proposed in Bernard et al. [2019]. Combining both procedures can lead to a magneto-elastic hysteresis model with input magnetostriction strain and induction and outputs magnetic field and stress.

- **Influence of plasticity on the magnetic hysteresis**

  In this thesis, mechanical loadings were considered below the elastic limit. However, plasticity effects induced by manufacturing or assembly processes can significantly modify the magnetic characteristic of magnetic materials and increase hysteresis losses Domenjoud and Daniel [2023], El Youssef et al. [2021], Maazaz et al. [2024]. Modifications in anhysteretic multiscale modeling to consider the influence of plasticity are proposed in Domenjoud and Daniel [2023], Taurines et al. [2024]. Incorporating such extensions in the vector-play approach is a promising prospect.

Bibliography

K. Ali, K. Atallah, and D. Howe. Prediction of mechanical stress effects on the iron loss in electrical machines. *Journal of Applied Physics*, 81(8):4119–4121, 1997.

C. Appino, E. Ferrara, F. Fiorillo, C. Ragusa, and O. de la Barrière. Static and dynamic energy losses along different directions in go steel sheets. *Journal of Magnetism and Magnetic Materials*, 500:166281, 2020.

ArcelorMittal. DC04 datasheet. URL https://www.matweb.com/search/datasheet.aspx?matguid=a3b0be2743384d968c215913322c22c2&ckck=1, 1996.

W. D. Armstrong. An incremental theory of magneto-elastic hysteresis in pseudo-cubic ferromagnetostrictive alloys. *Journal of Magnetism and Magnetic Materials*, 263(1):208–218, 2003. ISSN 0304-8853. doi: https://doi.org/10.1016/S0304-8853(02)01567-6.

U. Aydin, P. Rasilo, F. Martin, D. Singh, L. Daniel, A. Belahcen, M. Rekik, O. Hubert, R. Kouhia, and A. Arkkio. Magneto-mechanical modeling of electrical steel sheets. *Journal of Magnetism and Magnetic Materials*, 439:82–90, 2017.

U. Aydin, F. Martin, P. Rasilo, A. Belahcen, A. Haavisto, D. Singh, L. Daniel, and A. Arkkio. Rotational single sheet tester for multiaxial magneto-mechanical effects in steel sheets. *IEEE Transactions on Magnetics*, 55(3):1–10, 2019a.

U. Aydin, P. Rasilo, F. Martin, A. Belahcen, L. Daniel, A. Haavisto, and A. Arkkio. Effect of multi-axial stress on iron losses of electrical steel sheets. *Journal of Magnetism and Magnetic Materials*, 469:19–27, 2019b. ISSN 0304-8853. doi: https://doi.org/10.1016/j.jmmm.2018.08.003.

F. Bachmann, R. Hielscher, and H. Schaeben. Texture analysis with MTEX–free and open source software toolbox. *Solid state phenomena*, 160:63–68, 2010.

N. Banu, E. Ferrara, M. Pasquale, F. Fiorillo, O. De la Barrière, D. Brunt, A. Wilson, and S. Harmon. Temperature and frequency dependence of magnetic losses in fe-co. *IEEE Access*, 2023.

J. P. A. Bastos and N. Sadowski. *Electromagnetic modeling by finite element methods*. CRC press, 2003.

A. Benabou, J. V. Leite, S. Clenet, C. Simão, and N. Sadowski. Minor loops modelling with a modified Jiles–Atherton model and comparison with the Preisach model. *Journal of Magnetism and Magnetic Materials*, 320(20):e1034–e1038, 2008.

A. Bergqvist. A simple vector generalization of the jiles-atherton model of hysteresis. *IEEE Transactions on Magnetics*, 32(5):4213–4215, 1996.

A. Bergqvist. Magnetic vector hysteresis model with dry friction-like pinning. *Physica B: Condensed Matter*, 233(4):342–347, 1997.

A. Bergqvist and G. Engdahl. A stress-dependent magnetic Preisach hysteresis model. *IEEE Transactions on Magnetics*, 27(6):4796–4798, 1991. doi: 10.1109/20.278950.

L. Bernard and L. Daniel. Effect of stress on magnetic hysteresis losses in a switched reluctance motor: Application to stator and rotor shrink fitting. *IEEE Transactions on Magnetics*, 51(9): 1–13, 2015. doi: 10.1109/TMAG.2015.2435701.

L. Bernard, B. J. Mailhé, N. Sadowski, N. J. Batistela, and L. Daniel. Multiscale approaches for magneto-elasticity in device simulation. *Journal of Magnetism and Magnetic Materials*, 487:1–13, 2019. ISSN 0304-8853. doi: https://doi.org/10.1016/j.jmmm.2019.04.093. Art. no. 165241.

L. Bernard, B. J. Mailhé, S. L. Ávila, L. Daniel, N. J. Batistela, and N. Sadowski. Magnetic hysteresis under compressive stress: A multiscale Jiles–Atherton approach. *IEEE Transactions on Magnetics*, 56(2):1–4, 2020. doi: 10.1109/TMAG.2019.2946115.

S. Bobbio, G. Milano, C. Serpico, and C. Visone. Models of magnetic hysteresis based on play and stop hysterons. *IEEE Transactions on Magnetics*, 33(6):4417–4426, 1997.

G. Bolshakov and A. Lapovok. A Preisach model for magnetoelastic hysteresis. *Journal of Magnetism and Magnetic Materials*, 162(1):112–116, 1996. ISSN 0304-8853. doi: https://doi.org/10.1016/0304-8853(96)00073-X.

S. Bouterfas, Y. Le Bihan, L. Santandrea, and L. Daniel. Mechanical stress identification method in anisotropic ferromagnetic materials using eddy current testing. *IEEE Transactions on Magnetics*, 59(5):1–4, 2023.

S. P. Boyd and L. Vandenberghe. *Convex optimization*. Cambridge University Press, 2004.

N. Buiron, L. Hirsinger, and R. Billardon. A multiscale model for magneto-elastic couplings. *Le Journal de Physique IV*, 09(PR9):187–196, 1999. doi: 10.1051/jp4:1999919.

H.-J. Bunge. *Texture analysis in materials science: mathematical methods*. Elsevier, 2013.

S. Chikazumi. *Physics of ferromagnetism*. Number 94. Oxford University Press, 1997.

G. Consolo, G. Finocchio, M. Carpentieri, E. Cardelli, and B. Azzerboni. About identification of scalar Preisach functions of soft magnetic materials. *IEEE Transactions on Magnetics*, 42 (4):923–926, 2006.

B. D. Cullity and C. D. Graham. *Introduction to Magnetic Materials*. Wiley, New Jersey, 2009.

L. G. da Silva, A. Abderahmane, M. Domenjoud, L. Bernard, and L. Daniel. An extension of the vector-play model to the case of magneto-elastic loadings. *IEEE Access*, 10:126674–126686, 2022. doi: 10.1109/ACCESS.2022.3222833.

L. G. da Silva, L. Bernard, F. Martin, A. Belahcen, and L. Daniel. Multiaxial validation of a magneto-elastic vector-play model. *IEEE Transactions on Magnetics*, 59(11):1–10, 2023. doi: 10.1109/TMAG.2023.3309154.

L. Daniel. *Modélisation multi-échelle du comportement magnéto-mécanique des matériaux ferromagnétiques texturés*. PhD thesis, École normale supérieure de Cachan-ENS Cachan, 2003.

L. Daniel. An analytical model for the magnetostriction strain of ferromagnetic materials subjected to multiaxial stress. *The European Physical Journal Applied Physics*, 83(3):1–6, 2018. Art. no. 30904.

L. Daniel and N. Galopin. A constitutive law for magnetostrictive materials and its application to terfenol-d single and polycrystals. *The European Physical Journal-Applied Physics*, 42 (2):153–159, 2008.

L. Daniel and O. Hubert. An equivalent stress for the influence of multiaxial stress on the magnetic behavior. *Journal of Applied Physics*, 105(7):1 – 3, 2009. Art. no. 07A313.

L. Daniel, O. Hubert, N. Buiron, and R. Billardon. Reversible magneto-elastic behavior: A multiscale approach. *Journal of the Mechanics and Physics of Solids*, 56(3):1018–1042, 2008. ISSN 0022-5096. doi: https://doi.org/10.1016/j.jmps.2007.06.003.

L. Daniel, M. Rekik, and O. Hubert. A multiscale model for magneto-elastic behaviour including hysteresis effects. *Archive of Applied Mechanics*, 84(9):1307–1323, 2014.

L. Daniel, O. Hubert, and M. Rekik. A simplified 3-D constitutive law for magnetomechanical behavior. *IEEE Transactions on Magnetics*, 51(3):1–4, 2015. doi: 10.1109/TMAG.2014.2361643.

L. Daniel, B. Ducharne, Y. Liu, and G. Sebald. Choosing the best magnetostrictive material for energy harvesting applications: A simple criterion based on Ericsson cycles. *Journal of Magnetism and Magnetic Materials*, 587:171281, 2023.

L. Daniel. An analytical model for the effect of multiaxial stress on the magnetic susceptibility of ferromagnetic materials. *IEEE Transactions on Magnetics*, 49(5):2037–2040, 2013. doi: 10.1109/TMAG.2013.2239264.

M. J. Dapino. On magnetostrictive materials and their use in adaptive structures. *Structural Engineering and Mechanics*, 17(3-4):303–330, 2004.

O. de La Barrière, C. Appino, F. Fiorillo, C. Ragusa, M. Lécrivain, L. Rocchino, H. B. Ahmed, M. Gabsi, F. Mazaleyrat, and M. Lobue. Extended frequency analysis of the loss under rotating induction excitation in soft magnetic composites (smc). *Journal of Applied Physics*, 111(7), 2012.

E. D. T. De Lacheisserie. *Magnetostriction Theory and applications of magnetoelasticity*. CRC press, 1993.

E. Della Torre, E. Pinzaglia, and E. Cardelli. Vector modeling—part i: Generalized hysteresis model. *Physica B: Condensed Matter*, 372(1-2):111–114, 2006.

M. B. d. S. Dias and F. J. G. Landgraf. Compressive stress effects on magnetic properties of uncoated grain oriented electrical steel. *Journal of Magnetism and Magnetic Materials*, 504: 166566, 2020.

L. Dobranski, D. Jiles, and D. Atherton. Dependence of the anhysteretic magnetization on uniaxial stress in steel. *Journal of Applied Physics*, 57(8):4229–4231, 1985.

L. Domenig, K. Roppert, A. Gschwentner, A. Sauseng, and M. Kaltenbacher. Identification of parameters to correctly adapt energy-based hysteresis models regarding rotational losses. *IEEE Transactions on Magnetics*, pages 1–4, 2023. doi: 10.1109/TMAG.2023.3325287.

M. Domenjoud and L. Daniel. Effects of plastic strain and reloading stress on the magneto-mechanical behavior of electrical steels: Experiments and modeling. *Mechanics of Materials*, 176:104510, 2023.

M. Domenjoud, É. Berthelot, N. Galopin, R. Corcolle, Y. Bernard, and L. Daniel. Characterization of giant magnetostrictive materials under static stress: influence of loading boundary conditions. *Smart Materials and Structures*, 28(9):1–10, 2019. Art. no. 095012.

A. Dorfmann and R. Ogden. Magnetoelastic modelling of elastomers. *European Journal of Mechanics - A/Solids*, 22(4):497–507, 2003. ISSN 0997-7538. doi: https://doi.org/10.1016/S0997-7538(03)00067-6.

M. El Youssef, S. Clenet, A. Van Gorp, A. Benabou, P. Faverolle, and J.-C. Mipo. Improving global ferromagnetic characteristics of laminations by heterogeneous deformation. *IEEE Transactions on Energy Conversion*, 36(3):1953–1961, 2021.

A. C. Eringen and G. A. Maugin. *Electrodynamics of continua I: foundations and solid media*. Springer-Verlag, 1990.

A. Errigo, J.-K. Choi, and K. Kissock. Techno-economic-environmental impacts of industrial energy assessment: Sustainable industrial motor systems of small and medium-sized enterprises. *Sustainable Energy Technologies and Assessments*, 49:101694, 2022.

A. D. Eslamlou, A. Ghaderiaram, E. Schlangen, and M. Fotouhi. A review on non-destructive evaluation of construction materials and structures using magnetic sensors. *Construction and Building Materials*, 397:132460, 2023.

P. G. Evans and M. J. Dapino. Efficient magnetic hysteresis model for field and stress application in magnetostrictive galfenol. *Jounal of Applied Physics*, 107(6):063906, 2010. doi: 10.1063/1.3318494.

J. F. Fernandes, P. P. Bhagubai, and P. J. Branco. Recent developments in electrical machine design for the electrification of industrial and transportation systems. *Energies*, 15(17):6390, 2022.

K. Fonteyn, A. Belahcen, R. Kouhia, P. Rasilo, and A. Arkkio. Fem for directly coupled magneto-mechanical phenomena in electrical machines. *IEEE Transactions on Magnetics*, 46(8):2923–2926, 2010. doi: 10.1109/TMAG.2010.2044148.

V. François-Lavet, F. Henrotte, L. Stainier, L. Noels, and C. Geuzaine. An energy-based variational model of ferromagnetic hysteresis for finite element computations. *Journal of Computational and Applied Mathematics*, 246:243–250, 2013.

M. Frenea-Robin and J. Marchalot. Basic principles and recent advances in magnetic cell separation. *Magnetochemistry*, 8(1):11, 2022.

J. Garcia and M. Rivas. A quasi-static magnetic hysteresis loop measurement system with drift correction. *IEEE Transactions on Magnetics*, 42(1):15–17, 2005.

J. I. Goldstein, D. E. Newbury, J. R. Michael, N. W. Ritchie, J. H. J. Scott, and D. C. Joy. *Scanning electron microscopy and X-ray microanalysis*. Springer, New York, 2003.

I. Griva, S. G. Nash, and A. Sofer. *Linear and Nonlinear Optimization*. SIAM, Philadelphia, PA, USA, 2008.

Y. Guo, X. Ba, L. Liu, H. Lu, G. Lei, W. Yin, and J. Zhu. A review of electric motors with soft magnetic composite cores for electric drives. *Energies*, 16(4):2053, 2023.

H. Hauser. Energetic model of ferromagnetic hysteresis: Isotropic magnetization. *Journal of Applied Physics*, 96(5):2753–2767, 2004.

F. Henrotte, A. Nicolet, and K. Hameyer. An energy-based vector hysteresis model for ferromagnetic materials. *COMPEL*, 25:71–80, 2006. doi: 10.1108/03321640610634344.

F. Henrotte, S. Steentjes, K. Hameyer, and C. Geuzaine. Iron loss calculation in steel laminations at high frequencies. *IEEE Transactions on Magnetics*, 50(2):333–336, 2014.

J. Herskovits. Feasible direction interior-point technique for nonlinear optimization. *Journal of optimization theory and applications*, 99:121–146, 1998.

G. Houlsby and A. Puzrin. A thermomechanical framework for constitutive models for rate-independent dissipative materials. *International Journal of Plasticity*, 16(9):1017–1047, 2000. ISSN 0749-6419. doi: https://doi.org/10.1016/S0749-6419(99)00073-X.

A. Hubert and R. Schäfer. *Magnetic domains: the analysis of magnetic microstructures*. Springer Science & Business Media, 2008.

O. Hubert. Multiscale magneto-elastic modeling of magnetic materials including isotropic second order stress effect. *Journal of Magnetism and Magnetic Materials*, 491:1–16, 2019. ISSN 0304-8853. doi: https://doi.org/10.1016/j.jmmm.2019.165564. Art. no. 165564.

O. Hubert and K.-J. Rizzo. Anhysteretic and dynamic piezomagnetic behavior of a low carbon steel. *Journal of Magnetism and Magnetic Materials*, 320(20):e979–e982, 2008.

O. Hubert, L. Daniel, and L. Bernard. Multiscale modeling of magnetostrictive materials. In *Encyclopedia of Smart Materials*, pages 337–354. Elsevier, Oxford, 2022. ISBN 978-0-12-815733-6. doi: https://doi.org/10.1016/B978-0-12-803581-8.12058-2. URL https://www.sciencedirect.com/science/article/pii/B9780128035818120582.

S. Ito, T. Mifune, T. Matsuo, and C. Kaido. Macroscopic magnetization modeling of silicon steel sheets using an assembly of six-domain particles. *Journal of Applied Physics*, 117(17):1–4, 2015. doi: 10.1063/1.4915105. Art. no. 17D126.

S. Ito, T. Mifune, T. Matsuo, C. Kaido, Y. Takahashi, and K. Fujiwara. Simulation of the stress dependence of hysteresis loss using an energy-based domain model. *AIP Advances*, 8(4):1–7, 2018. doi: 10.1063/1.4993661. Art. no. 047501.

K. Jacques. *Energy-based magnetic hysteresis models-theoretical development and finite element formulations*. PhD thesis, 2018.

K. Jacques, S. Steentjes, F. Henrotte, C. Geuzaine, and K. Hameyer. Representation of microstructural features and magnetic anisotropy of electrical steels in an energy-based vector hysteresis model. *AIP Advances*, 8(4):1–10, 2018. Art. no. 047602.

F. Jiang, M. Rossi, and G. Parent. Anisotropy model for modern grain oriented electrical steel based on orientation distribution function. *AIP Advances*, 8(5), 2018.

D. Jiles. *Introduction to Magnetism and Magnetic Materials*. Chapman and Hall, London, 1991.

M. Kaltenbacher, K. Roppert, L. D. Domenig, and H. Egger. Comparison of energy based hysteresis models. In *2022 23rd International Conference on the Computation of Electromagnetic Fields (COMPUMAG)*, pages 1–4. IEEE, 2022.

S. Kankanala and N. Triantafyllidis. On finitely strained magnetorheological elastomers. *Journal of the Mechanics and Physics of Solids*, 52(12):2869–2908, 2004.

B. Kiefer, T. Bartel, and A. Menzel. Implementation of numerical integration schemes for the simulation of magnetic sma constitutive response. *Smart Materials and Structures*, 21(9): 094007, 2012.

A. Kovetz. *Electromagnetic theory*, volume 975. Oxford University Press Oxford, 2000.

K. Krabbenhoft, A. Lyamin, S. Sloan, and P. Wriggers. An interior-point algorithm for elastoplasticity. *International Journal for Numerical Methods in Engineering*, 69(3):592–626, 2007.

A. Krings, M. Cossale, A. Tenconi, J. Soulard, A. Cavagnino, and A. Boglietti. Magnetic materials used in electrical machines: A comparison and selection guide for early machine design. *IEEE Industry Applications Magazine*, 23(6):21–28, 2017.

C. M. Landis. Fully coupled, multi-axial, symmetric constitutive laws for polycrystalline ferroelectric ceramics. *Journal of the Mechanics and Physics of Solids*, 50(1):127–152, 2002.

J. V. Leite, A. Benabou, and N. Sadowski. Accurate minor loops calculation with a modified Jiles-Atherton hysteresis model. *COMPEL*, 28(3):741–749, 2009.

Z. Li, Z. Tang, O. Messal, A. Benabou, and S. Wang. Consideration of tensile stress in the odf-based approach for modelling the first magnetization curves of grain-oriented electrical steels. *Journal of Magnetism and Magnetic Materials*, 590:171704, 2024.

J. Liu, G. Y. Tian, B. Gao, K. Zeng, and F. Qiu. Domain wall characterization inside grain and around grain boundary under tensile stress. *Journal of Magnetism and Magnetic Materials*, 471:39–48, 2019.

Y. Liu, L. Daniel, G. Sebald, M. Lallart, K. Makihara, and B. Ducharne. Energy harvesting using magnetostrictive materials: Effects of material anisotropy and stress multiaxiality. *Sensors and Actuators A: Physical*, 366:115017, 2024.

M. LoBue, C. Sasso, V. Basso, F. Fiorillo, and G. Bertotti. Power losses and magnetization process in Fe–Si non-oriented steels under tensile and compressive stress. *Journal of Magnetism and Magnetic Materials*, 215-216:124–126, 2000. ISSN 0304-8853. doi: https://doi.org/10.1016/S0304-8853(00)00092-5.

Z. Maazaz, O. de La Barrière, and O. Hubert. Influence of plastic shear strain on the magnetic behaviour of pure iron. *Journal of Magnetism and Magnetic Materials*, 591:171753, 2024.

B. J. Mailhé, L. D. Bernard, L. Daniel, N. Sadowski, and N. J. Batistela. Modified-sst for uniaxial characterization of electrical steel sheets under controlled induced voltage and constant stress. *IEEE Transactions on Instrumentation and Measurement*, 69(12):9756–9765, 2020.

F. Martin, U. Aydin, A. Ruzibaev, Y. Ge, L. Daniel, L. Bernard, P. Rasilo, A. Benabou, and A. Belahcen. Analysis of the magneto-mechanical anisotropy of steel sheets in electrical applications. *IEEE Transactions on Magnetics*, 56(2):1–4, 2020.

T. Matsuo and M. Shimasaki. Two types of isotropic vector play models and their rotational hysteresis losses. *IEEE Transactions on Magnetics*, 44(6):898–901, 2008.

T. Matsuo, Y. Takahashi, and K. Fujiwara. Pinning field representation using play hysterons for stress-dependent domain-structure model. *Journal of Magnetism and Magnetic Materials*, 499:1–6, 2020. Art. no. 166303.

T. Matsuo, Y. Takahashi, and K. Fujiwara. Anisotropic vector play model and its application in magnetization analysis. *IEEE Transactions on Magnetics*, 59(5):1–4, 2023. doi: 10.1109/TMAG.2023.3234707.

G. A. Maugin. The saga of internal variables of state in continuum thermo-mechanics (1893–2013). *Mechanics Research Communications*, 69:79–86, 2015.

I. D. Mayergoyz. *Mathematical Models of Hysteresis*. Springer, New York, 1991.

C. Miehe, B. Kiefer, and D. Rosato. An incremental variational formulation of dissipative magnetostriction at the macroscopic continuum level. *International Journal of Solids and Structures*, 48(13):1846–1866, 2011.

G. Mörée and M. Leijon. Review of play and preisach models for hysteresis in magnetic materials. *Materials*, 16(6):2422, 2023.

A. J. Moses, P. I. Anderson, and T. Phophongviwat. Localized surface vibration and acoustic noise emitted from laboratory-scale transformer cores assembled from grain-oriented electrical steel. *IEEE Transactions on Magnetics*, 52(10):1–15, 2016.

A. Ouaddi, O. Hubert, J. Furtado, D. Gary, and S. Depeyre. Piezomagnetic behavior: experimental observations and multiscale modeling. *Mechanics & Industry*, 20(8):810, 2019.

L. Prigozhin, V. Sokolovsky, J. W. Barrett, and S. E. Zirka. On the energy-based variational model for vector magnetic hysteresis. *IEEE Transactions on Magnetics*, 52(12):1–11, 2016.

E. M. Purcell and D. J. Morin. *Electricity and magnetism*. Cambridge University Press, 2013.

B. S. Ram, A. Baghel, S. Kulkarni, L. Daniel, and I. Nlebedim. A frequency-dependent scalar magneto-elastic hysteresis model derived using multi-scale and jiles–atherton approaches. *IEEE Transactions on Magnetics*, 56(3):1–5, 2020.

P. Rasilo, D. Singh, U. Aydin, F. Martin, R. Kouhia, A. Belahcen, and A. Arkkio. Modeling of hysteresis losses in ferromagnetic laminations under mechanical stress. *IEEE Transactions on Magnetics*, 52(3):1–4, 2016. doi: 10.1109/TMAG.2015.2468599.

P. Rasilo, U. Aydin, F. Martin, A. Belahcen, R. Kouhia, and L. Daniel. Equivalent strain and stress models for the effect of mechanical loading on the permeability of ferromagnetic materials. *IEEE Transactions on Magnetics*, 55(6):1–4, 2019a.

P. Rasilo, D. Singh, J. Jeronen, U. Aydin, F. Martin, A. Belahcen, L. Daniel, and R. Kouhia. Flexible identification procedure for thermodynamic constitutive models for magnetostrictive materials. *Proceedings of the Royal Society A*, 475(2223):20180280, 2019b.

M. J. Sablik and D. C. Jiles. Coupled magnetoelastic theory of magnetic and magnetostrictive hysteresis. *IEEE Transactions on Magnetics*, 29(4):2113–2123, 1993.

M. J. Sablik and D. C. Jiles. Modeling the effects of torsional stress on hysteretic magnetization. *IEEE Transactions on Magnetics*, 35(1):498–504, 1999.

M. J. Sablik, H. Kwun, G. L. Burkhardt, and D. C. Jiles. Model for the effect of tensile and compressive stress on ferromagnetic hysteresis. *Journal of Applied Physics*, 61(8):3799–3801, 1987. doi: 10.1063/1.338650.

M. J. Sablik, G. L. Burkhardt, H. Kwun, and D. C. Jiles. A model for the effect of stress on the low-frequency harmonic content of the magnetic induction in ferromagnetic materials. *Journal of Applied Physics*, 63(8):3930–3932, 1988. doi: 10.1063/1.340609.

M. J. Sablik, S. W. Rubin, L. A. Riley, D. C. Jiles, D. A. Kaminski, and S. B. Biner. A model for hysteretic magnetic properties under the application of noncoaxial stress and field. *Journal of Applied Physics*, 74(1):480–488, 1993. doi: 10.1063/1.355257.

M. J. Sablik, B. Augustyniak, and M. Chmielewski. Modeling biaxial stress effects on magnetic hysteresis in steel with the field and stress axes noncoaxial. *Journal of Applied Physics*, 85 (8):4391–4393, 1999.

A. Sauseng, L. Domenig, K. Roppert, and M. Kaltenbacher. Adaptions of the energy-based hysteresis model for correct rotational losses. In *2022 IEEE 20th Biennial Conference on Electromagnetic Field Computation (CEFC)*, pages 01–02. IEEE, 2022.

R. Scorretti and F. Sixdenier. An analytical formula to identify the parameters of the energy-based hysteresis model. *Journal of Magnetism and Magnetic Materials*, 548:1–16, 2022. ISSN 0304-8853. doi: https://doi.org/10.1016/j.jmmm.2021.168748. URL https://www.sciencedirect.com/science/article/pii/S0304885321009768. Art. no. 168748.

A. Selema, M. Beretta, M. Van Coppenolle, H. Tiismus, A. Kallaste, M. N. Ibrahim, M. Rombouts, J. Vleugels, L. A. Kestens, and P. Sergeant. Evaluation of 3d-printed magnetic materials for additively-manufactured electrical machines. *Journal of Magnetism and Magnetic Materials*, 569:170426, 2023.

D. Singh, F. Martin, P. Rasilo, and A. Belahcen. Magnetomechanical model for hysteresis in electrical steel sheet. *IEEE Transactions on Magnetics*, 52(11):1–9, 2016.

A. Sipeky and A. Ivanyi. Preisach-type stress-dependent magnetic vector hysteresis model. *Physica B: Condensed Matter*, 403(2):491–495, 2008. ISSN 0921-4526. doi: https://doi.org/10.1016/j.physb.2007.08.082.

F. Sixdenier, O. Messal, A. Hilal, C. Martin, M.-A. Raulet, and R. Scorretti. Temperature-dependent extension of a static hysteresis model. *IEEE Transactions on Magnetics*, 52(3): 1–4, 2015.

D. Stojakovic. Electron backscatter diffraction in materials characterization. *Processing and Application of Ceramics*, 6(1):1–13, 2012.

A. Sutor, S. J. Rupitsch, and R. Lerch. A Preisach-based hysteresis model for magnetic and ferroelectric hysteresis. *Applied Physics A*, 100:425–430, 2010.

N. Takahashi, H. Morimoto, Y. Yunoki, and D. Miyagi. Effect of shrink fitting and cutting on iron loss of permanent magnet motor. *Journal of Magnetism and Magnetic Materials*, 320 (20):e925–e928, 2008.

W. L. Tan and D. M. Kochmann. An effective constitutive model for polycrystalline ferroelectric ceramics: Theoretical framework and numerical examples. *Computational Materials Science*, 136:223–237, 2017.

J. Taurines, M. Olive, R. Desmorat, O. Hubert, and B. Kolev. Integrity bases for cubic nonlinear magnetostriction. *Journal of Magnetism and Magnetic Materials*, 546:167885, 2022.

J. Taurines, B. Kolev, R. Desmorat, and O. Hubert. Modeling of the morphic effect using a vanishing 2nd order magneto-elastic energy. *Journal of Magnetism and Magnetic Materials*, 570:1–6, 2023. Art. no. 170471.

J. Taurines, F. Martin, P. Rasilo, and A. Belahcen. Thermodynamic description for magneto-plastic coupling in electrical steel sheets. *Journal of Magnetism and Magnetic Materials*, page 171846, 2024.

G. C. Tolentino, J. V. Leite, M. Rossi, O. Ninet, G. Parent, and J. Blaszkowski. Modeling of magnetic anisotropy in electrical steel sheet by means of cumulative distribution functions of gaussians. *IEEE Transactions on Magnetics*, 58(8):1–5, 2022.

B. Upadhaya, P. Rasilo, L. Perkkiö, P. Handgruber, A. Belahcen, and A. Arkkio. Comparison of anisotropic energy-based and Jiles–Atherton models of ferromagnetic hysteresis. *IEEE Transactions on Magnetics*, 56(4):1–7, 2020.

K. Yamazaki and H. Takeuchi. Impact of mechanical stress on characteristics of interior permanent magnet synchronous motors. *IEEE Transactions on Industry Applications*, 53(2): 963–970, 2017. doi: 10.1109/TIA.2016.2616408.

B. F. T. Zangho, Y. Liu, S. Zhang, M. Lallart, L. Morel, G. Sebald, P. Tsafack, and B. Ducharne. Magnetostrictive energy conversion ability of iron cobalt vanadium alloy sheet: Experimental and theoretical evaluation. *Journal of Intelligent Material Systems and Structures*, page 1045389X231225502, 2024.

W. Zhao, S. Wang, X. Xie, X. Zhou, and L. Liu. A simplified multiscale magneto-mechanical model for magnetic materials. *Journal of Magnetism and Magnetic Materials*, 526:1–9, 2021. ISSN 0304-8853. doi: https://doi.org/10.1016/j.jmmm.2020.167695. Art. no. 167695.

H. Ziegler. Linear elastic stability: A critical analysis of methods. *Zeitschrift für angewandte Mathematik und Physik ZAMP*, 4(3):167–185, 1953.

S. E. Zirka, Y. I. Moroz, R. G. Harrison, and K. Chwastek. On physical aspects of the Jiles-Atherton hysteresis models. *Journal of Applied Physics*, 112(4):1–7, 2012. doi: 10.1063/1.4747915. Art. no. 043916.

A Appendix A: Elements of convex analysis

In this appendix, some elements of convex analysis discussed in the work are introduced. First, it is introduced the notion of convex set. A set S is convex if, for any elements $x_1, x_2 \in S$, a line segment that connects x_1 and x_2 is also in S, so Boyd and Vandenberghe [2004]:

$$\alpha x_1 + (1-\alpha)x_2 \in S \qquad \text{with} \qquad 0 \leq \alpha \leq 1 \tag{A.0.1}$$

A function $f : {R_e}^n \rightarrow R_e$ is convex on a convex set S if, for any $x_1, x_2 \in S$, it satisfies Boyd and Vandenberghe [2004]:

$$f\left(\alpha x_1 + (1-\alpha)x_2\right) \leq \alpha f(x_1) + (1-\alpha) f(x_2) \tag{A.0.2}$$

As an example, consider the concave function f represented in Fig. A.0.1. The inequality requirement of (A.0.2) means that the line segment connecting x_1 and x_2 lies above the graph of the function for all $0 \leq \alpha \leq 1$.

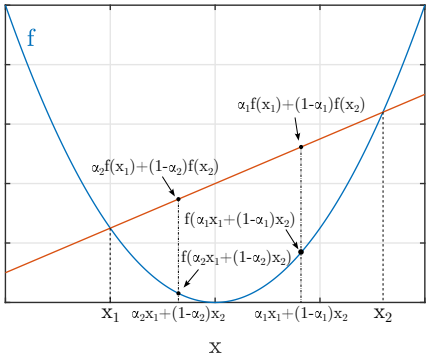

Figura A.0.1: Example of a convex function.

An important element of convex analysis used in this work is the notion of subdifferential. At x, the subdifferential of a convex function f is defined by Prigozhin et al. [2016]:

$$\partial f(x) := \left\{ z \in {R_e}^n : \; f(y) \geq f(x) + z^t (y-x), \quad \forall\, y \in {R_e}^n \right\} \tag{A.0.3}$$

with z the subgradients of f at x. The subgradients are a generalization of the concept of gradient to a non-differentiable function. If the function is differentiable, then:

$$\partial f(x) = \text{grad}\, f(x) \tag{A.0.4}$$

For example, the convex function $f(x) = \|x\|$ illustrated in Fig. A.0.2 is non-differentiable at $x = 0$. In this case, from the definition of (A.0.3) the subgradient results in:

$$\|y\| \geq zy \qquad \rightarrow \qquad z \in [-1,1] \tag{A.0.5}$$

For $x > 0$ and $x < 0$, the function is differentiable and results in $\text{sign}(x)$. The subdifferential for this example then is:

$$\partial f(x) = \begin{cases} -1, & \text{if } x < 0 \\ [-1,1], & \text{if } x = 0 \\ 1, & \text{if } x > 0 \end{cases} \tag{A.0.6}$$

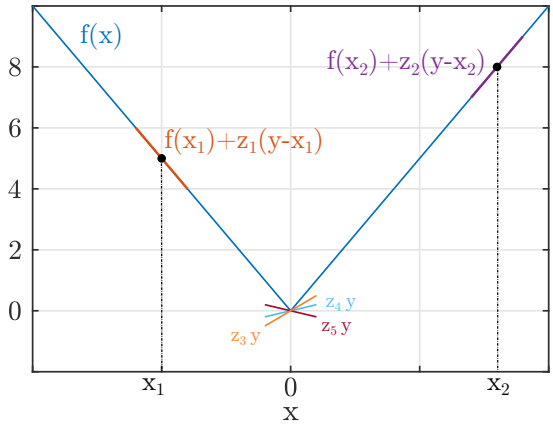

Figura A.0.2: Example of a non-differentiable convex function.

B Appendix B: Identification of the magnetostriction constant λ_s'

The identification of the second-order magnetostriction constant λ_s' is obtained from the analysis of the anhysteretic relative magnetic permeability $\mu_r^{anh}(\sigma)$, considering isotropic materials, and the magnetic field in the direction of the uniaxial stress da Silva et al. [2022]. The starting point is the expression of the magnetization given bellow (see (67) from Hubert [2019]).

$$M = \int_0^\pi \left[\frac{M_s \cos\phi e^{\left(\frac{3\chi_0 H}{M_s}\cos\phi + B(\sigma)(\cos^2\phi - 1/3)\right)}}{\int_0^\pi e^{\left(\frac{3\chi_0 H}{M_s}\cos\phi + B(\sigma)(\cos^2\phi - 1/3)\right)}\sin(\phi)d\phi} \sin\phi d\phi \right] \tag{B.0.1}$$

where $B(\sigma)$ is:

$$\begin{aligned} B(\sigma) &= 1.5A_s\lambda_s'\left(\sigma^2 + \sigma\frac{\lambda_s}{\lambda_s'}\right) \\ &= 1.5A_s\lambda_s'\left(\left(\sigma - \left(\frac{-\lambda_s}{2\lambda_s'}\right)\right)^2 - \left(\frac{-\lambda_s}{2\lambda_s'}\right)^2\right). \end{aligned} \tag{B.0.2}$$

The quantity $-\lambda_s/2\lambda_s'$ (homogeneous to a stress) is denoted by σ_m. It can be noticed that, for any stress σ, one has $B(\sigma_m + \sigma) = B(\sigma_m - \sigma)$. This shows that independently of the magnetic field, the magnetization as a function of stress is always symmetric with respect to $\sigma = \sigma_m$. Such symmetry is naturally inherited by the relative permeability. Furthermore to prove that μ_r^{anh} is maximal at σ_m, we first carry out the integration with respect to ϕ in (B.0.1) which yields:

$$M = M_s\left[\frac{e^B\left(e^{\frac{3\chi_0 H}{M_s}} - e^{-\frac{3\chi_0 H}{M_s}}\right)e^{\left(\frac{9H^2{\chi_0}^2}{4{M_s}^2 B}\right)}}{\sqrt{B\pi}\left(\text{erfi}\left(\sqrt{B} - \frac{3H\chi_0}{2M_s\sqrt{B}}\right) + \text{erfi}\left(\sqrt{B} + \frac{3H\chi_0}{2M_s\sqrt{B}}\right)\right)} - \frac{3H\chi_0}{2M_s B}\right], \tag{B.0.3}$$

where erfi is the imaginary error function given as:

$$\text{erfi}(x) = \frac{2}{\sqrt{\pi}}\int_0^x e^{t^2}dt. \tag{B.0.4}$$

Upon taking the limit of $\partial M/\partial H$ at $H \to 0$ one gets:

$$\mu_r^{anh}(\sigma) = 1 + 3\chi_0 \left(\frac{e^{B(\sigma)}}{\sqrt{B(\sigma)\pi}\,\mathrm{erfi}(\sqrt{B(\sigma)})} - \frac{1}{2B(\sigma)} \right). \tag{B.0.5}$$

This gives an analytical expression of the relative magnetic permeability, in the case of isotropic materials when the uniaxial loading is applied parallel to the magnetic field. By studying the function $\mu_r^{anh}(\sigma)$, one can show that: (a) it is maximal at $\sigma_m = -\lambda_s/2\lambda_s'$, (b) it has $\sigma = \sigma_m$ as an axis of symmetry, (c) it has $\mu_r^{anh} = 1$ as a horizontal asymptote and (d) equals $1 + \chi_0$ for $\sigma = 0$ (using a second-order Taylor series expansion).

C Appendix C: Identification of the crystallographic orientations

C.1 Crystallographic orientations

A polycrystalline material is composed of several grains (or crystals) with a given orientation, as shown in Fig. C.1.1 (a). Two coordinate systems can be introduced: (a) X,Y,Z corresponding to the sample coordinate system, which for laminated steel is defined by rolling (RD), transverse (TD), and normal directions (ND), and (b) defined by the grain coordinate system, which for cubic symmetry corresponds to the edges direction of a cube [1 0 0], [0 1 0], and [0 0 1]. Both coordinate systems are illustrated in Fig. C.1.1 (b). The grain orientation can be represented by rotations that relate the sample coordinate system to the grain coordinate system. These rotations are described by the Euler angles $(\varphi_1, \Phi, \varphi_2)$ Stojakovic [2012].

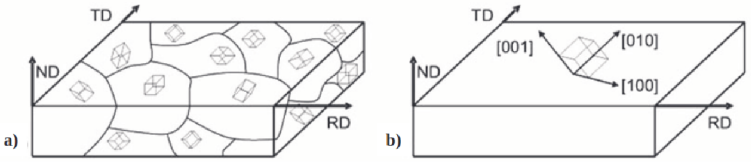

Figura C.1.1: Representation of a polycrystal material with cubic symmetry: (a) arrangement of grains, and (b) definition of the coordinate systems Stojakovic [2012].

To illustrate the Euler angles $(\varphi_1, \Phi, \varphi_2)$, consider the two coordinate systems previously introduced and shown in Fig. C.1.2 (a). The Euler angles representation is usually performed following the Bunge convention Bunge [2013]: the angle φ_1 is defined from a rotation about the ND axis, resulting in a new coordinate system $(\mathrm{RD}', \mathrm{TD}', \mathrm{ND})$ (see Fig. C.1.2 (b)). A second rotation is performed about the RD' axis, resulting in the angle Φ, and in the coordinate system $(\mathrm{RD}', \mathrm{TD}'', \mathrm{ND}'')$ (see Fig. C.1.2 (c)). Note that now the axis ND'' corresponds to the axis [0 0 1]. A final rotation about the axis ND'' corresponds to the angle φ_2. The final coordinate system $(\mathrm{RD}''', \mathrm{TD}''', \mathrm{ND}''')$ lies parallel to the grain coordinate system $\big([1\,0\,0]\ [0\,1\,0]\ [0\,0\,1]\big)$.

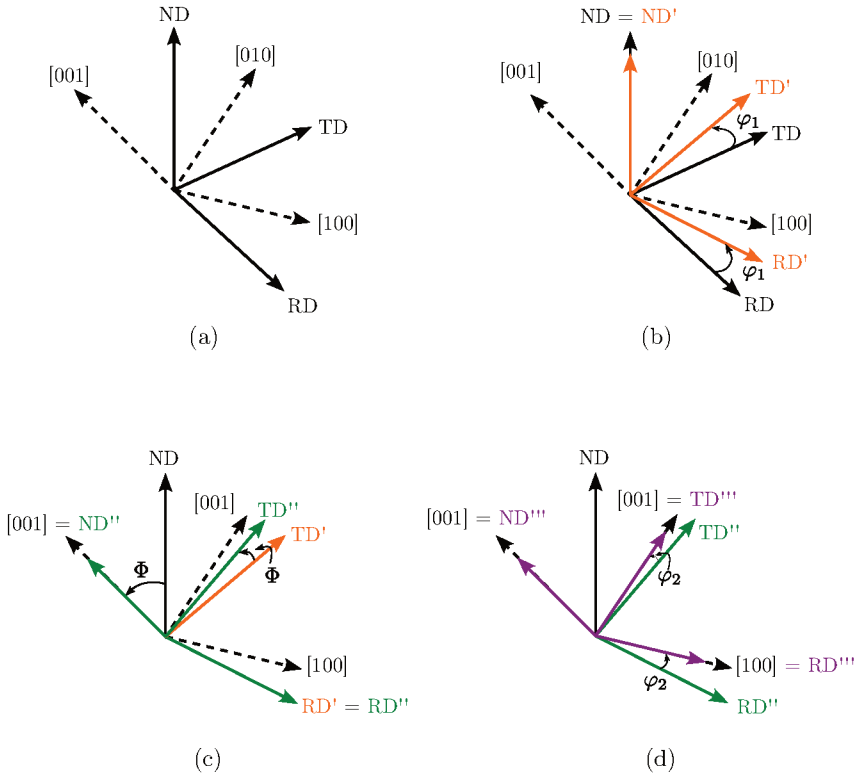

Figura C.1.2: Representation of a polycrystal material with cubic symmetry: (a) arrangement of grains, and (b) definition of the coordinate systems Stojakovic [2012].

Thus, the rotation matrix $R(\varphi_1, \Phi, \varphi_2)$ is defined from each rotation contribution Bunge [2013]:

$$
\begin{aligned}
R(\varphi_1,\Phi,\varphi_2) &= R_1(\varphi_1)\,R_2(\Phi)\,R_3(\varphi_2) \qquad \text{with} \\
R_1(\varphi_1) &= \begin{bmatrix} \cos\varphi_1 & \sin\varphi_1 & 0 \\ -\sin\varphi_1 & \cos\varphi_1 & 0 \\ 0 & 0 & 1 \end{bmatrix} \\
R_2(\Phi) &= \begin{bmatrix} 1 & 0 & 0 \\ 0 & \cos\Phi & \sin\Phi \\ 0 & -\sin\Phi & \cos\Phi \end{bmatrix} \\
R_3(\varphi_2) &= \begin{bmatrix} \cos\varphi_2 & \sin\varphi_2 & 0 \\ -\sin\varphi_2 & \cos\varphi_2 & 0 \\ 0 & 0 & 1 \end{bmatrix} .
\end{aligned}
\tag{C.1.1}
$$

C.2 Representation of an orientation

A crystallographic texture - with orientation defined by the Euler angles - can be illustrated by the pole figures. Such figures are built from the stereographic projection of the crystallographic directions on an equatorial plane. For example, consider two coordinate systems (for the sample and the grain) shown in Fig. C.2.1 (left). The resulting 100 pole figure from the stereographic projection is shown in Fig. C.2.1 (right).

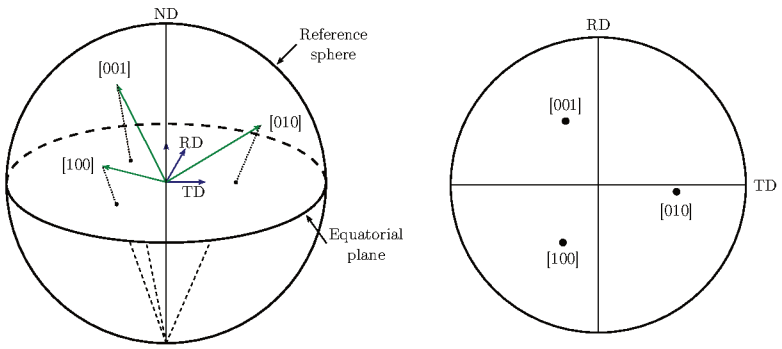

Figura C.2.1: Construction of a 100 pole figure (adapted from Bunge [2013]).

The pole figures analysis of polycrystalline materials - with many more grains - can be simplified by using the representation of the orientation distribution function (ODF). The

volume fraction of grains with the same orientation defines the ODF, which can be represented by a probability density Bunge [2013].

C.3 Texture measurements

The crystallographic orientation of grains in polycrystalline materials can be identified using diffraction techniques. In the results presented in this work, the electron backscatter diffraction (EBSD) implemented in a scanning electron microscope (SEM) was employed to identify the crystallographic texture of the studied materials. The EBSD measurement technique consists of illuminating a point of interest on a sample with an electron beam (see the schematic of Fig. C.3.1). The diffracted electrons form a set of cones. A fluorescent screen positioned near the sample captures these cones (two per atom lattice plane). The set of grain lattice planes form the EBSD patterns - also called Kikuchi patterns. Fig. C.3.2 depicts the Kikuchi patterns for a sample of Fe-Si. Each line pair (or band) represents a crystallographic plane in the grain, and the distances between the bands represent the angles between the crystallographic plans. The Kikuchi patterns are then image processed, and several methods can be employed to determine the crystal orientation Goldstein et al. [2003].

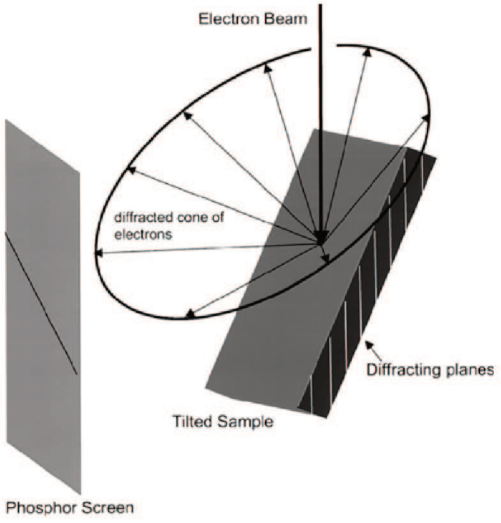

Figura C.3.1: Illustration of the experimental apparatus for the EBSD measurements Goldstein et al. [2003].

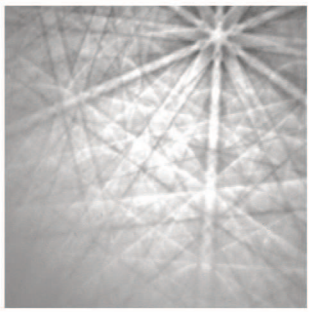

Figura C.3.2: Kikuchi patterns from a sample of Fe-Si Daniel [2003].

D Appendix D: Conservation of energy

Considering an arbitrary volume $\mathscr{B}$ with boundary $\partial\mathscr{B}$, the first law of thermodynamics for the magneto-mechanical case can be stated as Kovetz [2000]:

$$\dot{E} = P_{mec} + P_{mag} + P_{th}, \tag{D.0.1}$$

with $\dot{E}$ the time-derivative of the total energy E, P_{mec} the mechanical power, P_{mag} the magnetic power, and P_{th} the thermal power. The total energy E can be expressed in terms of the internal energy u and the kinetic energy by:

$$E = \int_{\mathscr{B}} \left[u + \frac{1}{2}\rho\, \dot{\vec{u}} \cdot \dot{\vec{u}} \right] dv. \tag{D.0.2}$$

with $\dot{\vec{u}}$ the time-derivative of the displacement $\vec{u}$, and ρ the mass density. From the continuum mechanics framework presented in Chapter 2, the mechanical power is defined by:

$$\begin{aligned} P_{mec} &= \int_{\mathscr{B}} \vec{b} \cdot \dot{\vec{u}}\, dv + \int_{\partial\mathscr{B}} (\sigma\vec{n}) \cdot \dot{\vec{u}}\, ds \\ &= \int_{\mathscr{B}} \vec{b} \cdot \dot{\vec{u}}\, dv + \int_{\mathscr{B}} \operatorname{div}(\sigma \cdot \dot{\vec{u}})\, dv \\ &= \int_{\mathscr{B}} \vec{b} \cdot \dot{\vec{u}}\, dv + \int_{\mathscr{B}} \left[\sigma : \operatorname{grad} \dot{\vec{u}} + \dot{\vec{u}} \cdot \operatorname{div} \sigma \right] dv \\ &= \int_{\mathscr{B}} \left[\dot{\vec{u}} \cdot \left(\vec{b} + \operatorname{div} \sigma \right) + \sigma : \operatorname{grad} \dot{\vec{u}} \right] dv, \end{aligned} \tag{D.0.3}$$

with $\vec{b}$ the body forces and σ the symmetric second-order stress tensor. The surface integral is transformed into a volume integral by using the divergence theorem. From the balance of linear momentum, it is defined the following identity Kovetz [2000]:

$$\rho\, \frac{d}{dt} \dot{\vec{u}} = \vec{b} + \operatorname{div} \sigma. \tag{D.0.4}$$

The mechanical power is then:

$$P_{mec} = \int_{\mathscr{B}} \left[\dot{\vec{u}} \cdot \rho\, \frac{d}{dt} \dot{\vec{u}} + \sigma : \operatorname{grad} \dot{\vec{u}} \right] dv. \tag{D.0.5}$$

The magnetic power is defined by Kovetz [2000]:

$$P_{mag} = -\int_{\partial\mathscr{B}} \vec{n}\cdot\left(\vec{E}\times\vec{H}\right)\, ds = -\int_{\mathscr{B}} \operatorname{div}(\vec{E}\times\vec{H})\, dv, \tag{D.0.6}$$

with $\vec{E}$ the electrical field, and $\vec{H}$ the magnetic field. The term $(\vec{E}\times\vec{H})$ represents the electromagnetic power density, also denoted as Poynting vector. By using the Maxwell equations under quasi-static regime, the divergence of the Poynting vector can be expanded as:

$$\operatorname{div}(\vec{E}\times\vec{H}) = \operatorname{curl}\vec{E}\cdot\vec{H} - \vec{E}\cdot\operatorname{curl}\vec{H} = -\dot{\vec{B}}\cdot\vec{H} - \vec{E}\cdot\vec{J}_c, \tag{D.0.7}$$

with $\vec{J}_c$ the current density. The magnetic power is then:

$$P_{mag} = \int_{\mathscr{B}} \left[\dot{\vec{B}}\cdot\vec{H} + \vec{E}\cdot\vec{J}_c\right]\, dv. \tag{D.0.8}$$

The thermal power is written as Kovetz [2000]:

$$P_{th} = \int_{\mathscr{B}} r\, dv - \int_{\partial\mathscr{B}} \vec{q}\cdot\vec{n}\, ds = \int_{\mathscr{B}} r\, dv - \int_{\mathscr{B}} \operatorname{div}\vec{q}\, dv, \tag{D.0.9}$$

with r the heat power source, and $\vec{q}$ the heat flux. Combining the previous equations, the energy balance can be written as:

$$\begin{gathered}\frac{d}{dt}\left[u + \frac{1}{2}\rho\,\dot{\vec{u}}\cdot\dot{\vec{u}}\right] = \dot{\vec{u}}\cdot\rho\,\frac{d}{dt}\dot{\vec{u}} + \boldsymbol{\sigma} : \operatorname{grad}\dot{\vec{u}} - \dot{\vec{B}}\cdot\vec{H} - \vec{E}\cdot\vec{J}_c + r - \operatorname{div}\vec{q} \\ \dot{u} = \boldsymbol{\sigma} : \operatorname{grad}\dot{\vec{u}} - \dot{\vec{B}}\cdot\vec{H} - \vec{E}\cdot\vec{J}_c + r - \operatorname{div}\vec{q}.\end{gathered} \tag{D.0.10}$$

The velocity gradient tensor $\operatorname{grad}\dot{\vec{u}}$ can be split into a symmetric and anti-symmetric parts as:

$$\operatorname{grad}\dot{\vec{u}} = \frac{1}{2}\left[\operatorname{grad}\dot{\vec{u}} + \left(\operatorname{grad}\dot{\vec{u}}\right)^T\right] + \frac{1}{2}\left[\operatorname{grad}\dot{\vec{u}} - \left(\operatorname{grad}\dot{\vec{u}}\right)^T\right]. \tag{D.0.11}$$

Due to the symmetry of the stress tensor, the product of $\boldsymbol{\sigma}$ with the second term on the right side of (D.0.11) is zero. From the small strain hypothesis, the first term on the right side (D.0.11) is the rate of the strain tensor $\boldsymbol{\varepsilon}$. Neglecting the electric field contribution and the heat power source, the first law of thermodynamics for the magneto-mechanical case is:

$$\dot{u} = \sigma : \dot{\varepsilon} + \vec{H} \cdot \dot{\vec{B}} - \operatorname{div} \vec{q}. \tag{D.0.12}$$

E Appendix E: Identification of the pinning field distribution

The identification of the pinning field distribution was performed following the procedure given in Henrotte et al. [2014], Jacques et al. [2018]. Starting from the demagnetized state, after the application of a unidirectional magnetic field H_a, the homogenized reversible field is

$$H_{rev}(0 \to H_a) = \int_0^\infty \max(H_a - \kappa, 0)\ \omega(\kappa) d\kappa = F(H_a), \tag{E.0.1}$$

where the max operation indicates that only the cells with $\kappa < H_a$ will be modified. An auxiliary function $F(H)$ is then defined:

$$F(H) = \int_0^H \omega(\kappa)(H - \kappa)\ d\kappa, \tag{E.0.2}$$

with first and second derivatives:

$$\frac{\partial F(H)}{\partial H} = \int_0^H \omega(\kappa)\ d\kappa \qquad \text{and} \qquad \frac{\partial^2 F(H)}{\partial H^2} = \omega(H). \tag{E.0.3}$$

From the previous magnetic state, if now the magnetic field is decreased until the coercive field $-H_c$, with $0 < H_c < H_a$, the homogenized reversible field is Henrotte et al. [2014], Jacques et al. [2018]:

$$H_{rev}\ (0 \to H_a \to -H_c) = F(H_a) - 2F\left(\frac{H_a + H_c}{2}\right). \tag{E.0.4}$$

Because the magnetization is null at the coercive field $M(H_{rev}(0 \to H_a \to -H_c)) = 0$ Henrotte et al. [2014], Jacques et al. [2018]:

$$F(H_a) - 2F\left(\frac{H_a + H_c}{2}\right) = 0. \tag{E.0.5}$$

Therefore, the identification of $F(H)$ can be performed through experimental measurements of coercive field curve under increasing magnetic field $H_c(H_{peak})$ Henrotte et al. [2014]. The pinning field distribution is evaluated from (E.0.3).

The steps to construct $F(H)$ are Henrotte et al. [2014], Jacques et al. [2018]:

- Starting from a saturating magnetic field H_s, where $H_c(H_s) = H_c^{max}$, from (E.0.2) is observed that:

$$F(H_s) = H_s - H_c^{max} \qquad \text{with} \qquad H_c^{max} = \int_0^{H_s} \kappa\omega(\kappa)d\kappa. \tag{E.0.6}$$

- Because $H_c(H) < H$:

$$\frac{H + H_c(H)}{2} < H. \tag{E.0.7}$$

A strictly decreasing series is defined:

$$H^n = \frac{H^{n-1} + H_c(H^{n-1})}{2} < H^{n-1}, \tag{E.0.8}$$

with

$$F(H^n) = \frac{F\left(H^{n-1}\right)}{2}. \tag{E.0.9}$$

For numerical simulation purposes, a discrete approximation of $\omega(\kappa)$ can be evaluated. The magnetic field is decomposed into N discrete parts and the discrete set $(\omega^k, \kappa^k)_{k=1,\dots,N}$ is Henrotte et al. [2014]:

$$\begin{aligned} \omega^k &= \int_{H^{k-1}}^{H^k} \omega(\kappa)d\kappa = \frac{\partial F(H^k)}{\partial H} - \frac{\partial F(H^{k-1})}{\partial H} \\ \kappa^k &= \frac{\int_{H^{k-1}}^{H^k} \kappa\omega(\kappa)d\kappa}{\int_{H^{k-1}}^{H^k} \omega(\kappa)d\kappa} = \frac{\left[H\partial_H F(H) - F(H)\right]_{H^{k-1}}^{H^k}}{\omega^k}. \end{aligned} \tag{E.0.10}$$

F Appendix F: Numerical implementation of the minimization

The minimization of the magneto-elastic hysteresis model with the domain volume fractions as internal variables is here detailed. The minimization problem is defined in Chapter 5 and is given by:

$$\begin{aligned} \min_{p_\alpha} \quad & \Omega = \sum_{\alpha=1}^{n} p_\alpha^{n+1} \left[g_\alpha + \frac{1}{A_s} \log p_\alpha^{n+1} \right] + \sum_{\alpha=1}^{n} |\kappa_\alpha \left(p_\alpha^{n+1} - p_\alpha^{n} \right)| \\ \text{s.t.} \quad & \left(\sum_{\alpha=1}^{n} p_\alpha^{n+1} \right) - 1 = 0, \\ & 0 \leq p_\alpha^{n+1} \leq 1 \end{aligned} \tag{F.0.1}$$

To avoid the derivative, the absolute value function is replaced by the constant y_α, defined by:

$$|\kappa_\alpha \left(p_\alpha^{n+1} - p_\alpha^{n} \right)| = y_\alpha, \tag{F.0.2}$$

with additional constraints added to the minimization problem:

$$-y_\alpha \leq \kappa_\alpha \left(p_\alpha^{n+1} - p_\alpha^{n} \right) \leq y_\alpha, \tag{F.0.3}$$

such that the minimization problem is given by:

$$\begin{aligned} \min_{p_\alpha} \quad & \Omega = \sum_{\alpha=1}^{n} p_\alpha^{n+1} \left[g_\alpha + \frac{1}{A_s} \log p_\alpha^{n+1} \right] + \sum_{\alpha=1}^{n} y_\alpha \\ \text{s.t.} \quad & \left(\sum_{\alpha=1}^{n} p_\alpha^{n+1} \right) - 1 = 0, \\ & -y_\alpha \leq \kappa \left(p_\alpha^{n+1} - p_\alpha^{n} \right) \leq y_\alpha. \end{aligned} \tag{F.0.4}$$

Following the interior-point methodology, the inequality constraints are transformed to equality constraints by introducing the slack variables Griva et al. [2008], Krabbenhoft et al. [2007]. By using this strategy, a penalty term is added to the objective function:

$$
\begin{aligned}
\min_{p_\alpha} \quad & \Omega = \sum_{\alpha=1}^{n} p_\alpha^{n+1}\left[g_\alpha + \frac{1}{A_s}\log p_\alpha^{n+1}\right] + \sum_{\alpha=1}^{n} y_\alpha + \mu_i\left[\log(s_1)+\log(s_2)\right] \\
\text{s.t.} \quad & \left(\sum_{\alpha=1}^{n} p_\alpha^{n+1}\right) - 1 = 0, \\
& \kappa\left(p_\alpha^{n+1} - p_\alpha^{n}\right) + y_\alpha - s_1 = 0, \\
& -\kappa\left(p_\alpha^{n+1} - p_\alpha^{n}\right) + y_\alpha - s_2 = 0, \\
& \text{with} \qquad s_1, s_2 \geq 0,
\end{aligned}
\tag{F.0.5}
$$

with s_1, s_2 slack variables and μ_i a small positive constant. The Lagrangean can be build as:

$$
\begin{aligned}
\mathscr{L}(p_\alpha, s, \lambda, \mu^\alpha) = \Omega + \lambda\left[\left(\sum_{\alpha=1}^{n} p_\alpha\right) - 1\right] + \mu_1^\alpha\left[\kappa\left(p_\alpha^{n+1} - p_\alpha^{n}\right) + y_\alpha - s_1\right] + \\
+ \mu_2^\alpha\left[-\kappa\left(p_\alpha^{n+1} - p_\alpha^{n}\right) + y_\alpha - s_2\right].
\end{aligned}
\tag{F.0.6}
$$

The necessary and sufficient Karush-Kuhn-Tucker (KKT) conditions are:

$$\frac{\partial \mathscr{L}}{\partial p_\alpha^{n+1}} = 0 \tag{F.0.7a}$$

$$\frac{\partial \mathscr{L}}{\partial y_\alpha} = 0 \tag{F.0.7b}$$

$$\frac{\partial \mathscr{L}}{\partial s} = 0 \tag{F.0.7c}$$

$$\frac{\partial \mathscr{L}}{\partial \lambda} = 0 \tag{F.0.7d}$$

$$\frac{\partial \mathscr{L}}{\partial \mu^\alpha} = 0. \tag{F.0.7e}$$

From the KKT conditions, the residual vector is given by:

$$
\begin{aligned}
R_a &= \frac{\partial \mathscr{L}}{\partial p_\alpha^{n+1}} = \exp\left[A_s\left(-g_\alpha - \lambda + \kappa(-\mu_1^\alpha + \mu_2^\alpha) - 1\right] - p_\alpha^{n+1} = 0,\\
R_b &= \frac{\partial \mathscr{L}}{\partial y_\alpha} = 1 + \mu_1^\alpha + \mu_2^\alpha = 0,\\
R_c &= \frac{\partial \mathscr{L}}{\partial s_1} = -s_1\mu_1^\alpha + \mu_i = 0,\\
R_d &= \frac{\partial \mathscr{L}}{\partial s_2} = -s_2\mu_2^\alpha + \mu_i = 0,\\
R_e &= \frac{\partial \mathscr{L}}{\partial \lambda} = \left(\sum_{\alpha=1}^{n} p_\alpha\right) - 1 = 0,\\
R_f &= \frac{\partial \mathscr{L}}{\partial \mu_1^\alpha} = \kappa\left(p_\alpha^{n+1} - p_\alpha^n\right) + y_\alpha - s_1 = 0,\\
R_g &= \frac{\partial \mathscr{L}}{\partial \mu_2^\alpha} = -\kappa\left(p_\alpha^{n+1} - p_\alpha^n\right) + y_\alpha - s_2 = 0.
\end{aligned}
\tag{F.0.8}
$$

The variables are iteratively solved using a Newton method Griva et al. [2008]:

$$
\begin{bmatrix} R_a^{(k)} \\ R_b^{(k)} \\ R_c^{(k)} \\ R_d^{(k)} \\ R_e^{(k)} \\ R_f^{(k)} \\ R_g^{(k)} \end{bmatrix}
= -
\begin{bmatrix}
\frac{\partial R_a^{(k)}}{\partial p_\alpha^{n+1}} & \frac{\partial R_a^{(k)}}{\partial y_\alpha} & \frac{\partial R_a^{(k)}}{\partial s_1} & \frac{\partial R_a^{(k)}}{\partial s_2} & \frac{\partial R_a^{(k)}}{\partial \lambda} & \frac{\partial R_a^{(k)}}{\partial \mu_1^\alpha} & \frac{\partial R_a^{(k)}}{\partial \mu_2^\alpha} \\
\vdots & \vdots & \vdots & \vdots & \vdots & \vdots & \vdots \\
\frac{\partial R_g^{(k)}}{\partial p_\alpha^{n+1}} & \frac{\partial R_g^{(k)}}{\partial y_\alpha} & \frac{\partial R_g^{(k)}}{\partial s_1} & \frac{\partial R_g^{(k)}}{\partial s_2} & \frac{\partial R_g^{(k)}}{\partial \lambda} & \frac{\partial R_g^{(k)}}{\partial \mu_1^\alpha} & \frac{\partial R_g^{(k)}}{\partial \mu_2^\alpha}
\end{bmatrix}
\begin{bmatrix} \Delta p_\alpha \\ \Delta y_\alpha \\ \Delta s_1 \\ \Delta s_2 \\ \Delta\lambda \\ \Delta\mu_1^\alpha \\ \Delta\mu_2^\alpha \end{bmatrix},
\tag{F.0.9}
$$

with k indicating the iteration step.